Sede Amministrativa: Università degli Studi di Padova

Centro Interdipartimentale Di Ricerca Di Studi Ed Attivita' Spaziali "G.Colombo"

SCUOLA DI DOTTORATO DI RICERCA IN: SCIENZE TECNOLOGIE E MISURE SPAZIALI

INDIRIZZO: ASTRONAUTICA E SCIENZE DA SATELLITE

CICLO: XXV

A TELEDETECTION SYSTEM BASED ON SURFACE PLASMON RESONANCE SENSORS FOR ENVIRONMENTAL POLLUTANTS

Direttore della Scuola: Ch.mo Prof. Giampiero Naletto

Coordinatore d'indirizzo: Ch.mo Prof. Giampiero Naletto

Supervisore: Dott. ssa Maria Guglielmina Pelizzo

Co-Supervisore: Dott.ssa Zuppella Paola

Dottorando: Silvia Tosatto

Summary of this Ph.D Thesis

Surface Plasmon Resonance (SPR) based sensors are optical devices composed of a light source,a Transverse Magnetic polarizer, a coupling element as a prism, a grating or a waveguide, a structure supporting the surface plasmon, a biorecognition layer, a flow cell and a detector.
The surface plasmon is in fact a surface wave that corresponds to a coherent oscillation of electrons (Pluchery et al. (2011))which takes place at a metal-dielectric interface.
The biorecognition layer instead is conceived for creating reversible chemical bounds with the target substances.
SPR sensors are in particular based on the coupling occurring under precise circumstances between the radiation and the surface plasmon.

Depending on the refraction indexes of the materials and radiation wavelength it is possible to observe, for a specific incidence angle, a reflectivity coupling feature in the transmitted light intensity, usually a minimum, and a phase variation.
The presence of the analytes increases the refraction index of the biorecognition layer and so changes the coupling angle proportionally to its concentration.
The presence, and also the concentration, of the analyte is thus determinated by mean of the reflected light intensity or phase.

The aim of my research activity was to study the feasibility of a teledetection system for the detection of environmental pollutants based on Surface Plasmon Resonance sensors.

In order to achieve this objective my research activity has involved

- ⋆ to gather documentation on the state of the art in Surface Plasmon Resonance based sensors
- ⋆ to implement computer simulations to evaluate innovative SPR sensors, using also peculiar materials
- ⋆ to realize Surface Plasmon prototypes in laboratory in order to create innovative setups and also for a future miniaturization
- ⋆ to study and determinate the more suitable components and characteristics for the target wireless sensor network
- ⋆ to test the possibility to create in laboratory a wireless two-sensors network

Many sensors based on the Surface Plasmon Resonance have been created in order to detect dangerous gases as NH_3, NO_2, SiO2, CO and aqueous environment pollutants as arsenic, ricin, endocrine disruptors, pesticides, heavy metals, bacteria, toxins and others.
Moreover this kind of optical sensor can be used in the research of organic or prebiotic molecules on the surface of Solar System bodies or comets, or to monitor space missions with human crew.

I made computer simulations of optical structures supporting the surface plasmon polaritons and comprising peculiar materials.
Regarding this aspect I simulated SPR sensors including metals showing Inverted Surface Plasmon Resonance, which is a maximum of reflectivity at the coupling angle instead of the common

minimum of reflectivity, and graphene. In particular the simulated SPR sensors were composed of a SF6 cylindrical prism with a coating of Chrome, a thin film of Iridium, Palladium, Terbium or Gold as reference and a single Graphene layer.
These sensors are conceived for the detection of Single Stranded DNA hybridization during the Double Stranded DNA formation and they are innovative because Iridium hasn't been used before in SPR sensors to my knowledge and the obtained signal is a sharp maximum of reflectivity that could be useful in SPR with static setup where a limited range of incidence angles is possible or in noisy conditions. Moreover the graphene layer acts as a protective layer from oxidation as well as a biorecognition layer for this chemical interaction.
An article on these results has been submitted.

I implemented a first SPR sensor with dynamic setup and I made observations of Helium and Pentane gases with it.
Then, in order to make observations in liquid environments and to reduce the measurement time, I built up an SPR sensor with static setup, in which the whole coupling reflectivity feature is observed at the same time, and I used an SF6 cylindrical prism.
I also refined the obtainable data image both simulating the effect of the collimating lens, the cylindrical prism and the real light intensity distribution and post-processing the image itself by correcting it for a slight rotation and applying a Gaussian filter.
Then as a following improvement I introduced an adaptive mirror on a similar optical setup.
Making use of an adaptive mirror in a SPR sensor it was possible to minimize the effects of a lens defocusing (or displacement) and of Spherical aberration, while Astigmatism and Coma aberrations did not seem to generate mayor contributions.

Moreover I documented myself on the existing wireless sensor networks (WSN) and I determined the elements of a feasible wireless sensor network based on Surface Plasmon Resonance sensors.
The SPR sensors would be powered and controlled by microcontroller sensor motes that would collect the data and send them by means of wireless antennas to some rooters. The latter devices would re-transmit the data by means of long range antennas to a base station consisting on a laptop with a receiving antenna and bidirectional broadband Internet connection via satellites.
I also found out the possible data that can be inferred from a SPR sensor and a possible data handling strategy.

In addition to that I chose some real components and I made some tests in order to build a small WSN with two SPR sensors in laboratory.
The test sensor network was composed of two SPR sensors connected to Linux motes that transmitted the data images by means of ZigBee antennas to a Windows PC, which analyzed and spread the data into Internet.
I therefore implemented C programs that actuate the operations that must be performed by such a WSN in order to operate.
Every mote had to control the SPR sensor light source, save an image from the detector, handle and transmit it by means of the ZigBee antennas, then to read data from a GPS receiver and send them in the same fashion. Moreover the base station computer had to receive the data correctly, process them as necessary and then spread them into Internet via satellite.

As a first setup for such a test network, I created two SPR sensors, composed by a laser diode, a T.M. polarizer, a pinhole, a diverging lens, two mirrors, a circular slit, a focusing lens, an SF6 glass prism with a coating of 2 nm of Chrome for adherence and 50 nm of Gold and a CMOS camera.
One of the two cameras, a Edmund Optics EO-0413M, was controlled along with a ZigBee antenna and a GPS receiver by a Desktop computer with Linux operative system, while the other SPR sensor, whose detector was a HP 1300 web-cam, and a ZigBee antenna have been commanded by means of an SX Arm Linux 1L microcontroller.

After that I implemented another sensor network test setup, comprising again two SPR sensors, each one formed by a laser diode, a T.M. polarizer, a pinhole, a diverging lens, two mirrors, a circular slit, a focusing lens, an SF6 glass prism with a coating of 2 nm of Chrome for adherence and 50 nm of Gold and a CMOS web-cam.
The two detectors, a DIGITUS DA-70815 and a HP 1300, were finally both controlled by SX Arm Linux 1L microcontrollers, as the laser diodes, two ZigBee antennas and a GPS receiver.

In both these configurations the receiving base station was composed by a Desktop computer with a Zigbee antenna and a broadband internet connection.

I thus demonstrated the feasibility of a Wireless Sensor Network based on SPR sensors, conceived for environmental pollutants detection and with broadband internet connection, and I also succeeded in implementing two different laboratory setups for a test Wireless Sensor Network based on Surface Plasmon Resonance Sensors.

Riassunto della mia tesi di dottorato

La mia attività di ricerca è stata finalizzata allo studio di fattibilità di una rete wireless, con accesso internet a banda larga tramite satellite, di sensori basati sulla plasmonica di superficie e concepiti per il rilevamento di sostanze inquinanti.

I sensori ottici basati sulla plasmonica di superficie (Surface Plasmon Resonance Sensors) utilizzano quale metodo di trasduzione del segnale l' eccitazione per risonanza dei plasmoni di superficie ad opera della radiazione luminosa polarizzata Transversal Magnetic.
I plasmoni di superficie sono oscillazioni quantizzate del plasma di elettroni presente nelle interfacce tra un materiale con indice di rifrazione positivo ed uno negativo.
Tali sensori in particolare si compongono in una sorgente di radiazione luminosa, un polarizzatore che selezioni la componente della radiazione Transverse Magnetic, un mezzo di accoppiamento quale un prisma, una guida d' onda, un reticolo oppure una fibra ottica, una struttura multistrato supportante un plasmone di superficie ed uno strato (bio-recognition layer) capace di formare legami chimici reversibili con le sostanze da analizzare, una cella di flusso ed un rivelatore.
A seconda dell' indice di rifrazione dei vari materiali formanti il sensore e della lunghezza d' onda della sorgente utilizzata, per un determinato angolo di incidenza si osserverà un minimo di riflettività ed una variazione di fase della luce riflessa, dovuti alla cessione di energia al plasmone di superficie stesso da parte della radiazione.
Utilizzando come output la lunghezza d' onda, l' angolo di incidenza, la variazione di fase o l' intensità della radiazione luminosa del minimo di riflettività è quindi possibile quantificare la concentrazione di un analita mediante la variazione tra l' indice di rifrazione dello strato del sensore in contatto con il mezzo esterno in assenza ed in presenza delle sostanze da rilevare. Tale strato infatti aumenta il proprio indice di rifrazione proporzionalmente alla loro concentrazione e la reversibilità del legame inoltre rende possibile la ripetitività delle analisi.

La mia ricerca si è quindi articolata in

1. documentazione su varie tipologie di sensori SPR
2. implementazione in laboratorio di tali dispositivi ottici
3. simulazioni al computer di strutture multistrato supportanti i plasmoni di superficie e comprendenti anche materiali peculiari al fine di ideare sensori innovativi basati sulla plasmonica di superficie
4. Nello studio di fattibilità di una rete wireless di sensori SPR ideata per il monitoraggio ambientale
5. Nell' implementazione e test in laboratorio di una piccola rete wireless di sensori SPR

Inizialmente mi sono documentata su vari sensori basati sulla plasmonica di superficie utilizzati per applicazioni spaziali, per l' individuazione di varie sostanze inquinanti allo stato liquido e gassoso, al fine di identificare i sensori da poter utilizzare in una rete wireless per monitoraggio ambientale e per poter ideare modelli competitivi ed innovativi.

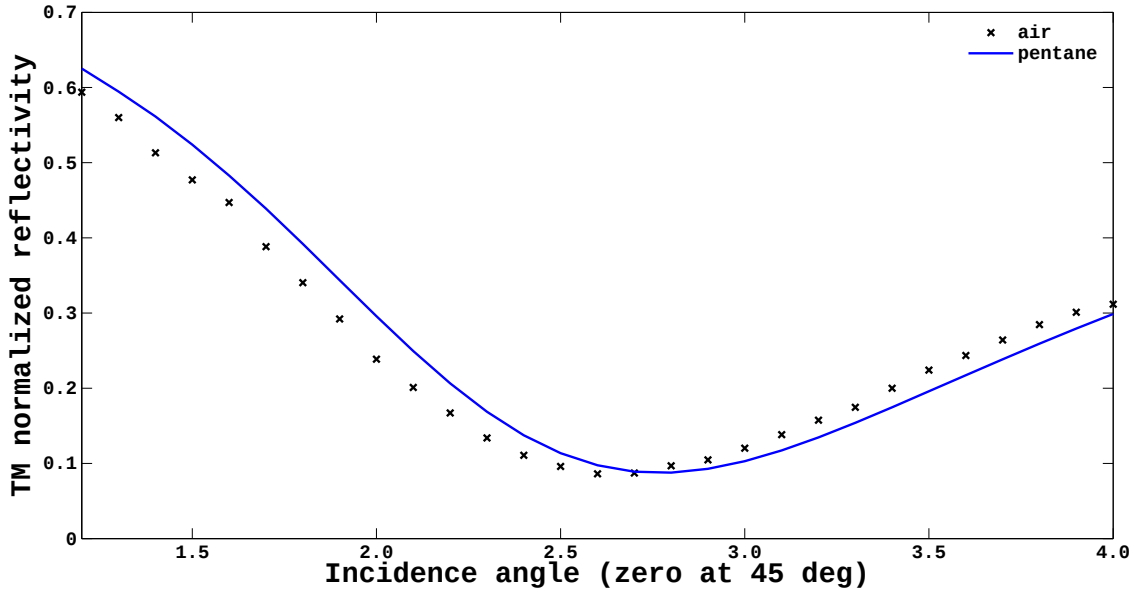

Figure 1: Variazione del segnale del sensore SPR tra le misurazioni di aria e gas pentano

Vari sensori SPR sono stati infatti creati per l' individuazione di gas, quali NH_3, NO_2, SiO2, CO, idrogeno ed inquinanti ambientali in ambiente acquoso quali arsenico, ricina, distruttori endocrini, pesticidi,metalli pesanti, batteri, virus e tossine.
Inoltre i sensori basati sulla plasmonica di superficie possono essere utilizzati per la ricerca di molecole prebiotiche in missioni spaziali o per il monitoraggio di missioni con equipaggio; una prova di utilizzo di sensori Surface Plasmon Resonance (SPR) per l' esplorazione di Marte, Europa od altri corpi celesti dovrebbe essere effettuato in Antartide.

Riguardo all' implementazione di sensori SPR in laboratorio ho in un primo momento costituito un sensore Surface Plasmon Resonance composto da un laser helium-neon, un polarizzatore, un prisma retto in fused silica, un vetrino in BF33 con un deposito di 50 nm in oro, una cella di flusso in silicone ed un fotodiodo ed ho effettuato delle misure di riflettività con vari gas quali elio e pentano per valutare la sensibilità dello strumento e per calibrare la cella di flusso.

La variazione del segnale del sensore SPR tra le misurazioni di aria e gas pentano è mostrato quale esempio in figura (1)

Quindi al fine di effettuare misure su sostanze liquide, dopo aver verificato la non adeguatezza del prisma precedente, ho implementato un sensore SPR utilizzante un setup di tipo statico, ovvero nel quale la figura di accoppiamento tra radiazione e plasmone di superficie è osservabile con una sola misura, costituito da un laser He-Ne, un polarizzatore Trasverse Magnetic, una pinhole di 200 μm di diametro, una fenditura circolare, due filtri neutri per attenuare l' intensità del fascio luminoso e non saturare il detector, una lente collimatrice con lunghezza focale 155 mm, un prisma cilindrico in vetro SF6 su cui sono stati depositati 1.4 nm di Cromo e 59 nm di Oro ed una camera CMOS.
Oltre a ciò ho analizzato e simulato la distribuzione di intensità luminosa del fascio reale, rappresentabile come una formula di tipo sinc quadro, migliorando inoltre il più possibile la qualità del fascio ottico e filtrandolo opportunamente.
In seguito ho innovato ulteriormente il setup ottico utilizzando nello stesso un prototipo di specchio deformabile in grado di correggere le aberrazioni ottiche presenti nello stesso.

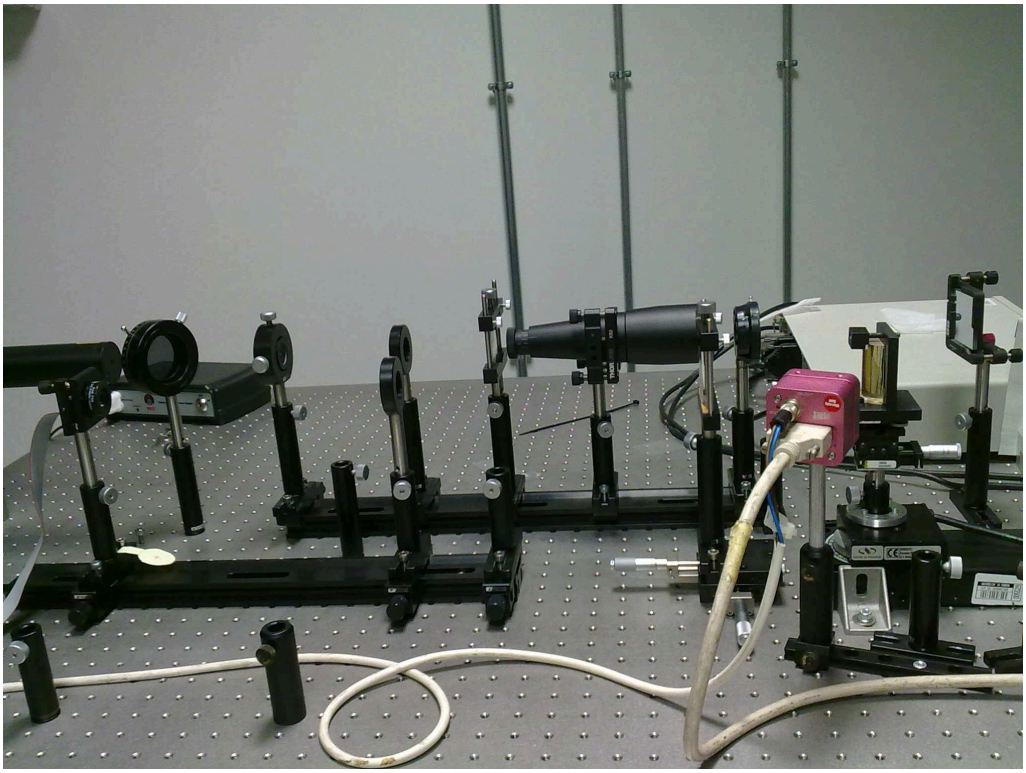

Figure 2: Foto del sensore SPR con specchio adattivo e setup statico

Il setup era composto da un laser He-Ne,un polarizzatore T.M., una pinhole avente diametro di 200 μm,una lente con lunghezza focale 220 mm per collimare il fascio uscente dalla pinhole, un beam expander 15x Thorlabs, un' apertura circolare, uno specchio, lo specchio deformabile, due filtri neutri per attenuare l' intensità del fascio, una lente cilindrica con lunghezza focale 155 mm,un prisma cilindrico in vetro SF6 su cui sono stati depositati 1.4 nm di Cromo e 59 nm di Oro ed una camera CMOS.
Tale sistema ottico è mostrato in figura (2)

Oltre ad essere un sistema ottico mai stato utilizzato precedentemente, l' inserimento dello specchio adattivo ha permesso di migliorare la qualità, la sensitività, la robustezza e la durata dell' utilizzo del sensore. In particolare il Membrane electrostatic Deformable Mirror (MDM) è risultato utile nel correggere gli effetti dovuti all' errato posizionamento di una lente, o fuori fuoco, e all' aberrazione sferica, mentre l' astigmatismo e la coma sembrano non generare contributi significativi.

Ho inoltre simulato in ambiente Matlab strutture multistrato innovative supportanti plasmoni di superficie e comprendenti materiali peculiari, atti all' individuazione del processo di ibridazione del DNA a singola elica (ss-DNA) durante la formazione del DNA a doppia elica (ds-DNA) in ambiente acquoso.
Tali sensori comprendono in particolare metalli mostranti una Risonanza Plasmonica Invertita (ISPR) quali Palladio, Iridio e Terbio, ed un singolo strato di Graphene (SGL), agente da strato protettivo contro l' ossidazione, oltre che da Biorecognition Element per il fenomeno chimico in esame.
Le strutture simulate sono composte da un prisma semicilindrico in SF6, con un deposito di 2 nm di Cromo, quindi 12 nm di Iridio, 14 nm di Palladio, 26 nm di Terbio o 50 nm di oro come referenza e da un singolo strato di Grafene avente spessore 0.34 nm.
Il processo chimico di ibridizzazione del DNA a singola elica (ss-DNA) è stato rappresentato come

uno strato dielettrico con spessore 100 nm passante da un indice di rifrazione pari a 1.462 a 1.48.

Di tali sensori sono stati valutati il contrasto

$$C = \frac{I_{max} - I_{min}}{I_{max} + I_{min}}$$

,

la sensitività valutata come il rapporto tra la variazione angolare dell' angolo di risonanza e la variazione dell' indice di rifrazione dell' analita

$$S = \frac{d\vartheta_{coupling}}{dn_a}$$

l' ampiezza a mezza altezza (FWHM) del segnale ed un fattore di qualità

$$Q \propto \frac{C}{FWHM} \quad \left[RIU^{-1}\right]$$

oltre ad altri.

Gli aspetti innovativi di tali tipologie di sensori sono:

- ⋆ Secondo la mia conoscenza l' Iridio non è mai stato precedentemente utilizzato in sensori basati sulla Plasmonica di superficie
- ⋆ Il segnale ottenuto è un massimo di riflettività molto stretto e con contrasto elevato; queste caratteristiche potrebbero essere molto utili in condizioni rumorose o con un range di angoli di incidenza limitato, come nel caso di sensori SPR a setup statico
- ⋆ Il Graphene agisce da strato protettivo contro l' ossidazione, oltre che da Biorecognition Element per il fenomeno chimico in esame, come da nostre referenze

Il Terbio ha mostrato proprietà ottiche inferiori agli altri metalli analizzati, mentre invece gli studi effettuati per le strutture Ir/SGL e Pd/SGL sono stati recentemente sottomessi per una possibile pubblicazione.

Ho inoltre sviluppato la simulazione del prisma cilindrico, degli effetti di una lente collimatrice sul sensore SPR simulato, della distribuzione di intensità luminosa generata dalla pinhole e dell' immagine teorica ottenibile sul rivelatore, oltre che un trattamento delle immagini SPR ottenute dai sensori SPR implementati in laboratorio, comprendente la necessaria normalizzazione, una correzione per una piccola rotazione ed un filtraggio gaussiano del rumore ad alte frequenze.

Mi sono quindi documentata su possibili dispositivi elettronici e metodi di telecomunicazione wireless e di collegamento ad internet via satellite al fine di studiare la realizzabilità di una rete wireless di sensori SPR progettata per il monitoraggio ambientale.

In particolare alcuni ricevitori di segnale GPS e vari sensori SPR miniaturizzati sarebbero alimentati e gestiti da dei microcontollori (motes), che trasmetterebbero inoltre mediante antenne wireless i dati ottenuti a dei rooter. Questi ultimi, dotati di antenne a lungo raggio, ri-trasmetterebbero i dati ad una stazione base formata da un PC portatile dotato di antenna ricevente e di un accesso Internet bidirezionale a banda larga via satellite. La struttura di questa possibile rete wireless di sensori è mostrata in immagine (3) ottenuta da immagini di Werner-Allen et al. (2006), Kota et al. (2011) e Adi Mallikarjuna Reddy V .

Una tale rete di sensori potrebbe essere posta anche in zone molto remote.

Possibili sostanze da rilevare potrebbero essere ad esempio la ricina,l' acido 2,4- Diclorofenossiacetico (2,4-D), i metalli pesanti, l' escherichiacoli.

Tali sostanze sono già state rilevate mediante sensori SPR ed utilizzano strati di bioricognizione relativamente poco complessi.

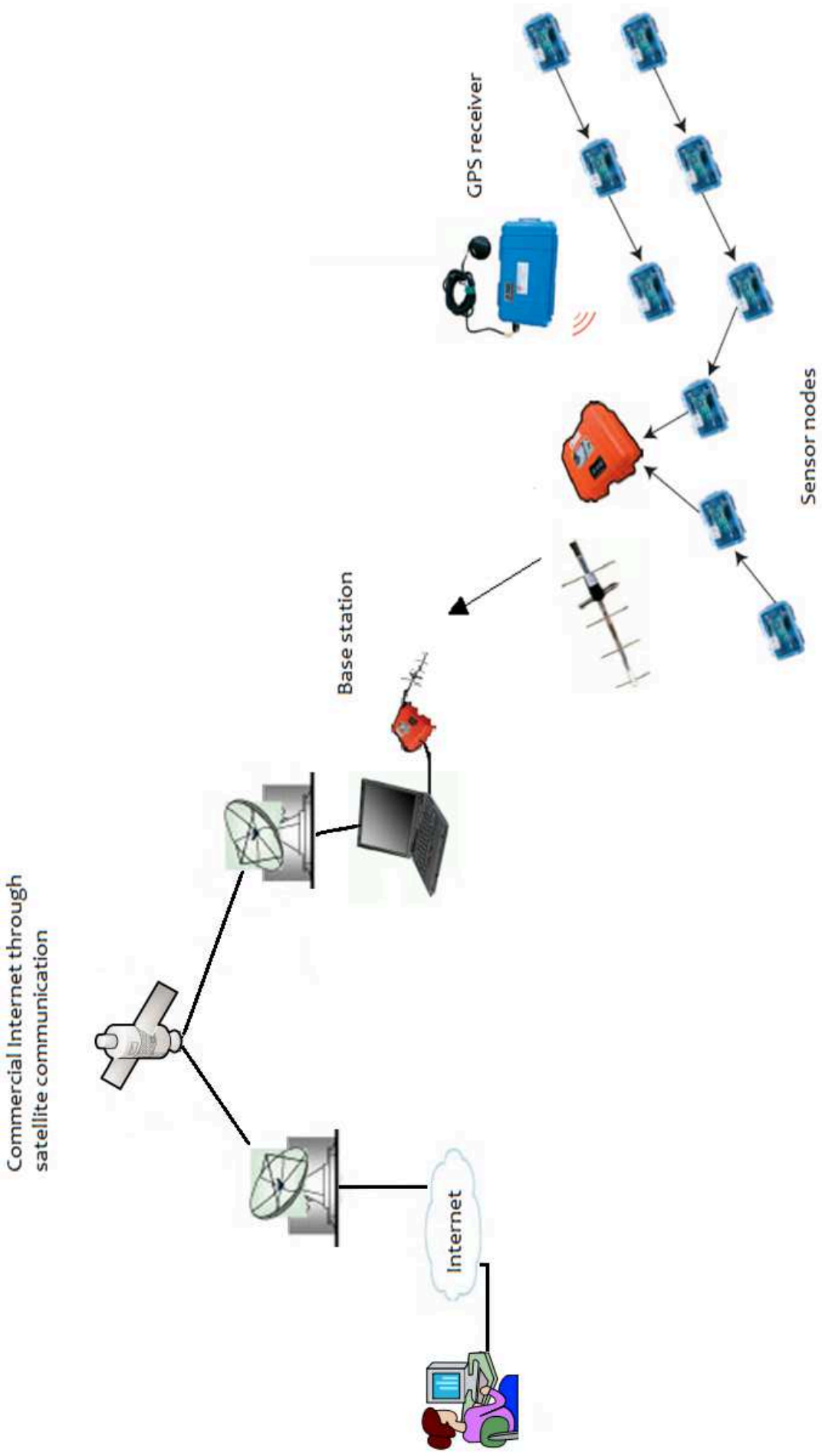
GPS receiver
Sensor nodes
Base station
Commercial Internet through satellite communication
Internet

Ho inoltre individuato i dati scientificamente più rilevanti ottenibili dai detector di tale rete wireless, quali la posizione angolare della figura di accoppiamento prima e durante il rilevamento delle sostanze prescelte, il valore normalizzato del massimo e del minimo di riflettività, l' ampiezza a mezza altezza del segnale, il valore misurato nel tempo della riflettività misurata ad un preciso angolo di incidenza.L' immagine dovrebbe essere inoltre opportunamente normalizzata.

Ho quindi creato in laboratorio una piccola rete wireless di prova, composta da due sensori basati sulla Surface Plasmon Resonance, studiandone gli elementi costitutivi e le modalità.
Quale prima implementazione i microcontrollori hanno inviato l' intera immagine al calcolatore della stazione base che ha provveduto all' estrazione ed analisi dei dati, mentre successivamente essi potrebbero essere programmati per la riduzione autonoma e l' invio dei dati stessi.

In seguito ho implementato un sensore SPR di dimensioni ridotte, testato lo stesso assieme a vari rivelatori CMOS, al corretto funzionamento delle antenne Zigbee ed ho creato in linguaggio C programmi eseguibili atti al funzionamento della rete di sensori stessa.
Tali programmi in particolare gestiscono in un sistema operativo Linux un ricevitore GPS e la camera CMOS scelta quale rivelatore, salvando l' immagine dei dati ottenuti in formato jpg, decomprimendo l' immagine in una matrice di numeri binari ed inviando quest' ultima ed i dati GPS mediante protocollo Zigbee ad un computer con sistema operativo Windows. Tale computer quindi salva i dati ricevuti, li processa e provvede alla loro diffusione mediante connessione internet a banda larga.
Tale procedura è riassunta in figura (4).

Inoltre ho ottenuto di controllare i diodi laser mediante i General Purpose DIO (GPIO) del microcontrollore ARM.

Ho quindi creato una prima implementazione di prova della mini rete wireless di sensori in laboratorio, comprendente due sensori SPR, ciascuno formato da un diodo laser quale sorgente di radiazione, una pinhole da 200 μm di diametro,una lente divergente con lunghezza focale -150 mm, due specchi,un' apertura circolare, una lente collimatrice,se necessario un filtro neutro per attenuare il fascio, un prisma cilindrico in vetro SF6 su cui sono stati depositati 2 nm di Cromo e 50 nm di Oro ed una camera CMOS.
Il rivelatore del primo dei due sensori SPR, la fotocamera CMOS Edmund Optics EO-0413M, è stata controllata assieme all' antenna Zigbee ed al ricevitore GPS da un computer con sistema operativo Linux Ubuntu.
Il secondo sensore SPR, avente per rivelatore la videocamera HP 1300, e la corrispondente antenna Zigbee sono stati invece comandati tramite il microcontrollore SX Arm Linux 1L .
Le immagini ed i dati GPS sono stati poi trasmessi ad una "base" formata da un computer con un' antenna Zigbee per la ricezione, software per l' analisi dei dati ed una connessione Internet a banda larga.

Ho in seguito implementato una diversa configurazione di prova per la mini rete wireless di sensori, sempre basata su due sensori SPR, mostrati nelle immagini (5 e 6) e composti da un diodo laser, una pinhole da 200 μm di diametro,una lente divergente con lunghezza focale -150 mm, due specchi,un' apertura circolare, una lente collimatrice,se necessario un filtro neutro per attenuare il fascio, un prisma cilindrico in vetro SF6 su cui sono stati depositati 2 nm di Cromo e 50 nm di Oro ed un rivelatore CMOS.
I due sensori CMOS, una webcam DIGITUS DA-71810 ed una HP 1300, sono stati controllati, assieme ai diodi laser, alle antenne Zigbee ed a un ricevitore GPS, da due microcontrollori SX Arm Linux 1L.

La "base" di ricezione è stata invece mantenuta uguale a quella del setup precedente.

Le immagini (7) e (8) sono rispettivamente un esempio delle immagini trasmesse da tale mini rete di sensori SPR e del fit dei dati ottenuti con i valori teorici attesi.

Ho quindi dimostrato la possibilità della creazione di una rete wireless di sensori basati sulla Plasmonica di Superficie e con accesso Internet a banda larga, implementandone inoltre due pic-

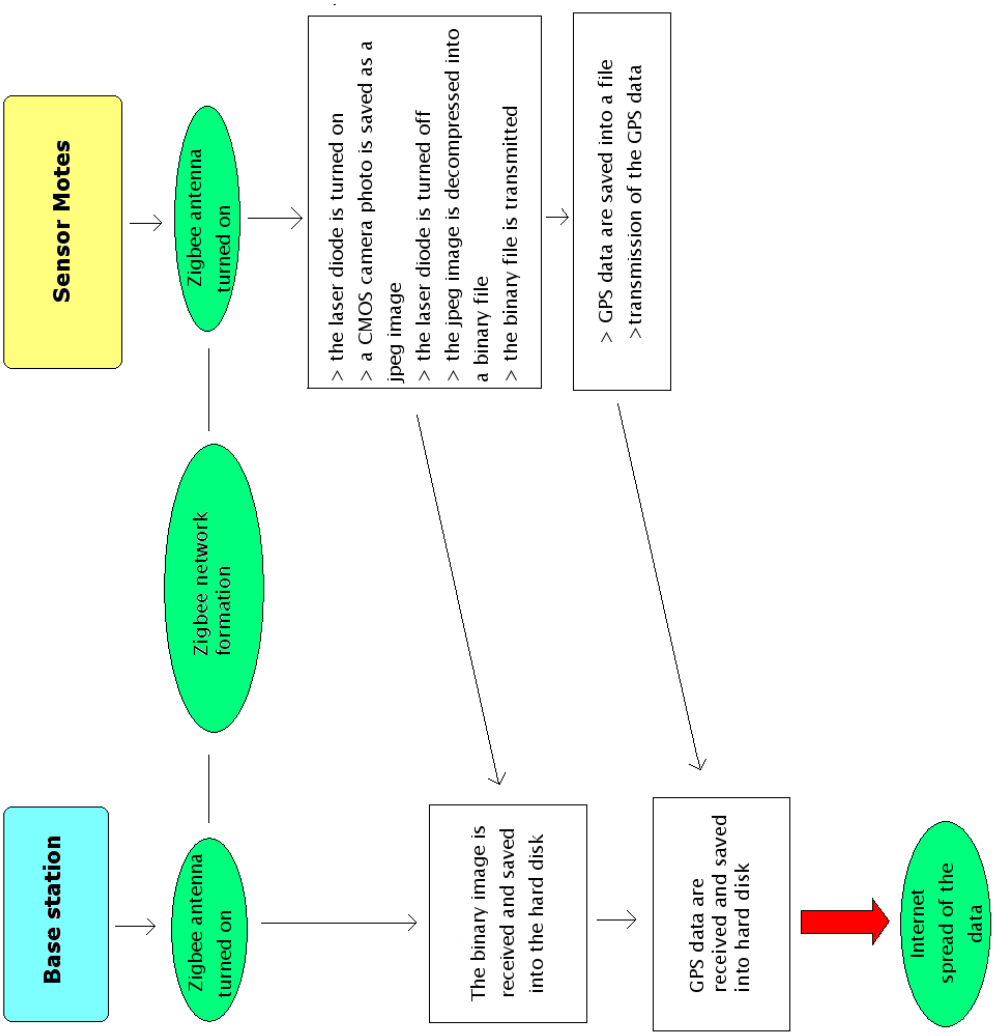

Figure 4: Azioni basilari che la rete wireless basata su sensori SPR deve attuare

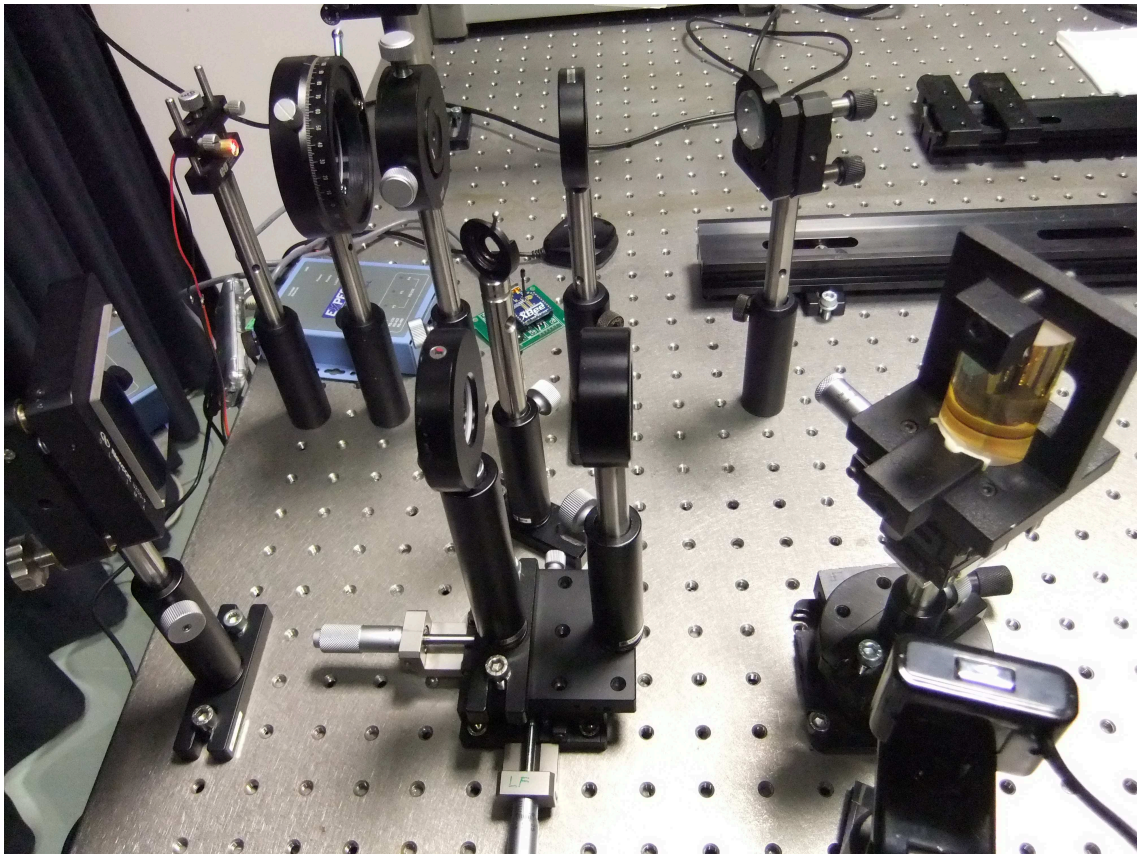

Figure 5: Foto del primo sensore SPR e del microcontrollore con cui esso viene comandato, nell' ultima configurazione in laboratorio della rete wireless di sensori basati sulla plasmonica di superficie

cole versioni di prova in laboratorio.

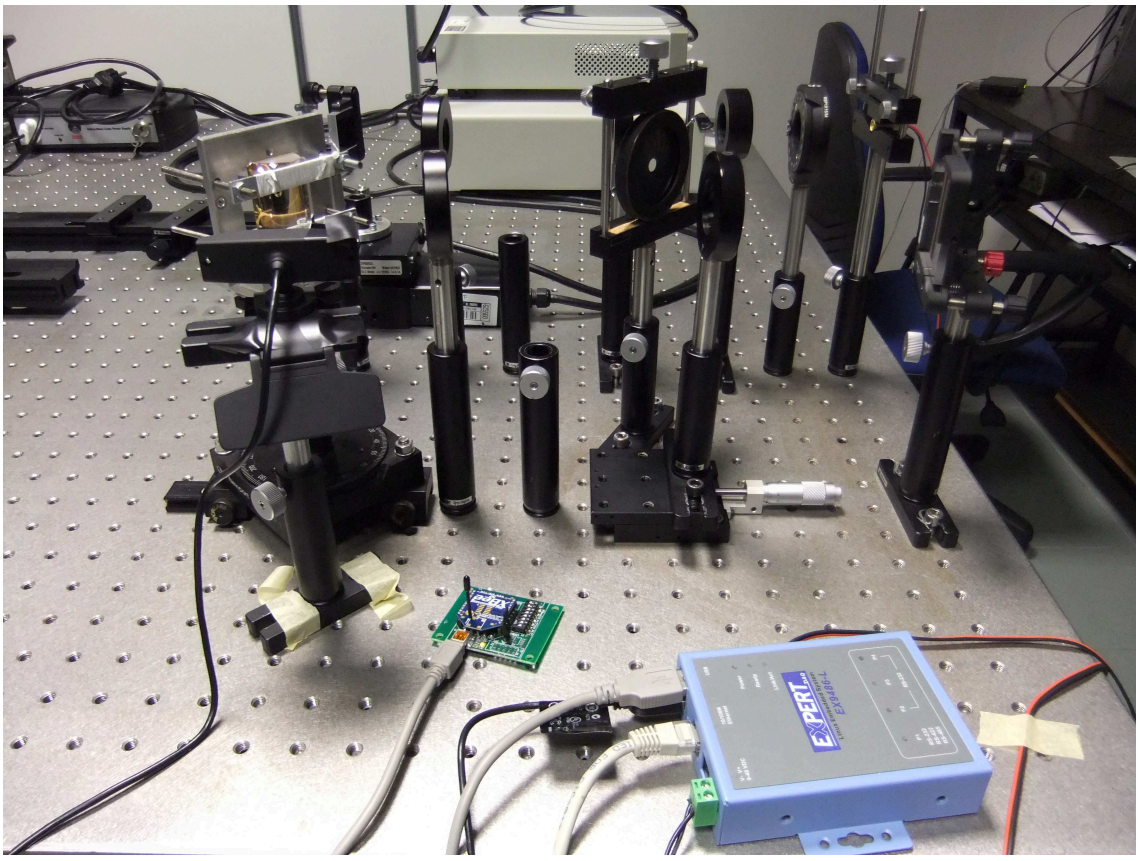

Figure 6: Foto del secondo sensore SPR e del microcontrollore con cui esso viene comandato, nell' ultima configurazione in laboratorio della rete wireless di sensori basati sulla plasmonica di superficie

Figure 7: Immagine trasmessa da uno dei due sensori ultima implementazione in laboratorio di una mini rete wireless di sensori basati sulla Plasmonica di Superficie

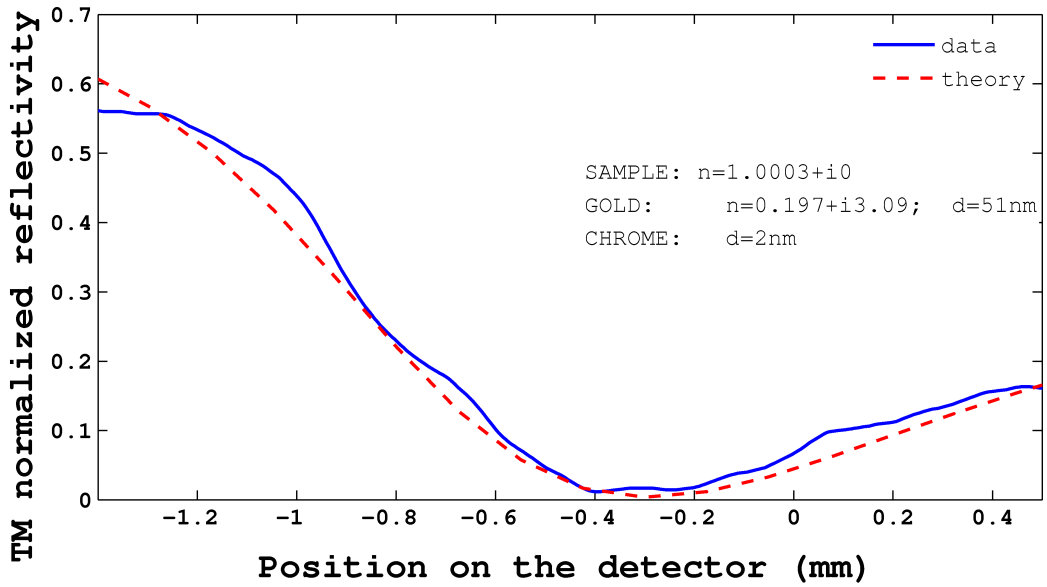

Figure 8: Esempio di fit dei dati ottenuti dall' ultima implementazione in laboratorio di una mini rete wireless di sensori basati sulla Plasmonica di Superficie

Contents

Chapter 1

Surface Plasmons

This chapter is about the physical concepts that define the Surface Plasmon Polaritons phenomenon and the conditions for their existence on dielectric-metal-dielectric slabs. The propagation of electro-magnetic fields into a multilayer structure will also be discussed.

This theory consequently allows to understand and model Surface Plasmon Resonance sensors.

1.1 Surface Plasmons

The Surface Plasmon is a surface wave confined at the interface between a dielectric, having a positive refractive index, and a metal or a doped dielectric having a negative refractive index and it corresponds to a coherent oscillation of electrons that takes place at the interface between the two media (Pluchery et al. (2011), see image 1.1 from Benson (2011), Zhang et al. (2012)). When Surface Plasmons couple with a photon, the resulting excitation is called a Surface Plasmon Polariton (SPP) and it can propagate along the interface into the two media until its energy is lost.

This propagation is then used to determinate the refractive index of the medium after the metal layer and thus optical sensors based on this physical phenomenon have been created.

They are named Surface Plasmon Based Sensors.

The first observation of such a Plasmon wave was made by A Otto in 1968(Otto (1968)).

1.2 Electro - Magnetic theory of Surface Plasmons

The Maxwell equations for a space without free charges are
(Homola et al. (2006))

$$\nabla \times \vec{E} = -\mu \partial \vec{H}/\partial t \tag{1.1}$$

$$\nabla \cdot \varepsilon_0 \varepsilon_r \vec{E} = 0 \tag{1.2}$$

$$\nabla \times \vec{H} = \varepsilon_0 \varepsilon_r \partial \vec{E}/\partial t \tag{1.3}$$

$$\nabla \cdot \mu \vec{H} = 0 \tag{1.4}$$

if the relative permittivity is $\varepsilon = \varepsilon_0 \varepsilon_r$,where ε_0 is the free-space permittivity, the magnetic permittivity is μ , E and H the electric and the magnetic fields.

For linear and isotropic, non-magnetic ($\mu = \mu_0$) materials the Maxwell' s equations became the wave equations

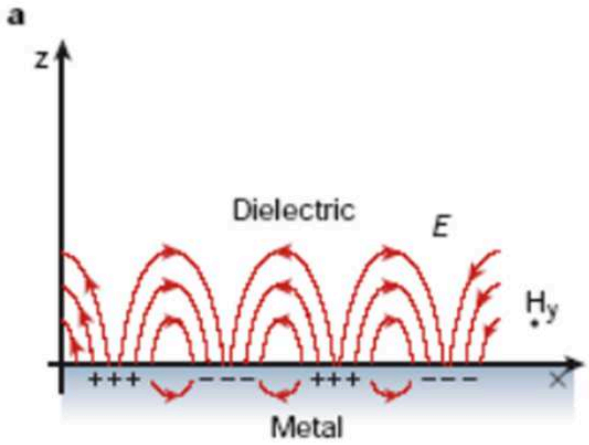

Figure 1.1: Surface Plasmon Polaritons

$$\Delta E - \mu_0 \varepsilon_0 \varepsilon_r \partial^2 \vec{E}/\partial t^2 = \nabla \left(E \cdot \nabla ln \left(\varepsilon_0 \varepsilon_r \right) \right) \tag{1.5}$$

$$\Delta H - \mu_0 \varepsilon_0 \varepsilon_r \partial^2 \vec{H}/\partial t^2 = \left(\nabla \times H \right) \times \nabla ln \left(\varepsilon_0 \varepsilon_r \right) \tag{1.6}$$

where

$$\nabla \cdot A = \frac{\delta A_x}{\delta x} + \frac{\delta A_y}{\delta y} + \frac{\delta A_z}{\delta z} \tag{1.7}$$

$$\nabla \times A = \left(\frac{\delta A_y}{\delta z} - \frac{\delta A_z}{\delta y} \right) x_0 + \left(\frac{\delta A_z}{\delta x} - \frac{\delta A_x}{\delta z} \right) y_0 + \left(\frac{\delta A_x}{\delta y} - \frac{\delta A_y}{\delta x} \right) z_0 \tag{1.8}$$

$$\nabla g = \frac{\delta g}{\delta x} x_0 + \frac{\delta g}{\delta y} y_0 + \frac{\delta g}{\delta z} z_0 \tag{1.9}$$

$$\Delta A = \left(\partial^2 \vec{A_x}/\partial x^2 + \partial^2 \vec{A_x}/\partial y^2 + \partial^2 \vec{A_x}/\partial z^2 \right) x_0 + \left(\partial^2 \vec{A_y}/\partial x^2 + \partial^2 \vec{A_y}/\partial y^2 + \partial^2 \vec{A_y}/\partial z^2 \right) y_0 + \left(\partial^2 \vec{A_z}/\partial x^2 + \partial^2 \vec{A_z}/\partial y^2 + \partial^2 \vec{A_z}/\partial z^2 \right) z_0 \tag{1.10}$$

the scalar coordinates are (x, y, z) and x_0, y_0, z_0 are unit vectors.

If we assume the electromagnetic wave to propagate along the z axis and time dependence of the fields to be $exp\left(-i\omega t\right)$ if ω is the angular frequency and $i = \sqrt{-1}$ than the electric and magnetic fields can be considered of the form

$$E = e\left(x, y\right) exp\left[i\left(\beta z - \omega t\right)\right] \tag{1.11}$$

$$H = h\left(x, y\right) exp\left[i\left(\beta z - \omega t\right)\right] \tag{1.12}$$

being β the propagation constant of an electromagnetic mode.

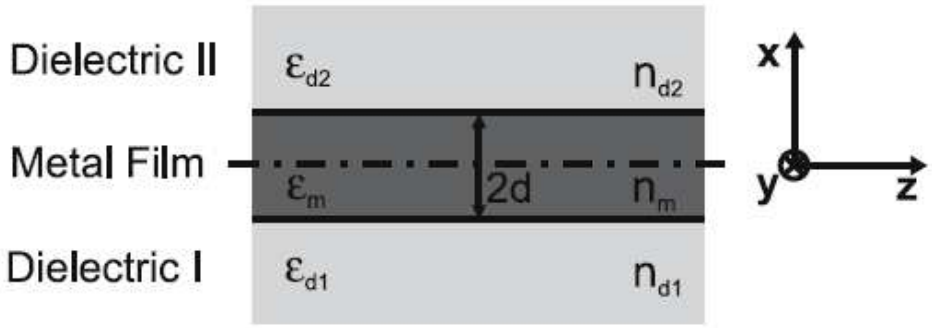

Figure 1.2: Scheme of the waveguide composed of the layers supporting the Surface Plasmon Polaritons, from (Homola et al. (2006))

Considering an optical waveguide composed of three homogeneous media of half-width $d_i, (i = 1, 2, 3)$, with permittivities

$$\varepsilon(x) = \quad \varepsilon_3 = n_3^2, \quad x > d_2 \tag{1.13}$$
$$\varepsilon_2 = n_2^2, \quad -d_2 \leq x \leq d_2 \tag{1.14}$$
$$\varepsilon_1 = n_1^2, \quad x < -d_2 \tag{1.15}$$

and orienting the layers in the y-z plane as shown in image (1.2) from (Homola et al. (2006)) the fields become

$$E = e(x)\, exp\left[i\left(\beta z - \omega t\right)\right] \tag{1.16}$$
$$H = h(x)\, exp\left[i\left(\beta z - \omega t\right)\right] \tag{1.17}$$

and the wave equations are

$$\left(\Delta_{transv} + \omega^2 \varepsilon \varepsilon_0 \mu_0 - \beta^2\right) e_i = 0 \tag{1.18}$$
$$\left(\Delta_{transv} + \omega^2 \varepsilon \varepsilon_0 \mu_0 - \beta^2\right) h_i = 0 \tag{1.19}$$

where $(i = x, y, z)$.

The solutions of the equations (1.18) and (1.19) set above produce two different modes, one with $h_z = 0$ called Transverse Magnetic (TM) and one with $e_z = 0$, denominate Transverse Electric (TE).

They have this notation because, being the incidence plane is the one made by the E-M wave propagation direction and a vector perpendicular to the plane of a layer surface, the component of the Electric field parallel to this plane is then referred to as Transverse Magnetic, while the component perpendicular to the incidence plane are denominated Transverse Electric.

Thus (Homola et al. (2006))

$$\frac{\partial^2 e_y(x)}{\partial x^2} + \left(\omega^2 \varepsilon \varepsilon_0 \mu_0 - \beta^2\right) e_y = 0 \quad for\, TE\, modes \tag{1.20}$$
$$\frac{\partial^2 h_y(x)}{\partial x^2} + \left(\omega^2 \varepsilon \varepsilon_0 \mu_0 - \beta^2\right) h_y = 0 \quad for\, TM\, modes. \tag{1.21}$$

From equations (1.1, 1.2, 1.3, 1.4) and the definition of cross product

$$\frac{\partial e_z}{\partial y} - \frac{\partial e_y}{\partial z} = -i\omega\mu h_x \tag{1.22}$$
$$\frac{\partial e_x}{\partial z} - \frac{\partial e_z}{\partial x} = -i\omega\mu h_y \tag{1.23}$$
$$\frac{\partial e_y}{\partial x} - \frac{\partial e_x}{\partial y} = -i\omega\mu h_z \tag{1.24}$$
$$\frac{\partial h_z}{\partial y} - \frac{\partial h_y}{\partial z} = i\omega\varepsilon e_x \tag{1.25}$$
$$\frac{\partial h_x}{\partial z} - \frac{\partial h_z}{\partial x} = i\omega\varepsilon e_y \tag{1.26}$$
$$\frac{\partial h_y}{\partial x} - \frac{\partial h_x}{\partial y} = i\omega\varepsilon e_z \tag{1.27}$$

and if we set

$$\frac{\partial}{\partial y} = 0 \tag{1.28}$$

and

$$k_i^2 = \omega^2\varepsilon_i\varepsilon_0\mu_0 - \beta^2, \quad i = 1, 2, 3 \tag{1.29}$$

the solutions of equations (1.20) and (1.21) are

⋆ for TE modes

$$e_y(x) = a_i^+ exp(ik_i x) + a_i^- exp(-ik_i x) \tag{1.30}$$
$$h_x(x) = \frac{\beta}{\mu_0\omega} e_y(x) \tag{1.31}$$
$$h_z(x) = \frac{-k_i}{\mu_0\omega} e_y(x) \tag{1.32}$$

⋆ and for TM modes

$$h_y(x) = b_i^+ exp(ik_i x) + b_i^- exp(-ik_i x) \tag{1.33}$$
$$e_x(x) = \frac{-\beta}{\varepsilon_i\varepsilon_0\omega} h_y(x) \tag{1.34}$$
$$e_z(x) = \frac{-k_i}{\varepsilon_i\varepsilon_0\omega}{}_y(x) \tag{1.35}$$

so that

⋆ for TE modes

$$e_y(x) = a_i^+ exp(ik_i x) + a_i^- exp(-ik_i x) \tag{1.36}$$
$$h_x(x) = \frac{\beta}{\mu_0\omega}\left[a_i^+ exp(ik_i x) + a_i^- exp(-ik_i x)\right] \tag{1.37}$$
$$h_z(x) = \frac{-k_i}{\mu_0\omega}\left[a_i^+ exp(ik_i x) - a_i^- exp(-ik_i x)\right] \tag{1.38}$$

⋆ for TM modes

$$h_y(x) = b_i^+ exp(ik_i x) + b_i^- exp(-ik_i x) \tag{1.39}$$

$$e_x(x) = \frac{-\beta}{\varepsilon_i \varepsilon_0 \omega}\left[b_i^+ exp(ik_i x) + b_i^- exp(-ik_i x)\right] \tag{1.40}$$

$$e_z(x) = \frac{-k_i}{\varepsilon_i \varepsilon_0 \omega}\left[b_i^+ exp(ik_i x) - b_i^- exp(-ik_i x)\right]. \tag{1.41}$$

⋆ in the first and third layer the fields decay exponentially with the distance to the second layer, that represents the metal , so $a_1^+ = a_3^- = 0$,, $b_1^+ = b_3^- = 0$

The boundary conditions of the Maxwell equations are such that the components of the electric and magnetic fields parallel to the boundaries of the layers must be continuous at the borders of the second layer
($x = d_2$ and $x = -d_2$).

SO for TE modes

$$e_y(x = d_2) = a_2^+ exp(ik_2 d_2) + a_2^- exp(-ik_2 d_2) = a_3^+ exp(ik_3 d_2) \tag{1.42}$$

$$h_z(x = d_2) = \frac{-k_2}{\mu_0 \omega}\left[a_2^+ exp(ik_2 d_2) - a_2^- exp(-ik_2 d_2)\right] = \\ = \frac{-k_3}{\mu_0 \omega}\left[a_3^+ exp(ik_3 d_2)\right] \tag{1.43}$$

$$e_y(x = -d_2) = a_2^+ exp(-ik_2 d_2) + a_2^- exp(ik_2 d_2) = a_1^- exp(ik_1 d_2) \tag{1.44}$$

$$h_z(x = -d_2) = \frac{-k_2}{\mu_0 \omega}\left[a_2^+ exp(-ik_2 d_2) - a_2^- exp(ik_2 d_2)\right] = \\ = \frac{-k_1}{\mu_0 \omega}\left[a_1^- exp(ik_3 d_2)\right] \tag{1.45}$$

The surface wave definition demands the existence of scattered fields without incident waves (Popov et al. (1996)).

Therefore the determinant of the associated matrix E (equation 1.46) must be equal to zero and thus formula (1.47) can be found:

$$E = \begin{bmatrix} 0 & k_2 exp(-ik_2 d_2) & -k_2 exp(ik_2 d_2) & k_3 exp(ik_3 d_2) \\ 0 & exp(-ik_2 d_2) & exp(ik_2 d_2) & -exp(ik_3 d_2) \\ -exp(ik_1 d_2) & exp(ik_2 d_2) & exp(-ik_2 d_2) & 0 \\ -k_1 exp(ik_1 d_2) & k_2 exp(ik_2 d_2) & -k_2 exp(-ik_2 d_2) & 0 \end{bmatrix} \tag{1.46}$$

$$[(k_2 - k_1)(k_3 - k_2)] exp(i2k_2 d_2) + [(k_2 + k_1)(k_3 + k_2)] exp(-i2k_2 d_2) = 0. \tag{1.47}$$

For TM modes instead

$$h_y\left(x=d_2\right) = b_2^+ exp\left(ik_2d_2\right) + b_2^- exp\left(-ik_2d_2\right) = b_3^+ exp\left(ik_3d_2\right) \tag{1.48}$$

$$e_z\left(x=d_2\right) = \frac{k_2}{\varepsilon_2\varepsilon_0\omega}\left[b_2^+ exp\left(ik_2d_2\right) - b_2^- exp\left(-ik_2d_2\right)\right] = \\ = \frac{k_3}{\varepsilon_3\varepsilon_0\omega}\left[b_3^+ exp\left(ik_3d_2\right)\right] \tag{1.49}$$

$$h_y\left(x=-d_2\right) = b_2^+ exp\left(-ik_2d_2\right) + b_2^- exp\left(ik_2d_2\right) = b_1^- exp\left(ik_1d_2\right) \tag{1.50}$$

$$e_z\left(x=-d_2\right) = \frac{-k_2}{\varepsilon_2\varepsilon_0\omega}\left[b_2^+ exp\left(-ik_2d_2\right) - b_2^- exp\left(ik_2d_2\right)\right] = \\ = \frac{-k_1}{\varepsilon_1\varepsilon_0\omega}\left[b_1^- exp\left(ik_3d_2\right)\right] \tag{1.51}$$

and the null determinant of the matrix T (equation 1.52) leads to the equation (1.53).

$$T = \begin{bmatrix} 0 & exp\left(-ik_2d_2\right) & exp\left(ik_2d_2\right) & -exp\left(ik_3d_2\right) \\ -exp\left(ik_1d_2\right) & exp\left(ik_2d_2\right) & exp\left(-ik_2d_2\right) & 0 \\ 0 & -\left(\frac{k_2}{\varepsilon_2}\right) exp\left(-ik_2d_2\right) & \left(\frac{k_2}{\varepsilon_2}\right) exp\left(ik_2d_2\right) & -\left(\frac{k_3}{\varepsilon_3}\right) exp\left(ik_3d_2\right) \\ \left(\frac{k_1}{\varepsilon_1}\right) exp\left(ik_1d_2\right) & -\left(\frac{k_2}{\varepsilon_2}\right) exp\left(ik_2d_2\right) & \left(\frac{k_2}{\varepsilon_2}\right) exp\left(ik_2d_2\right) & 0 \end{bmatrix} \tag{1.52}$$

$$\left[\left(\frac{k_1}{\varepsilon_1} - \frac{k_2}{\varepsilon_2}\right)\left(\frac{k_2}{\varepsilon_2} - \frac{k_3}{\varepsilon_3}\right)\right] exp\left(ik_2d_2\right) + \\ \left[\left(\frac{k_1}{\varepsilon_1} + \frac{k_2}{\varepsilon_2}\right)\left(\frac{k_2}{\varepsilon_2} + \frac{k_3}{\varepsilon_3}\right)\right] exp\left(-ik_2d_2\right) = 0 \tag{1.53}$$

It can be additionally observed that

$$exp\left(i2k_2d_2\right) = cos\left(2k_2d_2\right) + i\, sin\left(2k_2d_2\right) \tag{1.54}$$

$$exp\left(i2k_2d_2\right) = cos\left(2k_2d_2\right) - i\, sin\left(2k_2d_2\right) \tag{1.55}$$

and the following parameters can be settled:

$$\gamma_1 = -i\, k_1 \tag{1.56}$$

$$\gamma_3 = -i\, k_3 \tag{1.57}$$

1.2.1 Surface Plasmons on metal-dielectric interface

A metal-dielectric interface comprises a metal layer with complex refractive index ε_m and a dielectric layer with refractive index ε_d.
The interaction of Surface Plasmon Polaritons (SPP) on a metal-dielectric interface can be modeled from equations (1.29, 1.47, 1.53, 1.54, 1.55, 1.56 and 1.57) considering

$$
\begin{aligned}
d_2 &= 0 \\
k_2 = \varepsilon_2 &= 0 \\
\gamma_1 &= \gamma_m \\
\varepsilon_1 &= \varepsilon_m \\
\gamma_3 &= \gamma_d \\
\varepsilon_3 &= \varepsilon_d
\end{aligned}
$$

For TE modes equation (1.47) becomes

$$\tan\left(2k_2 d_2\right) = \frac{\gamma_m k_2 + \gamma_d k_2}{k_2^2 - \gamma_m \gamma_d} = 0 \tag{1.58}$$

and with formula (1.29) it leads to

$$\varepsilon_m = \varepsilon_d, \tag{1.59}$$

demonstrating that SPP can't be bound to a metal-dielectric interface for TE modes (Raether (1988), Homola et al. (2006)).

For TM modes equation (1.53) changes into

$$\tan\left(2k_2 d_2\right) = \frac{\left(\frac{\gamma_m}{\varepsilon_m}\right)\left(\frac{\varepsilon_2}{k_2}\right) + \left(\frac{\gamma_d}{\varepsilon_d}\right)\left(\frac{\varepsilon_2}{k_2}\right)}{1 - \left(\frac{\gamma_m \varepsilon_2}{\varepsilon_m k_2}\right)\left(\frac{\gamma_d \varepsilon_2}{\varepsilon_d k_2}\right)} = 0 \tag{1.60}$$

meaning

$$\frac{\gamma_m}{\varepsilon_m} = -\frac{\gamma_d}{\varepsilon_d} \tag{1.61}$$

and from equation (1.29) it can be found that consequently

$$\beta = \frac{\omega}{c}\sqrt{\frac{\varepsilon_d \varepsilon_m}{\varepsilon_d + \varepsilon_m}}, \tag{1.62}$$

which is the solution for a bounded-mode SPP
(Raether (1988), Homola et al. (2006)).

The real part of the refractive index of a media is associated to the effective refractive index while its imaginary part with light absorption inside the medium itself.

For lossless metals and dielectrics ($\mathrm{Im}\left(\varepsilon_m\right) = \mathrm{Im}\left(\varepsilon_d\right) = 0$) a bounded mode TM polarized SPP can exist only if $\mathrm{Re}\left(\varepsilon_m\right)$ and $\mathrm{Re}\left(\varepsilon_d\right)$ have a different sign and $\mathrm{Re}\left(\varepsilon_m\right) < -\mathrm{Re}\left(\varepsilon_d\right)$.

Dielectrics usually have $\mathrm{Re}\left(\varepsilon_d\right) > 0$ and real metals absorb, so that $\mathrm{Im}\left(\varepsilon_m\right) \neq 0$.
This allows bounded SPP, in this case named evanescent modes, to exists even for $\mathrm{Re}\left(\varepsilon_m\right) > -\mathrm{Re}\left(\varepsilon_d\right)$ if $\mathrm{Re}\left(\varepsilon_m\right) < 0$ and $\left|\mathrm{Re}\left(\varepsilon_m\right)\right| << \left|\mathrm{Im}\left(\varepsilon_m\right)\right|$

The real part of the propagation constant β is related to the SPP propagation speed while its imaginary part gives informations about the SPP attenuation.

The propagation length L is the distance at which the Surface Plasmon Polariton energy decreases of $1/e$.

This is expressed as (Homola et al. (2006))

$$L_{SPP} = \frac{1}{2\ \mathrm{Im}\left(\beta\right)}. \tag{1.63}$$

The Electro-Magnetic fields have a maximum intensity at the metal-dielectric interface and decrease exponentially with the distance from the latter.

The skin depths at which the E-M fields decrease of $1/e$ are, according to Raether (1988)

$$l_{SPP,\,m} = \frac{\lambda}{2\pi}\left(\frac{\mathrm{Re}\left(\varepsilon_m\right)+\varepsilon_d}{\mathrm{Re}\left(\varepsilon_m\right)^2}\right)^{1/2} \tag{1.64}$$

into the metal and

$$l_{SPP,\,d} = \frac{\lambda}{2\pi}\left(\frac{\mathrm{Re}\left(\varepsilon_m\right)+\varepsilon_d}{\left(\varepsilon_d\right)^2}\right)^{1/2} \tag{1.65}$$

into the dielectric.

1.2.2 Surface Plasmons on Dielectric-Metal-Dielectric Waveguides

A Dielectric-Metal-Dielectric Waveguide is composed of a metal film sandwiched between two semi-infinite dielectric media.

This kind of structure supports two TM SPP modes, that is two surface plasmons at the opposite boundaries of the metal film, when the metal film is much thicker than the penetration depth of a Surface Plasmon at each metal-dielectric interface. When instead the metal thickness decreases, coupling between the two surface plasmons occurs, leading to mixed modes of electromagnetic fields (Homola et al. (2006)).

Taking into consideration a symmetric waveguide, that is a dielectric-metal-dielectric interface where the two dielectric media are equal and making use of equations ((1.29, 1.54, 1.55, 1.56 and 1.57)) imposing

$$\varepsilon_1 = \varepsilon_3 = \varepsilon_d \tag{1.66}$$
$$\gamma_1 = \gamma_3 = \gamma_d \tag{1.67}$$
$$\varepsilon_2 = \varepsilon_m \tag{1.68}$$
$$k_2 = k_m \tag{1.69}$$

the solutions for TE modes from equation (1.47) become then

$$\tan\left(k_m d\right) = \frac{\gamma_d}{k_m}\ \ and \tag{1.70}$$
$$\cot\left(k_m d\right) = \frac{-\gamma_d}{k_m} \tag{1.71}$$

while for TM modes equation (1.53) gives

$$\tan\left(k_m d\right) = \frac{\varepsilon_m \gamma_d}{\varepsilon_d k_m}\ \ and \tag{1.72}$$
$$\tan\left(k_m d\right) = \frac{-\varepsilon_d k_m}{\varepsilon_m \gamma_d} \tag{1.73}$$

as it is also reported in Raether (1988) .
For a generic asymmetric waveguide the SPP modes are for reference

$$\tan\left(2k_m d\right) = \frac{\left(\frac{\gamma_1}{k_2}\right) + \left(\frac{\gamma_3}{k_2}\right)}{1 - \left(\frac{\gamma_1}{k_2}\right)\left(\frac{\gamma_3}{k_2}\right)} \tag{1.74}$$

for the TE modes and

$$\tan\left(2k_m d\right) = \frac{\left(\frac{\gamma_1 \varepsilon_2}{k_2 \varepsilon_1}\right) + \left(\frac{\gamma_3 \varepsilon_2}{k_2 \varepsilon_3}\right)}{1 - \left(\frac{\gamma_1 \varepsilon_2}{k_2 \varepsilon_1}\right)\left(\frac{\gamma_3 \varepsilon_2}{k_2 \varepsilon_3}\right)} \tag{1.75}$$

for TM modes (Homola et al. (2006)).

1.3 Study of the Electro-Magnetic fields in a metal-dielectric interface

I studied the Electro-Magnetic fields inside a metal-dielectric interface for Transverse Magnetic polarized radiation, creating a computer simulation that reproduces the results of Homola et al. (2006).

The images 1.3, 1.4 and 1.5 show the fields Hy, Ex and Ez respectively, for a monochromatic light source with wavelength 800 nm, a gold layer with refractive index $n_m = -25 + 1.44i$ and a dielectric layer with refractive index $n_d = 1.32$.

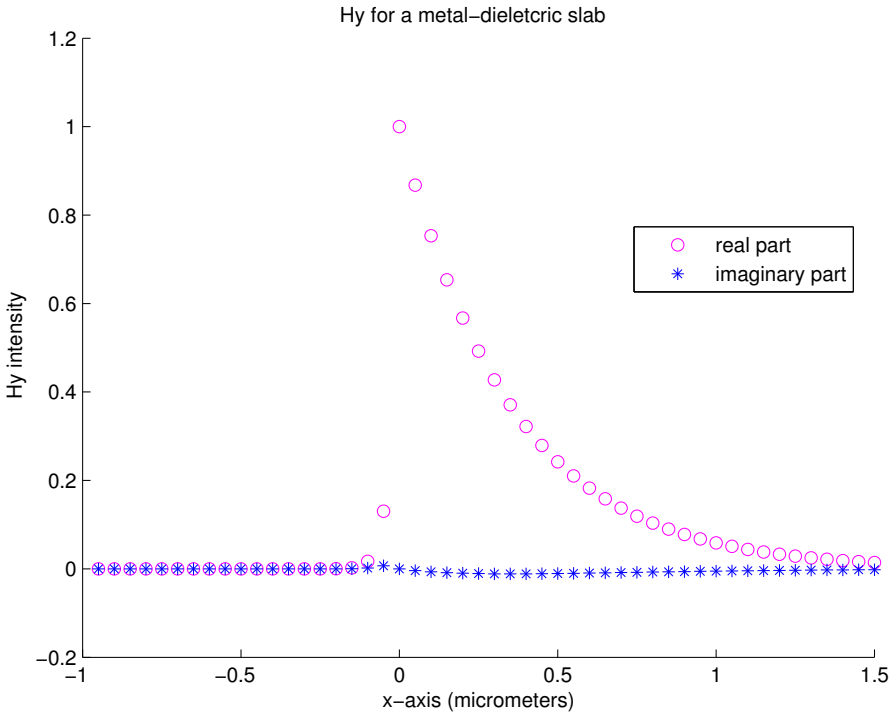

Figure 1.3: Hy for a metal-dielectric slab (Homola et al. (2006))

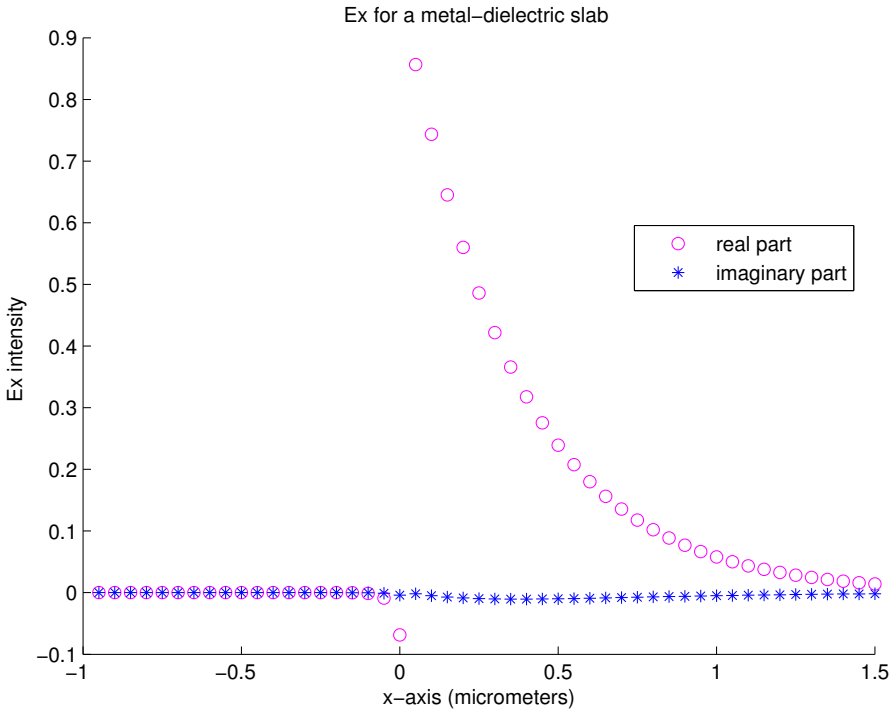

Figure 1.4: Ex for a metal-dielectric slab (Homola et al. (2006))

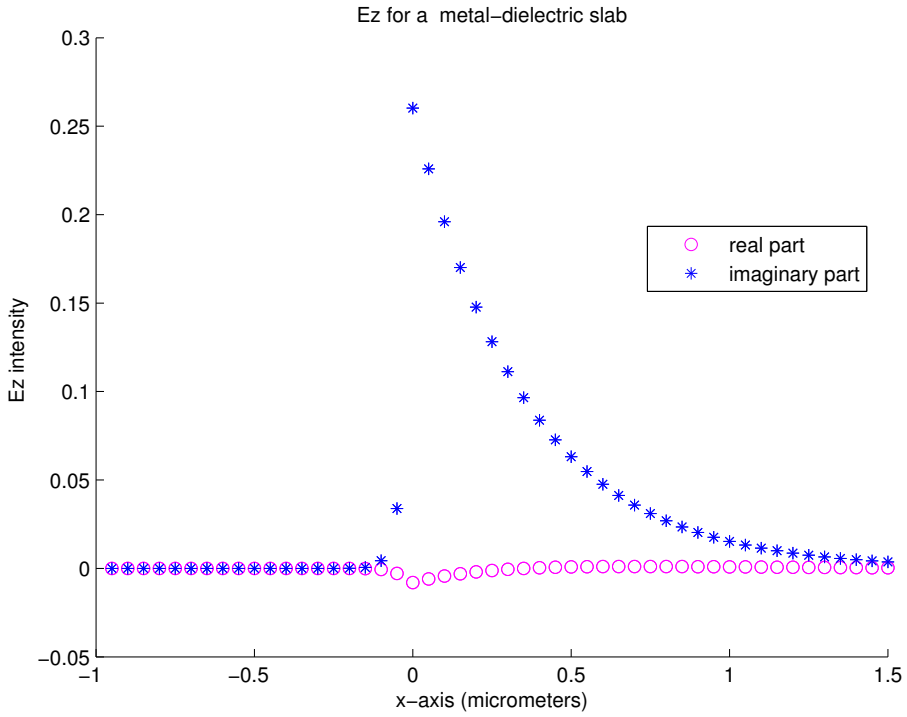

Figure 1.5: Ez for a metal-dielectric slab (Homola et al. (2006))

1.4 Study of the Electro-Magnetic fields in a symmetrical waveguide

Then I reproduced the graphs by Homola et al. (2006) to study the coupling of the light to the surface plasmons supported by a symmetrical waveguide.

If β is the propagation constant of the surface plasmons the effective refractive index is

$$n_{eff} = \frac{c}{\omega} \mathrm{Re}\,(\beta) \tag{1.76}$$

and the modal attenuation

$$b = \frac{0.2}{ln\,(10)} \mathrm{Im}\,(\beta) \tag{1.77}$$

The effective index and the attenuation for a monochromatic light source with wavelength 800 nm, a gold film with refractive index $n_m = -25 + 1.44i$ laying between two dielectric layers with refractive index $n_{d1} = n_{d2} = 1.32$ are shown in figures 1.6 and 1.7 .

I also varied the optical parameters to evaluate their influence on the propagation constant.

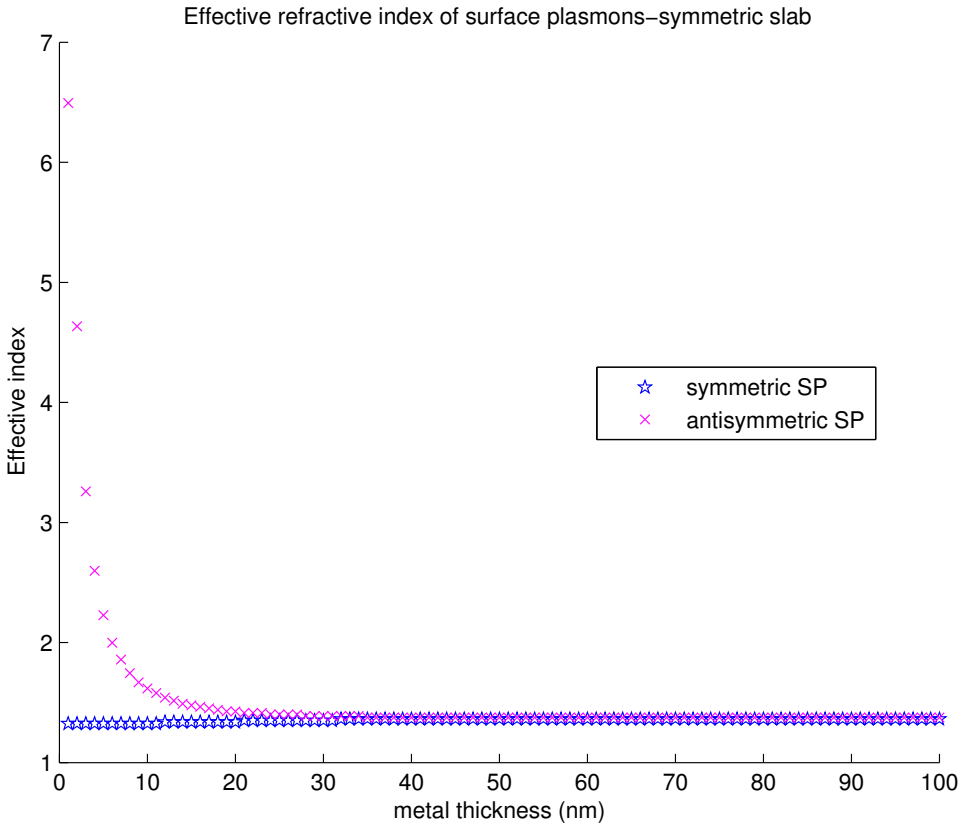

Figure 1.6: fig:Effective index of surface plasmons in a symmetric waveguide (Homola et al. (2006))

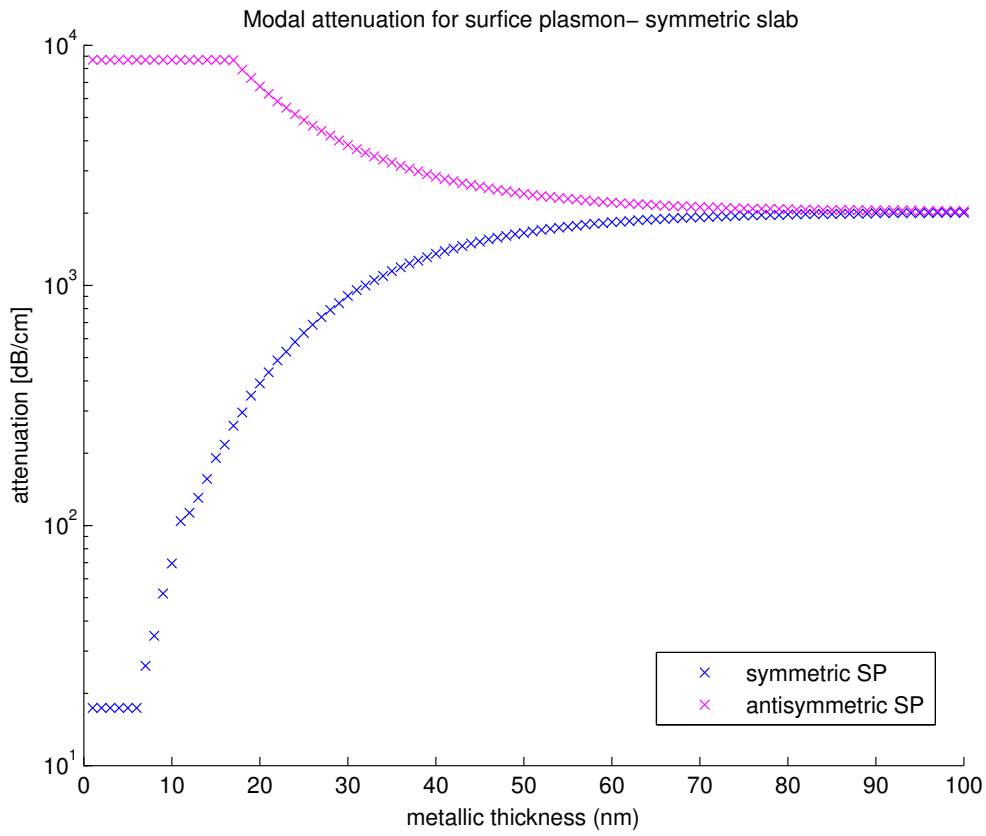

Figure 1.7: Modal attenuation of surface plasmons in a symmetric waveguide (Homola et al. (2006))

Chapter 2

Surface Plasmon Resonance Sensors

This chapter is aimed to give a description and a classification of the different Surface Plasmon Resonance sensors, an evaluation of their characteristics and in particular of their sensitivity.

2.1 Surface Plasmon Resonance sensors

An optical sensor is a device which optically converts the measurand physical quantity to another one, usually encoded into a light wave
(Homola et al. (2006)).

SPR sensors are thin-film refractometers that measure changes in the refractive index that take place at the surface of a metal film supporting a surface plasmon (Homola (2008)) .

The surface plasmon excited by an electromagnetic wave propagates along the metal-dielectric interface and its evanescent field probes the sample in contact with the metal.

Surface Plasmon Resonance sensors are composed of

- ⋆ a light source
- ⋆ a polarizer that selects the Transverse Magnetic component of the radiation
- ⋆ a coupler as a waveguide, a grating or a prism
- ⋆ a Surface Plasmon supporting structure, comprising in the simplest form a metal and a dielectric layer
- ⋆ a micro-fluidic system to control the flux of the fluid that contains the analyte and to clean the sensor if needed
- ⋆ the analyte
- ⋆ a light detector

and acquiring the reflected light intensity or phase the concentration of the analyte is determinated by means of the refractive index of the medium to be analyzed.

So a minimum of reflectivity in the transmitted light and a phase variation , determinated by the refraction indexes of the materials and radiation wavelength, can be observed.

The external layer of the device is coated with a material capable of creating reversible chemical bounds with the analytes and is thus named biorecognition layer.

The analyte binding itself with this layer increases the refraction index of the latter and so changes the coupling angle proportionally to its concentration . Studying the coupling angle, wavelength, light intensity or phase variations the analyte concentration can be then determinated.

2.2 Types of Surface Plasmon Resonance sensors

2.2.1 Light-Plasmon couplers

Light couples with the surface plasmons only when their propagation constants β are equal.

However light has a diferent propagation constant than the one of SPP, consequently Surface plasmons cant't couple directly with light but a coupler is needed as a prism in total reflection method (ATR), a waveguide or a grating.

One first classification of SPR sensors is therefore given by the coupler used.

⋆ One of the most common means to couple the light with the Plasmon surface wave is a `prism` used in the Attenuated Total Reflection (ATR) (Homola et al. (2006)).

– In the *Kretschmann geometry* a prism with a high refractive index n_p is in contact with a thin metal film with thickness in the range between 8 and 80 nm and complex refractive index n_m interfaced with a dielectric layer with refractive index n_d, $n_d < n_p$ as shown in image (2.1). For angles greater than the critical angle for total reflection of light a small amount of the radiation propagates in the metal as a inhomogeneous evanescent wave that decays exponentially through the medium. If the metal layer is thinner than approximately 100 nm the evanescent wave couples with the surface plasmon present at the outer side of the metal.

It should be noted that the Surface Plasmon Polariton at the prism-metal interface can't be excited because for it
$\beta_{SPP} > \beta_{radiation}$ and only the SPP at the metal-external medium interface can couple with the evanescent radiation
(Popov et al. (1996)).

Coupling occurs when the propagation constant of the surface plasmon

$$\beta^{SP} = \mathrm{Re}\left(\frac{\omega}{c}\sqrt{\frac{\varepsilon_d \varepsilon_m}{\varepsilon_d + \varepsilon_m}} + \Delta\beta\right) \tag{2.1}$$

where $\Delta\beta$ is the effect due to the presence of the prism is equal to the propagation constant of the electromagnetic wave

$$\beta^{EM} = \frac{2\pi}{\lambda} n_p sin\left(\vartheta\right) \tag{2.2}$$

– In the *Otto geometry*, illustrated in figure (2.2) a prism is interfaced with a thin dielectric film in contact with a metal layer. The light incident on prism with angles greater than the critical angle is reflected to the detector but a small amount of it as an evanescent wave, provided the dielectric layer to be few microns thick, can couple with the surface plasmon at the metal interface.

Again for the coupling the two propagation constants are required to be equal.

– A `metal grating` can be also used to couple the light with the surface plasmon.
A light wave incident through a dielectric medium with refractive index n_d to a metal grating with grating period Λ, grating depth q and refractive index n_m is diffracted

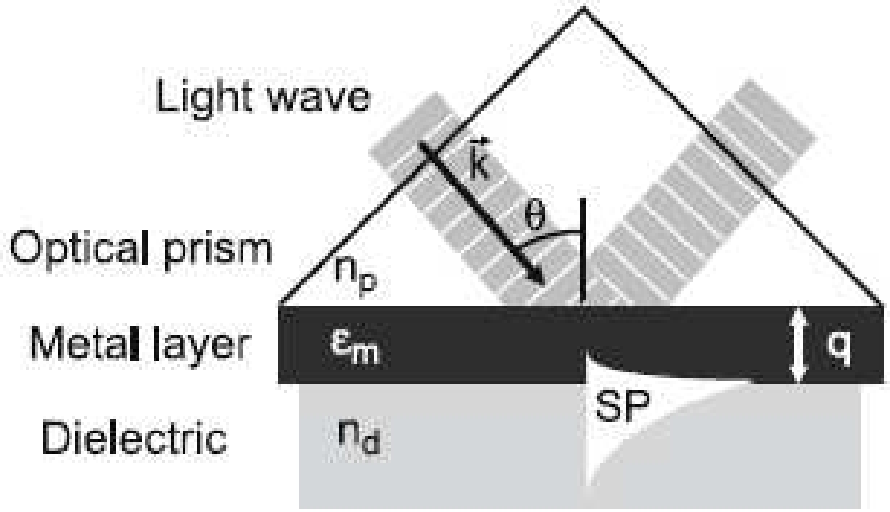

Figure 2.1: Excitation of surface plasmons in the Kretschmann geometry of the attenuated total reflection (ATR) method, image from (Homola et al. (2006))

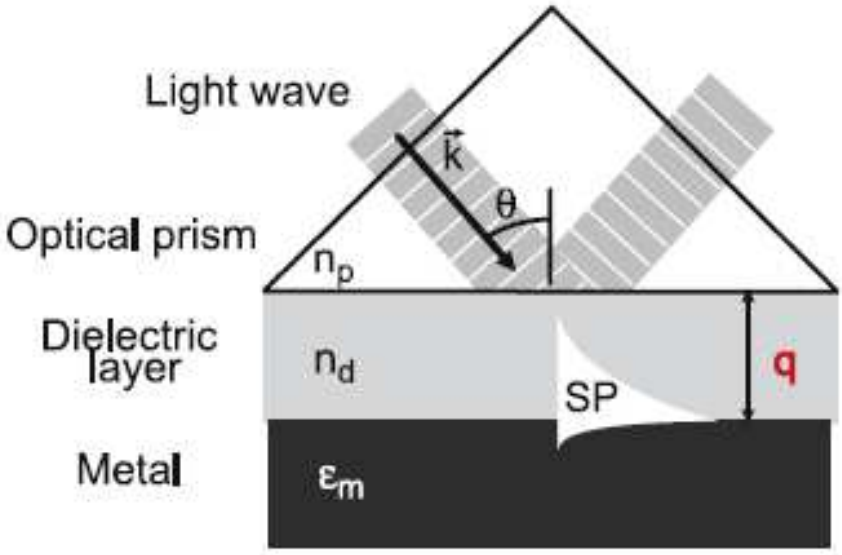

Figure 2.2: Excitation of surface plasmons in the Otto geometry of the attenuated total reflection (ATR) method, image from (Homola et al. (2006))

from the latter.
The component of the wavevector of the diffracted light in the plane of the grating is

$$k = k_z + m\frac{2\pi}{\Lambda}z_0 \tag{2.3}$$

and thus coupling happens when the propagation constant of the electromagnetic wave

$$\beta^{EM} = \frac{2\pi}{\lambda}n_d sin\left(\vartheta\right) + m\frac{\lambda}{\Lambda} \tag{2.4}$$

matches the surface plasmon one,

$$\beta^{SP} = \mathrm{Re}\left(\frac{\omega}{c}\sqrt{\frac{\varepsilon_d\varepsilon_m}{\varepsilon_d + \varepsilon_m}} + \Delta\beta\right) \tag{2.5}$$

where $\Delta\beta$ is the effect due to the presence of the grating.

– An other option is to use a `metal-dielectric waveguide` as a coupler. In a region of the waveguide a thin metal film is placed between the waveguiding layer and the sensing medium. In this case a mode of the waveguide propagates through the latter and in the region previously mentioned it penetrates the metal film and couples with the surface plasmon at the interface between the metal and the sensing layer. This happens when the propagation constant of the waveguide mode matches the one of the surface plasmon.

2.2.2 Surface Plasmon Resonance sensors light encoding of the informations

Surface Plasmon Resonance (SPR) sensors can be also classified according to the property of light in which the informations are encoded.

– `angular SPR sensors`: the light source used in this kind of sensor is monochromatic and the angle at which the minimum of reflectivity is observed is the data to be measured
– `wavelength SPR sensors`: A policromatic light beam is incident on the coupler with a precise angle and the reflected light is dispersed to a detector array. The important information is the wavelength at which the coupling occurs
– `Intensity SPR sensors`:In this configuration a monochromatic light source is made incident on the coupler with a precise angle close to the coupling one and the intensity of the reflected light is correlated to the strength of the coupling between the light and the surface wave and is the desired data.
– `phase SPR sensors`:When the coupling between the light and the surface plasmon occur a sharp TM phase change is observable. The angle, for a given wavelength, or the wavelength, for a single angle, where the Transversal Magnetic radiation change its phase is the stored information

The first three methods of encoding informations in light are the most commonly and widely used in SPR sensors. Figure 2.3 dispays different light encoding kinds in SPR sensors

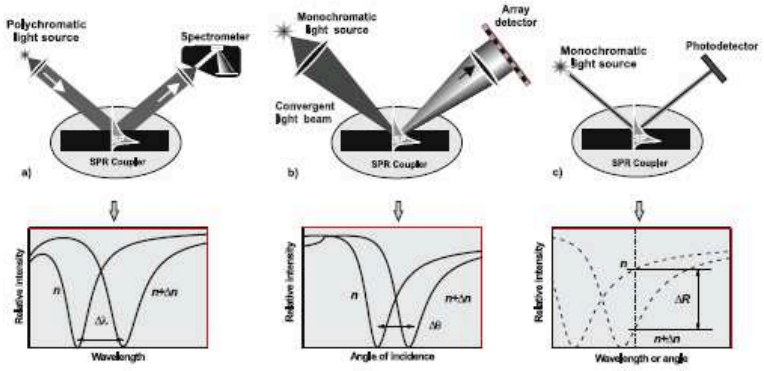

Figure 2.3: Different light encoding in SPR sensors, image from (Homola et al. (2006))

2.3 Surface Plasmon Resonance sensors characteristics

Surface Plasmon Resonance sensors have many attractive characteristics that would make them a good choice as biosensors or chemical sensors:

- They offer great sensitivity and an impressive limit of detection: for example for simazine Vedrine et al. (2003) obtained a detection limit of 0.5 $\mu g/l$ with optical fluorescence,
  Koblizek et al. (2002) a detection limit of 0.806 $\mu g/l$ with an elettrochemical sensor, Mouvet et al. (1997) with a waveguide SPR sensor achieved a detection limit of 0.2 $\mu g/l$
- They don't alter the medium to be sensed and so they can be used even in dangerous conditions, as for explosives, or in space missions on moons, comets or planets where is extremely important not to contaminate the environment.
- Because of their label-free protocol the detected molecules aren't altered, thus SPR sensor are well suited for medical and biology applications (Islam and Kouzani (2011))
- this kind of sensor can consist of a really simple design and they have a great potential for improving device integration
  (Islam and Kouzani (2011))
- Miniaturized Surface Plasmon Resonance sensors exists and are already in commerce

2.4 Sensitivity of a SPR sensor

The response of a SPR sensor is usually defined as the shift in wavelength or angle of the SPR minimum in reflected light intensity associated with changes in the index of refraction of the medium in contact with the metal surface of the SPR device Jung et al. (1998).

Using an SPR sensor with prism coupler and angular interrogation the sensitivity can be thus expressed as

$$S = \frac{d\vartheta}{dn_a} \tag{2.6}$$

if ϑ is the resonance angle and n_a is the refractive index of the analyte (Homola et al. (1999)).

This relation can be fitted with a quadratic relation according to the Maxwell equations but for small changes in the refractive indexes it can be linearly approximated (Jung et al. (1998), Liedberg et al. (1993)) as

$$R = \Delta\vartheta = m\left(\Delta n\right) \tag{2.7}$$

where m is the local slope of the relation.

In the case of a structure comprising a prism, a metal layer and the dielectric analyte it can be estimated as (Homola et al. (1999) Homola (1997))

$$S = \frac{\varepsilon_{mr}\sqrt{-\varepsilon_{mr}}}{\left(\varepsilon_{mr} + n_a^2\right)\sqrt{\varepsilon_{mr}\left(n_a^2 - n_p^2\right) - n_a^2 n_p^2}} \tag{2.8}$$

where ε_{mr} is the real part of the refractive index of the metal and n_p is the refractive index of the prism, n_a as above.

The presence of another dielectric binding layer used to attach a selective receptor to the metal surface, if the layer has a thickness around some nanometers it will cause a change in the coupling angle of the SPR minimum for any given index of refraction of the analyte, but this change is constant (Jung et al. (1998)).

From the refractive index of the analyte it is possible to evaluate its concentration so graphs of the coupling angle shift against the target molecule concentration are commonly reported as in image (2.4) from
Gobi et al. (2007)

A widely used evaluation value for a Surface Plasmon Based Sensor is the Full Width at Half Maximum (FWHM) of the SPR signal, that is of the coupling minimum or maximum of reflectivity.

Szunerits et al. (2008) following (Sherry et al. (2005)) thus propose as a Figure Of Merit (FOM) for this kind of sensor using a slope coefficient m analogue to m in equation (2.7)

$$FOM = \frac{m\ \left[degree\ RIU^{-1}\right]}{fwhm\ \left[degree\right]} \tag{2.9}$$

or the slope of the ratio $\Delta\vartheta/fwhm$ as m in equation (2.9)

Another way to study the detection of molecules is a graph of the SPR coupling angle plotted against time as in Gobi et al. (2007) and as shown in the image (2.5) from the same author.

Zacher and Wischerhoff (2002) instead make use of the following formula for estimating the sensitivity

$$S = \frac{\Delta I}{\Delta\vartheta} \tag{2.10}$$

being ΔI the change of intensity at a fixed angle of incidence and $\Delta\vartheta$ the variation of the coupling angle.

An example from Zacher and Wischerhoff (2002) is reported in figure (2.6)

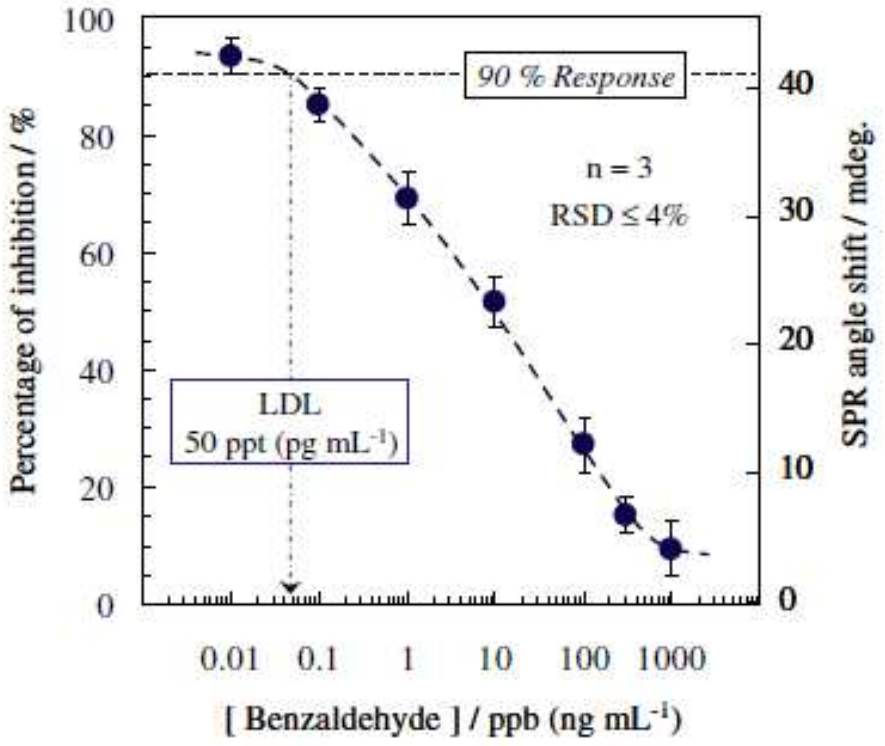

Figure 2.4: coupling angle shift against the target molecule concentration

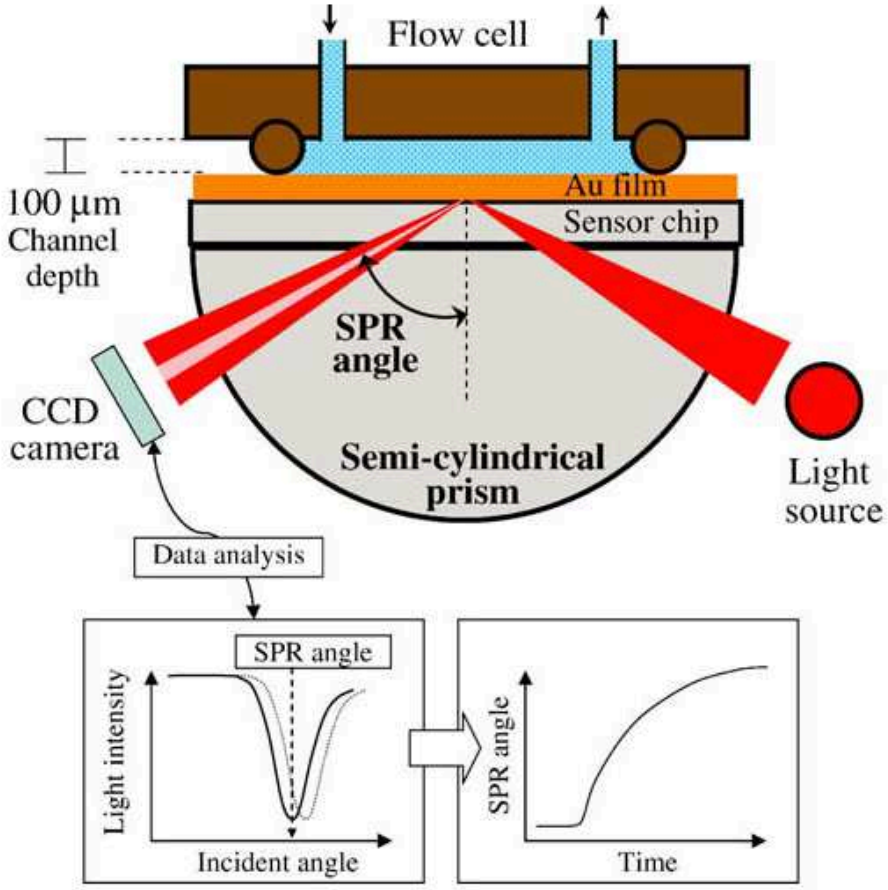

Figure 2.5: How to create a coupling angle shift against time SPR graph

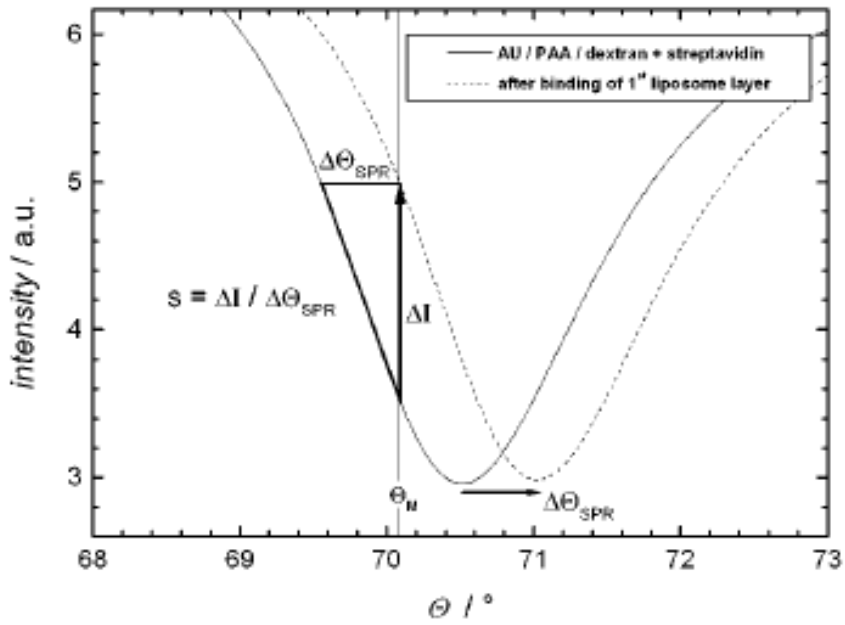

Figure 2.6: example of a graph about the change of intensity at a fixed angle of incidence plotted against the variation of the coupling angle

Chapter 3

Surface Plasmon Resonance sensors applications

This chapter will illustrate some applications of SPR sensor and in particular their employment in the detection of environmental pollutants and in space missions.

This chapter is therefore intended as a " Wide angle picture " of the fields where SPR sensor can be utilized.

3.1 Environmental monitoring applications

Surface Plasmon Resonance biosensors have been created for many aqueous pollutants detection, as arsenic (Forzani et al. (2007)), ricin (Tran et al. (2008), Feltis et al. (2008)) endocrine disruptors (Seifert et al. (1999), Hock et al. (2002)), pesticides (Mouvet et al. (1997), Mauriz et al. (2006a), Mauriz et al. (2006b), Mauriz et al. (2006c)), methane (Boulart et al. (2008)), heavy metals (Kang et al. (2005)), bacteria and toxins (Chinowsky et al. (2007), Koubova et al. (2001), Kim et al. (2007), Oh et al. (2004)), copper ions (Palumbo et al. (2003)).
Some of them have been tested in real lake water, surface water or groundwater samples, and many more will in the future.

Gaseous pollutants as NH_3 (Maciak et al. (2001)), CO (Kitenge et al. (2009)), NO_2 (El-Basaty et al. (2006), Watanabe et al. (2010)), hydrogen (Bevenot et al. (2002), Tobiska et al. (2001)), SiO2 (Hu et al. (2009)), ammonia and amine gases (Kitade et al. (2004)), petroleum hydrocarbon vapors (Aguirre et al. (2007)) and others have also been detected.

This kind of optical sensor has also other medical and environmental applications, as Food Quality and Safety Analysis, detection of Cancer, Allergy and Heart Attack Markers, Dioxins, Phenols and Aromatic Hydrocarbons, as reported in Homola (2008)

SPR sensors are particular suited for pollutant and explosive detection because they only optically act on the surrounding ambient and thus they don't alter it, moreover these sensors can achieve a great sensitivity.

As an example a small incomplete list of SPR sensors with their detection limits is:

- ⋆ Mouvet et al. (1997) : detection limit of 0.2 $\mu g/l$ for simazine in ground and surface water
- ⋆ Seifert et al. (1999) : detection limit of 0.1 $\mu g/l$ for Estradiol (ECDs) in lake water
- ⋆ Forzani et al. (2007) : detection limit of 1-3 ppm for arsenic in groundwater samples
- ⋆ Boulart et al. (2008) : detection limit of 0.2 nano-molar of methan in water

- ⋆ Chinowsky et al. (2007) : detection limit of $1 \cdot 10^4$ CFU/ml for Francisella tularensis, $9 \cdot 10^4$ CFU/ml for Bacillus subtilis and of 1nM for Staphylococcus Enterotoxin B
- ⋆ Koubova et al. (2001) : detection limit of 10^6 cells/mL for Salmonella enteritidis and Listeria monocytogenes, Drugs and Drug-Induced Antibodies,
- ⋆ El-Basaty et al. (2006) : detection limit 0.14 ppm for NO2 detection in ambient conditions
- ⋆ Bevenot et al. (2002) : quantitative detection in the range from 1 to 100 per cent for Hydrogen leakages
- ⋆ Maciak et al. (2001) : detection limit below 30 ppm for Ammonia (NH3) in synthetic air

3.2 Space applications

As described above Surface Plasmon Resonance sensors don't alter the external medium or ambient and can be miniaturized so they are suited for

- ⋆ **astrobiologial missions**: can be used in the research of organic or prebiotic molecules on the surface of planets, moons or comets , for example
  - with molecularly imprinted polymers, as in Izenberg et al. (2009) , Izenberg et al. (2006),Farinha et al. (2007)
  - The ESA ExoMars mission is currently planned for launch in 2016 and will land in 2018 in Mars; the `Life Marker Chip (LMC)` on board of the rover is one instrument conceived to detect signs of past and present life on the red planet.The Rover subsurface sampling device will autonomously drill to the required depth (maximum 2 m) while investigating the borehole wall mineralogy, and collect a small sample. This sample will be delivered to the analytical laboratory in the heart of the vehicle (from ESA site) By means of a dosing station the powder will then be presented to other instruments for performing a detailed chemistry, physical, and spectral analyses.
  - a prototype instrument for the Life Marker Chip will possibly be tested in Antarctica (Siegert et al. (2007))
- ⋆ **space stations or spacecrafts monitoring**: bacteria, viruses or dangerous substances can be detected even in low concentrations (few ppm) in the International Space Station or in missions with human crews; (http://www.cfdrc.com/bio/biological-and-chemical-sensors/nanoplasmonic-sensors) for reference

3.2.1 The Life Marker Chip

The design aim of the Life Marker Chip (LMC) is to detect 20-25 biomarker molecules on 20-50 samples by of Surface Plasmon Resonance and fluorescently labeled tracers.Specific Molecular Identification of Life Experiment (SMILE) has been proposed as a possible Life Marker Chip.

In particular Leinse et al. (2011) report that light with wavelength 635 nm is coupled into the Life Marker Chip by fiber coupling. The light is then guided by a Si3N4 (stoichiometric silicon nitride) waveguide (refractive index n=2.01) standing between SiO2 (silicon oxide, n=1.47) top and bottom claddings. Locally, the top SiO2 cladding layer is selectively removed. In these regions the evanescent field is available for probing the fluorescent spots and the top cladding consists of water.

This is shown in image (3.1 from Leinse et al. (2011)).

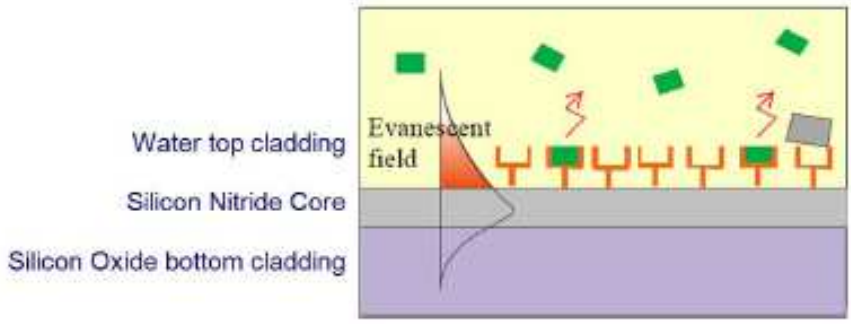

Figure 3.1: Concept of the LMC: the evanescent field of the propagating lightwave excites the fluorescent labels (green blocks) bound to the immobilized groups (red forks) on the chip surface

Fluorescent spots are placed in arrays to do multiple experiments and in order to make use at the same time of all the spots the incoming waveguide is divided into 10 parallel waveguides, each addressing 10 spots. An 11th waveguide is used as a monitor waveguide and fed back into a photo detector for monitoring purposes.

The image 3.2 from Leinse et al. (2011) shows scheme and the realization of the waveguides of the LIfe Marker Chip .

The fluidic chip consist of 2 bonded fused silica layers, each 0.5 mm thick. Channels with depth 50 μm and chambers, having depth 250 μm, are formed by wet etching in HF using an LPCVD polysilicon mask and photolithographic techniques. Through holes are formed by powder blasting using a photosensitive dry film resist mask. The conductivity sensors for fluid front detection are of platinum and made using a liftoff technique. The two wafers are then bonded using a direct bonding technology, and hashed into chips of 52 x 16 mm^2.

The assay chamber should be 0.8 μl.

The block diagram and a photo of the fluidic chip for the LMC is shown in images 3.3 and 3.4 from Leinse et al. (2011)

The optical chip and the fluidic chip are placed in a titanium holder and sealed together by means of a Viton gasket. Moreover, the holder accommodates a clamp for the laser diode, first stage amplifier electronics for the conductivity sensors, a driving mechanism for the rotary valve and a camera window for reading the fluorescent signals.

Other references on this are Prak et al. (2011), Laan et al. (2006), Schulte et al. (2007), Sims et al. (2005).

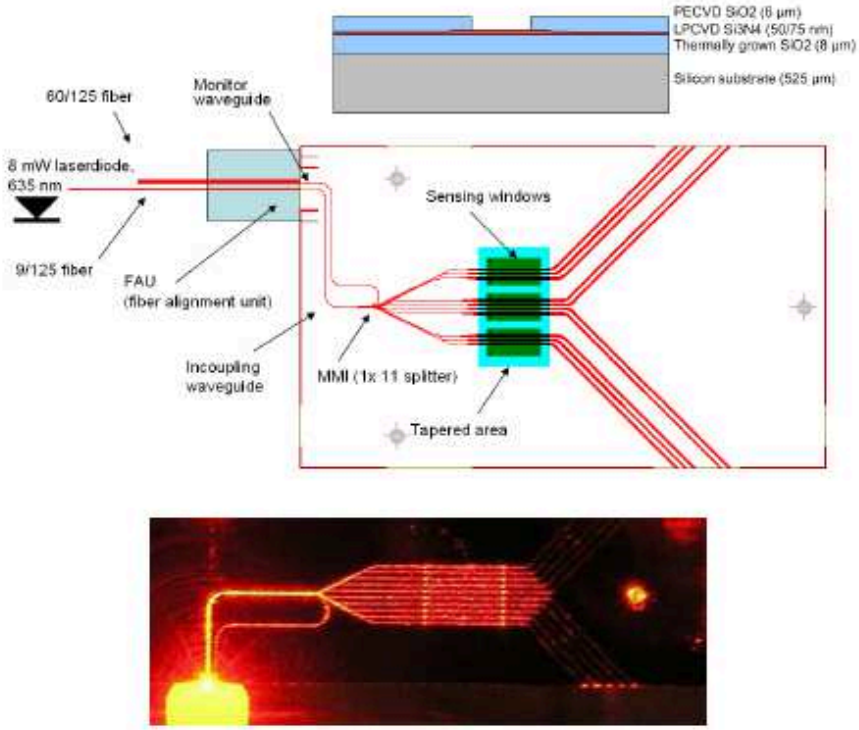

Figure 3.2: Schematic of a waveguide chip (top) and photo of realized chip (bottom) for the Life Marker Chip. Waveguides are shown in red.

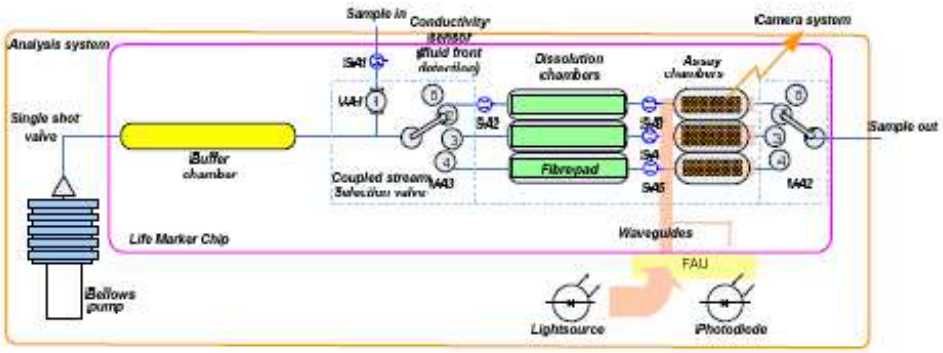

Figure 3.3: Block diagram of the fluidic chip for the LMC

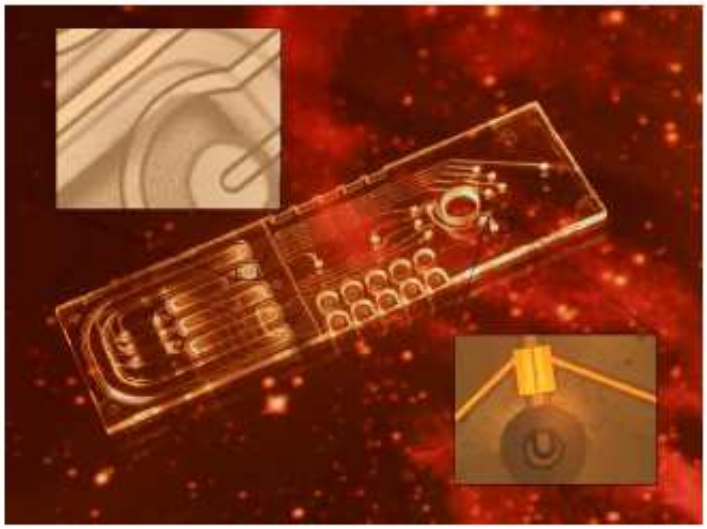

Figure 3.4: Photograph of the fluidic chip for the LMC

3.2.2 Lake Ellsworth exploration

In December 2012 a British Antarctic Survey expedition will attempt to drill through 3.2km of ice into the surface of Lake Ellsworth, a lake in the middle of the West Atlantic Ice Shelf, and consecutively to drop a probe into the ice to sample the lake's water column and floor as shown in image (3.5 from Page (2009)).

The main aim of this mission is to detect microbial lifeforms that could survived in isolation from the rest of the biosphere since Lake Ellsworth froze over for the last time between 200,000 and one million years ago.

These environments may be the closest analogues on Earth to Europa, which has a thick icy crust above a liquid ocean.

Depending to the technology state of the art and the mission budget and time requirements, if possible they will use also a prototype of the Life Marker Chip, that would be the central experiment of the expedition.

Recent References are Connor (2011), Connor (2009)

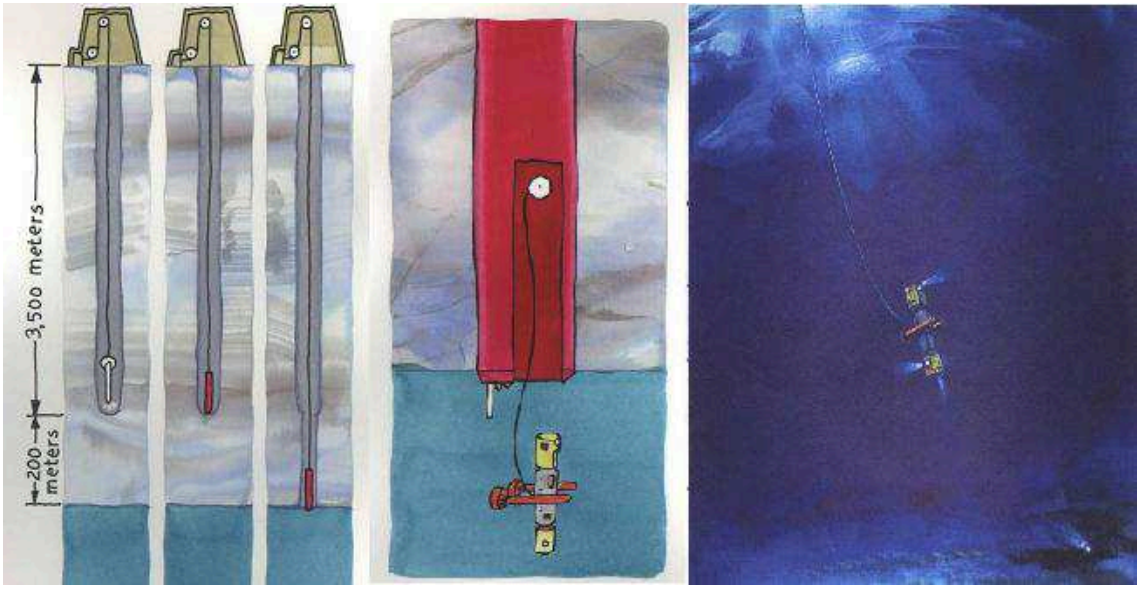

Figure 3.5: Concept of the probe for the Ellsworth lake exploration

A small research about the possible astronomical sites in the Solar System for astrobiological research with Surface Plasmon Resonance sensors is presented in appendix (A)

Chapter 4

Computer simulation of Surface Plasmon Resonance sensors

In order to investigate the possibility of innovative SPR sensors part of my research activity was to study and implement computer simulations of optical structures supporting surface plasmon polaritons and comprising peculiar materials. In particular, my models are conceived to study the SPR transduction effect in order to improve the quality of the acquired signal from these biosensors .

This chapter will therefore mainly introduce the applied simulation model of an SPR sensor and the results of simulations about innovative SPR sensors incorporating materials which show reflectivity maxima.

4.1 Transfer-matrix method

In order to obtain theoretical simulations of the SPR sensors a Matlab program has been used, which calculates the Fresnel formulas of transmission and reflection on each layer by means of the transfer-matrix method from Born and Wolf (1986).
According to this widely used method the radiation is assumed to propagate along the z-axis through a multilayer comprising N different layers. Every film medium k is defined by its thickness d_k,dielectric constant ε_k and complex refractive index $\tilde{n}\,(k)$.

The tangential components of the electromagnetic fields at the interface of the first layer (z=0) are then related to the ones at the boundary of the N-th layer (z=N-1) by the Characteristic Matrix of the system M.

$$\begin{bmatrix} E_1^T \\ H_1^T \end{bmatrix} = M \cdot \begin{bmatrix} E_{N-1}^T \\ H_{N-1}^T \end{bmatrix} \tag{4.1}$$

The latter is the product of the matrices that express the transmission and reflection Fresnel coefficients at each layer (Sharma and Mohr (2008) Born and Wolf (1986)):

$$M = \prod_{j=2}^{N-1} [M_j]\,, \tag{4.2}$$

being

$$M_j = \begin{bmatrix} \cos(\beta_j) & -i\,(\sin(\beta_j))\,/q_j \\ -i\,(\sin(\beta_j)) \cdot q_j & \cos(\beta_j)\,, \end{bmatrix} \tag{4.3}$$

$$q_j = \frac{\sqrt{\left[\varepsilon(j) - \tilde{n}(1)^2 \, sin^2(\vartheta)\right]}}{\varepsilon(j)} \quad (j = 2, .., N-1). \tag{4.4}$$

and β_j the propagation constant in each layer (equation 4.5).

$$\beta_j = \frac{2\pi}{\lambda} \cdot d(j) \cdot \sqrt{\left[\varepsilon(j) - \tilde{n}(1)^2 \, sin^2(\vartheta)\right]} \quad (j = 2, .., N-1) \tag{4.5}$$

In equations (4.4) and (4.5) λ is the radiation wavelength, ϑ the incidence angle of the radiation on the prism,$\varepsilon(j)$ is the complex dielectric function of the j-th layer, $d(j)$ its thickness and $\tilde{n}(1)$ the refractive index of the prism glass.

Thus taking into consideration the elements of the Characteristic Matrix

$$M = \begin{bmatrix} M_{11} & M_{12} \\ M_{21} & M_{22} \end{bmatrix} \tag{4.6}$$

the amplitude reflection coefficient for TM polarized light is given by

$$r_{TM} = \frac{(M_{11} + M_{12}q_N)\, q_1 - (M_{21} + M_{22}q_N)}{(M_{11} + M_{12}q_N)\, q_1 + (M_{21} + M_{22}q_N)} \tag{4.7}$$

and the intensity reflection coefficient by

$$R = |r_{TM}|^2 \tag{4.8}$$

This program from the previous formulas thus calculates the reflectivity (equation 4.8) for the desired angles of incidence of an SPR sensor with monochromatic light source, angular scan, prism coupler and Kretschmann geometry for Attenuated Total Reflection configuration.

4.2 Simulations of SPR sensors incorporating materials showing reflectivity maxima

4.2.1 Purpose of the research

In Surface Plasmon Resonance based sensors under coupling conditions, generally a minimum of reflectivity can be seen on the detector.

Palladium has the peculiarity with few other metals as Vanadium and Iridium to provide instead a maximum of reflectivity
(Kohns et al. (2005), Logacheva et al. (2006), Horne et al. (1994)).
The physical phenomenon is known as Inverted Surface Plasmon Resonance (ISPR).

Logacheva et al. (2006) affirm that, in Surface Plasmon Resonance coupling with light, part of the E-M radiation is transformed into a propagating Surface Plasmon Polariton and part of it is reflected back from the system.

The prism also reflects back part of the light by means of volume radiation, so if the two waves are out of phase this generates a destructive interference and thus the presence of a minimum of reflectivity.
When instead the two waves are in phase a maximum of reflectivity is visible because of constructive interference.
Metals showing ISPR generally have high adsorbance , meaning $|\mathrm{Re}(\tilde{n})| << |\mathrm{Im}(\tilde{n})|$ (Kohns et al. (2005)).

Finally according to Popov et al. (1996) the common minimum of reflectivity and the inverted surface plasmon resonance only differ for the change in position of the complex pole and the zero of the reflectivity amplitude.

This physical phenomenon could be useful not only in order to create innovative SPR sensors but also to improve the quality of these biosensors.
For example the detection of the angular/pixel position of a maximum of light intensity can be easier than detecting an intensity minimum in noisy conditions.

For this reason SPR sensors comprising thin layers of metals showing a coupling maximum as Palladium, Iridium and Terbium have been simulated.

Palladium has the advantage of being highly reactive with respect to Hydrogen and thus it is utilized as a sensitive sensor for the latter (Tobiska et al. (2001), Bevenot et al. (2002)).

Iridium and Terbium have also been evaluated because they are more inert than Palladium and they thus are able to provide more robustness and resistance over time than the latter.
Additionally to my knowledge Iridium hasn't yet been utilized in SPR sensors.

According to Bunch et al. (2008) and Jiang et al. (2009) a graphene sheet is impermeable to gases as small as Helium. This property allows graphene to protect sensors from oxidation and contaminations.
Coraux et al. (2008) and Kwon et al. (2009) attest the feasibility of depositing a graphene layer on Pd and Ir. In literature to my knowledge there aren't articles about graphene deposition on Terbium up to the present moment, but this could still be realized in future works.

Thus in order to avoid oxidation, which is a key factor in degrading the performances of optical sensors, and accordingly improve their ruggedization and quality even more, a Single Graphene coating Layer (SGL) has been added to the modelized biosensors.

One possible strategy to improve the sensitivity of SPR biosensors is to use Biomolecular Recognition Elements (BRE) Homola (2003), nanoparticles, nanoholes and metallic nanoslits as adhesion elements (Zhao et al. (2006), Stewart et al. (2008), Lee et al. (2007)).

The single-stranded DNA hybridization has been chosen as target chemical reaction, as in Wu et al. (2010) and Choi et al. (2011), and, with regard to this chemical states, Graphene acts both as a BRE (Husale et al. (2010)) and as a protective capping layer at the same time.
In fact ss-DNA having a size of approximately 100 nm (Wu et al. (2010) and Kowalczyk et al. (2010)) isn't able to pass through the Graphene pores and come into contact with the metal while the ds-DNA, which has a much smaller diameter, can.

4.2.2 Simulation model and characterization

The Matlab program simulating the optical sensor makes use of the transfer-matrix method from (Born and Wolf (1986)) as reported in section (4.1).

The simulated SPR sensors are based on angular interrogation, prism coupler and on the Kretschmann geometry for Attenuated Total Reflection configuration (Homola et al. (2006) , Homola (2008)).

In particular they comprehend a He-Ne laser as a light source, a Transversal Magnetic polarizer, an SF6 cylindrical prism, where a 2 nm thick layer of Chromium (for adherence) and a thin metal layer have been deposited, and a detector.

Among the simulated noble metals showing reflectivity maxima, Palladium, Iridium and Terbium have been studied in a deeper extent and are reported in this thesis.

A single layer of graphene as in Wu et al. (2010) and Choi et al. (2011) has been added as the top layer.

The results for a SPR biosensor comprising 50 nm of Gold and a Single Graphene Layer for the same chemical states are reported for comparison.

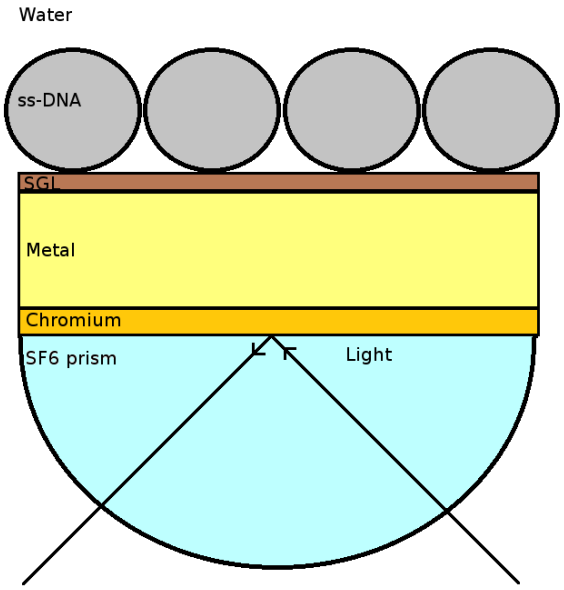

Figure 4.1: Schematic model of ISPR biosensors based on Single Graphene Layer (SGL) and ISPR metals. A noble metal is deposited on a SF6 prism substrate with an interposed chromium layer 2 nm thick. A SGL (0.34 nm) is added on the top of the metal.

The refractive indexes of the various materials are reported in table (4.1) where n and k are the real and imaginary part of the complex refractive index of the medium ($\tilde{n} = n + i \cdot k$).

Table 4.1: Refractive indexes of the materials

Material	n (632.8 nm)	k (632.8 nm)	reference
Water	1.332	0.000	Hale and Querry (1973)
SF6	1.799	0.000	SCHOTT (2011)
Cr	3.135	3.310i	SOPRALAB (2012)
graphene	3.000	1.149i	Bruna and Borini (2009)
Ir	2.528	4.613i	Palik (1991)
Tb	1.695	2.242i	Azofeifa et al. (2005)
Pd	1.770	4.289i	SOPRALAB (2012)
Au	0.197	3.090i	Palik (1991)
ss-DNA	1.462	0.000	Choi et al. (2011)
hybrid ss-DNA	1.480	0.000	Choi et al. (2011)

The thicknesses of the various materials, shown in table (4.2), have been chosen in order to obtain the best compromise between the contrast as defined in equation 4.9 and the sharpness of the coupling signal, evaluated by means of its Full Width at Half Maximum.

The single stranded DNA (ss-DNA) size is approximately 100 nm according to (Wu et al. (2010)) and (Kowalczyk et al. (2010)).
The biomolecular reaction of ss-DNA hybridization has been thus accordingly modeled as a 100 nm thick layer with refractive index varying from 1.462 to 1.48 during the double stranded DNA

formation (according to Gray et al. (1997) and Elhadj et al. (2004)).

Table 4.2: Thicknesses of the materials

Material	Film thickness (nm)
Cr	2
Ir	12
Pd	14
Tb	26
Graphene	0.34
ss-DNA	100

4.2.3 Numerical results

The SPR signal from the simulated Pd, Ir and Tb comprising stacks are shown in figures 4.2 4.3 and 4.4 respectively.
The Surface Plasmon Resonance coupling feature for gold is shown for comparison in image 4.5.
The sensors are conceived for detections in an aqueous environment so in every plot are reported the SPR curves for Water, ss-DNA and Hybrid-ss-DNA.
Relevant peak shifts and variations in the profile are visible passing from the refractive index of Water to the one of DNA.

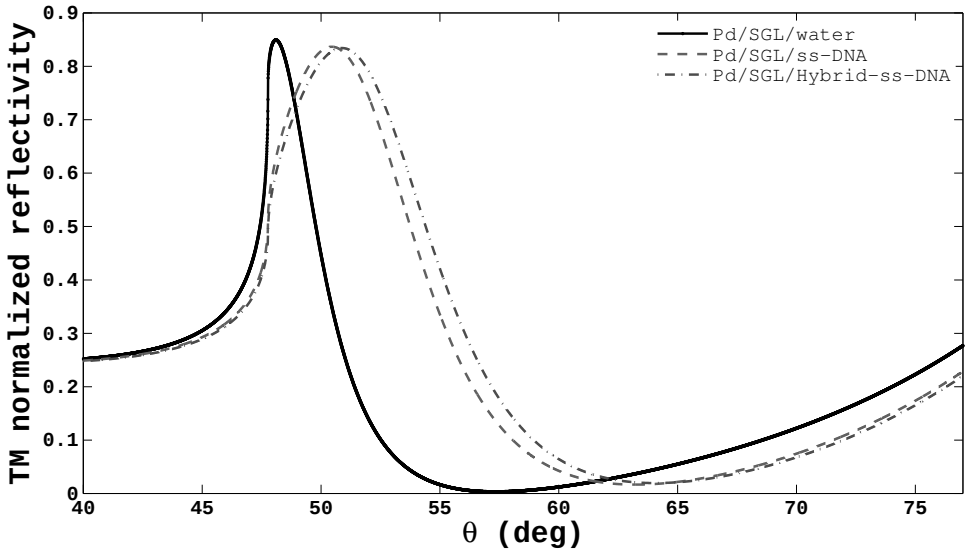

Figure 4.2: The SPR coupling features for Pd/SGL

The first two parameters by which the SPR sensors have been evaluated are the Contrast and the "peak shift".

The contrast C is defined as

$$C = \frac{I_{max} - I_{min}}{I_{max} + I_{min}} \tag{4.9}$$

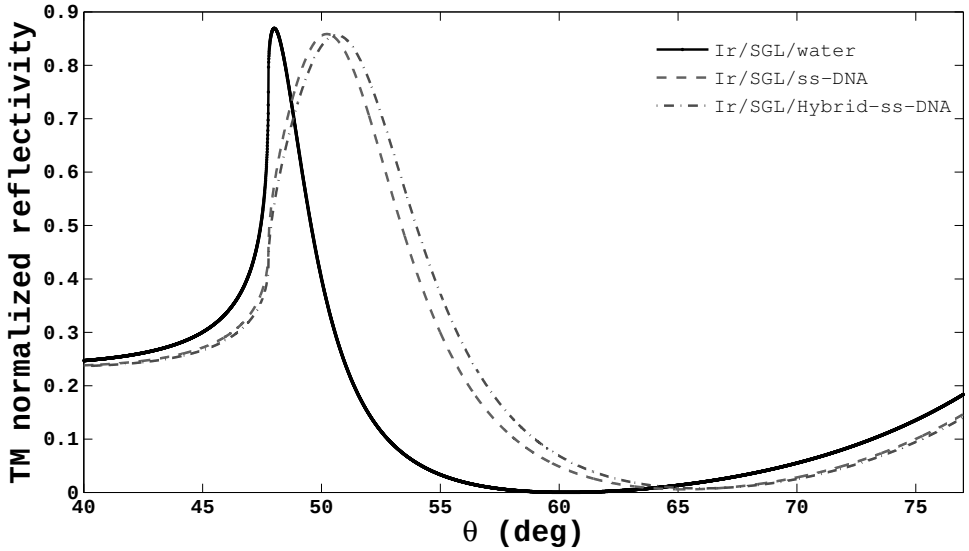

Figure 4.3: The SPR sensor signal from Ir/SGL

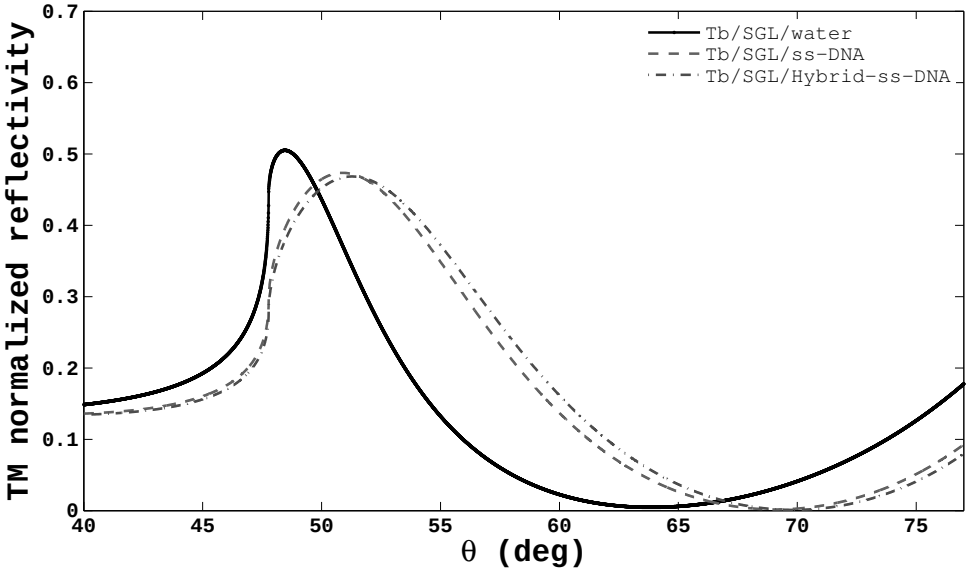

Figure 4.4: The SPR coupling features for Tb/SGL

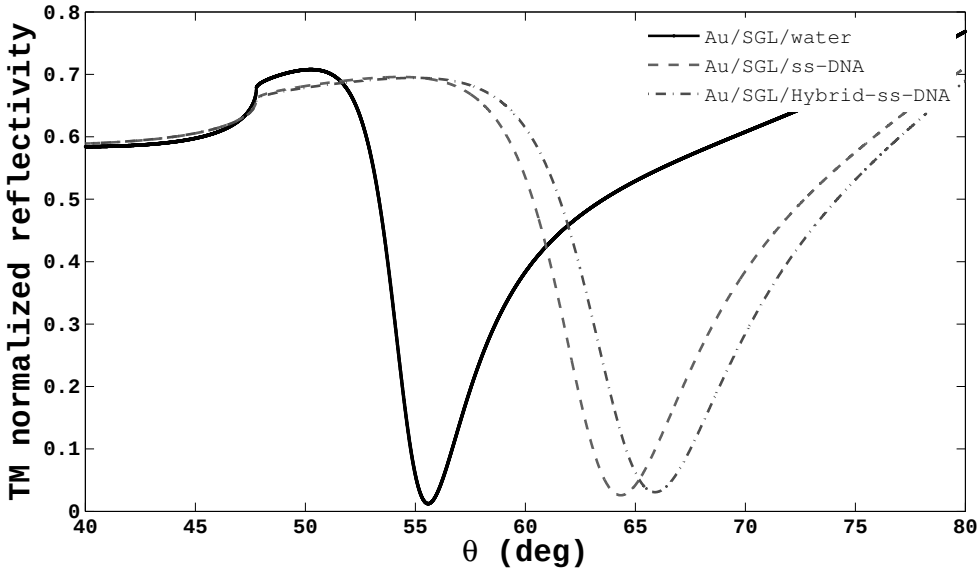

Figure 4.5: The SPR signal for Au/SGL

being I_{max} and I_{min} the maximum and minimum values for the transmitted light intensity, and its related uncertainty is

$$\Delta C = \left[\left(\frac{\Delta I_{max} + \Delta I_{min}}{(I_{max} - I_{min})} \right)^2 + \left(\frac{\Delta I_{max} + \Delta I_{min}}{(I_{max} + I_{min})} \right)^2 \right]^{1/2} \cdot \left[\frac{I_{max} - I_{min}}{(I_{max} + I_{min})} \right] \tag{4.10}$$

The change of the angular position of the maximum of reflectivity dp, or the "peak shift", caused by the change in the refractive index of the analyte is instead

$$dp = \left(\vartheta^{fin}_{coupling} - \vartheta^{in}_{coupling} \right) = d\vartheta_{coupling} \tag{4.11}$$

and the associated maximum error is

$$\Delta dp = \left[\Delta \left(\vartheta^{fin}_{coupling} \right) + \Delta \left(\vartheta^{in}_{coupling} \right) \right]. \tag{4.12}$$

In table 4.3 are shown the contrasts of the evaluated multilayer and in table 4.4 are reported for the simulated multilayer structures the change in angular position of the peak of the SPR signal

For all the structures dp changes linearly with the refractive index as it is shown in Figure 4.6 for the simulated Iridium based sensor.

It is worth to be noticed that the peak shift is still appreciable for the two different states of the DNA, so that the simulated biosensors are not only able to detect the presence of DNA but also to distinguish its chemical status.

The sensitivity of a SPR sensor can be expressed as the coefficient m between the variation of the SPR coupling angle and the corresponding variation of the analyte refractive index (Jung et al. (1998), Liedberg et al. (1993)) as in the equation (2.7) of the section (2.4) of this thesis

$$S = \frac{d\vartheta_{coupling}}{\Delta n_a} = \frac{dp}{dn_a}$$

and its related error is

Table 4.3: Contrast of the simulated SPR sensors

Multilayer	Contrast	Δ Contrast
Pd/SGL/ssDNA	0.9612	$1.6254 \cdot 10^{-4}$
Pd/SGL/Hybrid-ss-DNA	0.9545	$1.6191 \cdot 10^{-4}$
Pd/SGL/water	0.9927	$1.6525 \cdot 10^{-4}$
Ir/SGL/ss-DNA	0.9866	$1.6247 \cdot 10^{-4}$
Ir/SGL/Hybrid-ss-DNA	0.9824	$1.6217 \cdot 10^{-4}$
Ir/SGL/water	1.0000	$1.6267 \cdot 10^{-4}$
Tb/SGL/ssDNA	0.9926	$2.9649 \cdot 10^{-4}$
Tb/SGL/Hybrid-ss-DNA	0.9952	$3.0048 \cdot 10^{-4}$
Tb/SGL/water	0.9819	$2.7497 \cdot 10^{-4}$
AU/SGL/ssDNA	0.9284	$2.6720 \cdot 10^{-4}$
AU/SGL/Hyb-ssDNA	0.9152	$2.6410 \cdot 10^{-4}$
AU/SGL/water	0.9658	$2.7302 \cdot 10^{-4}$

Table 4.4: change in angular position of the SPR signal for different nanostructures

initial state	final state	dp (deg)	Δ dp (deg)
Pd/SGL/ssDNA	Pd/SGL/Hybrid-ss-DNA	0.425	0.010
Ir/SGL/ss-DNA	Ir/SGL/Hybrid-ss-DNA	0.410	0.010
Tb/SGL/ss-DNA	Tb/SGL/Hybrid-ss-DNA	0.393	0.010
Au/SGL/ss-DNA	Au/SGL/Hybrid-ss-DNA	1.557	0.010
Pd/SGL/water	Pd/SGL/ss-DNA	2.350	0.010
Ir/SGL/water	Ir/SGL/ss-DNA	2.215	0.010
Tb/SGL/water	Tb/SGL/ss-DNA	2.428	0.010
Au/SGL/water	Au/SGL/ss-DNA	8.755	0.010
Pd/ss-DNA	Pd/Hybrid-ss-DNA	0.425	0.010
Ir/ss-DNA	Ir/Hybrid-ss-DNA	0.408	0.010
Tb/ss-DNA	Tb/Hybrid-ss-DNA	0.395	0.010
Au/ss-DNA	Au/Hybrid-ss-DNA	1.518	0.010

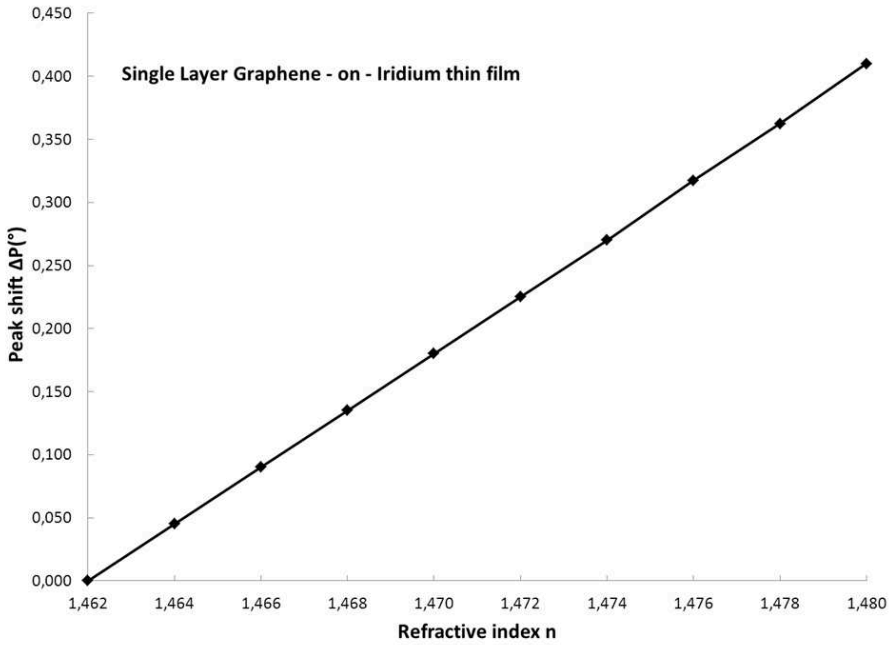

Figure 4.6: Sensitivity of the SGL/Ir SPR sensor during the ss-DNA hybridization

$$\Delta S = \left[\left(\frac{\Delta dp}{|dp|} \right)^2 + \left(\frac{\Delta dn_a}{|dn_a|} \right)^2 \right]^{1/2} \cdot |S| \tag{4.13}$$

In the proposed simulations the refractive indexes are considered to be exact.

The numerical results for the sensitivity of the different multilayers are shown in table(4.5)

Taking into account the Full Width at Half Maximum (FWHM) of the simulated multilayers, presented in table 4.6, is then possible to define a a Figure Of Merit (FOM) for SPR sensor (as stated from Szunerits et al. (2008), Sherry et al. (2005)) expressed in equation (2.9) of section (2.4).

$$FOM = \frac{S \ \left[deg \ RIU^{-1} \right]}{FWHM \ [deg]}$$

The numerical results along with the corresponding errors

$$\Delta(FOM) = \left[\left(\frac{\Delta S}{|S|} \right)^2 + \left(\frac{\Delta(FWHM)}{|FWHM|} \right)^2 \right]^{1/2} \cdot |FOM| \tag{4.14}$$

are reported in table 4.7.

The Figure Of Merit however didn't fully reveal the qualities of the ISPR metals.

Then in order to evaluate the simulated SPR sensors an evaluation factor E was considered

$$E \propto \frac{S \cdot C}{FWHM} \ \left[RIU^{-1} \right] \tag{4.15}$$

and table 4.8 reports the numerical results with the corresponding uncertainties

$$\Delta(E) = \left[\left(\frac{\Delta S}{|S|} \right)^2 + \left(\frac{\Delta C}{|C|} \right)^2 + \left(\frac{\Delta(FWHM)}{|FWHM|} \right)^2 \right]^{1/2} \cdot |E| \, . \tag{4.16}$$

Table 4.5: Sensitivity of the simulated multilayer structures

initial state	final state	dn (RIU)	S (deg/RIU)	ΔS(deg/RIU)
Pd/SGL/ssDNA	Pd/SGL/Hybrid-ss-DNA	0.018	23.611	0.556
Ir/SGL/ss-DNA	Ir/SGL/Hybrid-ss-DNA	0.018	22.778	0.556
Tb/SGL/ss-DNA	Tb/SGL/Hybrid-ss-DNA	0.018	21.833	0.556
Au/SGL/ss-DNA	Au/SGL/Hybrid-ss-DNA	0.018	86.500	0.556
Pd/SGL/water	Pd/SGL/ss-DNA	0.130	18.077	0.077
Ir/SGL/water	Ir/SGL/ss-DNA	0.130	17.038	0.077
Tb/SGL/water	Tb/SGL/ss-DNA	0.130	18.677	0.077
Au/SGL/water	Au/SGL/ss-DNA	0.130	67.346	0.077
Pd/ss-DNA	Pd/Hybrid-ss-DNA	0.018	23.611	0.556
Ir/ss-DNA	Ir/Hybrid-ss-DNA	0.018	22.667	0.556
Tb/ss-DNA	Tb/Hybrid-ss-DNA	0.018	21.944	0.556
Au/ss-DNA	Au/Hybrid-ss-DNA	0.018	84.333	0.556

Table 4.6: FWHM of the signal of the various multilayers

Structure	FWHM (deg)	Δ (FWHM) (deg)
Pd/SGL/ssDNA	6.728	0.010
Pd/SGL/Hybrid-ss-DNA	7.328	0.010
Pd/SGL/water	3.043	0.010
Pd/ss-DNA	6.620	0.010
Pd/Hybrid-ss-DNA	7.213	0.010
Ir/SGL/ss-DNA	6.101	0.010
Ir/SGL/Hybrid-ss-DNA	6.729	0.010
Ir/SGL/water	2.701	0.010
Ir/ss-DNA	5.989	0.010
Ir/Hybrid-ss-DNA	6.611	0.010
Tb/SGL/ssDNA	9.857	0.010
Tb/SGL/Hybrid-ss-DNA	10.508	0.010
Tb/SGL/water	5.710	0.010
Tb/ss-DNA	9.748	0.010
Tb/Hybrid-ss-DNA	10.401	0.010
Au/SGL/ssDNA	8.184	0.010
Au/SGL/Hybrid-ss-DNA	8.573	0.010
Au/SGL/water	5.673	0.010
Au/ss-DNA	7.438	0.010
Au/Hybrid-ss-DNA	7.792	0.010

Table 4.7: Figure Of Merit of the simulated sensors for Hybrid ss-DNA formation

Structure	FOM (RIU^{-1})	Δ (FOM) (RIU^{-1})
Pd/SGL/Hybrid-ss-DNA	3.222	0.076
Ir/SGL/Hybrid-ss-DNA	3.385	0.083
Tb/SGL/Hybrid-ss-DNA	2.078	0.053
Au/SGL/Hybrid-ss-DNA	10.090	0.066

Table 4.8: Evaluation factor and corresponding errors for Hybrid ss-DNA formation

Structure	E	Δ E
Pd/SGL/Hybrid-ss-DNA	3.075	0.073
Ir/SGL/Hybrid-ss-DNA	3.325	0.081
Tb/SGL/Hybrid-ss-DNA	2.068	0.053
Au/SGL/Hybrid-ss-DNA	9.234	0.060

Finally a quality factor Q

$$Q \propto \frac{C}{FWHM} \quad \left[RIU^{-1}\right] \tag{4.17}$$

has been chosen as the most appropriate one to evaluate the precision and accuracy of the simulated biosensor .
In fact, an higher contrast and a narrower profile allow more precise investigations with higher signal to noise ratio.
The errors on Q

$$\Delta(Q) = \left[\left(\frac{\Delta C}{|C|}\right)^2 + \left(\frac{\Delta(FWHM)}{|FWHM|}\right)^2\right]^{1/2} \cdot |Q| \tag{4.18}$$

and the numeric results are reported in table 4.9.

Image (4.7) shows the quality factor for the sensors comprising Ir (S_{Ir}), Pd (S_{Pd}) and Gold (S_{Au}) in water (black data) and during DNA hybridization (white squares), normalized to the higher value.

Table 4.9: Quality factor and corresponding errors for Hybrid ss-DNA formation

Structure	Q	Δ Q
Pd/SGL/ssDNA	0.1429	$2.1369 \cdot 10^{-4}$
Pd/SGL/Hybrid-ss-DNA	0.1303	$1.7911 \cdot 10^{-4}$
Pd/SGL/water	0.3263	$1.0738 \cdot 10^{-3}$
Ir/SGL/ss-DNA	0.1617	$2.6639 \cdot 10^{-4}$
Ir/SGL/Hybrid-ss-DNA	0.1460	$2.1829 \cdot 10^{-4}$
Ir/SGL/water	0.3703	$1.3724 \cdot 10^{-3}$
Tb/SGL/ssDNA	0.1007	$1.0650 \cdot 10^{-4}$
Tb/SGL/Hybrid-ss-DNA	0.0947	$9.4557 \cdot 10^{-5}$
Tb/SGL/water	0.1720	$3.0499 \cdot 10^{-4}$
AU/SGL/ssDNA	0.1134	$1.4242 \cdot 10^{-4}$
AU/SGL/Hyb-ssDNA	0.1068	$1.2829 \cdot 10^{-4}$
AU/SGL/water	0.1702	$3.0391 \cdot 10^{-4}$

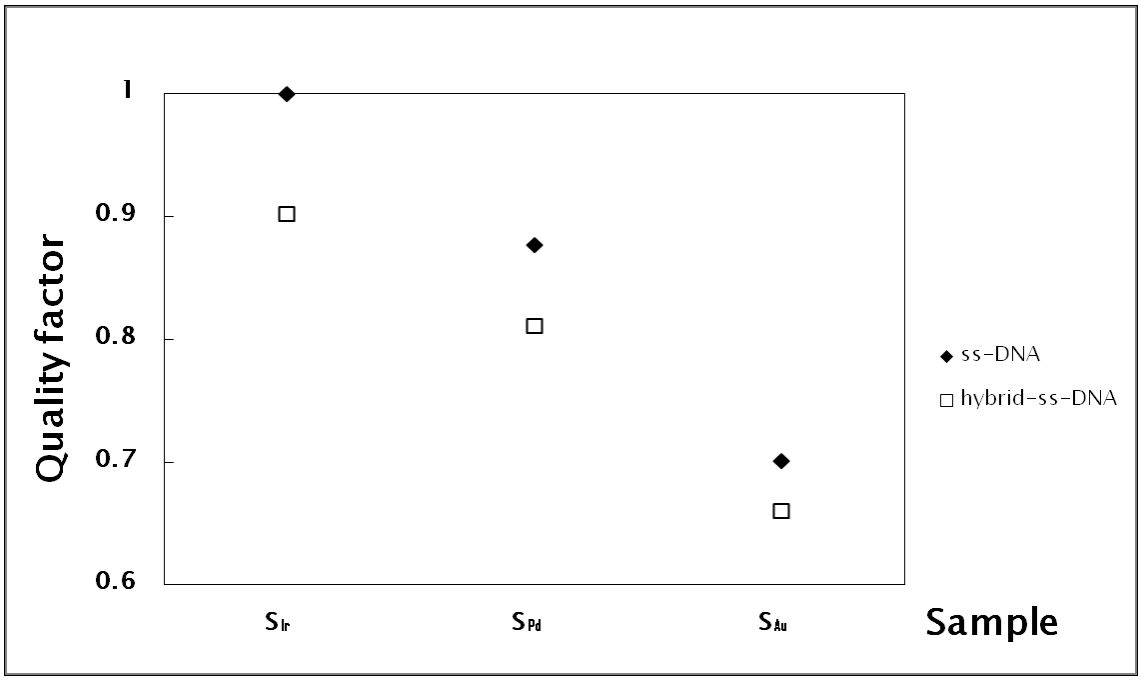

Figure 4.7: Quality factor for the sensors comprising Ir (S_{Ir}), Pd (S_{Pd}) and Gold (S_{Au}) in water (black data) and during DNA reaction (white squares), normalized to the higher value.

4.2.4 Conclusions

From the results, Gold comprising SPR sensors clearly provide the best sensitivity but, unfortunately, biomolecules poorly adsorb on gold and this drawback limits the performances of the conventional SPR devices.

Among the ISPR metals SGL/Pd owns the greater sensitivity but the SGL/Ir shows a sharper profile and a greater contrast . In fact, the sensitivity S is 4% better for the SGL/Pd than SGL/Ir, on the contrary the SLG/Ir has an higher contrast C of 3% and about FWHM of 9%.
Terbium shows a sensitivity comparable to the one of the other metals showing reflectivity maxima, but with lower Figure of Merit and Evaluation factor E.
Consequently Palladium is the most sensitive of the evaluated ISPR metals while Iridium offers better resolution and accuracy.
Therefore the SGL/Ir has overall better characteristics than the other ISPR metals.

In addition to that, the utilized Quality factor Q takes into account the sharpness and the contrast of the various structures.
The results of the analysis reveals a higher quality factor for the Ir and Pd based biosensors than for the conventional Au sensor. For example during the Hybrid ss-DNA detection the Q factor of S_{Ir} is 27% higher than the one for S_{Au} and of 11% than the quality factor for S_{Pd}.

These data suggests that, if a SPR sensor must be utilized with a limited incidence angle range, as in static setups, and in noisy conditions, perhaps a sharper profile, a higher contrast and the possibility to detect a maxima of reflectivity instead then a minimum could allow the ISPR based biosensors to offer greater advantages than the conventional SPR sensors, despite the latter having a higher sensitivity.

The only issue to the realization of this kind of detector is related to the SGL deposition development, but taking into account the state of art it seems to be soon feasible.

To summarize the analized ISPR sensors show three innovative aspects:

- ⋆ to my knowledge Iridium hasn't been utilized yet in SPR sensors
- ⋆ a sharp reflectivity maxima as a signal
- ⋆ a good resistance to oxidation and contamination. In particular the graphene layer acts as a Biomolecular Recognition Element as well as a protective element.

Therefore, they could potentially open new possibilities for innovative, sensitive and selective biosensors.

4.3 Implementation of the original Matlab program for simulations

Starting from the original Matlab program for the simulation of SPR sensors I also implemented it by adding some characteristics:

- ⋆ I modified the program so that it is possible to simulate the effect of a cylindrical prism additionally to the previous right angle prism
- ⋆ Simulating a static SPR sensor I evaluated into the Matlab program the spatial and angular effects of a collimating lens on the prism and the corresponding area on the detector
- ⋆ I also simulated the effect on SPR sensors of dicroic materials within but this part of my research activity would have required more time to be expanded.

Chapter 5

Implementation of a Surface Plasmon Resonance sensor in laboratory

In order to create innovative SPR sensors and miniaturized Surface Plasmon Resonance sensors for the Wireless Sensor Network, I have implemented some of these devices in laboratory.

They are based on angular interrogation, prism coupling and on the Kretschmann geometry for Attenuated Total Reflection.

5.1 Implementation of a SPR based sensor with dynamical setup

5.1.1 Optical setup

My first laboratory implementation of a SPR sensor had a dynamical setup. This kind of configuration required the light beam to be highly collimated and the prism to be rotated at every scanning incidence angle.

The optical setup consisted on

- ⋆ a 5 mW HRR050 Thorlabs He-Ne laser
- ⋆ a polarizer
- ⋆ a fused silica right angle prism
- ⋆ a 1 mm thick BF33 glass slide where a 1.4 nm thick layer of Chromium and a Gold layer with a thickness of 59 nm were coated
- ⋆ a silicone flowcell
- ⋆ a Thorlabs photodiode.

A photo of the whole SPR sensor is provided in figure (5.1) while figure (5.2) shows the prism and the coated glass slide in a first-prototype mount and the photodiode. Moreover figure (5.3) is a photograph of the flowcell on the same structure.

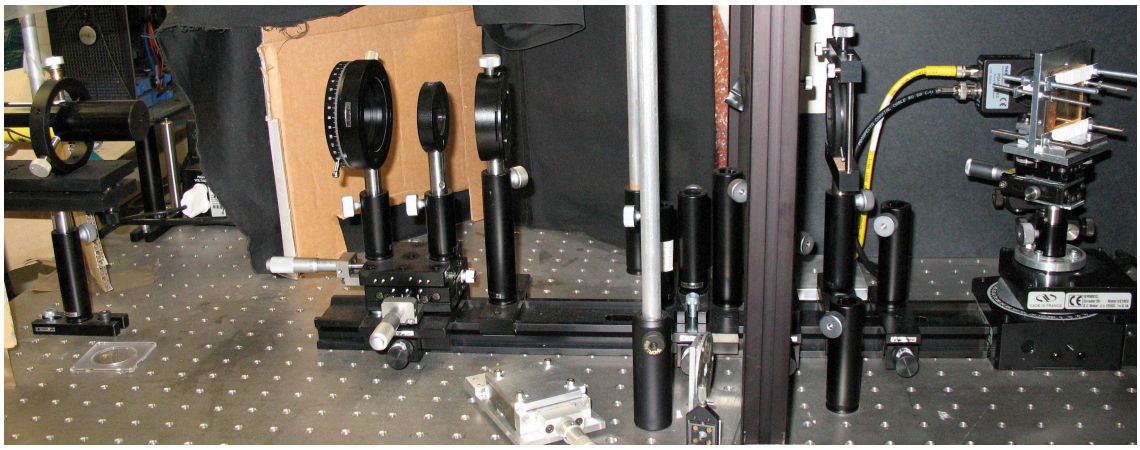

Figure 5.1: photo of the SPR sensor with dynamical optical system

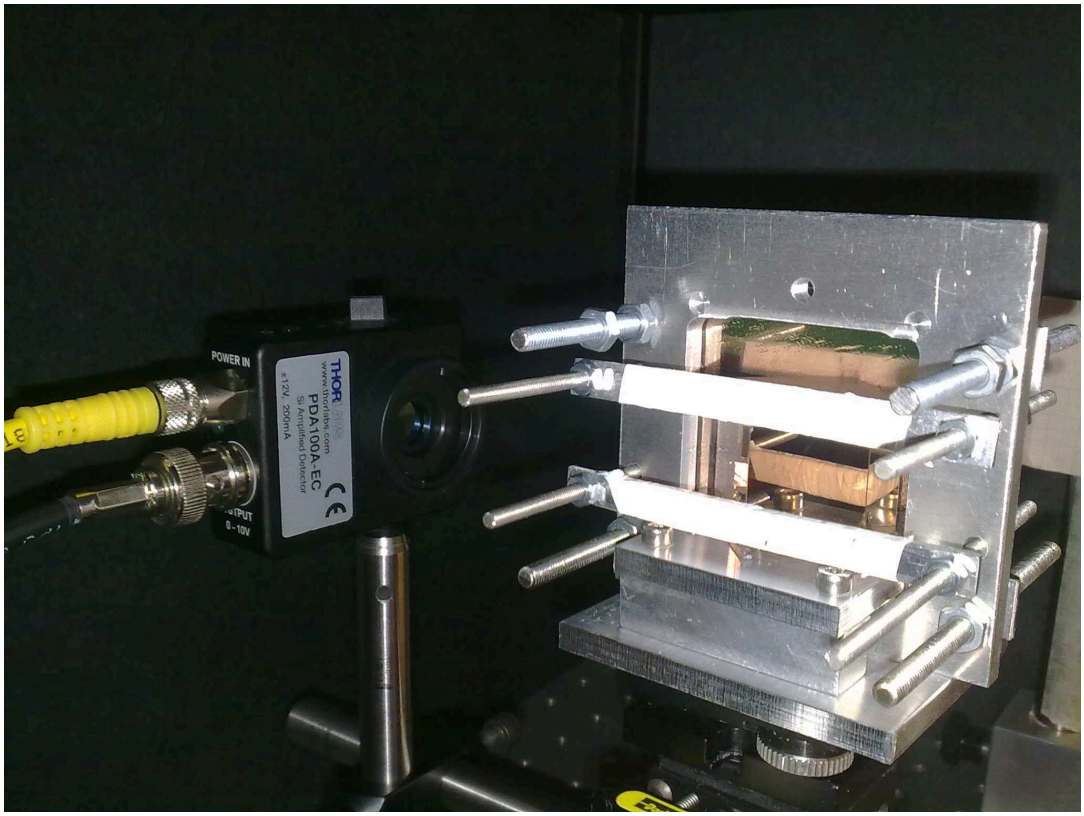

Figure 5.2: photo of the right angle prism and the coated glass slide in an first-prototype mount and the photodiode

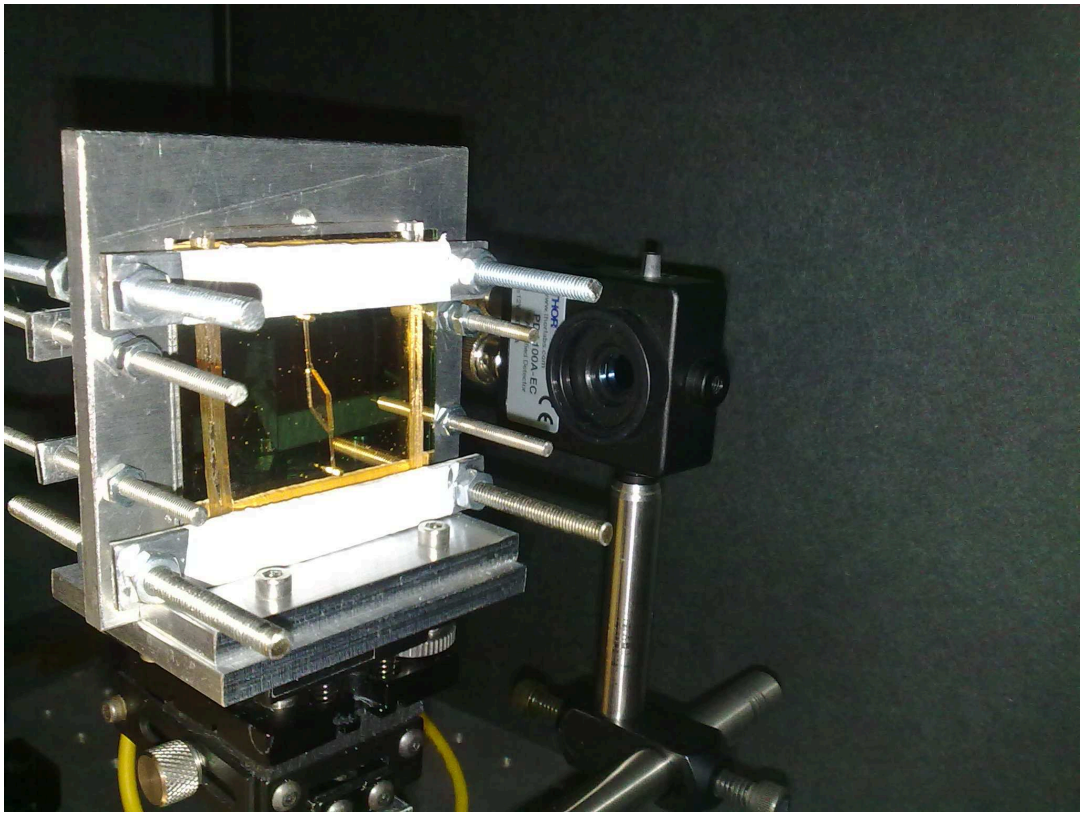

Figure 5.3: photo of the flowcell on the early-prototype mount and the photodiode

The He-Ne laser

The light source in use is a Thorlabs HRR050 He-Ne laser. Its characteristics are

- ⋆ a wavelength of 632.8 nm
- ⋆ $1/e^2$ beam diameter of 0.80 mm
- ⋆ a minimum output power of 5 mW
- ⋆ a maximum output power of 10 mW
- ⋆ a divergence of 1.01 mrad
- ⋆ random polarization

The source is the technical datasheet, available at
http://www.thorlabs.de/thorProduct.cfm?partNumber=HRR050

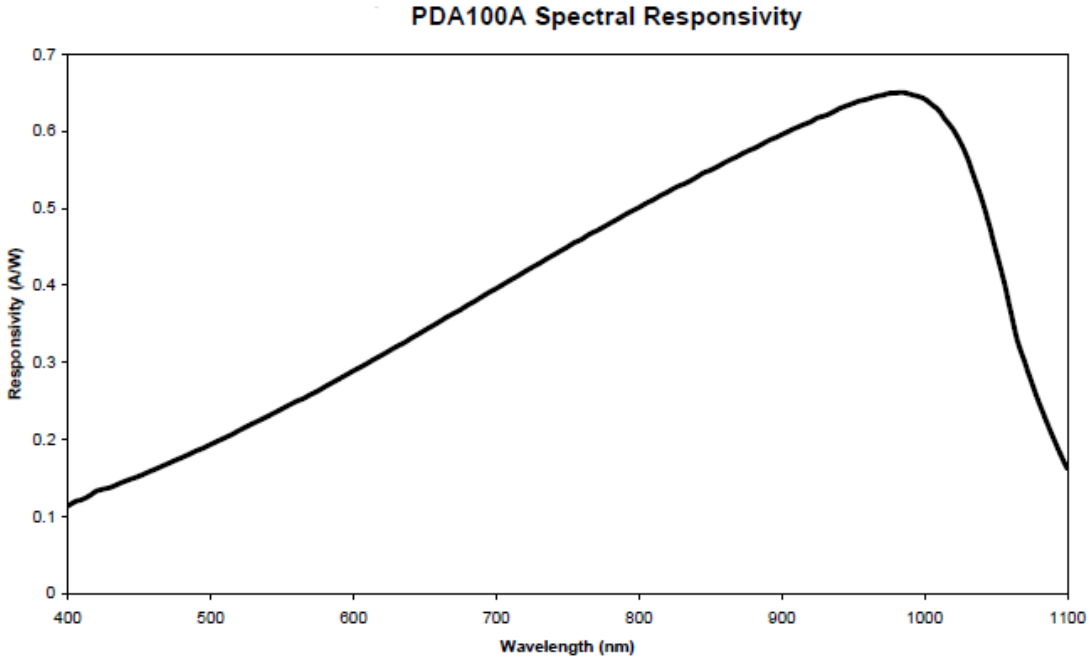

Figure 5.4: photodiode responsivity

Photodiode

The photodiode utilized in the dynamical setup was a Thorlabs PDA100A. This is an amplified, switchable-gain, silicon detector designed for detection of light signals in the 350-1100 nm wavelength range.
An eight-position rotary switch allows to vary the gain from 0 to 70 dB in 10 dB steps while the output range is 0 to 10 Volt.

The photodiode responsivity $R(\lambda)$ is plotted in image 5.4 and the output can be thus obtained by

$$Output\ [V/W] = R(\lambda) \cdot\ transimpedance\ gain\ [V/A] \tag{5.1}$$

5.1.2 Measurements: gas sensing

With the SPR sensor described above I made measurements with air, Helium and Pentane gases to determinate the sensitivity of the optical system and improve it.

Data Normalization procedure and noise

In order to normalize the reflectivity data for every measurement were taken:

1. the reflectivity observative intensity data, $I_{measured}$
2. dark values, I_{dark}, taken for the same angles of the observative data and with the laser turned off
3. the full intensity value, $I_{full-intensity}$, taken placing the photodiode before the prism in the optical path and scanning for a small statistic angular range centered to the normal to the

laser. The average of these data was taken as the value of the full beam intensity without the SPR coupling.

The normalized values for reflectivity were obtained subtracting the dark values to the measurement data and the full intensity value and then dividing the reflectivity observative data for the full intensity value.
Thus

$$R = \frac{I}{I_f} \tag{5.2}$$

being R the reflectivity, $I = I_{measured} - I_{dark}$ and $I_f = I_{full-intensity} - I_{dark}$.
The associated noise was then

$$\Delta R = \left[\left(\frac{\Delta I}{I} \right)^2 + \left(\frac{\Delta I_f}{I_f} \right)^2 \right]^{1/2} \cdot R. \tag{5.3}$$

Helium gas sensing

As a first step I obtained the reference SPR signal taking reflectivity measurements for air fluxes at 1 atm inside the flowcell and then normalizing them as described in 5.1.2. The steps in the prism movements were of 0.1 degrees with 0.01 deg of precision and the angular zero on the plots was established at 45 degrees of incidence. The measurements were thus made with incidence angles from -6 deg to 9 deg.

Then I made measurements for fluxes of Helium gas at 1.2 bar and 2.4 bar in the flowcell with the same angular scans and precisions.

The SPR signals are plotted in image (5.5).

Moreover I fitted the data with the theoretical expected intensity values, obtained from the Matlab program for the simulation of SPR sensor presented in chapter (4).
The refractive index of air at 633 nm is n=1.0003 from (Ciddor (1996)).

Also, from the Sellmeier equation expressed in (Burton (1908)), I calculated the refractive index for Helium gas at a pressure of 1 atm and wavelength of 633 nm, which resulted n= 1.00003497.

I consequently changed the analyte refractive index accordingly in the simulations and I verified a good fit with Helium measurements at 1.2 bar.

The change in the refractive index from air to Helium was too small to appreciate the shift in the coupling minimum of reflectivity, but it was still possible to notice some intensity differences in their SPR signals at lower incidence angles than the coupling one.

The angular zero on the plots was set at 45 degrees of incidence and the minimum of reflectivity was thus situated at 2.7 deg.

From the measurements of air and Helium fluxed with similar pressures, I found in the plot region between -3 deg and 1 deg, a reflectivity change of $-1.4 \cdot 10^{-2} \pm 0.6 \cdot 10^{-2}$ for the same angle.

Moreover, taking into consideration the reflectivities for He gas fluxed at 1.2 bar and 2.4 bar, the differences are up to $4.5 \cdot 10^{-2} \pm 0.8 \cdot 10^{-2}$, therefore showing that this SPR sensor is able to discriminate that pressure difference.

Pentane gas sensing

Making use of another BF33 glass slide with a coating of 0.8 nm of Chromium and 59 nm of Gold I made also measurements of Pentane gas detection.

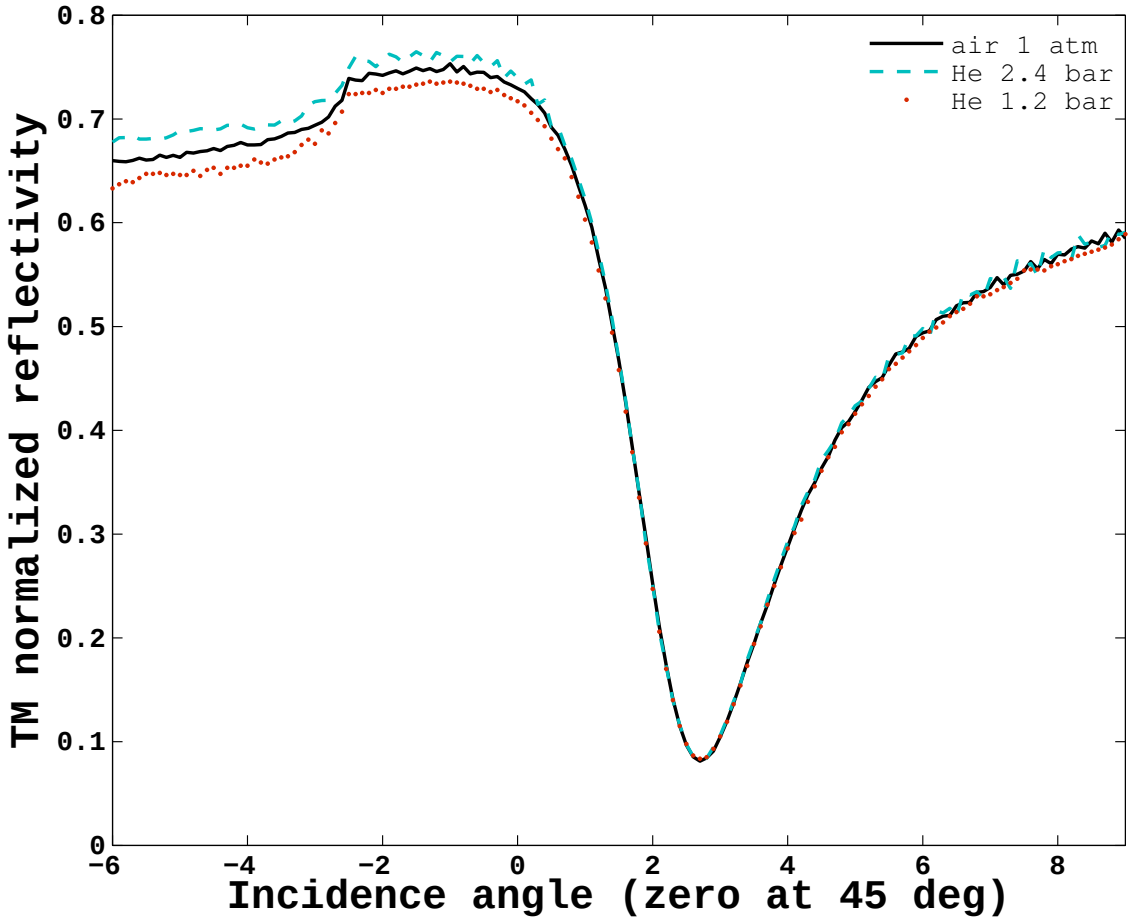

Figure 5.5: SPR measurements with dynamical setup for air at 1 atm, Helium gas at 1.2 bar and 2.4 bar of pressure

First of all I calculated the theoretical change in the angular position of the minimum of reflectivity due to the change of the refractive index of the analyte, in this case from n=1.0003 for air at 633 nm from (Ciddor (1996)) to n=1.00167 for Pentane at the same wavelength.
The latter has been obtained from the Sellmeier equation in (Lowery and Hartley (1931)).

As can be seen in image 5.6 the attended shift was 0.2 deg.

Then I made reflectivity measurements for air and pentane, setting again the angular zero of the plots at 45 degrees of incidence and therefore with angular scan from -1.5 to 8 deg, prism movement steps of 0.1 degrees and 0.01 deg of precision.

The SPR coupling features were consequently normalized as described in (5.1.2) and fitted with the theoretical curves obtained by means of the Matlab simulation program presented in chapter (4).

A zoom of the minima of the SPR signals for air and pentane gas are shown in figure 5.7, while the curve fitting for Pentane gas is plotted in figure 5.8.

The measured angular peak shift was about 0.2 deg, according to the expected value, moreover the intensity difference between the two SPR features, measured at the same angle, was $5.00 \cdot 10^{-2} \pm 1.18 \cdot 10^{-2}$.

The implemented SPR sensor was thus able to detect the presence of Pentane gas, discriminating the latter from air.

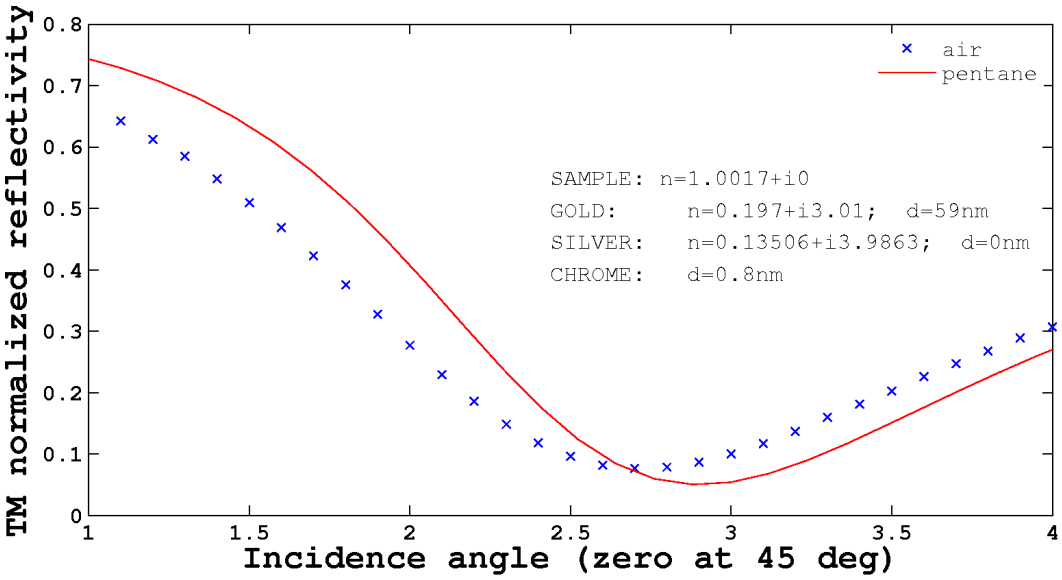

Figure 5.6: Theoretical change in the coupling minimum of the SPR sensor for Pentane gas detection

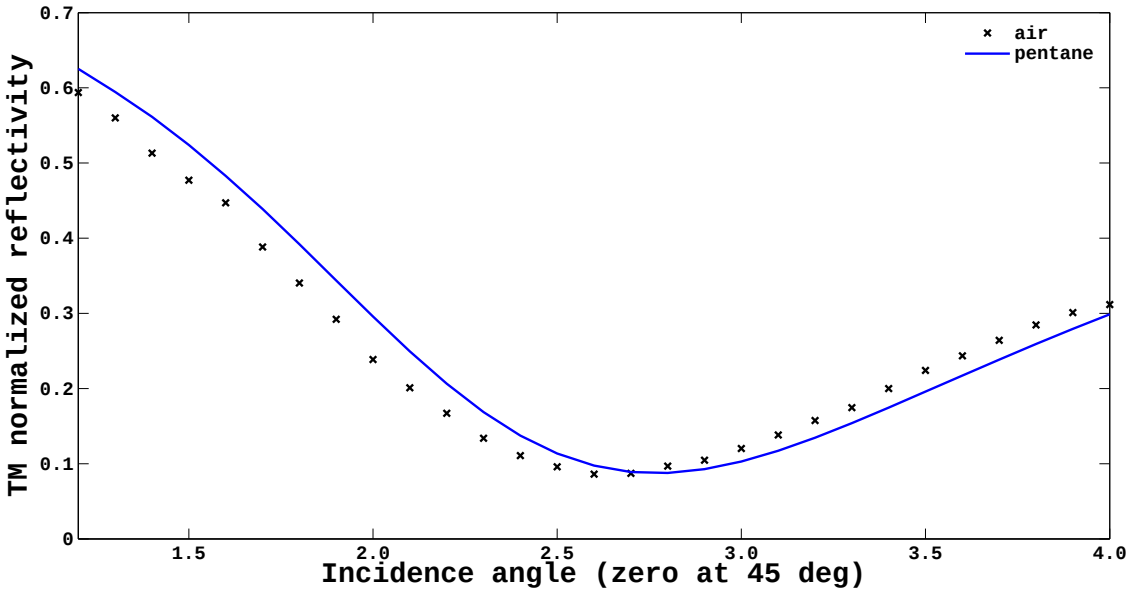

Figure 5.7: Measured change in the SPR signal from air to Pentane gas detection

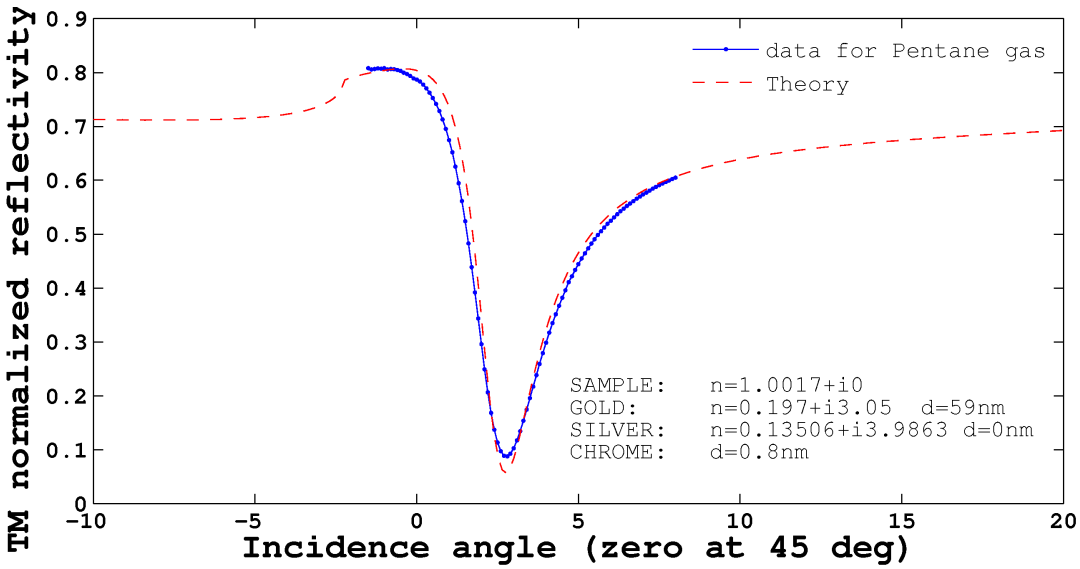

Figure 5.8: Fitting of the SPR signal for Pentane gas detection by means of the computer numerical simulations

5.2 First implementation of a SPR based sensor with static setup

The SPR sensor with dynamical setup was highly sensible but the measurement time was very long, about half an hour, this leading to possible errors and changes in the surrounding environment.

For this reason I improved the implemented SPR sensor making use of a static configuration. In this kind of setup the whole chosen angular range is scanned at the same time by the system and thus the whole coupling minimum is visible in a single measure. The measurement time is therefore greatly reduced.

5.2.1 Optical setup

The first used static setup configuration comprised

- ⋆ The 5 mW HRR050 Thorlabs He-Ne laser
- ⋆ a Transversal Magnetic polarizer
- ⋆ a pinhole with a 200 μm diameter
- ⋆ a circular slit
- ⋆ two neutral filters
- ⋆ a BK7 cylindrical lens with focal length 155 mm
- ⋆ An SF6 (refractive index 1.7988 at 632.8 nm) cylindrical prism with a coating of 2 nm of Chrome and 50 nm of Gold
- ⋆ a CMOS camera.

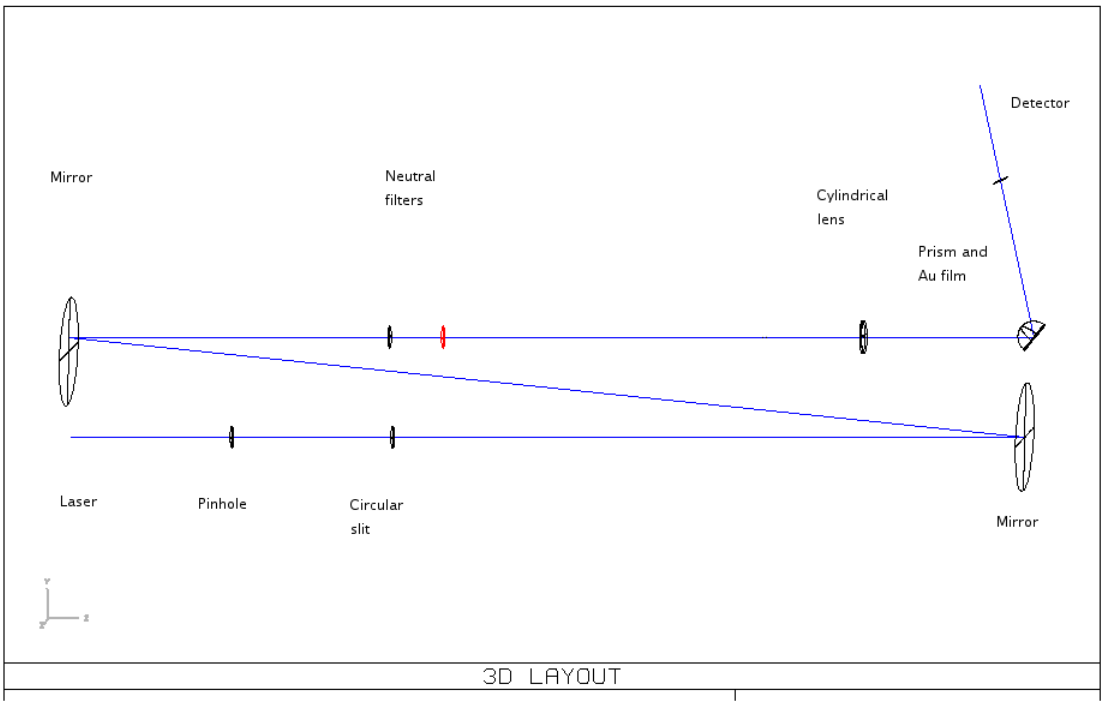

Figure 5.9: Zemax simulation of the first SPR sensor having a static optical system

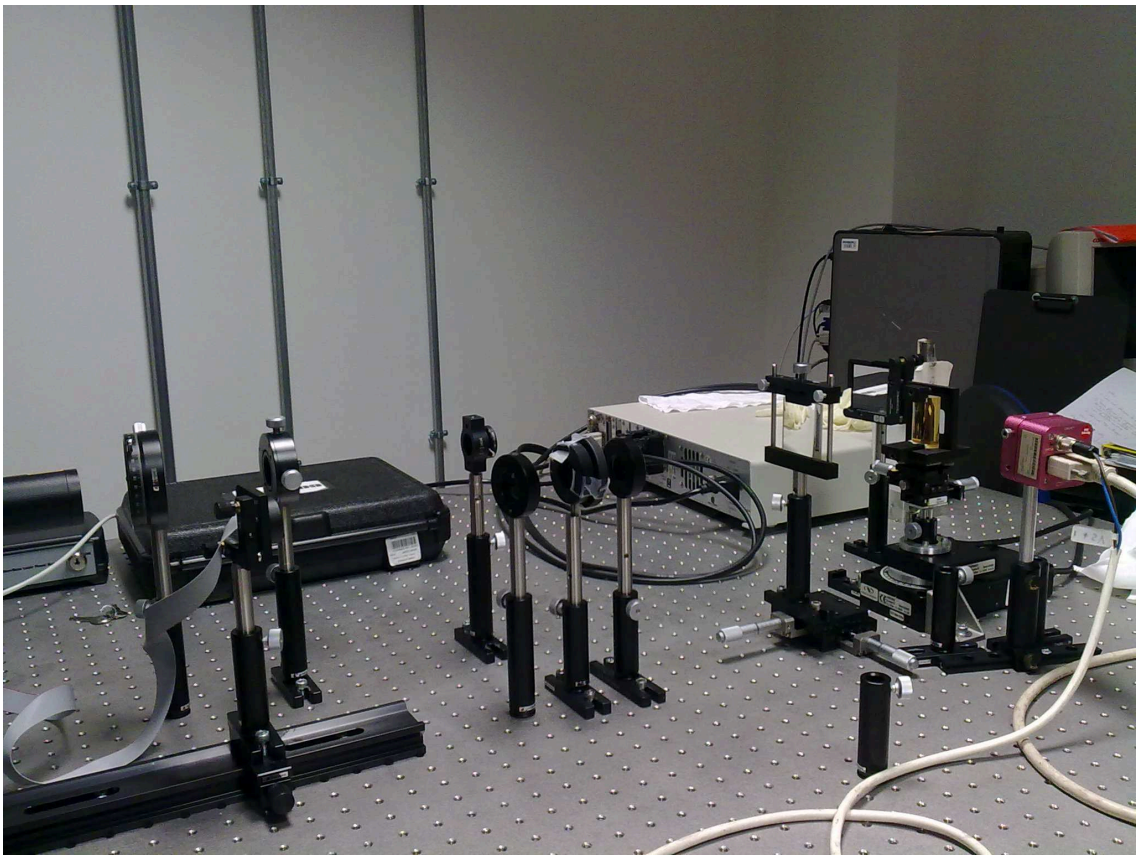

Figure 5.10: photo of the first SPR sensor with static optical system

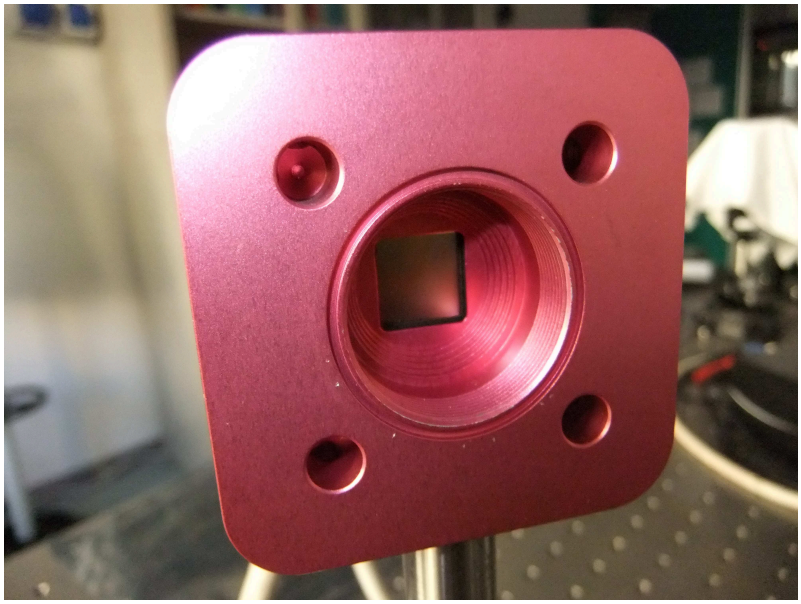

Figure 5.11: Photonfocus camera

The He-Ne laser beam was spatially filtered with a pinhole and a circular slit so that only the central Airy disk of the light diffraction figure was made use of. Two mirror were then employed, so that more elements could be used, and two neutral filters decreased the intensity of the radiation in order not to saturate the detector. After that the radiation passed through a cylindrical lens that on the horizontal plane focused the beam on the gold film and on the center of curvature of the cylindrical prism.

Attenuated Total Reflection occurred and the reflected light was then collected by the CMOS camera.

The images (5.9) and (5.10) show a Zemax simulation and a photo of the optical system.

The He-Ne laser in use was the same of the previous configuration and is described in (5.1.1).

The CMOS camera

As a the optical system detector a Photonfocus MV-D1024 camera was utilized.

It is a CMOS camera, shown in figure (5.11), with

- ⋆ a resolution of 1024 x 1024 pixels
- ⋆ an active optical area of 10.9 mm x 10.9 mm
- ⋆ a pixel size of 10.6 μm x 10.6 μm
- ⋆ a grayscale resolution of 8 bit
- ⋆ spectral range from 400 to 900 nm
- ⋆ a full well capacity of 200 ke^-

and its datasheet is at
(http://www.photonfocus.com/upload/manuals/MAN001_e_V1_2_1024-series.pdf)

5.2.2 The measurements

Normalization procedure for the static SPR sensor

In order to normalize the reflectivity data of the optical system, the following measurements were made:

1. an image with the laser turned off, or dark image
2. a reference image, that is an image taken at 5 degrees from the coupling angle. It doesn't show the coupling minimum of reflectivity so it is taken as a full beam reference.
3. the scientific data image, or measurement image, acquired at the coupling angle.

When air was measured the coupling angle was visible at 36 degrees from the normal to the prism and the reference image was taken at 41 degrees of incidence.

Picture (5.12) is an example of reference image and ((5.13) an image of the minimum of reflectivity for air.

As a first step the dark image was subtracted to the reference and the measurement images in order to delete the contribution of ambient light and burned pixels.

The normalization was therefore obtained dividing the pixel values of the measurement image by the maximum pixel value of the center of the beam of the reference image, so to discard the hot pixels if present.

The normalized SPR measurements are shown in the image (5.14).

For every image the 210 central rows were then scanned and 21 data series stored, each one being the convolution (and so the mean value) of 10 pixel columns. After that the data series were compared with the theoretical values and as a first evaluating function the relation (5.4) was used.

$$X(i) = \sqrt{\frac{\sum_j \left[data(i,j) - theory(i,j)\right]^2}{n_{data}}} \qquad i = 1, ...21, \quad j = 1, ...n_{data} \tag{5.4}$$

The latter is an estimation of a Root mean square deviation of the real measurements from the theoretical values.
The row corresponding to the minimum value of the vector X was then plotted against the theory.

The input light intensity distribution

In order to improve the data modeling and the adherence of the theory to real physical conditions a realistic approximation of the light intensity distribution was improved.

The pinhole diffracts the laser beam so that the light intensity is assumed to consequently follow a sinc distribution, and the Airy disks are visible.

As a first step the light intensity distributions for the horizontal x-axis and the vertical y-axis of the observations was evaluated by data fit of the final reference or direct beam images.

The formula that reproduced the x-axis (position on the camera detector corresponding to the incidence angles) light intensity was

$$XLI(i) = sinc\left(((i - 100)/650/0.01064) * 0.01064\right) \tag{5.5}$$

taking into account

1. the coupling minimum position

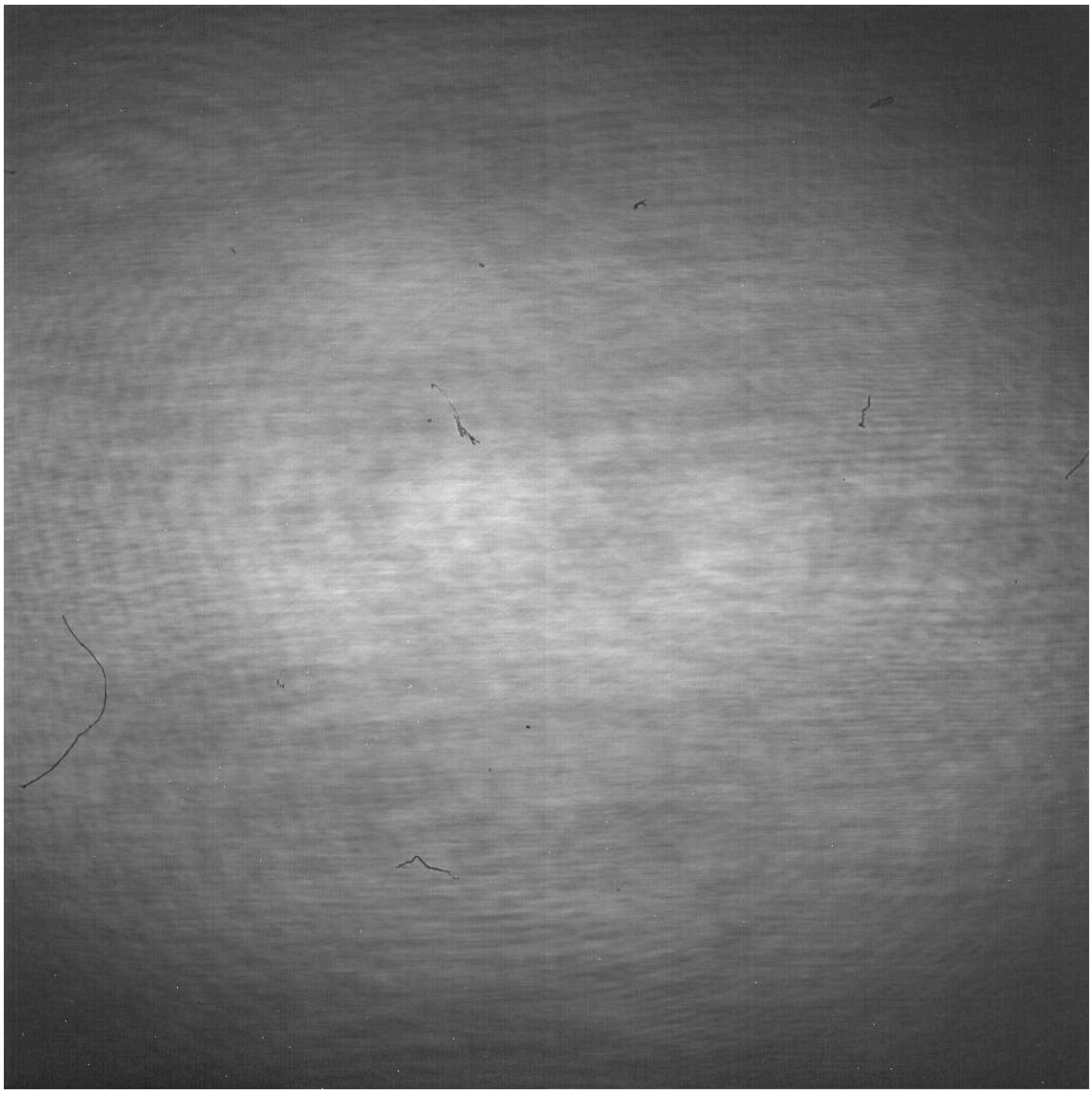

Figure 5.12: A reference image

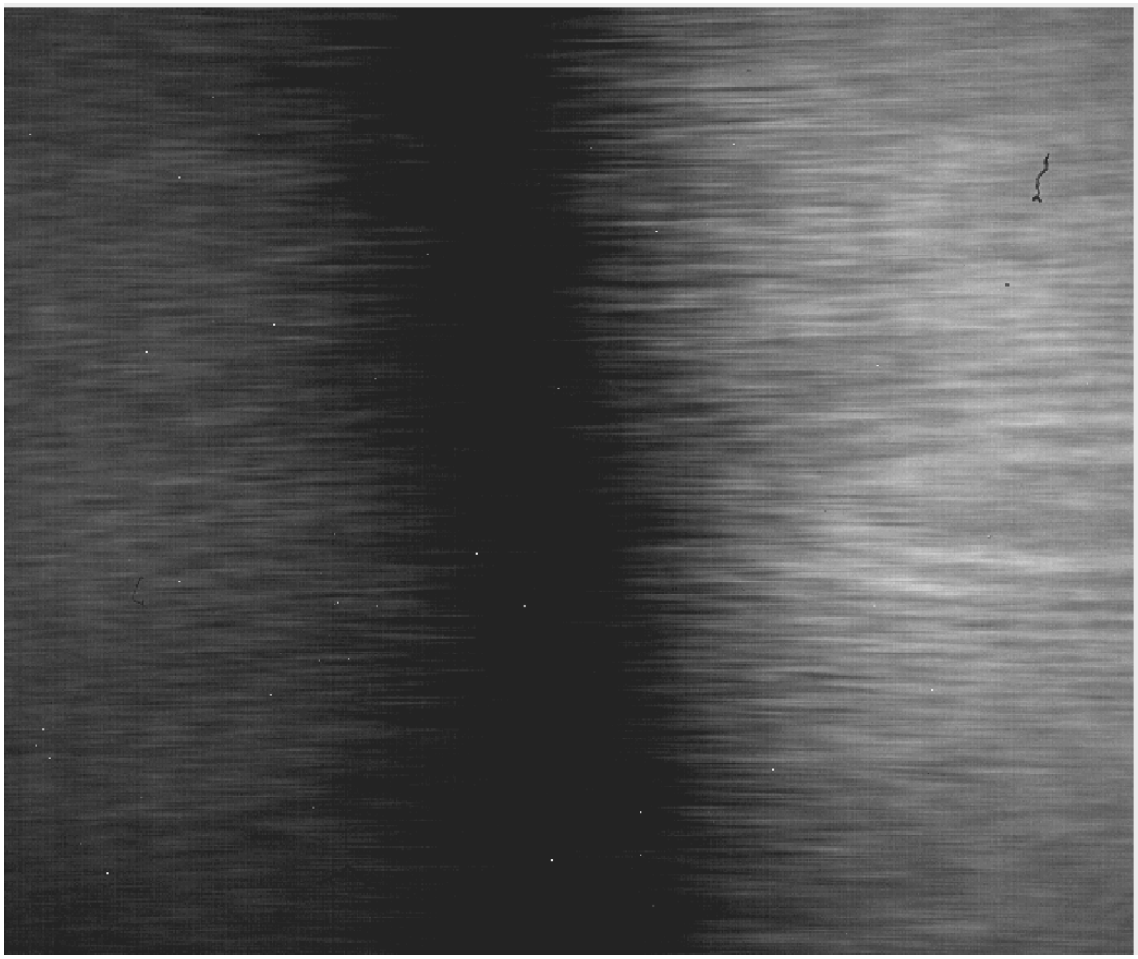

Figure 5.13: Measurement image of the coupling minimum of reflectivity for air

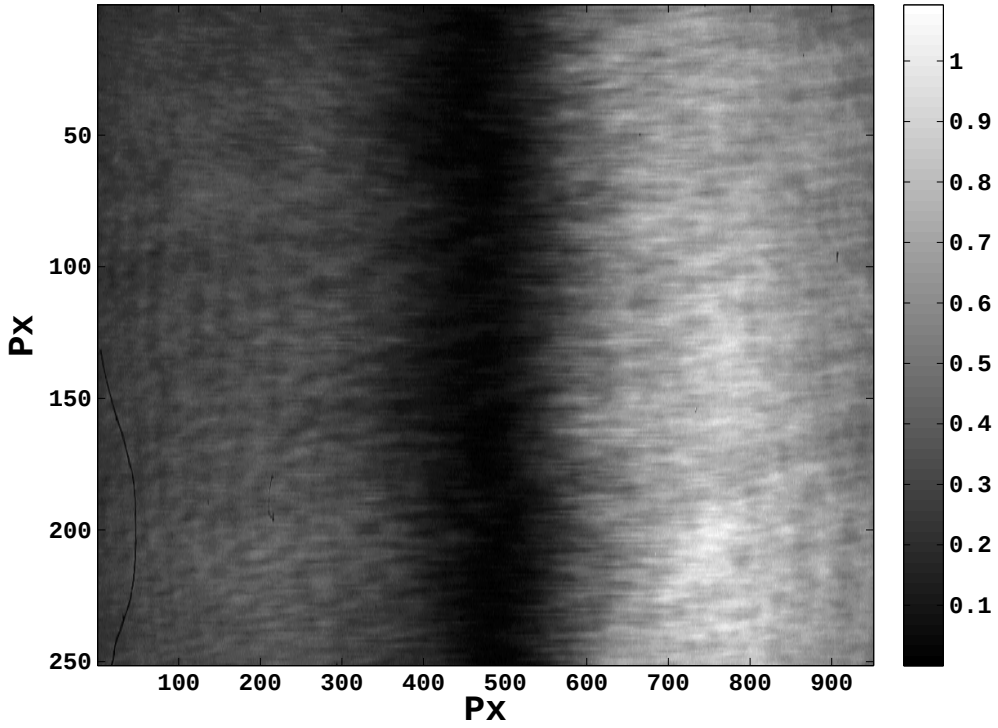

Figure 5.14: normalized SPR measurements

2. that every pixel had a physical dimension of 0.01064 x 0.01064 mm

3. that the image dimensions were 1024 x 1024 pixels.

For the y-axis the best fit formula was instead

$$YLI(j) = sinc\left(((j - 550)/580/0.01064) * 0.01064\right) \tag{5.6}$$

and the same considerations as for the x-axis distribution were made.

Light intensity so dropped near to zero around 650 pixels from the maximum value along the x-axis and 550 pixels from the maximum value along the y-axis.

This difference was due to the optical effects of the cylindrical lens and prism.

The theoretical reflectivity of the system was then on a first step evaluated by the product of the reflectivity for an uniform beam $Refl(i)$, the sinc distribution along the x-axis $XLI(i)$ and the one along the y-axis $YLI(j)$, as defined in the equations (5.5) and (5.6).

In particular 21 image columns were considered in the fitting, as espressed in (5.4), so the following equation could be used:

$$Theory(i, j) = Refl(i) \cdot XLI(i) \cdot YLI(j) \tag{5.7}$$

for $j = 1, ...21,\ i = 1, ...n_{data}$.

Later on a more correct and refined 3D sinc light intensity distribution was generated.

The SPR signal reflectivity calculated with the Matlab simulating program by means of the Transfer-matrix method (chapter 4) was then multiplied by an identity matrix, thus creating a matrix R representing the reflectivity of an uniform light intensity.

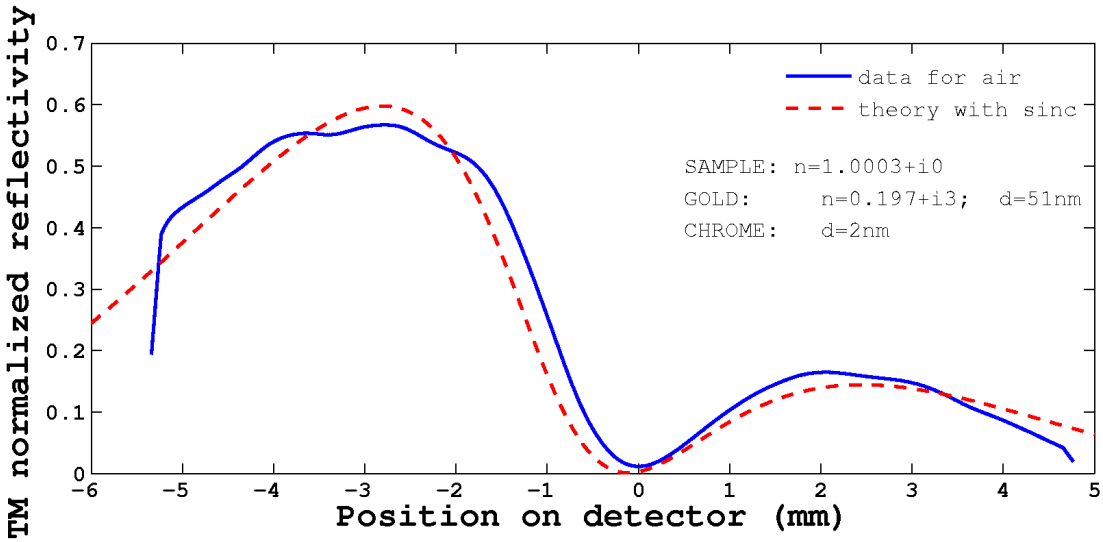

Figure 5.15: Data observations for air and theory fitting with a light distribution comprising the Pinhole diffraction

The diffraction intensity distribution by a pinhole with aperture a was then modeled as a matrix S with the same dimensions of the previous matrix and intensity d

$$v = (a \cdot \pi \cdot sin(\gamma))/\lambda \tag{5.8}$$
$$d = (sin(v)/v)^2 \tag{5.9}$$

being λ the lightsource wavelength and γ the angular distance from the center of the sinc function and thus of the light beam. The latter is defined as

$$\gamma = \left[x_a^2 + y_a^2\right]^{1/2} \tag{5.10}$$

where x_a^2 and y_a^2 are the elements along the two dimensions of an angular matrix A having the same dimensions as R and angular amplitude from -T to T, defined by

$$T = arcsin(\lambda/a). \tag{5.11}$$

Finally the real light intensity distribution was obtained by multiplying the matrix R representing the reflectivity of an uniform light intensity distribution and the sinc-contribution matrix S. The cylindrical lens contribution was then taken into account.

As can be seen in image (5.15) for test measurement with air, the simulated light intensity distribution was then more adhering to real data and therefore the SPR sensor simulations were improved.

Filtering and refinement of the SPR signal

The analyzed SPR signals also showed a high frequency noise, possibly due to the CMOS detector and to optical interferences.

I therefore applied a Gaussian filter with standard deviation σ=25 px to the images.
A Gaussian filter modifies the input signal by convolution with a Gaussian function and thus it is a low-pass filter.

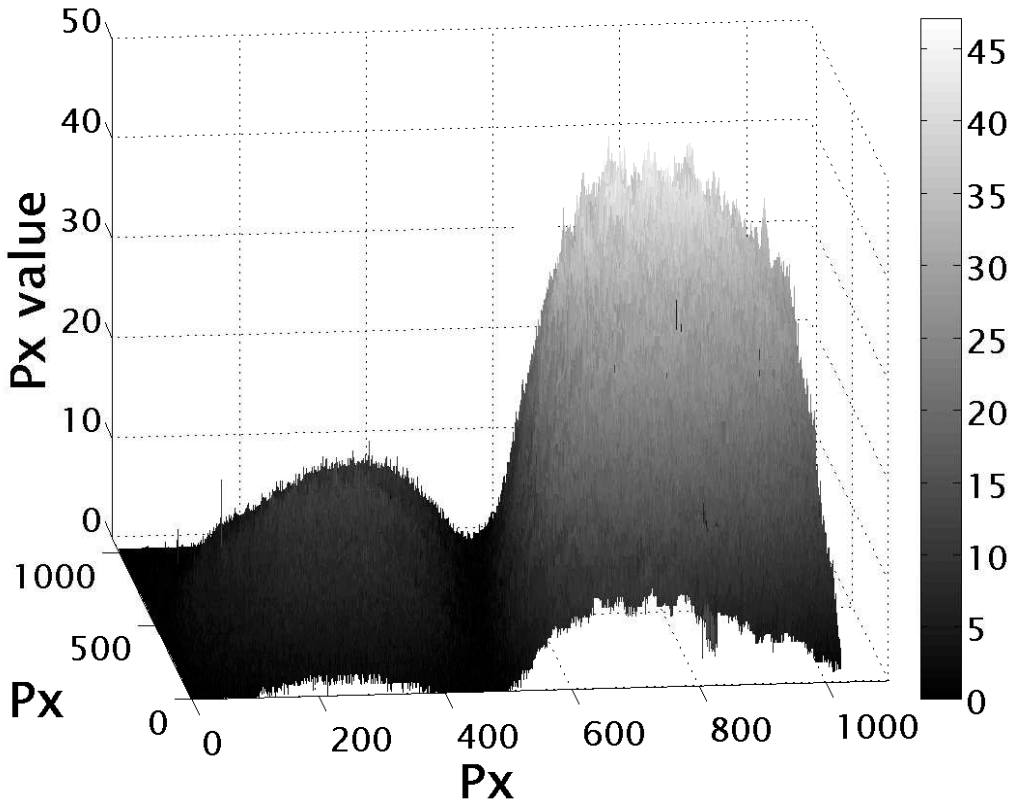

Figure 5.16: 3D image of the SPR signal

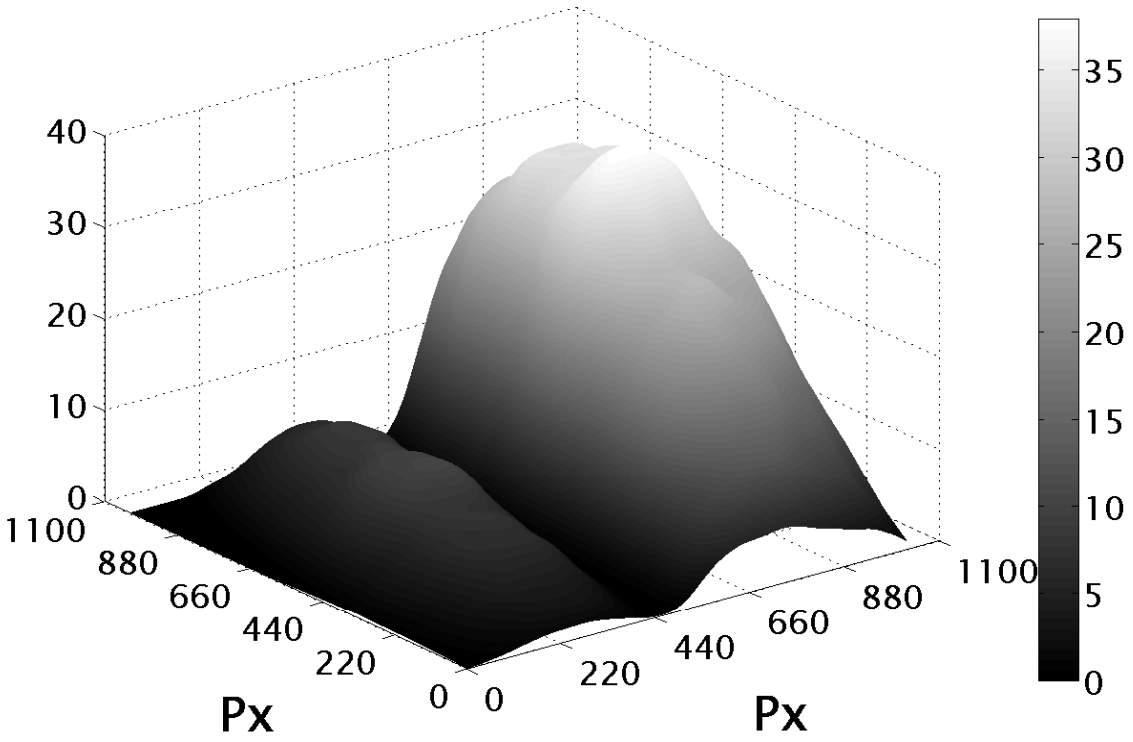

Figure 5.17: 3D image of the SPR signal after the application of the Gaussian filter

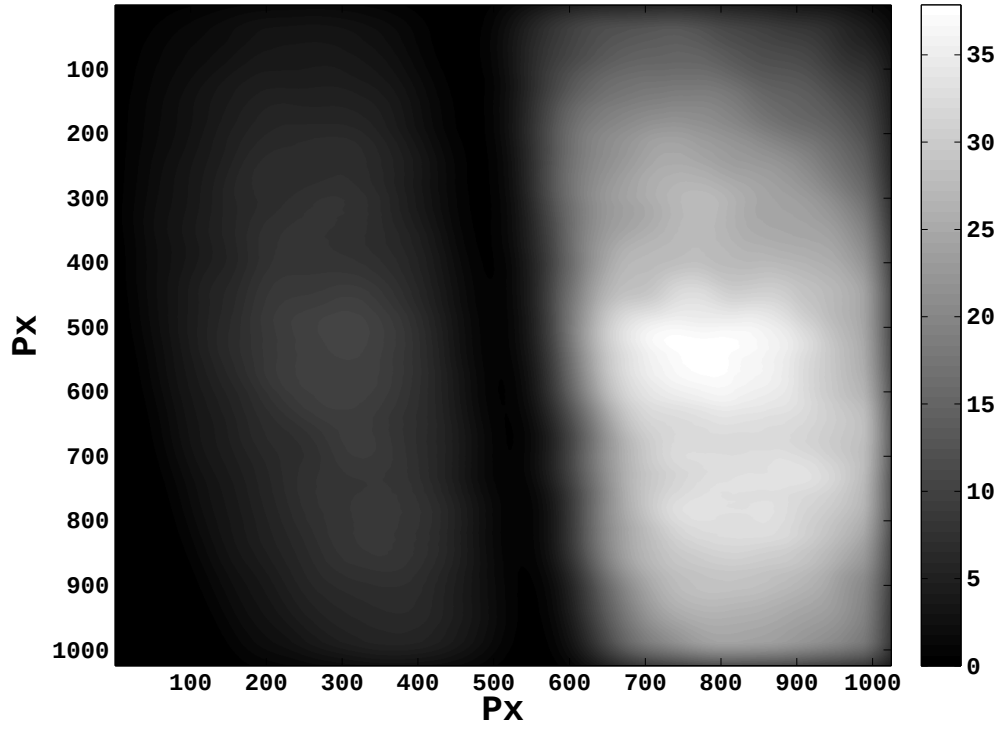

Figure 5.18: 2D image of the SPR signal after the application of the Gaussian filter

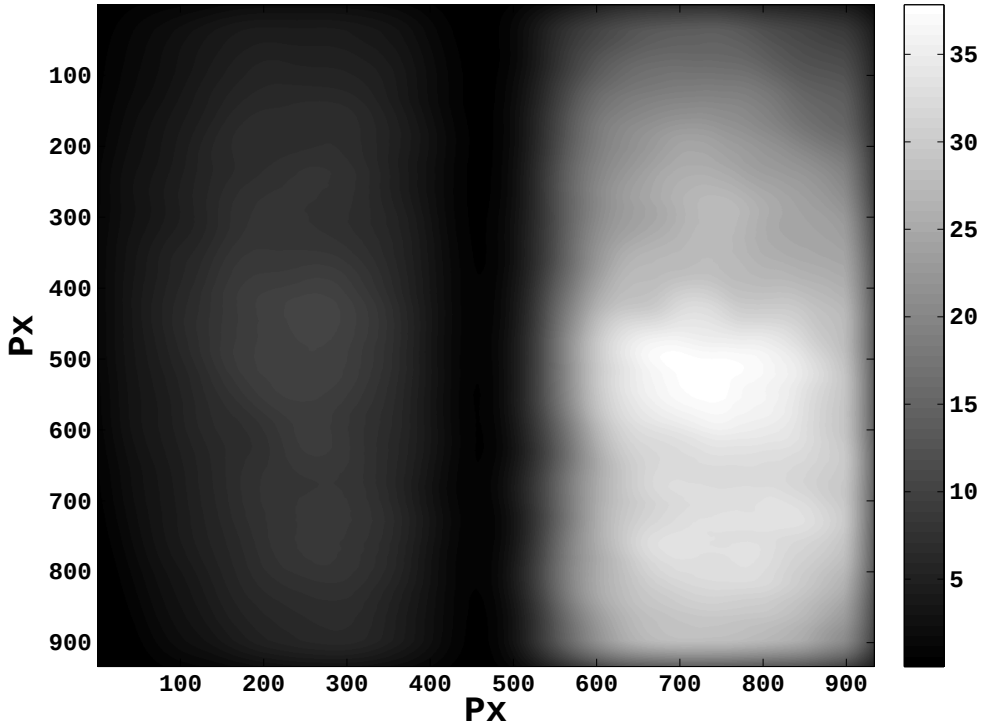

Figure 5.19: 2D image of the filtered SPR signal after the rotation correction

Images (5.16) and (5.17) are an example of the plots of the SPR signal, before and after the application of the Gaussian filter respectively.

Image (5.18) is a two-dimensional image of the filtered SPR coupling feature.

Moreover the observative images exhibited a 6 degrees rotation of the signal, so they were counter-rotated in order for the correct data sampling and analysis to be applied.
The cylindrical lens in fact only acts along one axis and it thus would have been inaccurate if a rotated axis data would have been analyzed.

Figure (5.19) shows the SPR signal after the rotation correction and it can be compared to image (5.18)

5.3 Second implementation of a SPR based sensor with static setup

Looking at the images of the SPR signal the light beam didn't seem totally Gaussian and homogeneous but some aberrations were present.

For this reason an adaptive mirror was added to the optical setup, that was accordingly modified.

The adaptive mirror can deform itself in order to counteract the low order aberrations and deformations of the light wavefront, thus enhancing the ruggedness and lifetime of the Surface Plasmon Sensor.

To my knowledge this was the first application of a deformable mirror to an SPR sensor.

5.3.1 Optical setup

For the SPR sensor comprising an adaptive mirror the following setup was used:

- ⋆ The 5 mW HRR050 Thorlabs He-Ne laser
- ⋆ a Transversal Magnetic polarizer
- ⋆ a pinhole with a 200 μm diameter
- ⋆ a BK7 lens with focal length 220 mm
- ⋆ a Thorlabs BE15M-A 15x beam expander
- ⋆ a circular slit
- ⋆ a mirror
- ⋆ a deformable mirror
- ⋆ two neutral filters
- ⋆ a BK7 cylindrical lens with focal length 155 mm
- ⋆ An SF6 cylindrical prism with a coating of 2 nm of Chrome and 51 nm of Gold
- ⋆ The Photonphocus MV-D1024 CMOS camera described in (5.2.1) .

The light produced by the He-Ne laser described in 5.1.1 was Trasversal Magnetic polarized, then it passed through a spatial filter consisting of a 200 micrometers pinhole, a collimating lens, a Thorlabs BE15M-A 15x beam expander and a circular slit. By means of these optical parts only a 11-mm-diameter circular portion of the central Airy disk was used.
A mirror reflected the electromagnetic light waves to the adaptive mirror, which was able to deform itself by means of actuators.
In particular the dimensions of the electromagnetic radiation stream were optimized for the adaptive optics.
After that the light beam intensity was reduced by means of neuter filters, in order to avoid the detector saturation, and collimated by a BK7 cylindrical lens to the surface plasmon supporting structure.
The latter consisted on a SF6 glass cylindrical prism with a coating of 2 nm of Chrome and 50 nm of Gold.
The electromagnetic radiation was then collimated at the center of curvature of the prism and into

the gold film. Finally light was back reflected, because of the total internal reflection occurring between the glass and the metal, and collected by the CMOS camera, which was controlled by means of a Matlab program.

Images 5.20 and 5.21 are the Zemax simulation and the photo of the described optical setup.

The adaptive mirrors

The first deformable mirrors used in the optical setup was the one described in (Bonora et al. (2006)) and its photo is image (5.22).
The mirror is a thin nitrocellulose membrane aluminum coated. It is deformed by electrostatic force created by applying a high voltage drop between its 37 electrodes. The membrane is 5 μm thick and the maximum mirror deformation, which is obtained pulling all the electrodes at the maximum voltage of 230 V, is a paraboloid that corresponds to a focal length of about 2 m.

From laboratory measurement this mirror was able to mend the effect of a lens put out of focus, however it wasn't able to minimize the effect of other aberrations by applying different deformations and thus the adaptive mirror from (Bonora (2011)) was then utilized.

The latter is a Membrane electrostatic Deformable Mirror (MDM) composed of a silvered nitrocellulose membrane (5 μm thick) suspended 70 μm over the actuators by polyamide spacers and based on the continuous voltage distribution over a resistive layer. The 3 actuators are placed on three concentric rings so that the first actuator has one contact, the second and the third ones have 4 contacts each. Every actuator is composed of a graphite layer 35 μm thick . Controlling the voltage distribution the membrane changes accordingly its shape, so this Deformable Mirror (DM) shown in figure (5.23) and in image (5.24) from (Bonora (2011)) can counteract spherical aberration, defocus, astigmatism and coma.

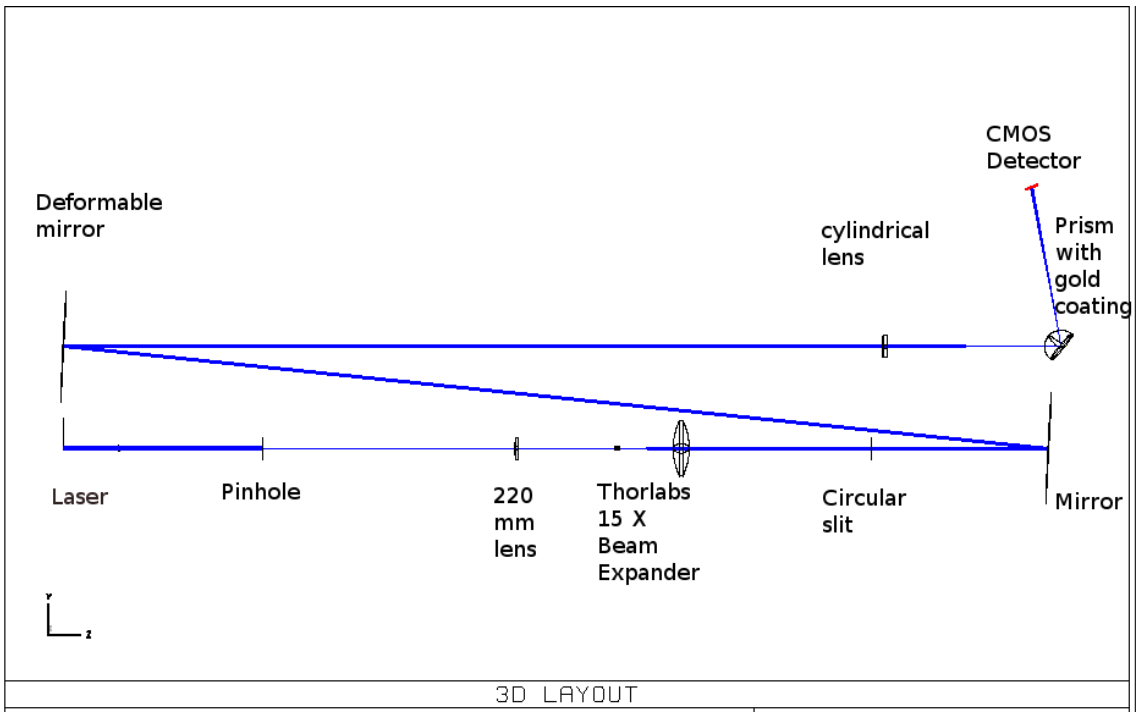

Figure 5.20: Zemax simulation of the SPR sensor comprising an adaptive mirror

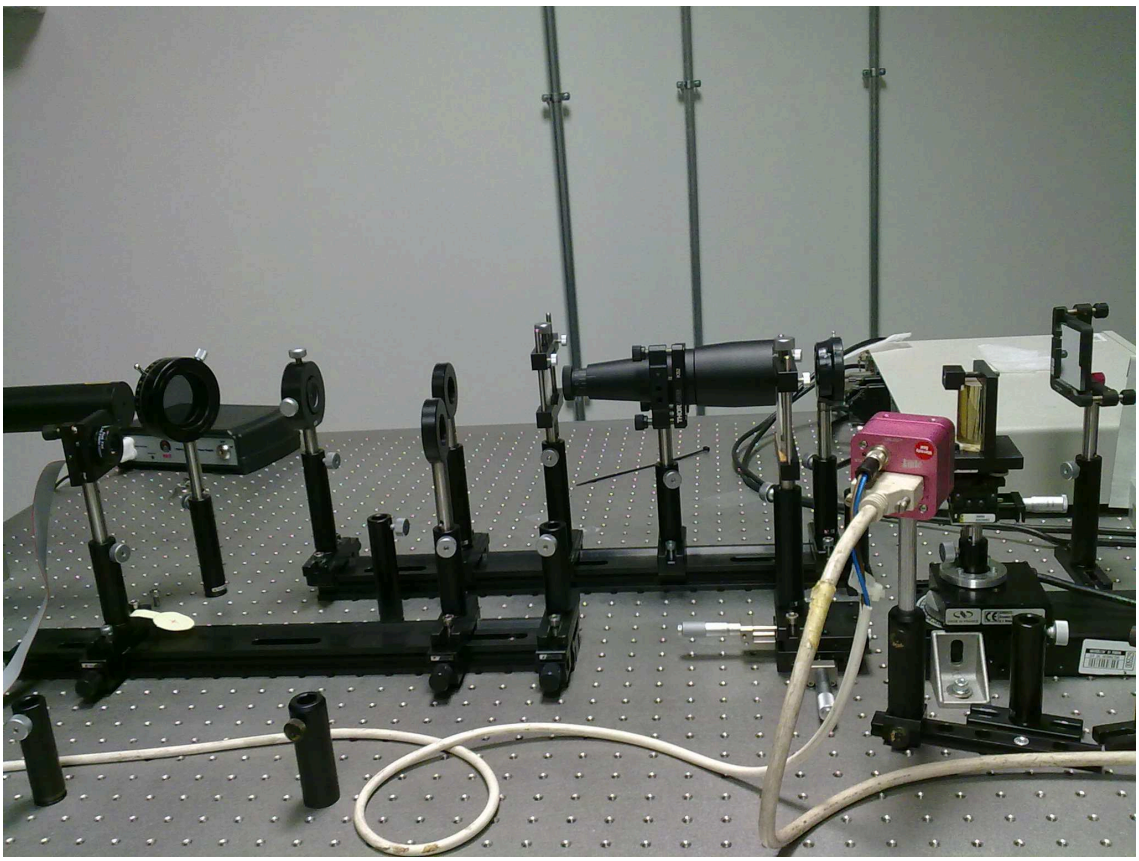

Figure 5.21: Photo of the SPR sensor comprising an adaptive mirror

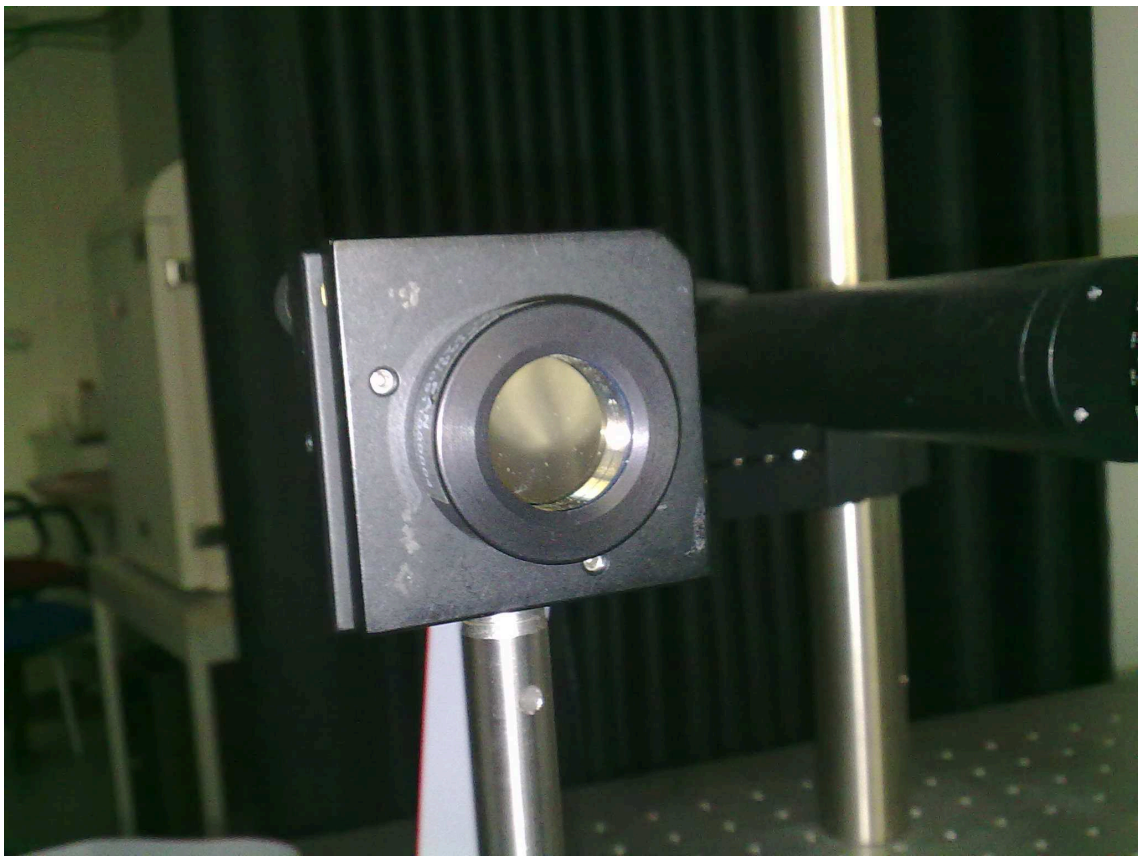

Figure 5.22: Photo of the first adaptive mirror utilized

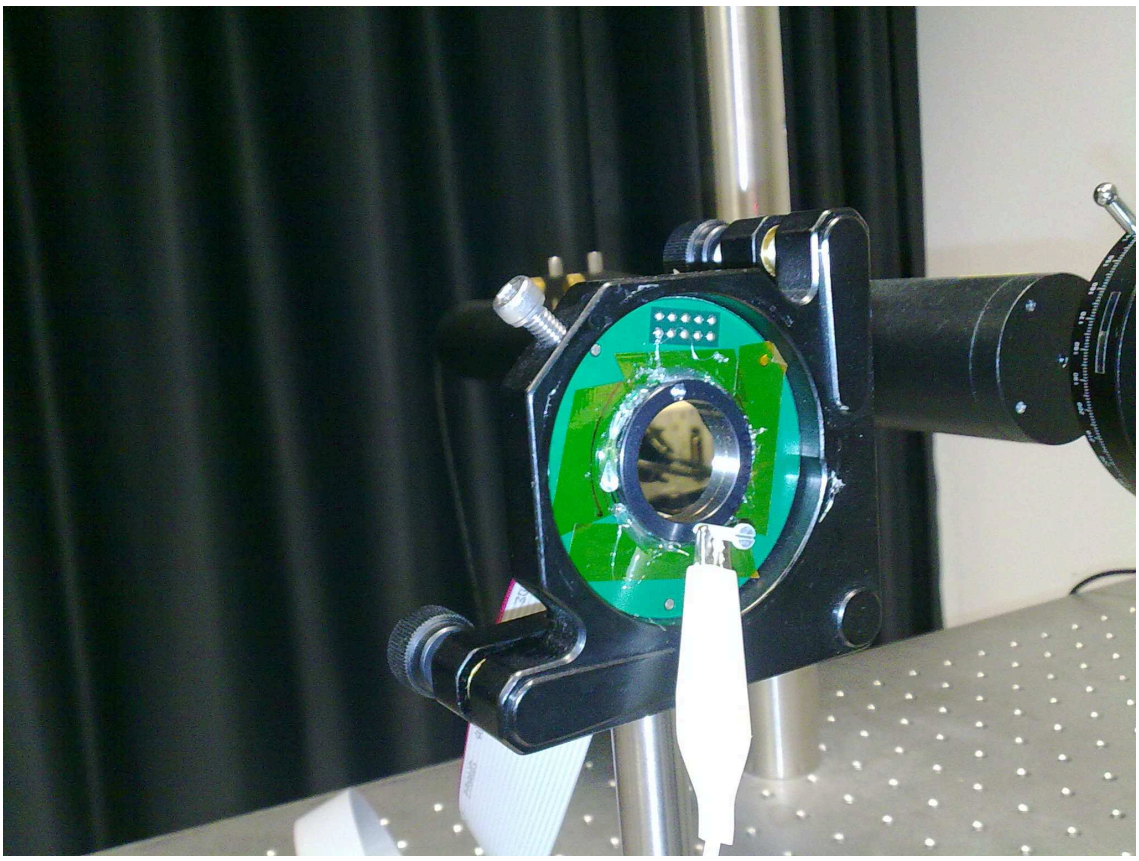

Figure 5.23: Photo of the second adaptive mirror utilized

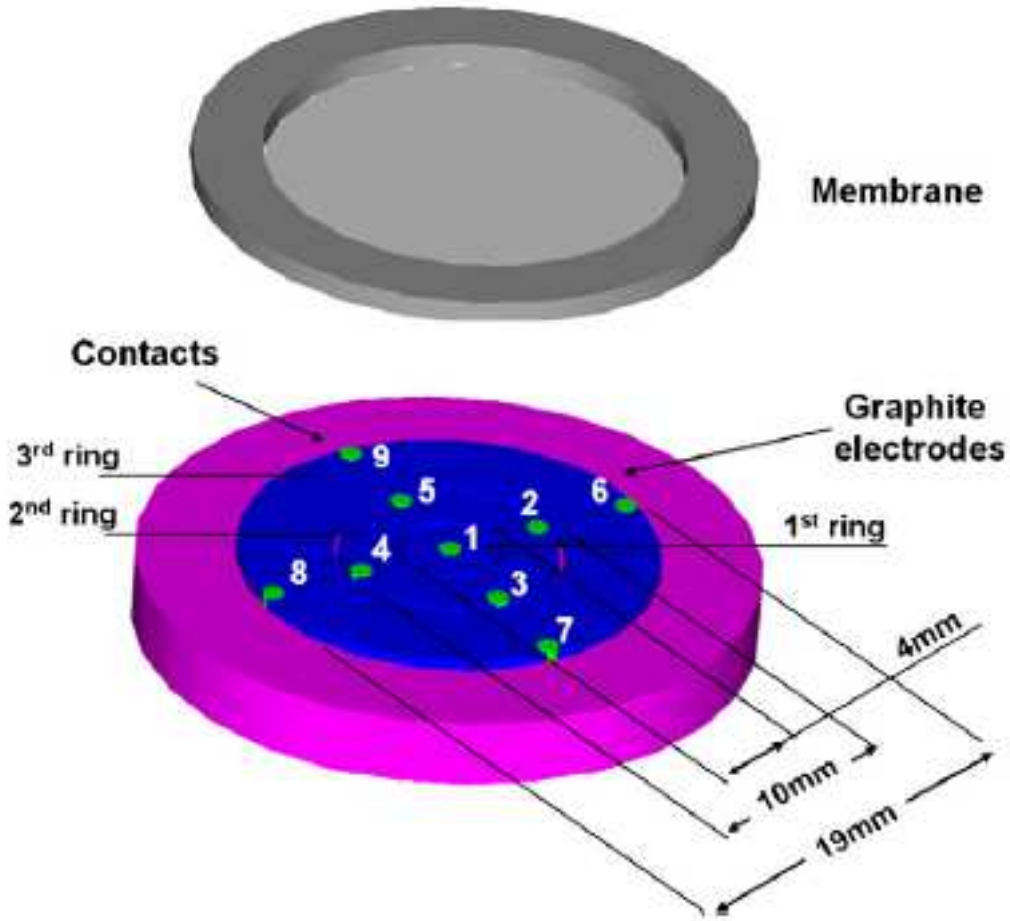

Figure 5.24: Structure of the second adaptive mirror utilized

Table 5.1: refractive indexes of the materials comprising the static SPR sensor with adaptive optics

Material	n (632.8 nm)	k (632.8 nm)	reference
Air	1.0003	0.0000i	Ciddor (1996)
SF6	1.799	0.000	SCHOTT (2011)
Cr	3.135	3.310i	SOPRALAB (2012)
Au	0.197	3.090i	Palik (1991)

5.3.2 SPR signal simulation

In order to simulate the SPR signal from the SPR sensor comprising the adaptive mirror an implementation of the simulating Matlab program described in (4.1) was used.

In particular the structure supporting the Surface Plasmon was described as a slab with materials having the refractive indexes reported in table (5.1).

On a first step the refractive indexes of the SF6 glass, Chrome and air were regarded as fixed, while the imaginary part of the refractive index of the Gold film and its thickness were fitted instead to the observative data. This was justified by the deposition process, that is the Chemical Vapor Deposition, which leads to a small uncertainty on this two parameters. Moreover the refractive index of a small metal layer can vary with different deposition methods, for example Shulz (1954) reports for Gold n = 0.20, k = 3.32 at the same wavelength.
The theoretical imaginary part of the refractive index of Gold was thus allowed to vary from 3.04 to 3.09 and the gold film thickness was evaluated to be from 50 to 55 nm.

The simulated light intensity distribution took into account the effect of the cylindrical lens and prism in addition to the diffraction by the pinhole as in 5.2.2.

5.3.3 Theoretical sensitivity of the SPR sensor

In the consequently generated simulations the minimum refractive index variation considered was $5 \cdot 10^{-5}$ Refractive Index Units and variations of $1 - 2 \cdot 10^{-4}$ Refractive Index Units have been made use of.

A Refractive Index Change of $1 \cdot 10^{-4}$ was corresponding to a displacement of 2-3 pixels and so it was appreciable by the sensor, but in the fits for the merit function of the adaptive optics a resolution equal to 5 pixels, that is $2 \cdot 10^{-4}$ Refractive Index Units, has been used for computational easiness.

The theoretical shifts of the minimum of reflectivity caused by a small variation of the refractive index of the medium to be sensed are reported in table (5.2) and in image (5.25) and have an error of ± 0.006 degrees.

Moreover making use of equation (2.8)of (2.4)

$$S = \frac{\varepsilon_{mr}\sqrt{-\varepsilon_{mr}}}{\left(\varepsilon_{mr} + n_a^2\right)\sqrt{\varepsilon_{mr}\left(n_a^2 - n_p^2\right) - n_a^2 n_p^2}}$$

the calculated sensitivity was 81 Deg/RIU for air and 132 Deg/RIU for water.

5.3.4 SPR signal processing

As a first step a full intensity beam reference image was taken at 5 degrees from the coupling angle, that is at 31 degrees of incidence to the normal to the prism, before the data image. The pixel values

Table 5.2: theoretical angular shifts of the minimum of reflectivity caused by the change of the refractive index of the analyte

dn (10^{-4} R.I.U) of the media	shift of the minimum (degrees)
0	0.000
2	0.015
4	0.029
6	0.037
8	0.045
10	0.057
12	0.065
14	0.077
16	0.090
18	0.098
20	0.110

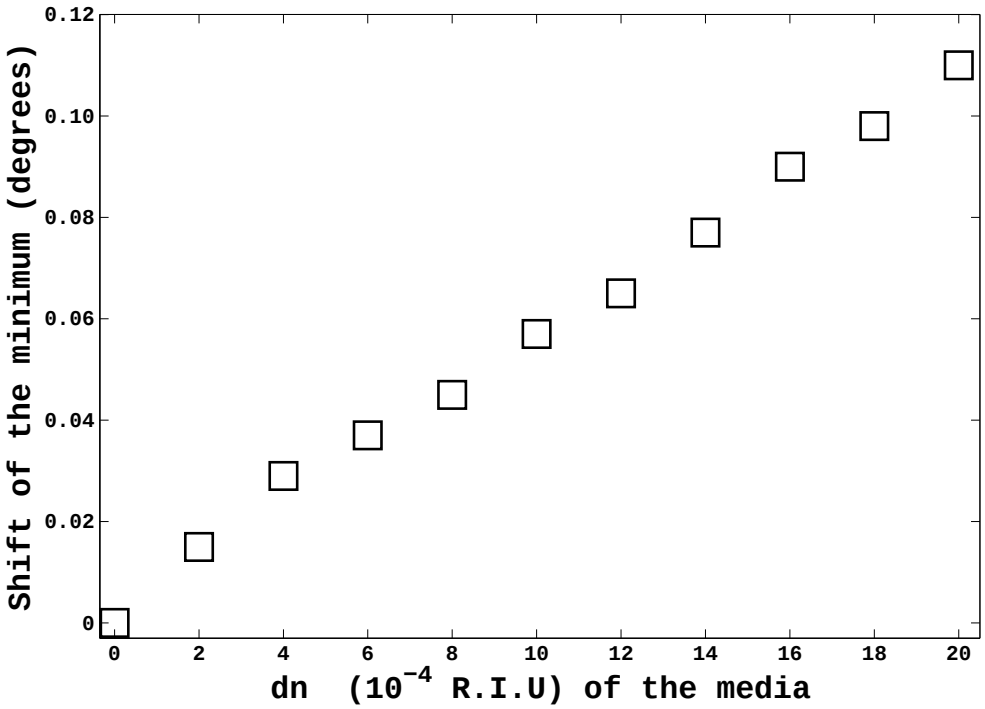

Figure 5.25: sensitivity of the implemented SPR sensor with adaptive mirror

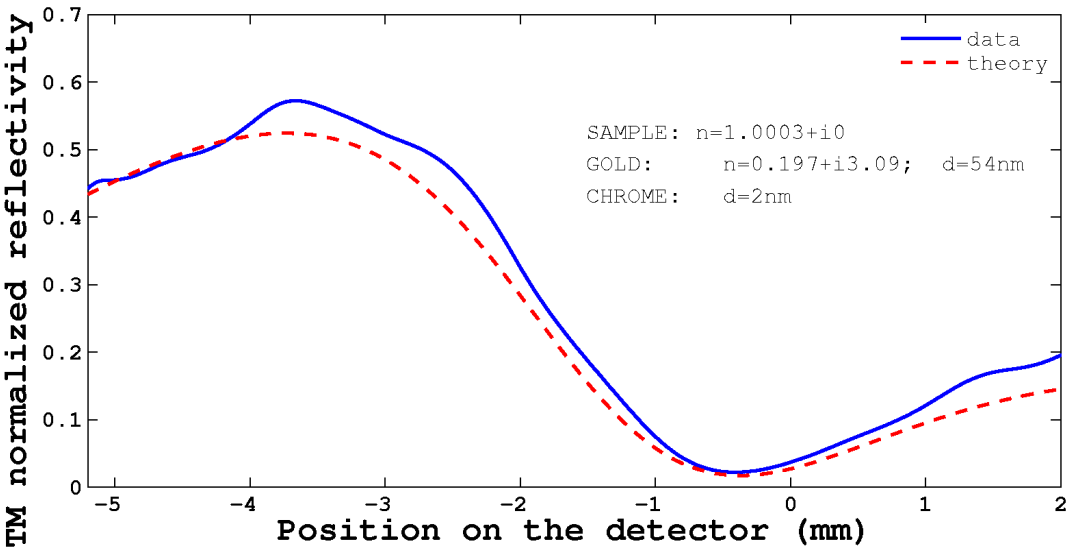

Figure 5.26: Theoretical and observed reflectivity of the SPR signal plotted against the position on the detector

of a dark image, taken with the laser turned off, was then subtracted to the reflectivity data image taken at the coupling angle and to the reference image, in order to delete the contribution of the ambient light and burned pixels.
These images were also filtered by means of a Gaussian filter to delete the effect of high frequency noises and a rotation correction was applied as in (5.2.2)

After that, in order to normalize the reflectivity obtained from the data image, its pixel values were divided by the maximum pixel value of the center of the beam of the reference image as in (5.2.2).

Twenty-one data series were acquired for every resulting image and fitted against the theoretical reflectivity, which was evaluated by means of the Matlab program described in (5.3.2).

The deviations from the expected reflectivities were thus calculated by means of the formula 5.4

$$X\left(i\right)=\sqrt{\frac{\sum_{j}\left[data(i,j)-theory(i,j)\right]^{2}}{n_{data}}}.$$

The value of the minimum X(i) for every measurement was therefore the best value of the merit function.

An example of the obtained fitting and SPR curves is reported in image (5.26)

5.3.5 Experiments on the deformable mirror

Defocus

As a first experiment the cylindrical lens was positioned on purpose out of focus in order to simulate an error or a displacement in its location. The curvature of the adaptive mirror was then accordingly changed. The observative data for the MDM reported in table (5.3) and in image (5.27) show that it has been possible to restore the faultlessness of the sensor and thus to minimize the errors between theoretical and real reflectivities.

Image (5.28) shows the same graph for the first adaptive mirror for reference.

Table 5.3: Defocus effect correction observative data

focal length (m)	MDM Mirror defocus parameter	Error values for best fit
infinite	0.0	0.1421
11.281	0.2	0.0530
5.641	0.4	0.0530
4.513	0.5	0.0522
3.760	0.6	0.0491
2.820	0.8	0.0519
2.256	1.0	0.0598

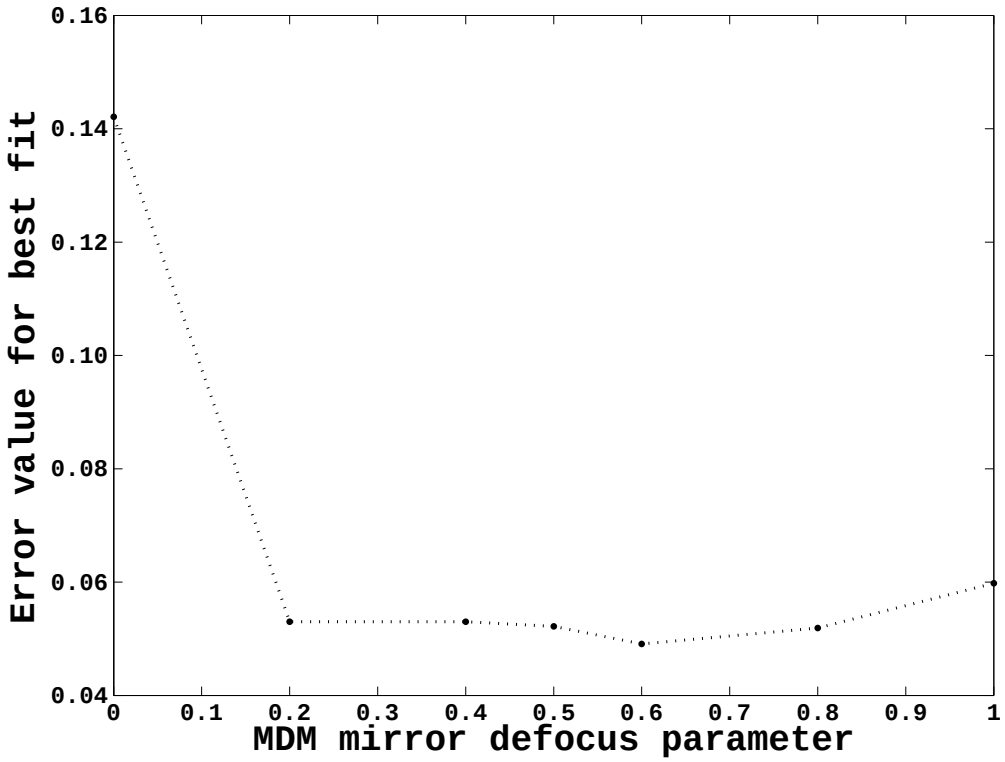

Figure 5.27: Defocus effect for the MDM

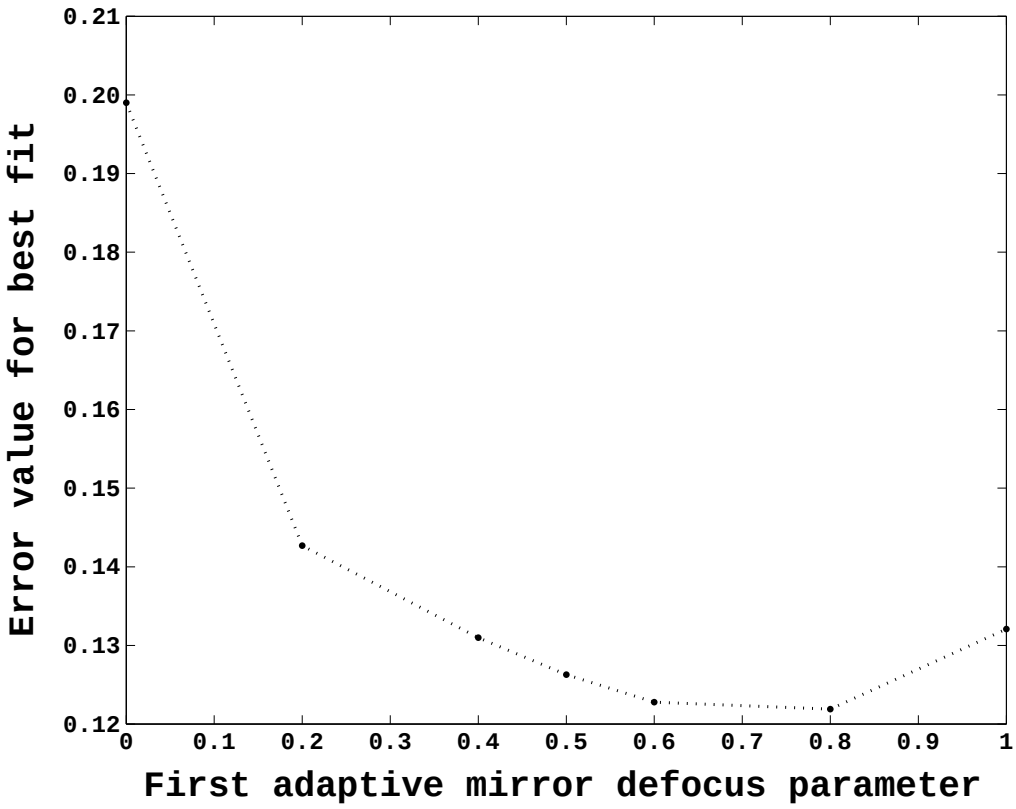

Figure 5.28: Defocus effect for the first deformable mirror

Image (5.29) displays the coupling reflectivity observed for the optical system with the defocused lens plotted against the theoretical reflectivity, for MDM Mirror defocus parameter equal to zero, while image (5.30) the observative reflectivity after the correction by means of the adaptive optics, again plotted against the theoretical reflectivity. The corresponding adaptive mirror defocus parameter is equal to 0.6.

Verified the improvement in the agreement of the observed SPR signals with the expected behavior, the sensor sensitivity was then evaluated.
In fact small analyte refractive index changes were simulated, and in addition to that it was evaluated how much the refractive index had to change for the effect to be visible against the data.

Images (5.31) and (5.32) show a zoom around the minimum of reflectivity of the displacement of the reflectivity minimum, for a perfectly focused optical system and for the altered optical system after the defocus correction by the Adaptive Mirror respectively. The curves were traced for variations of the the sensing medium refractive index of $5 \cdot 10^{-4}$ and $8 \cdot 10^{-4}$ R.I.U.

From the two images it should be noted that the SPR coupling feature was almost completely restored thanks to the adaptive optics contribution, moreover data show similar sensitivities. In fact in both plots changes of $5 - 8 \cdot 10^{-4}$ must be applied for the theory not to fit correctly the data anymore.

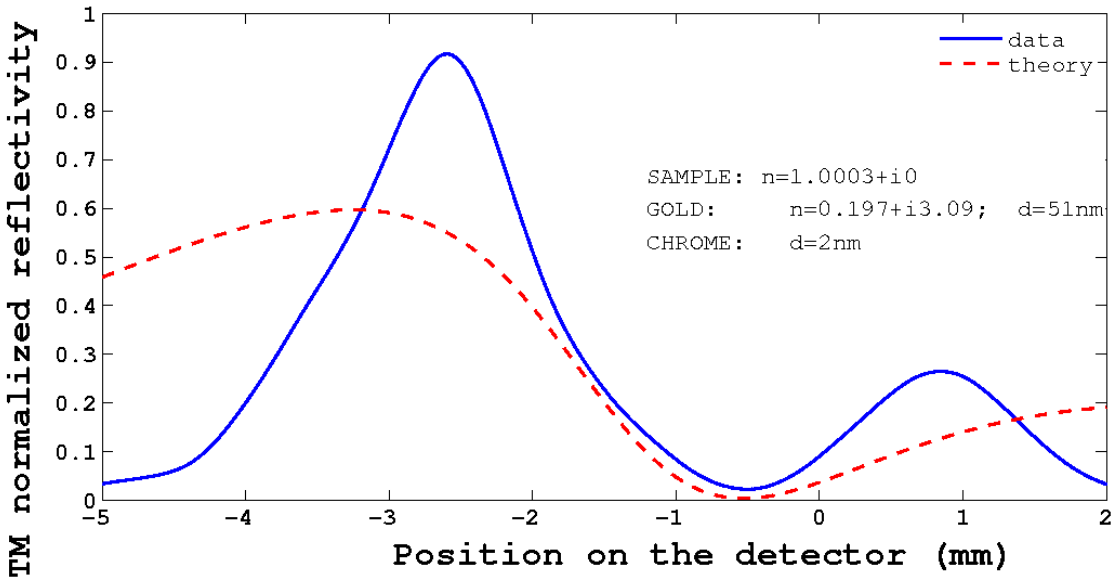

Figure 5.29: normalized reflectivity data for the optical system with the defocused lens plotted against the theoretical reflectivity. Data obtained for MDM Mirror defocus parameter equal to 0

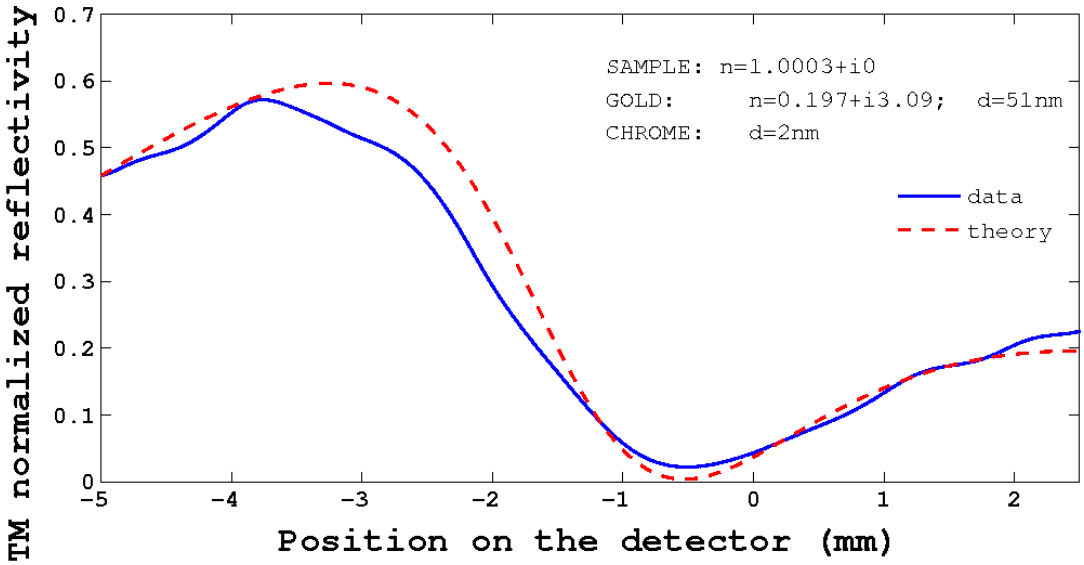

Figure 5.30: observed normalized reflectivity after the correction by means of the adaptive optics plotted against the theoretical reflectivity. Data obtained for MDM Mirror defocus parameter equal to 0.6

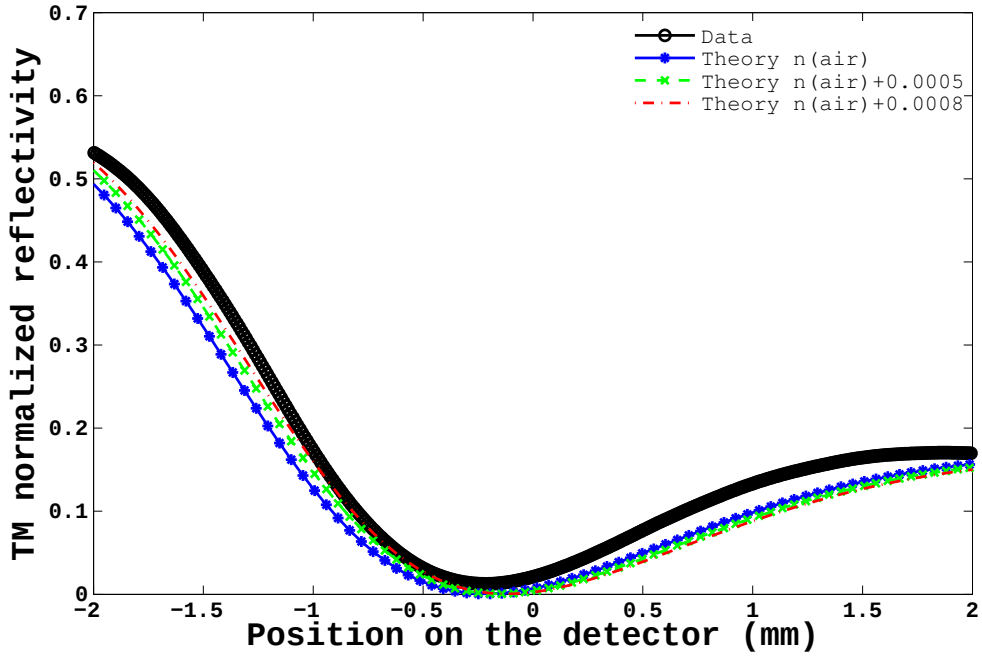

Figure 5.31: Sensitivity of the focused optical system without adaptive optics

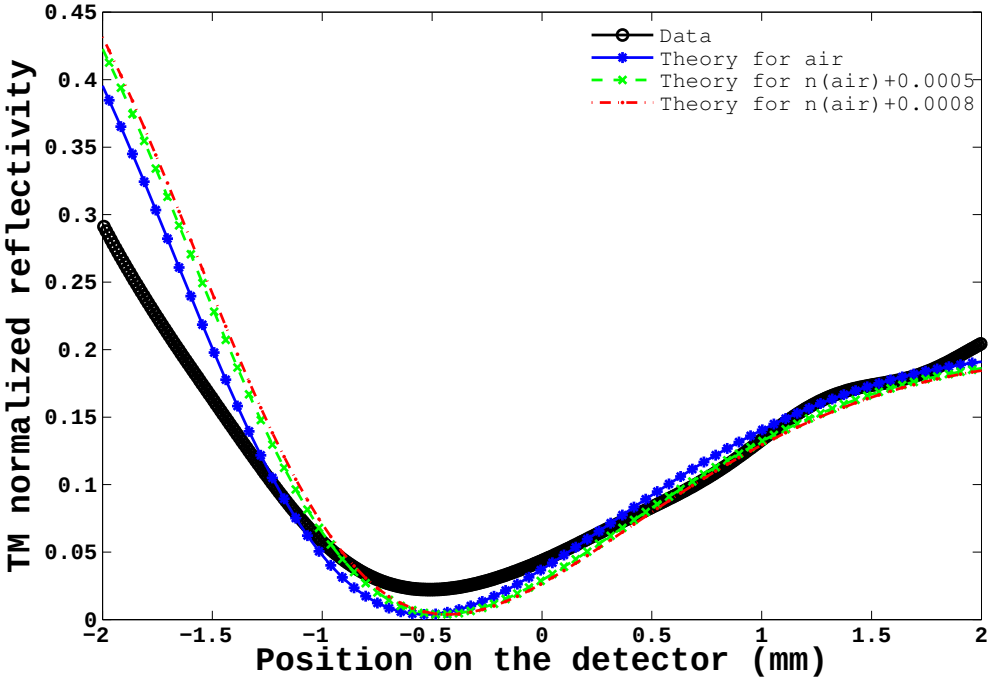

Figure 5.32: Sensitivity of the optical system with adaptive optics after defocus correction.

Table 5.4: Spherical aberration correction observative data

Spherical aberration coefficient	error value for best fit
0.0	0.1033
-0.1	0.0929
-0.3	0.0816
-0.5	0.0743
-0.7	0.0756
-0.8	0.0763
-0.9	0.0803
-1.0	0.0842

Spherical aberration

As the optical system was supposed to be affected by spherical aberrations it was tested the possibility to lessen its contribute by means of the adaptive mirror. The feasibility of this optimization was supported by the data shown in the table (5.4) and in the graph in image (5.33).

They have been obtained varying the shape of the deformable mirror only for the desired aberration.

From the data it was possible to at least partially correct the spherical aberration of the optical system by means of the adaptive mirror.

Images 5.34, 5.35 and 5.36 show the experimental data plotted against the theoretical values for an optical system without aberrations. The graphs refer to observations for Spherical aberration coefficients of the Adaptive Mirror equal to 0, 0.5 and 1.

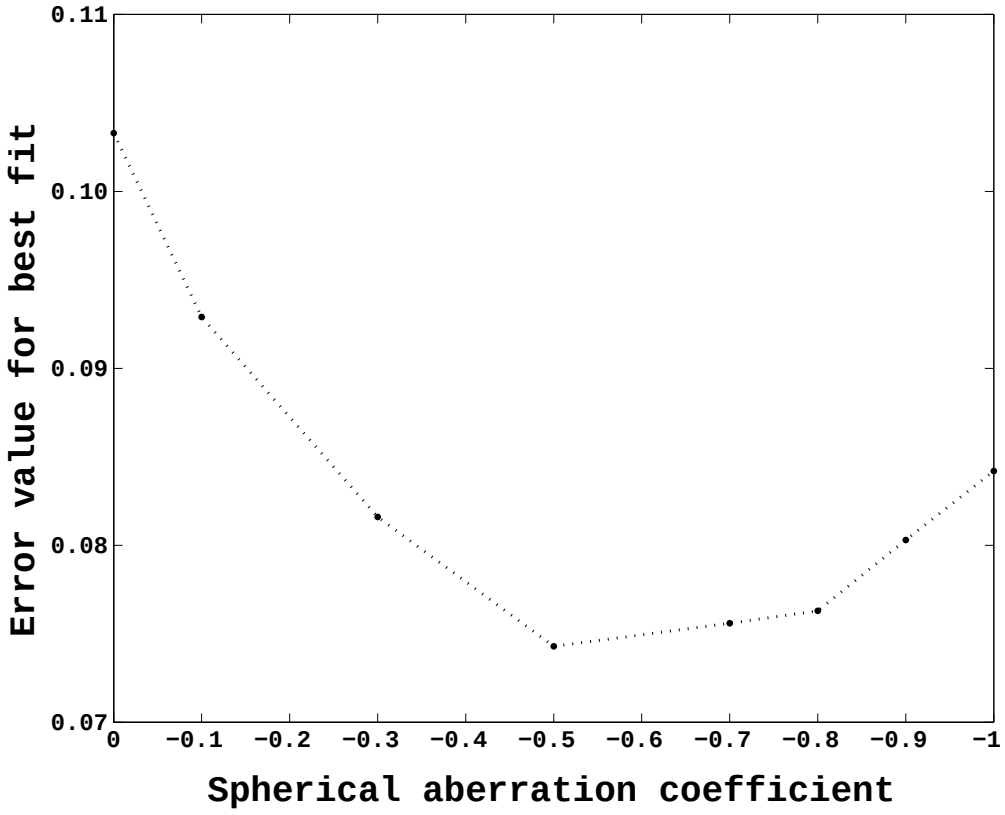

Figure 5.33: Spherical aberration correction for the MDM

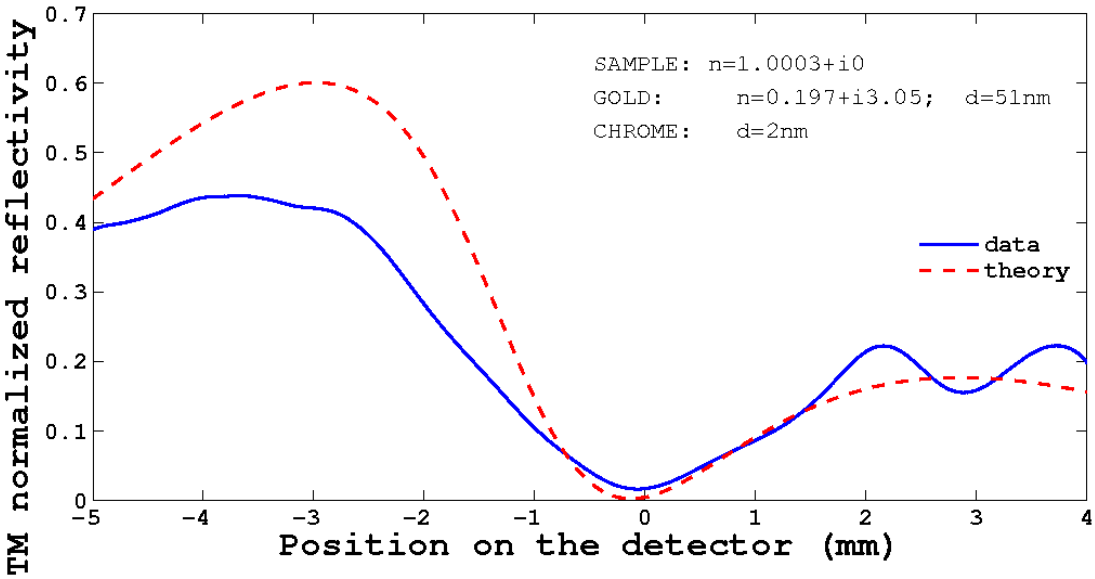

Figure 5.34: Observations for a Spherical aberration coefficient of the Deformable Mirror equal to 0

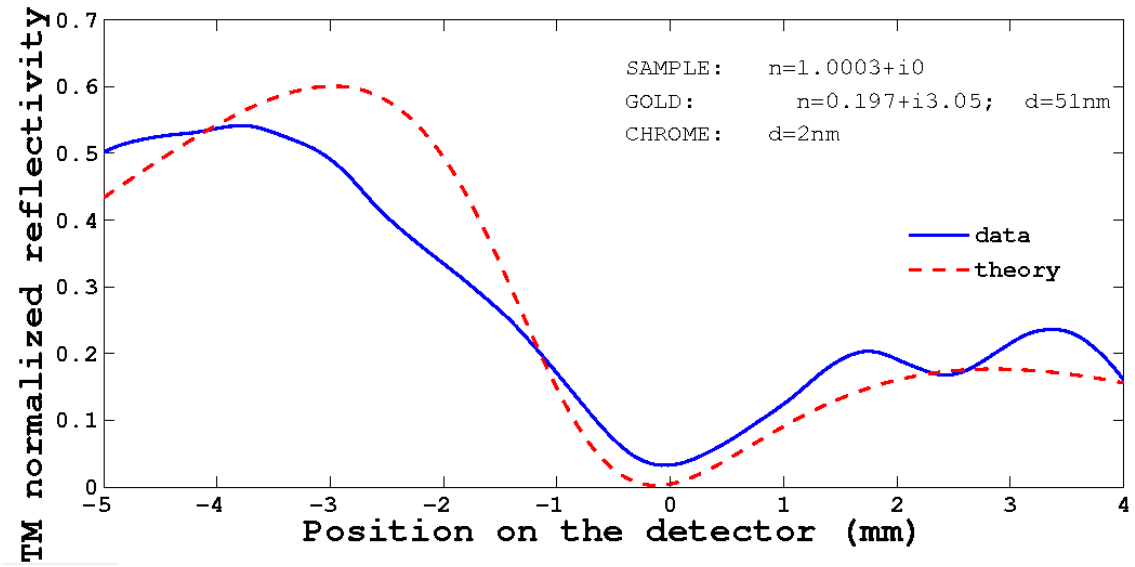

Figure 5.35: Observations for a Spherical aberration coefficient of the Deformable Mirror equal to 0.5

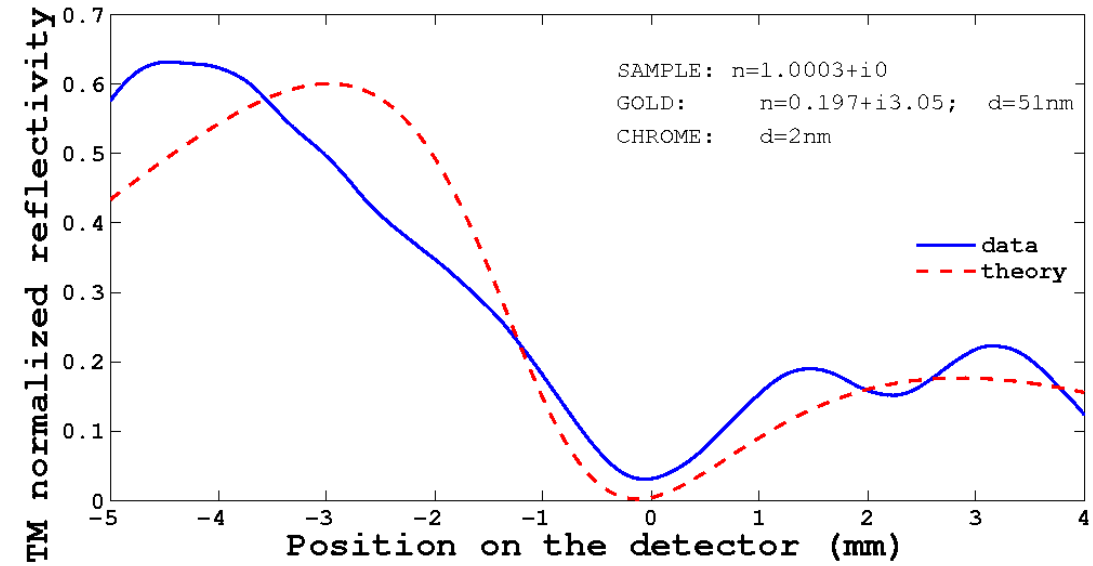

Figure 5.36: Observations for a Spherical aberration coefficient of the Deformable Mirror equal to 1

Table 5.5: Astigmatism correction observative data obtained varying its magnitude at a fixed angle

Astigmatism magnitude	Error values for best fit
0.0	0.0446
0.1	0.0446
0.2	0.0451
0.3	0.0432
0.4	0.0428
0.5	0.0470
0.6	0.0459
0.7	0.0459
0.8	0.0467
0.9	0.0472
1.0	0.0464

Astigmatism

After the measurements mentioned above the presence of astigmatism was evaluated in order to correct it by means of the adaptive optics.

The data reported in table (5.5) and image (5.37) are related to a varying astigmatism magnitude at the same angle of aberration (0 degrees)

The data reported in table (5.6) and image (5.38) are related instead to a varying astigmatism angle keeping a constant aberration magnitude (0.5)

From the observations the astigmatism didn't seem to bring a significant contribution to the optical aberrations of the sensor. This was possibly due to the limited field of view of the sensor.

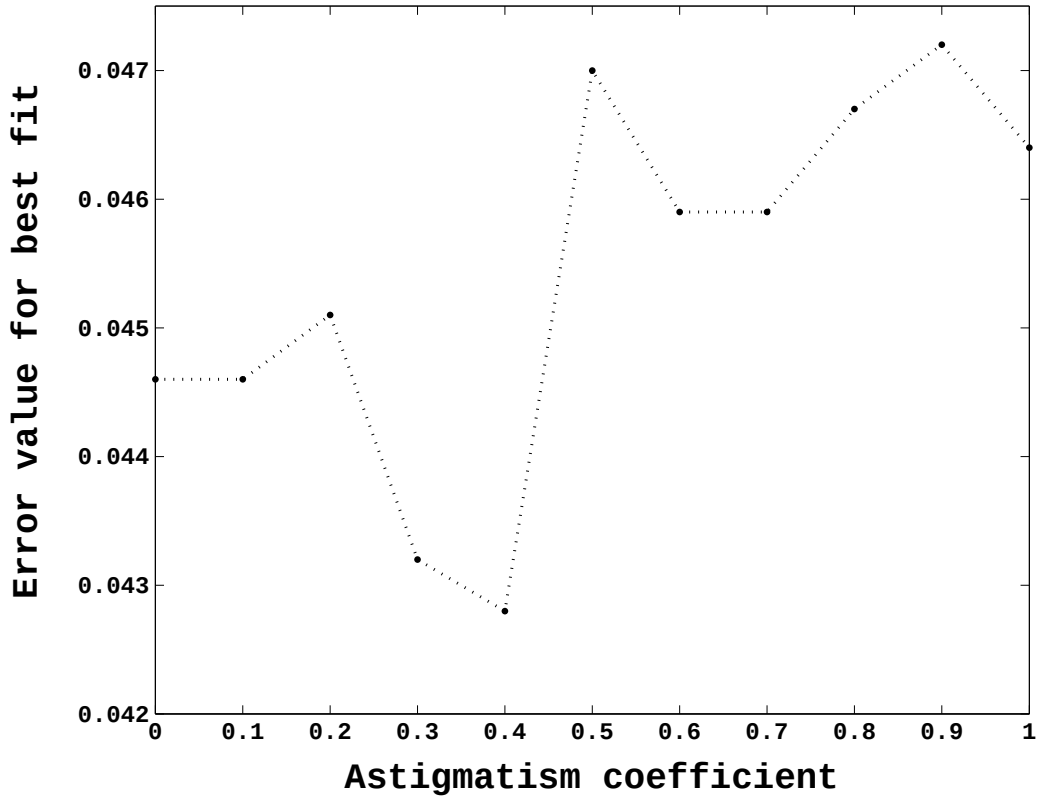

Figure 5.37: Astigmatism observative data with the adaptive mirror: varying magnitude at fixed angle

Table 5.6: Astigmatism observative data with adaptive mirror: varying angle at fixed magnitude

Astigmatism angle	Error values for best fit
0	0.0604
30	0.0615
60	0.0600
90	0.0624
120	0.0603
150	0.0575
180	0.0588
210	0.0577
240	0.0612
270	0.0610
300	0.0603
330	0.0618

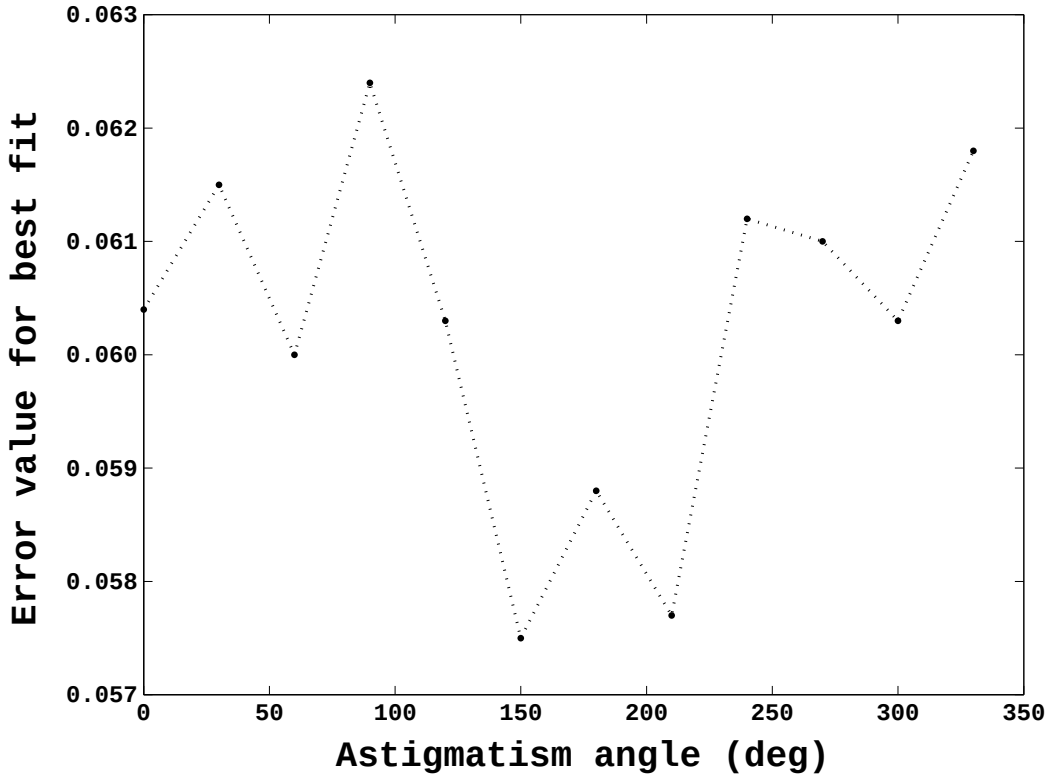

Figure 5.38: Astigmatism observative data with adaptive mirror: varying angle at fixed magnitude (0.5)

Table 5.7: Coma correction observative data

Coma coefficient	Error values for best fit
0.0	0.0639
0.1	0.0674
0.2	0.0682
0.3	0.0673
0.4	0.0676
0.5	0.0704
0.6	0.0697
0.7	0.0688
0.8	0.0674
0.9	0.0669
1.0	0.0674

Coma aberration

The presence of Coma aberration in the SPR sensor optical setup was also estimated.

The adaptive mirror shape was changed in order to add different coma aberration contributions to the optical sistem and the results are exposed in table (5.7) and image (5.39).

From the data it would seem that coma aberration didn't affect much the SPR sensor, even thought it might have been slightly overcorrected from the experiment.
In fact this is coherent with this aberration being proportional to the rays distances from the focal axis, while the setup was conceived to perform on axis.

First conclusions about the SPR sensor with embedded adaptive optics

A Surface Plasmon Sensor was implemented, whose innovative characteristics was the insertion of the adaptive optics.

From these first results the adaptive mirror prototype was able to counteract the effect of a lens defocus and of spherical aberration, allowing the observative results to adhere more to the theoretical reflectivity.
Astigmatism and Coma instead didn't seem to affect the optical system significantly.

Adaptive mirrors were thus able to mend or minimize the defects of the light wavefront, therefore enhancing the ruggedness and lifetime of the implemented Surface Plasmon Sensors while preserving the system sensitivity at the same time.

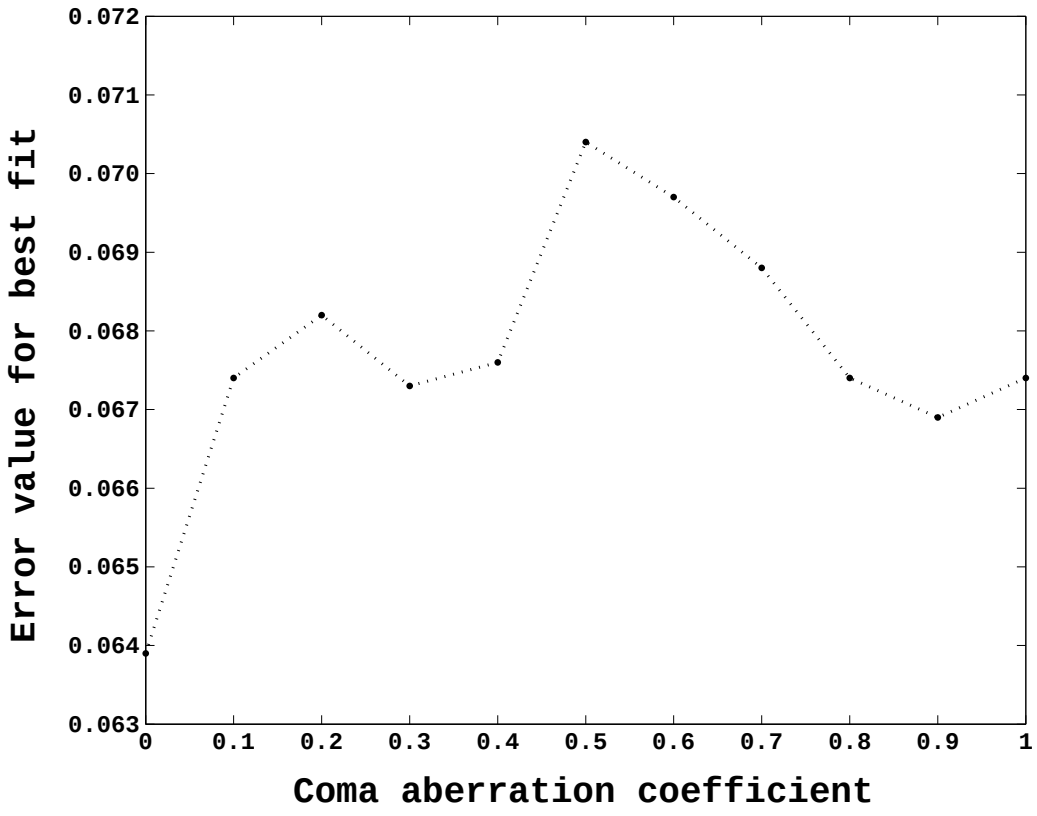

Figure 5.39: Coma aberration observative data with the adaptive mirror

Chapter 6

A wireless Surface Plasmon Resonance sensor Network for environmental pollutants

My project for a teledetection system for environmental pollutants detection consists on a Wireless Sensor Network (WSN) based on Surface Plasmon Resonance sensors and on a broadband bi-directional Internet connection via Satellite. The aim of such a sensor network is in particular river, lake and sea water monitoring.

My research activity has comprised the feasibility studies for this kind of network and the implementation of a small Surface Plasmon Resonance based WSN in laboratory.

I therefore determinated an architecture for this WSN, finding possible analytes to detect, evaluating the sensor network main elements, the data to be collected from the sensors and the information handling procedure.

Moreover I did an analysis on the power requirement of the different elements, in order to use an appropriate energy source.

In addition to that I have implemented in laboratory two different setups of a small test Wireless Sensor Network based on SPR sensors (SPR based WSN), which consisted on two sensor nodes, composed of two controllers actuating a SPR sensor, ZigBee antennas and a GPS receiver, a Desktop computer for collecting and analyzing the data and a broadband internet connection.

6.1 Feasibility studies on a Wireless Sensor Network based on SPR sensors

6.1.1 Components of the proposed Wireless Sensor Network based on SPR sensors

As I first step I documented myself on existing Wireless Sensor Networks in order to study their structure.

I implemented a possible architecture for my Wireless Sensor Network based on SPR sensors taking inspiration from Hart and Martinez (2006), Hart et al. (2006), Delin et al. (2003), Delin (2004), Garcia-Sanchez et al. (2010), Werner-allen et al. (2005), Werner-Allen et al. (2006), Werner-allen et al. (2006) Szewczyk et al. (2004), Mainwaring et al. (2002), Hartung et al. (2006), Cardell-oliver et al. (2004), Tolle et al. (2005), Chuo and Kaminska (2009), Padhy et al. (2010) and Farrington et al. (2003).

The proposed wireless Surface Plasmon Resonance sensor Network for environmental pollutants is therefore composed of

- ⋆ Many sensor nodes, or "motes", composed of
    1. A Surface Plasmon Resonance based sensor conceived for the detection of water pollutants
    2. A Controller board to power and command the SPR sensors and the other devices and possibly analyze the measurements data
    3. A GPS receiver to obtain time and position references for the data
    4. A Small wireless antenna
    5. sources of energy as batteries and small solar cells
- ⋆ One or more routers that will collect and re-transmit the signals by means of a long-range antenna or radio modem
- ⋆ A computer or laptop that will receive all the data, analyze them and spread them into the Internet
- ⋆ A broadband bi-directional wireless Internet connection via satellite
- ⋆ sources of energy

A possible structure is shown in figure (6.1) which has been created making use of images from Werner-Allen et al. (2006), Kota et al. (2011) and Adi Mallikarjuna Reddy V.

The bidirectional internet connection via satellite must be settled taking into account the country where the sensor network will be placed.
It can be acquired from dedicated companies such as BusinessCom (http://www.bcsatellite.net/international-satellite-internet/, level421 GmbH (www.europe-sat.net), Hughes Network Systems, LLC (www.bentley-walker.com) or Sat Link (http://www.satlinkcom.com).

SPR sensor structure

I took into consideration some miniaturized and innovative SPR sensors (as Chinowsky et al. (2007), Naimushin et al. (2002), Marchesini et al. (2007), Nakamoto et al. (2008), Kurita et al. (2006)), but unfortunately most of them was based on "home made" SPR sensors or on industrial SPR sensors not in commerce at the present time.

I also consequently chose to use "home made" SPR sensors.

As a first possible setup the surface Plasmon Resonance sensor created for the WSN therefore comprises

- ⋆ a red laser diode
- ⋆ a polarizer
- ⋆ a collimating lens
- ⋆ a prism coupler
- ⋆ the multilayer structure supporting a Surface Plasmon Polariton
- ⋆ a neuter filter for decreasing the beam intensity if needed to avoid the saturation of the detector
- ⋆ a flowcell
- ⋆ a fluidic system

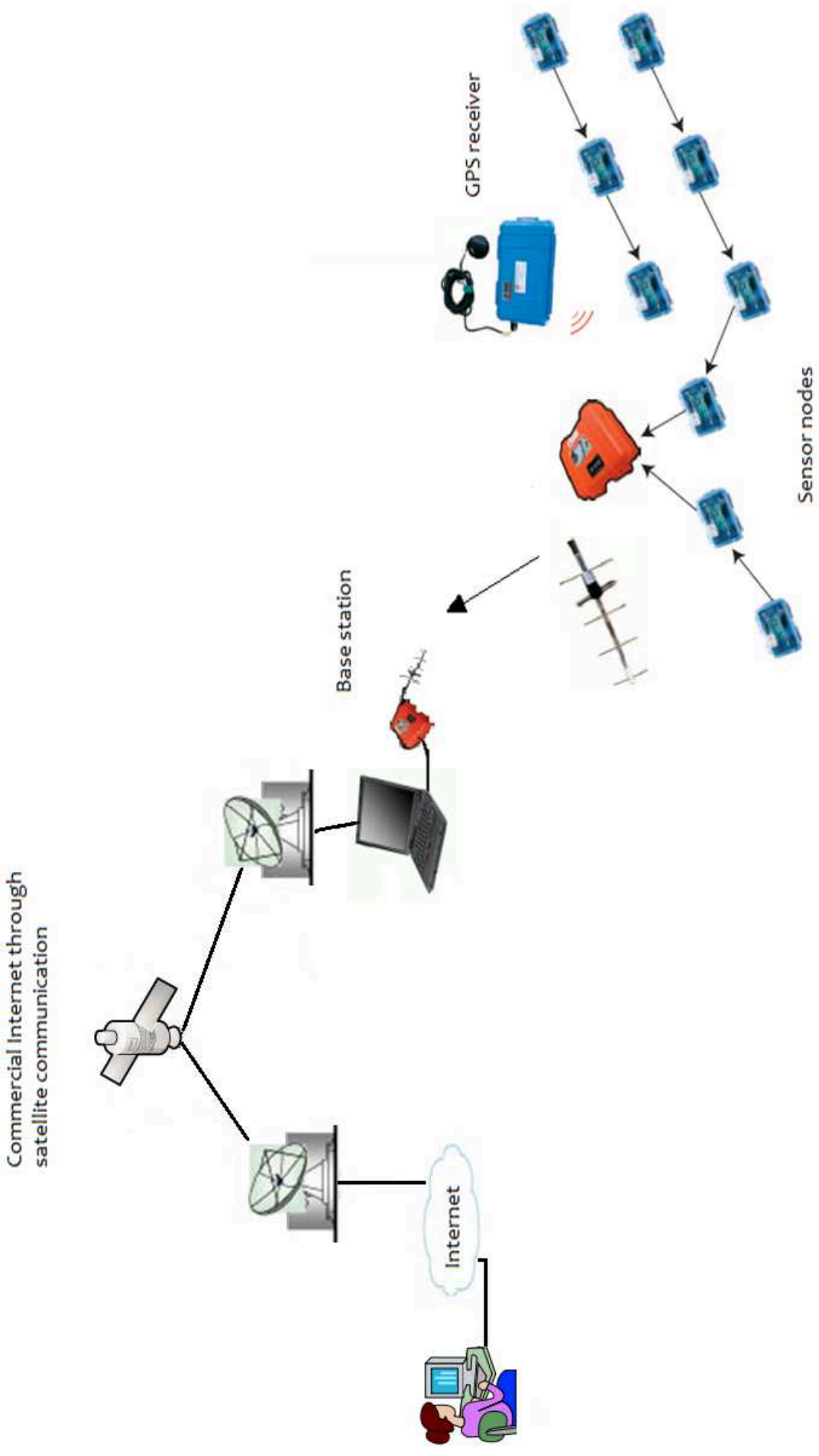
GPS receiver
Sensor nodes
Base station
Commercial Internet through satellite communication
Internet

Figure 6.2: Photo of the Apinex.com red laser diodes

⋆ a detector.

A red laser diode from Apinex.com (6.2) is the selected choice as a light source.

The prism can be optically coupled to a glass slide where a small chrome film for adhesion and a gold film with thickness 50 nm have been previously deposited, otherwise the metals can be directly deposited on the prism itself. The second option has been preferred for its greater ruggedness.

A biorecognition sensing layer is then added to the metal surface in order to bind and thus discriminate the chosen pollutants.

An injection system produces a controlled flow of the fluid samples to be analyzed into a flow-cell and to the sensor surface. In addition to that the fluidic valves allows also to flow water samples on the sensors in order to clean the sensor surfaces and prevent cross-contamination between samples.

A photodiode array or a CMOS camera for contemporary samples are the best solutions as detectors.

A smaller miniaturized SPR sensor could possibly be implemented with industrial components.

The light sources:selected red laser diodes

The 03008B Red laser diodes from Apinex.com have been chosen for their ruggedness, small dimensions and low consumption.

Their most relevant characteristics are

⋆ Wavelength: 650 nm

⋆ Output Power: 5 mW (nominal)

⋆ Operation Voltage: 3V DC

Figure 6.3: Photo of the SX Arm Linux 1L microcontroller

- ⋆ Operation Current: 30 mA
- ⋆ Divergence: <2.0 mrad
- ⋆ Case Material: Brass, for heat dispersion
- ⋆ Length: 23 mm
- ⋆ Diameter: 8.0 mm
- ⋆ Optics:A Plastic lens for varying the focal distance
- ⋆ Incorporated driver circuits.

The node controllers

The SX Arm Linux 1L board, shown in the image (6.3) and (6.4), has been chosen as a node controller for the proposed WSN.

The characteristics that make these motes suitable for this project are

Figure 6.4: Photo of the opened SX Arm Linux 1L board

- ⋆ low power consumption: 340 mA at 12 V DC, 4.5 W, full operativity, presence of the hibernation mode
- ⋆ small dimensions: 110 x 80 x 25 mm
- ⋆ 2 host USB 2.0, five RS232 and a Ethernet RJ45 10/100 mbps ports,which allow many connectivity options
- ⋆ a compatible GPS receiver
- ⋆ compatible Zigbee antennas

while other important data are

- ⋆ CPU: ATMEL AT91RM9200 (ARM9-core)
- ⋆ memory: Flash 16MB, RAM 64MB SDRAM, EEPROM 16Kb
- ⋆ Power: +9V DC to 48V DC
- ⋆ Real Clock Timer
- ⋆ Buzzer
- ⋆ SD memory support
- ⋆ OS: uCLinux, kernel 2.6

Thanks to the uCLinux operative system equipped with the bash shell and the busybox Linux utility it is possible to program this Arm mote with C/C++ language by means of the Arm-linux cross-compiler.

Moreover this board has enough memory to store a jpeg image from the detector and can therefore send it through the antennas to the laptop or the routers.

Zigbee antennas

The Zigbee protocol is optimized for the sensor networks and moreover ZigBee antennas have a small power consumption, so they have been chosen for the short distance transmission of the data.

The possibility of transmitting jpeg images over Zigbee is attested from (Pekhteryev et al. (2005)).

ZigBee antennas operate at the frequency band of 2.4 GHz, using 16 channels with a bandwidth of 5MHz per channel, as shown in figure (6.5) from Libelium (2010).

The ZigBee specification fulfills the IEEE 802.15.4 standard . Some of the characteristics of ZigBee include (from http://www.zigbee.org/ Specifications/ZigBee/Overview.aspx) :

- ⋆ Global operation in the 2.4 GHz frequency band, according to IEEE 802.15.4
- ⋆ Regional operation band in the 915 Mhz (Americas) and 868 Mhz (Europe).
- ⋆ 16 frequency channels in the 2.4 GHz band
- ⋆ Power saving mechanisms
- ⋆ Discovery mechanism

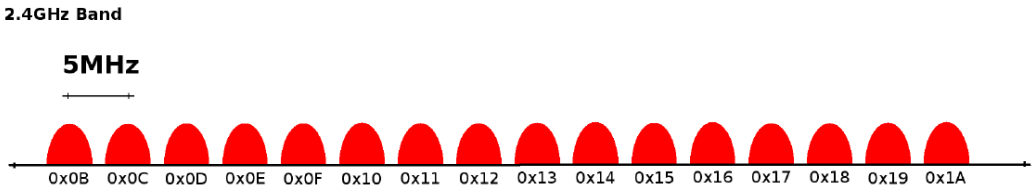

Figure 6.5: Zigbee 2.4 GHz band channels

- ⋆ Pairing mechanism
- ⋆ Multiple star topology and inter-personal area network (PAN) communication
- ⋆ Various transmission options including broadcast
- ⋆ Security key generation mechanism
- ⋆ Utilizes the industry standard AES-128 security scheme

The chosen Zigbee antennas, visible at image (6.6), in particular have a very low power consumption and high sensitivity.

Their most important characteristics are

- ⋆ Indoor/Urban range: up to 40 m
- ⋆ Outdoor line-of-sight: up to 120 m
- ⋆ Transmit Power: 2 mW with sensitivity +3 dBm
- ⋆ Receiver Sensitivity: -95 dBm
- ⋆ RF Data Rate: up to 250,000 bps
- ⋆ TX Current: 40 mA at 3.3 V
- ⋆ RX Current: 40 mA at 3.3 V
- ⋆ Power-down Current: < 1 μA at 25° C

The SX20 board

The Zigbee Antennas are connected to the SX Arm Linux 1L by means of the SX20 board.

The latter, shown in image (6.7) has a USB plug and moreover it allows the Zigbee antennas to be seen from the board as a serial device, making their use easier.

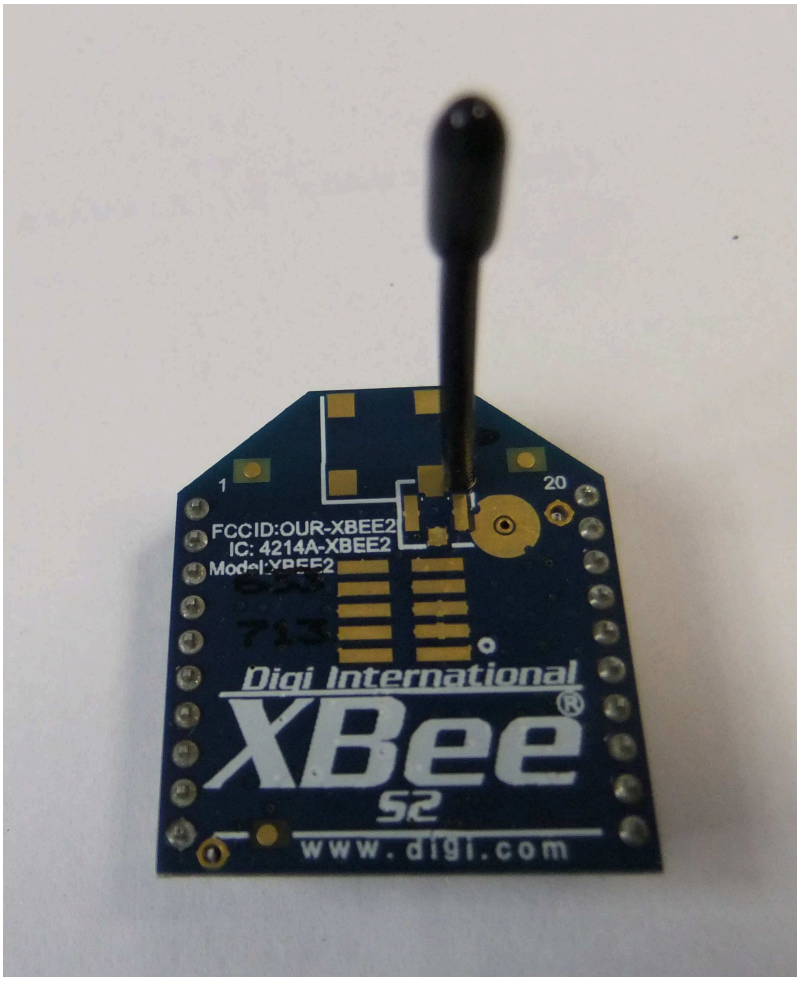

Figure 6.6: Photo of the Zigbee antenna

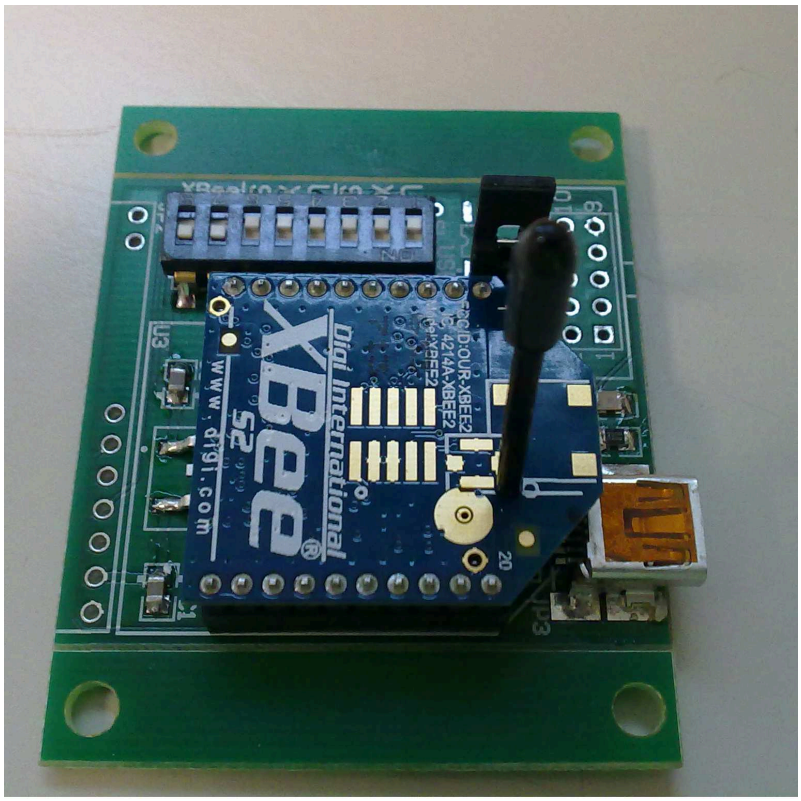

Figure 6.7: Photo of the SX20 board that connects the Zigbee antennas to the mote

Figure 6.8: Image of the Royaltek RGM-3600 GPS receiver

The GPS receiver

The chosen GPS receiver is the Royaltek RGM-3600, shown in image (6.8).

It has small dimensions, 48.4 x 48.4 x 15.1mm (L x W x H) and can be connected with a mote by means of a USB plug.

Moreover other important data (obtainable from RoyalTek (2008)) about this receiver are

- ⋆ SiRF Star III GPS chipset
- ⋆ 20 parallel scan channels
- ⋆ Chipset Sensitivity: -159 dBm
- ⋆ Used frequency band: L1 band at 575.42 MHz.
- ⋆ Cold Start in 35 sec
- ⋆ Warm Start in 35 sec
- ⋆ Hot Start in 1 sec
- ⋆ Re-acquisition: 0.1 sec. typical
- ⋆ Update Rate: 1 Hz
- ⋆ Position accuracy: 10 meters at 2D RMS.
- ⋆ I/O: USB
- ⋆ Weight < 30 g
- ⋆ Vcc: 5 V, DC
- ⋆ Operating Temperature: -20 to 60 ř C

This GPS makes use of the NMEA 0183 code which has the following characteristics (see Betke (2001)):

- ⋆ Baud (symbols per second) rate: 4800
- ⋆ Number of data bits: 8 (bit 7 is 0)
- ⋆ Stop bits: 1
- ⋆ Parity: none
- ⋆ Handshake: none

All data of NMEA0183 code are transmitted in the form of sentences in which only printable ASCII characters are allowed, plus `CR` (carriage return) and `LF` (line feed). Each sentence starts with a `"$"` sign and ends with `<CR><LF>`.

The Royaltek RGM-3600 supports the following NMEA-0183 Messages: GGA, GLL, GSA, GSV, RMC and VTG.
Their descriptions are listed in table (6.1), while their data structure is discussed in appendix (B).

I also studied the characteristics of the GPS signal during my PhD courses to better understand its features and the best way to make use of it in the sensor network.

Table 6.1: NMEA-0183 Output Messages

NMEA	Record Description
GGA	Global positioning system fixed data
GLL	Geographic position - latitude / longitude
GSA	GNSS DOP and active satellites
GSV	GNSS satellites in view
RMC	Recommended minimum specific GNSS data
VTG	Course over ground and ground speed

6.1.2 Physical configuration of the wireless sensor network

- ⋆ Every operative sensor node, called also mote, will be composed of a miniaturized SPR sensor connected to a SX Arm Linux 1L controller board, a ZigBee antenna to transmit the data to a router and a GPS receiver. The sensor motes will be shielded from water and connected to earth with a proper cable.
- ⋆ The routers will comprise a SX Arm Linux 1L board accordingly programmed and connected to a long-range antenna, for example a Yagi model as in Werner-Allen et al. (2006) ,
- ⋆ the ground station will be composed of a receiver antenna, a Laptop and a two way wireless Internet connection via satellite.

Every mote will be powered by means of a battery and possibly of a small solar cell.
The ground station will also have an appropriate energy source, possibly a generator.

6.1.3 Target analytes

As target water pollutants

- ⋆ 2,4-Dichlorophenoxyacetic acid (2,4-D) (see Schlecht et al. (2002))
- ⋆ ricin (as in Tran et al. (2008))
- ⋆ heavy metals (Kang et al. (2005) for reference)
- ⋆ if possible escherichia coli as in (Dudak and Boyaci (2007))

could be good candidates and the references provide suitable chemical layers for their discrimination.

6.1.4 Data to evaluate in the Wireless Sensor Network based on SPR sensors

Data to be sent to the final user in the net are:

1. Signals confirming the correct operativity of the motes, as battery voltage levels, correct operativity of the sensors and of fluidics
2. Data from every SPR sensor

3. Data loss if present and correct connectivity of the devices

4. Time and coordinates of every observation, obtained through GPS modules

The motes nearer to the ground station should be able to re-transmit data and status of more distant sensors if possible.

Final users should be able to remotely monitor the sensors and their status.

6.1.5 Data to be evaluated on SPR sensors

Taking into account the different evaluations of the SPR sensors sensitivity and response presented in section (2.4) of this thesis the data that can be collected from every SPR measurements are:

- ⋆ The position of the minimum of reflectivity corresponding to the environmental medium before the exposure to the target molecule, expressed in pixels or in degrees and to be used as reference
- ⋆ The position of the minimum of reflectivity during the detection of the analyte
- ⋆ The normalized minimum and maximum values of the reflected light intensity
- ⋆ The position, in angles or pixel, of the incidence angles at which the intensity is the middle value between the maximum and the minimum of the reflected light intensity I, $I = \frac{I_{min}+I_{max}}{2}$, in order to evaluate the Full Width at Half Maximum of the signal
- ⋆ The normalized light intensity for a fixed column of pixels, corresponding to a fixed incidence angle
- ⋆ Time and space coordinates of every measurement, by means of the GPS receiver and the internal clock of the mote

Every image must be normalized and corrected for dark current,burned pixels and for the different response of every pixels, by means of

- ⋆ a dark image, taken with the light source turned off
- ⋆ a reference image, collected making use of the Transverse Electric polarized light or a dedicated part of the sensor area

With these data it is then possible to determinate the pollutant concentrations along with the position and time coordinates of every measurement.

6.1.6 Strategy for data handling

The sensor data could be managed through the following steps:

- ⋆ The CMOS camera will collect the data images
- ⋆ The node controller will acquire the data from the CMOS camera and the GPS receiver by means of USB2 communication ports
- ⋆ The controller will also transmit the data by means of the Zigbee antenna and its USB2 connection board
- ⋆ Data will be received and re-transmitted on longer distances by rooters

- ⋆ Data will be then received from the base station computer
- ⋆ The base station computer will also spread the data into Internet trough a bi-directional satellite internet connection

and taking into consideration the data themselves

1. As a first step the raw versions of the data images will be sent as a matrix of pixel values or as jpeg images from the motes to the central computer of the sensor network, that will consequently perform the data analysis
2. As a second step, if it will be possible, the motes will be programmed to perform the images normalization and pre-processing
3. As a desiderable possible implementation the motes could be moreover programmed to perform all the data reduction and to send to the Laptop only the parameters expressed in the previous subsection.

6.1.7 Considerations on the Energy requirements of the test SPR WSN

An estimation of the energy adsorption of the elements of the SPR WSN has been calculated in order to provide a sufficient source of energy to the system.

The following aspects were taken into consideration:

- ⋆ the SX Arm linux 1L consumes 340 mA at 12 V DC
- ⋆ the SX20 board requires 100 mA when in use and 2.5 mA in stand-by mode
- ⋆ the Xbee Zigbee antenna utilizes 40 mA at 3.3 V
- ⋆ an USB CMOS camera detector is connected through USB and thus adsorbs 500 mA as the worst case during its use
- ⋆ The RGM-3600 GPS receiver from specification should consume around 75 mA, and 500 mA as a maximum value being also connected through a USB port,
- ⋆ the laser diode requires around 30 mA when turned on
- ⋆ a time estimate for SPR measurements is around 5 s

The maximum power requirement of the sensor node is around 690 mA/s.

The data transmission time is the greatest issue and a compromise must be taken between data loss due to high transmission rate and the power costs of the operation. It is apparent that if the transmission time increases then the power requirement will grow accordingly.

As an example if the data transmission lasts for 2 minutes and a measurement is performed every four hours, a battery of 24 Ah should roughly last more than three months, while with a transmission time of 5 minutes the same battery should last nearly 70 days.

However in addition to the batteries small solar cells could be made use of as source of energy.

As stated previously the ground station will have its own appropriate energy source, possibly a generator so that the Desktop or Laptop computer can be turned on for the required time.
A Netbook could be even less energy expensive.

Less energy consuming elements can still be researched in the future.

6.2 Implementation of a small test WSN based on SPR sensors in laboratory

A test SPR based WSN has been implemented in laboratory.
It was composed of two small SPR sensors commanded by means of controllers, which collected the data and transmitted them with Zigbee antennas to a base station. The latter was composed of a Desktop computer with internet connection and an antenna to receive the data.

6.2.1 Elements of the test WSN based on SPR sensors

The small test WSN with SPR sensors that I've implemented in laboratory consisted of:

1. Two SPR sensors, composed of
   - ⋆ a red laser diode,
   - ⋆ a TM polarizer
   - ⋆ a BK7 diverging lens
   - ⋆ a pinhole and a circular slit in order to spatially filter the light beam
   - ⋆ a BK7 collimating lens
   - ⋆ a neuter filter for decreasing the beam intensity
   - ⋆ an SF6 cylindrical prism with a coating of 2 nm of Chrome for adherence and 50 nm of Gold
   - ⋆ a CMOS camera
2. Two SX Arm Linux 1L board, described in (6.1.1) of this chapter, and a computer with Linux (Ubuntu) operative system as node controllers.
3. two 2GB SD memories, each of them mounted on a ARM microcontroller mote
4. Three XBEE-WHIP-S2 ZigBee Series 2 antennas, referring to (6.1.1) for technical data
5. Three SX20 boards, whose description is in (6.1.1)
6. A Royaltek RGM-3600 GPS receiver (see 6.1.1)
7. A USB hub
8. A Base Station computer with possibility of satellite internet connection
9. appropriate energy sources

A photodiode array could be chosen as the detector, and for this reason during my PhD courses I studied photodiode detectors, but, in order to create a two dimensional scanning with contemporary measurements, CMOS cameras have been tested.

The detectors

The Edmund Optics EO-0413M CMOS camera has been chosen as a first detector for the test Wireless Sensor Network.

It is a CMOS Monochrome camera that can be connected to other devices through a mini-USB to USB cable.
Its main characteristics are

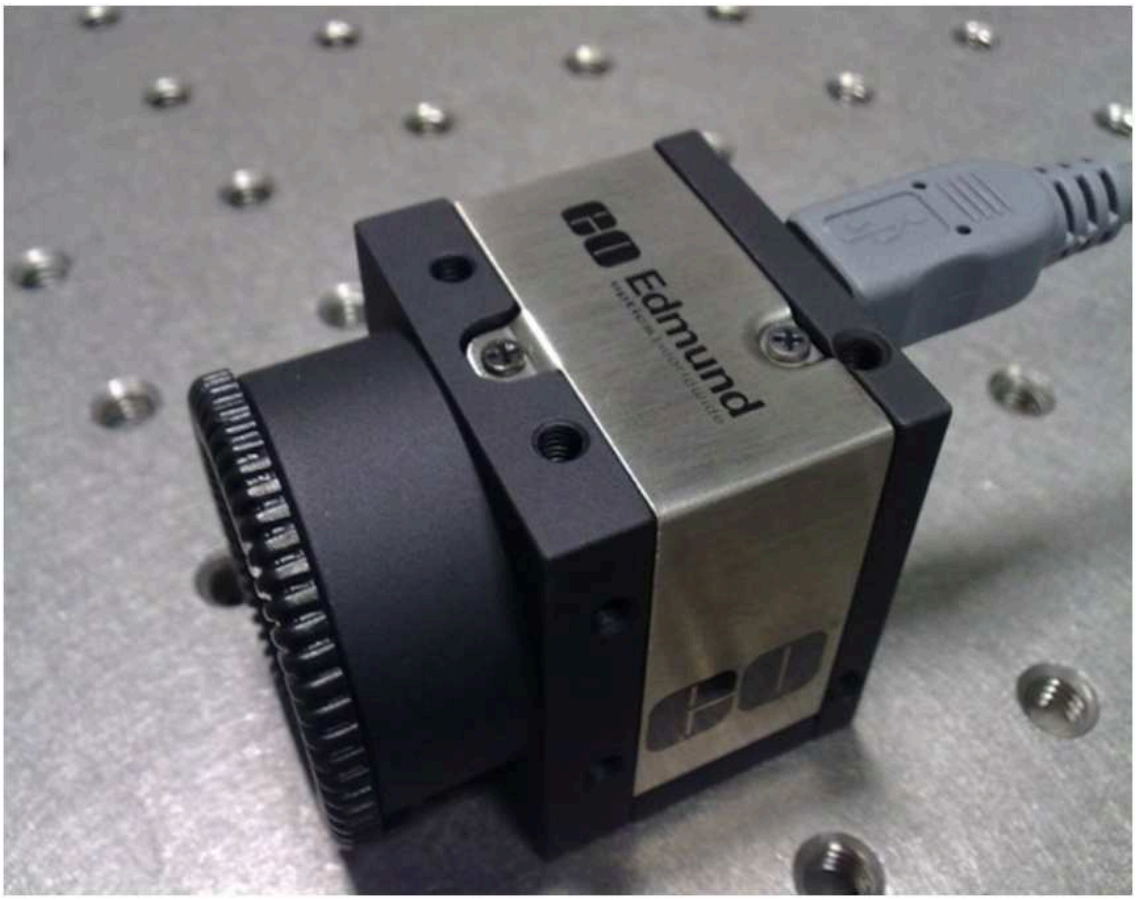

Figure 6.9: Photo of the EO-0413M CMOS camera

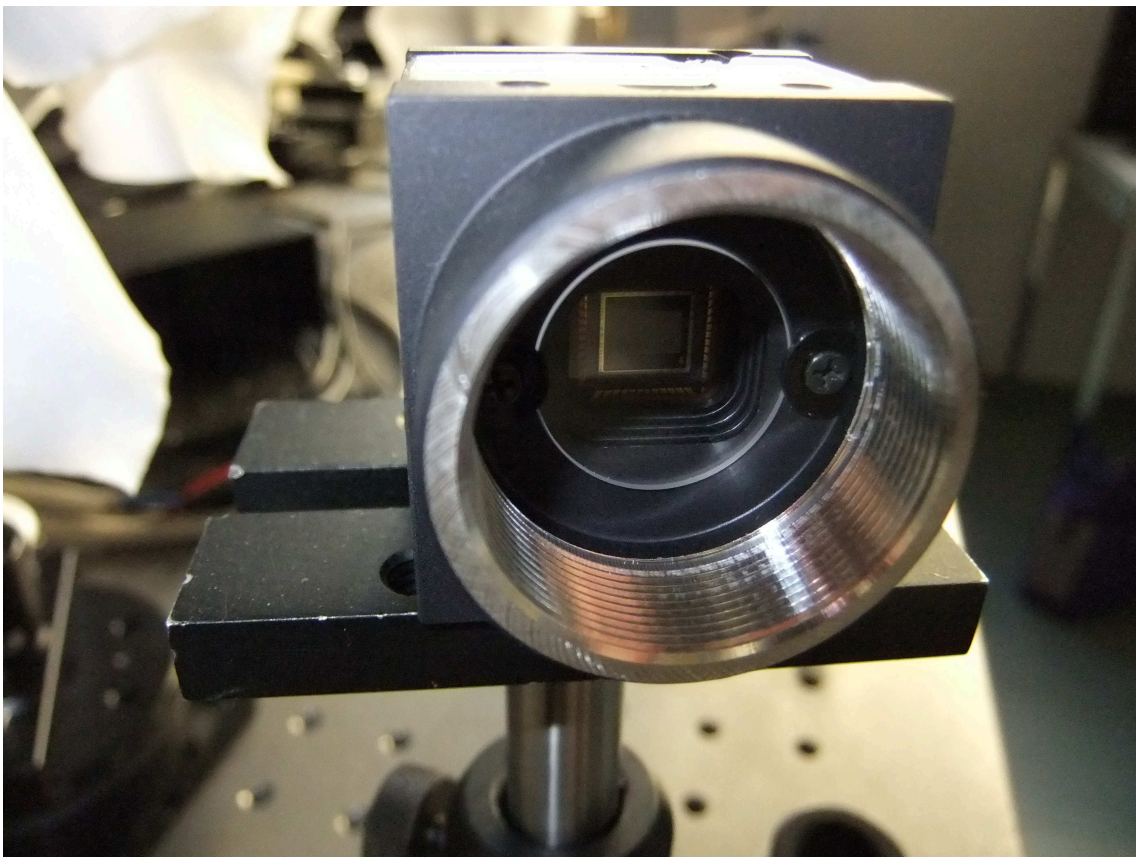

Figure 6.10: Photo of the EO-0413M CMOS camera

- ⋆ Type of Sensor: MT9V032
- ⋆ Sensing Area, H x V: 4.5 x 2.8 mm, 1/3" sensor
- ⋆ Pixels, H x V: 752 x 480
- ⋆ Pixel Size, H x V: 6.0 x 6.0 μm
- ⋆ Pixel Depth: 8 bit
- ⋆ Frame Rate: 87 fps
- ⋆ Global Shutter
- ⋆ USB 2.0 Output
- ⋆ Dimensions: 34 x 32 x 27.4 mm

Its Photos are shown in images (6.9) and (6.10).

This camera has been chosen because of its small dimensions, high quality of the image and the possibility to remove the glass protection and to directly expose the sensor.
This avoided the presence of possible interference fringes due to the interaction of the camera glass and the light source coherence.
Moreover the EO-0413M CMOS camera is provided with Linux drivers, although it is quite complex to adapt them to be used with a microcontroller.

The camera drivers can be downloaded from http://www.ids-imaging.com/ frontend/files/Edmund/Setup.htm

However the detectors of a Wireless Sensor Network should be quite cheap and easy to use.

Because of the EO-0413M CMOS camera prize and the complexity of its drivers, other CMOS sensors have been thus also evaluated and after some tests the HP 1300 and the DIGITUS DA-70815 webcams have been chosen for the laboratory tests.

The HP 1300 camera is shown in image (6.11) and its main characteristics are

- ⋆ a 300 K pixel CMOS sensor
- ⋆ a 640x480 pixels resolution
- ⋆ a fixed lens focus distance
- ⋆ a USB 2.0 UVC interface
- ⋆ a JPEG/BMP Picture capture
- ⋆ supports the USB Video Class
- ⋆ a built-in digital microphone
- ⋆ mount with the possibility of tilt and rotation.

Similarly the DIGITUS DA-71810, whose photo is image (6.12) presents

- ⋆ 1/6" 300 K pixel CMOS VGA sensor
- ⋆ 640x480 pixels resolution
- ⋆ High-quality optical glass lens

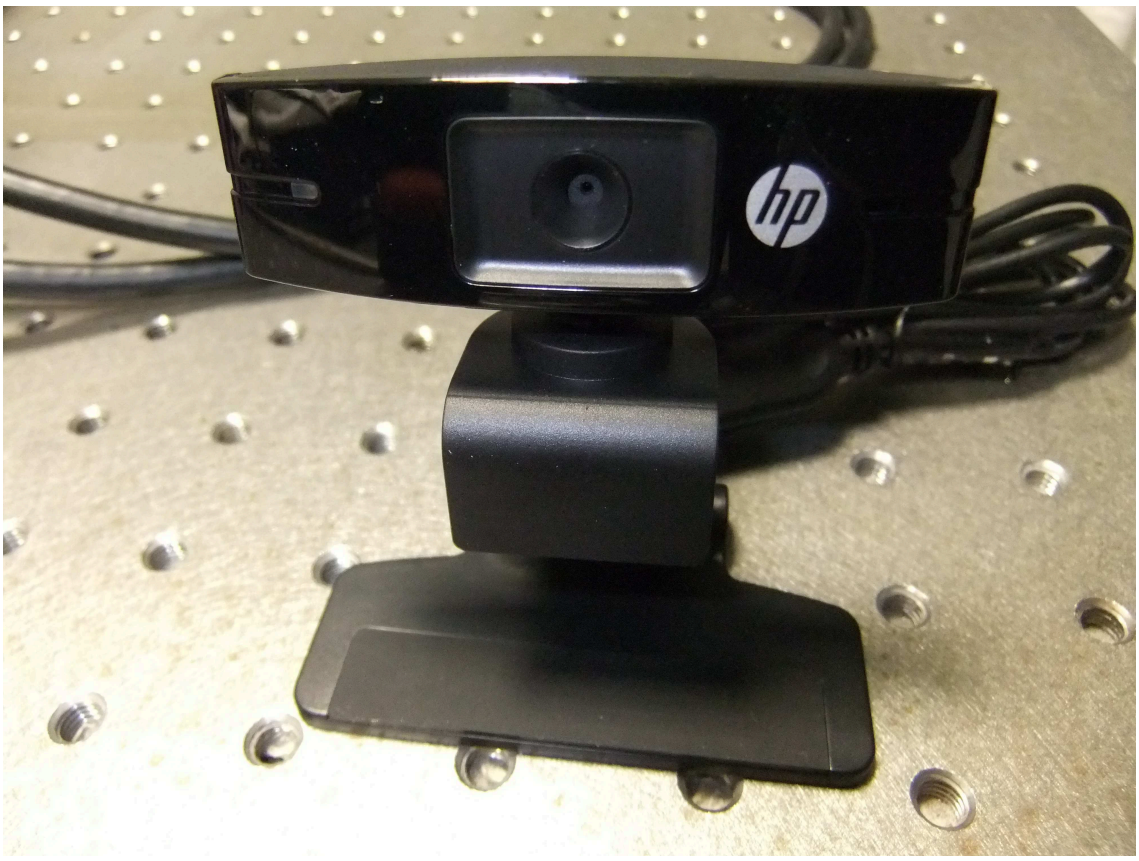

Figure 6.11: Photo of the HP 1300 CMOS camera

- ⋆ 50 mm to infinity lens focus distance (manual focus settings)
- ⋆ USB 2.0 UVC interface
- ⋆ JPEG/BMP Picture capture
- ⋆ MPEG 4 recording
- ⋆ integrated microphone
- ⋆ mount with the possibility of tilt and rotation.

These two cameras are compatible with the used drivers for the arm microcontroller.

Figure 6.12: Photo of the DIGITUS DA-71810 CMOS camera

6.2.2 Interconnection of the Elements of the test WSN with SPR sensors

The test Wireless Sensor Network based on SPR sensors consisted in two sensor nodes making use of SPR sensors and a ground station.

The ground station comprised a computer with internet connection and a SX20 board with a XBEE-WHIP-S2 Zigbee antenna inserted.

Every sensor node was composed of a SPR sensor, whose detector was a CMOS camera as stated previously, a computer or a microcontroller and a SX20 board connecting the Zigbee Antenna to the mote.
Moreover in one node a Royaltek RGM-3600 GPS receiver was added.

The CMOS cameras were connected to the motes with a USB cable and the same for the SX20 board. In order to make use of the GPS receiver, which was also connected trough a USB plug, a USB hub was thus used.

6.2.3 First assemblages and tests of the WSN SPR sensor nodes

As a firt step I implemented a sensor node and the base station setup in order to:

- ⋆ create and test the wireless connection between the ZigBee antennas,
- ⋆ implement the programs that actuates the sensor network tasks
- ⋆ make use of the Edmund Optics CMOS camera
- ⋆ test the data image transmission through ZigBee protocol.

The first prototype sensor node for the test WSN based on SPR sensors in laboratory comprised

1. An SPR sensor,shown in image (6.13) and composed of
   - ⋆ a red laser diode from Apinex.com,
   - ⋆ a TM polarizer
   - ⋆ a 200 μm pinhole
   - ⋆ a BK7 diverging lens with focal length -150 mm
   - ⋆ two mirrors
   - ⋆ a BK7 collimating lens having a focal length of 125 mm
   - ⋆ a neuter filter for decreasing the beam intensity
   - ⋆ an SF6 cylindrical prism with a coating of 2 nm of Chrome for adherence and 50 nm of Gold
   - ⋆ an Edmund Optics EO-0413M CMOS camera described previously,
2. a Desktop computer with Ubuntu 11.10 (Oneiric Ocelot) operative system as a node controller
3. a XBEE-WHIP-S2 ZigBee Series 2 antenna
4. An SX20 board, whose description is in (6.1.1)
5. A Royaltek RGM-3600 GPS receiver (see 6.1.1)
6. a USB hub.

Image (6.14) is a photo of this first test sensor node. The CMOS camera is not visible in this photograph but it is connected to the node controller.
In particular the Zigbee antenna was connected to the computer through a USB port while the GPS receiver and the CMOS camera were connected to the same port by means of a USB hub.
These connections were chosen to be also used in the SX Arm Linux 1L boards.

Image (6.15) instead is a picture of the test base station, comprising a computer with Windows XP operative system, a XBEE ZigBee antenna mounted on a SX20 board and an Internet connection.

As a first step I installed on both the node and the base station computers the appropriate drivers for the SX20 board and in the Linux computer the ones for the Edmund Optics camera and the GPS receiver.
Then I implemented the C programs to set and control the USB CMOS camera, to obtain from the latter a jpeg image and to use the GPS receiver.
After that I checked the connections between the Zigbee antennas through the XCTU program for Windows systems and I implemented the programs that allows the mote computer to transmit the sensor images and the GPS data trough its ZigBee antenna, and the base station to receive these data and save them appropriately.
The programs are reported in (6.2.6).

On a first run I tried to transmit the jpeg image but it wasn't properly recognized by the receiving system, possibly because of the jpeg header transmission handling.
I therefore decided to decompress the jpeg image into a binary file with an appropriate C program and then to send the binary data over Zigbee.

The received binary image was then correctly read and processed by Matlab.

(6.16) and (6.17) are a transmitted sensor image and the corresponding received data depiction respectively.

The two images are specular, probably because of the used programs, however this was an easy solved issue.

An example of received image data fit with the theoretical curve of reflectivity is shown in image (6.18)

With regards to the main concept of the Surface Plasmon Resonance sensor control by means of the ARM microcontroller, I managed to control the laser diode with an SX Arm Linux 1L board, as shown in picture (6.19).

In order to accomplish this I soldered a 10 Ohm resistance to the positive voltage electrical cable of the diode and then I connected the same cable to a General Purpose DIO (GPIO) of the SX Arm Linux 1L, which I had previously programmed to be a voltage and current output. After that I connected the negative voltage electrical cable to a ground GPIO of the same board, as it can be seen from image (6.20)
When the output pin is set to 1 it generates a 3.3 V potential and a 52 mA current, while when it is set to 0 the output is null.
Thanks to these connections is therefore possible to turn the laser on when the output pin is set to 1 and to turn it off when the pin is set to 0.

After that I inserted a circular slit on the previous optical system and the HP 1300 and the Digitus webcams have been tested with the Arm microcontroller motes.

They resulted to be compatible with the given drivers for the microcontroller and their optics could be easely removed in order to use the "naked" sensor.
In fact the lenses placed before the sensor collimated the beam from the optical system of the SPR sensor and thus they had to be demounted for obtaining the correct SPR signal and in particular its angular informations.

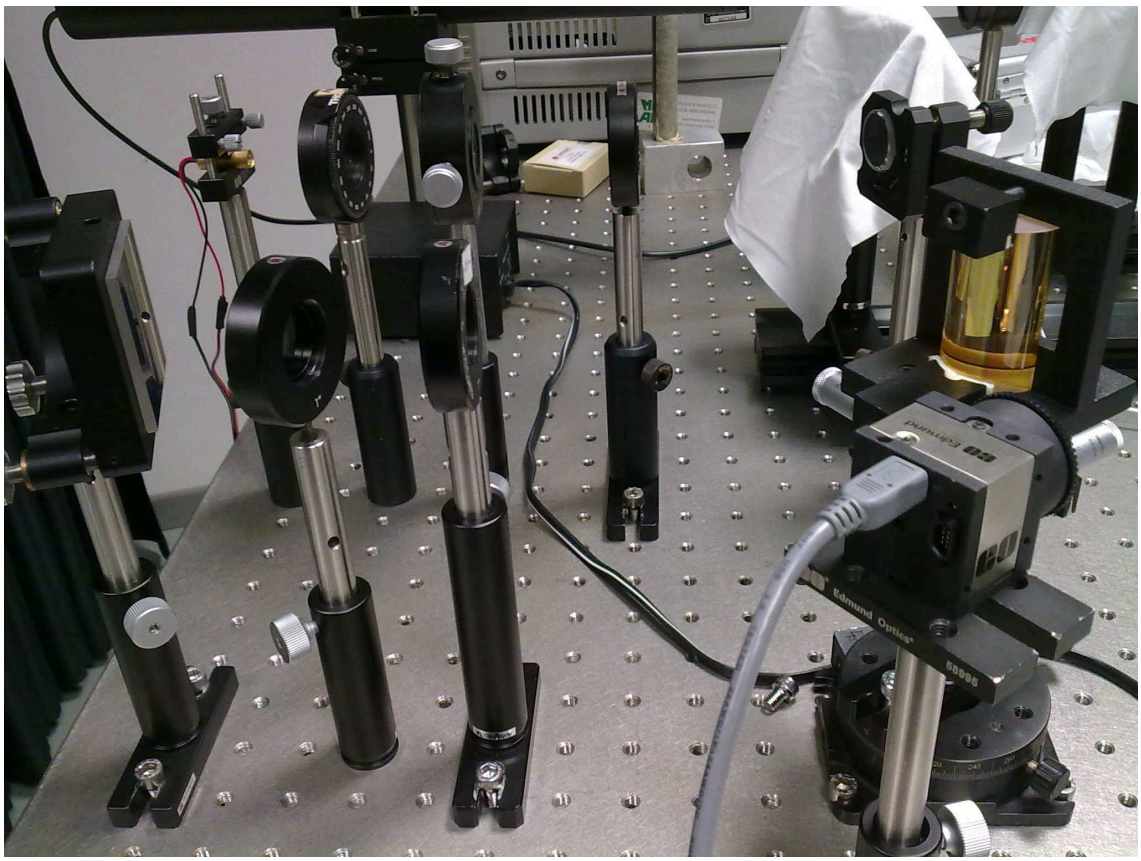

Figure 6.13: Photo of the SPR sensor for the first tests on the SPR WSN

Figure 6.14: Photo of the test mote for the first tests on the SPR WSN

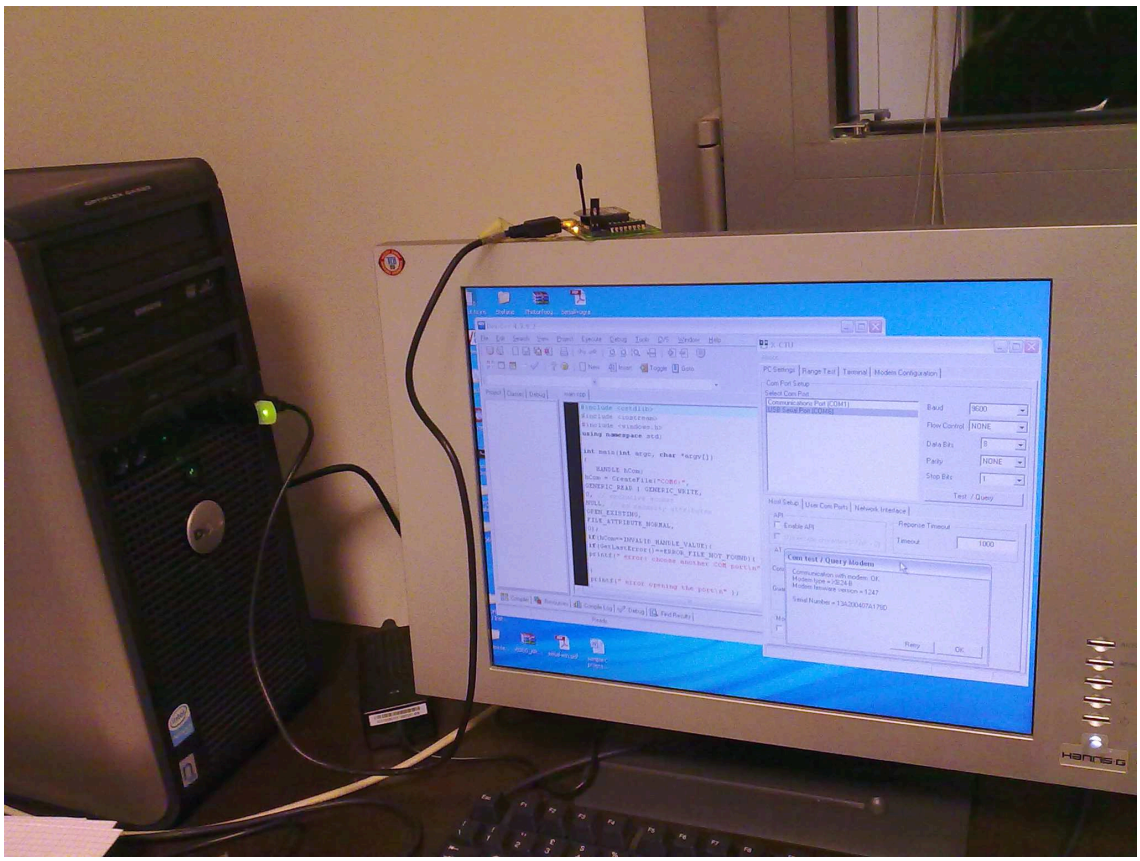

Figure 6.15: Photo of the base station for the first tests on the SPR WSN

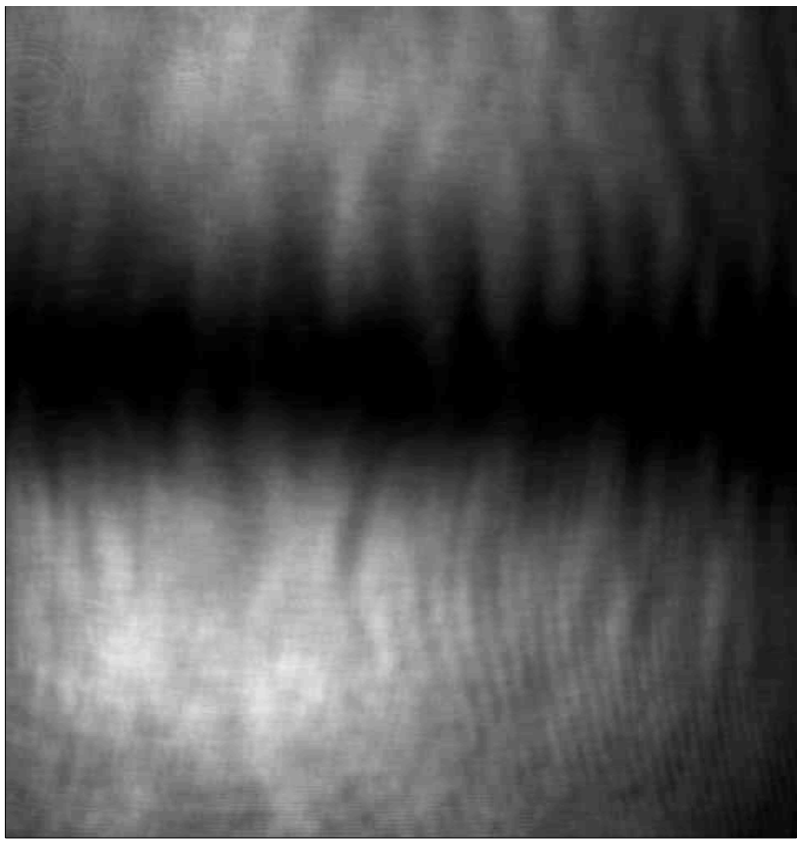

Figure 6.16: Transmitted image

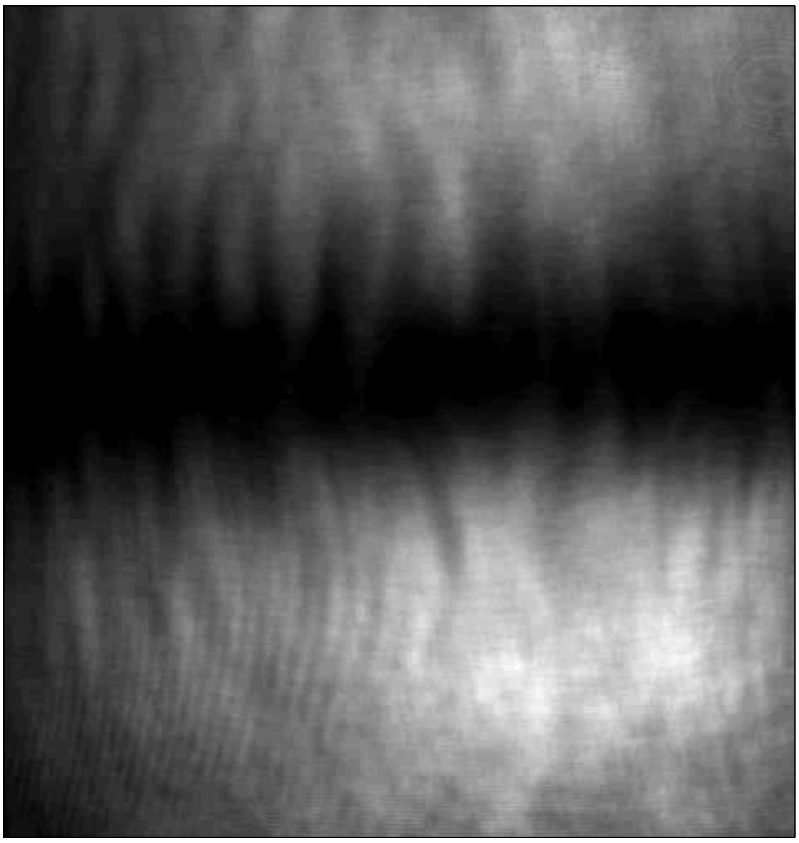

Figure 6.17: Received image

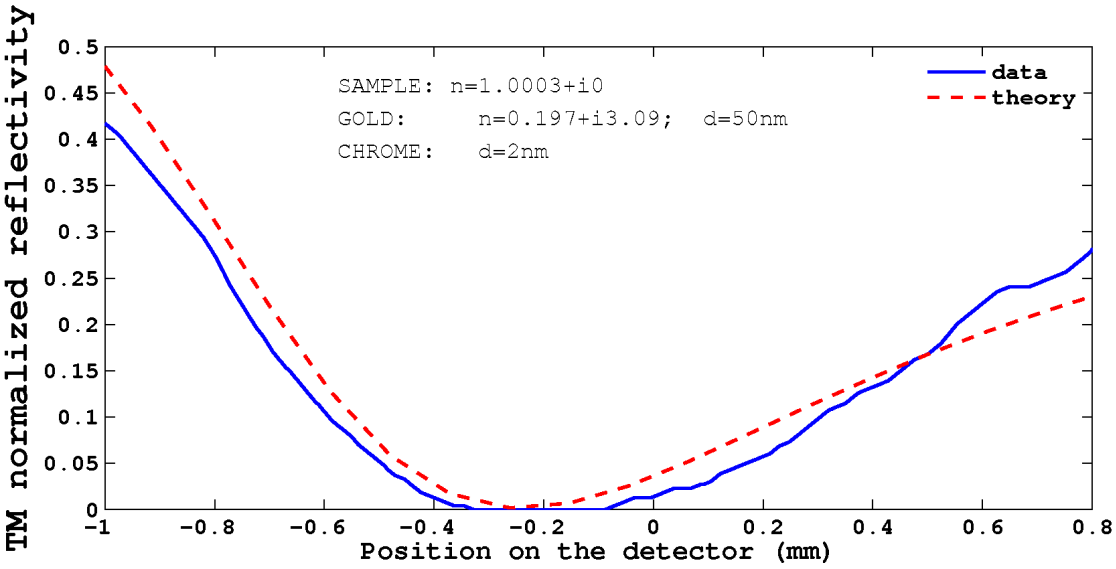

Figure 6.18: An example of a received image data fit with the theoretical curve of reflectivity

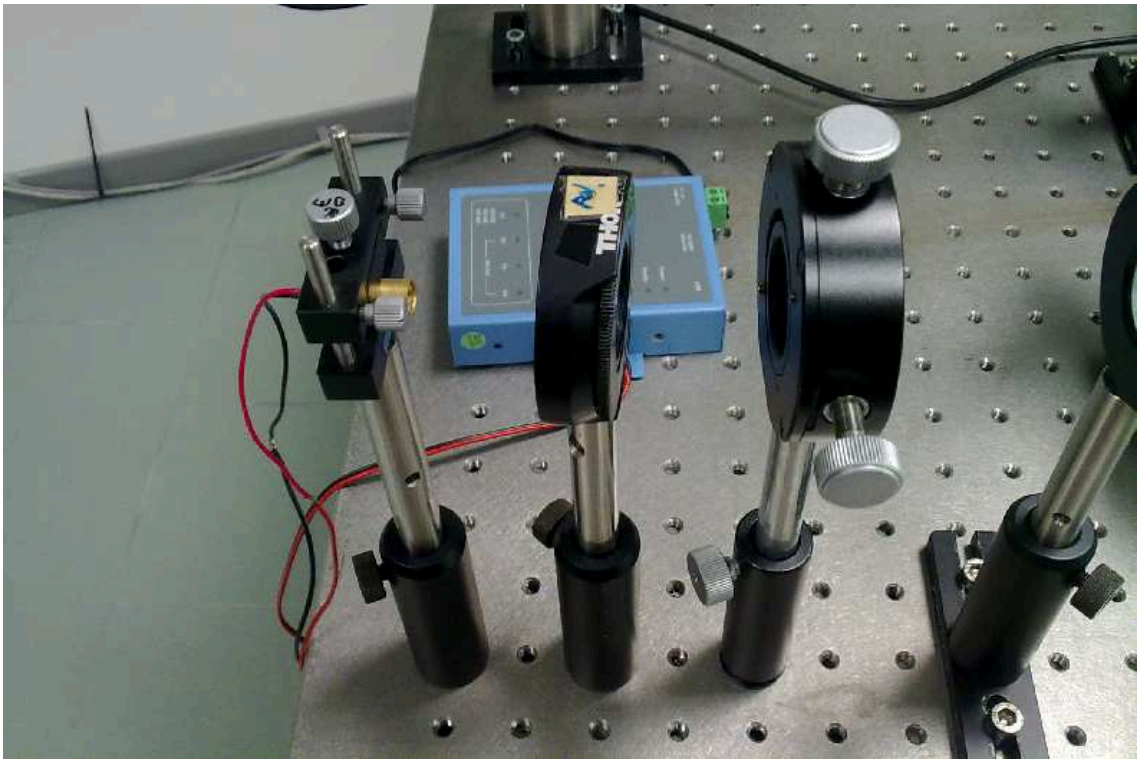

Figure 6.19: laser diode control by means of the SX Arm Linux 1L board

Figure 6.20: Photo of a opened SX Arm Linux 1L mote with the pin connections established for the laser diode control

6.2.4 First implementation of a Wireless Sensor Network based on SPR sensors in laboratory

The first implementation of the WSN based on SPR sensor was composed of two different controllers commanding two Surface Plasmon Resonance based sensors.

Image (6.21) is a Zeemax simulation of the first SPR sensor of the test WSN, comprising

- ⋆ a red laser diode from Apinex.com,
- ⋆ a TM polarizer
- ⋆ a 200 μm pinhole
- ⋆ a BK7 diverging lens with a focal length of -150 mm
- ⋆ two mirrors
- ⋆ a circular slit to select the central airy disk of the light beam
- ⋆ a BK7 collimating lens with focal length equal to 125 mm
- ⋆ an SF6 cylindrical prism with a coating of 2 nm of Chrome for adherence and 50 nm of Gold
- ⋆ an Edmund Optics EO-0413M CMOS camera

while image 6.22 is an image of the same.
Image (6.23) is a photograph of the used node, which consisted on

- ⋆ a Desktop computer with Ubuntu 11.10 (Oneiric Ocelot) operative system as a controller
- ⋆ a XBEE-WHIP-S2 ZigBee Series 2 antenna
- ⋆ An SX20 board, whose description is in (6.1.1)
- ⋆ A Royaltek RGM-3600 GPS receiver (see 6.1.1)
- ⋆ a USB hub,

6.24 is a transmitted image from the described above sensor, corresponding to the received image (6.25).

Image (6.26) instead is a fit of the received data with the theoretical values.

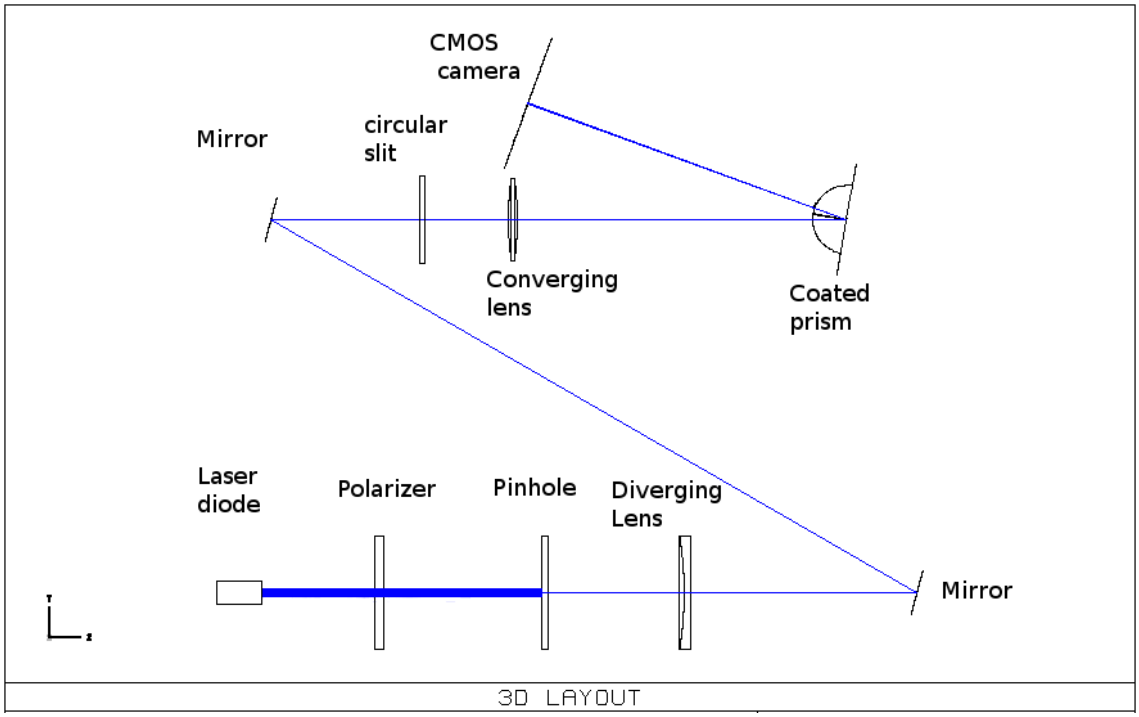

Figure 6.21: Zeemax simulation of the optical system that forms the first SPR sensor of the first laboratory implementation of the SPR WSN

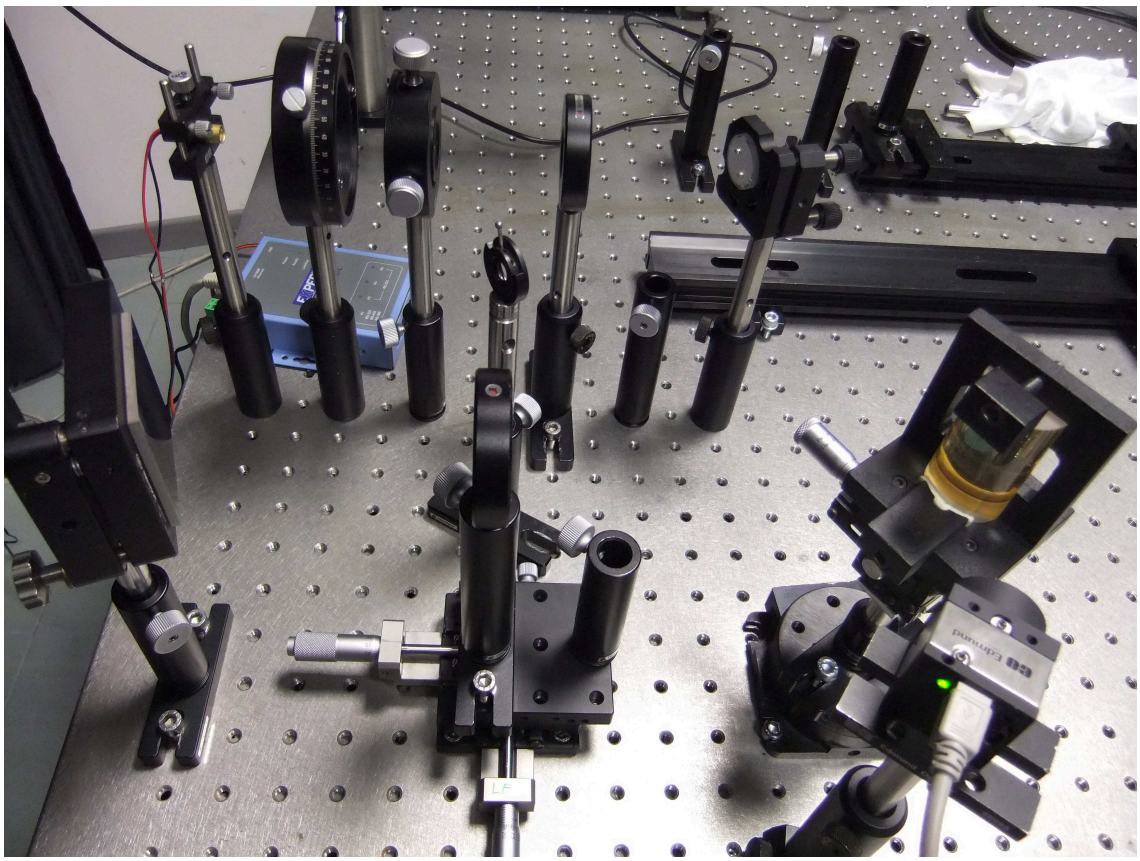

Figure 6.22: Photo of the first SPR sensor of the first laboratory implementation of the SPR WSN

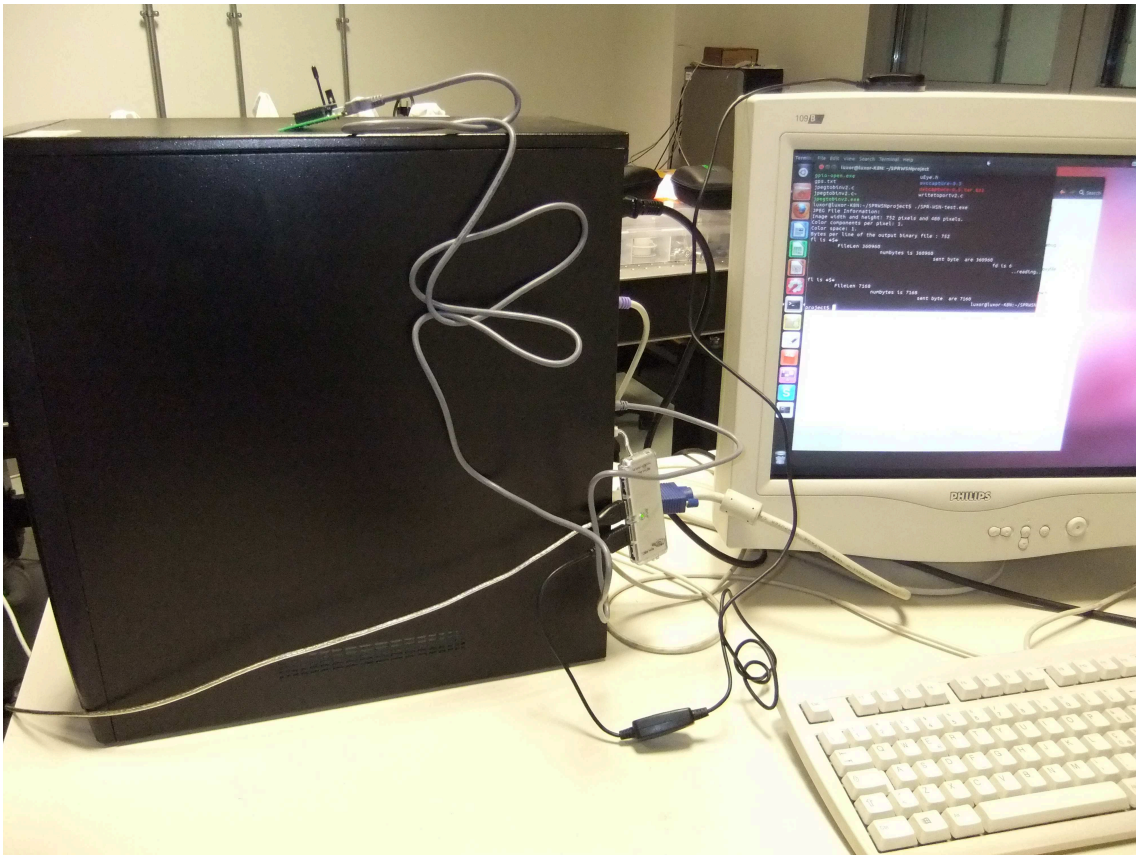

Figure 6.23: Photo of the first sensor node of the first laboratory implementation of the SPR WSN

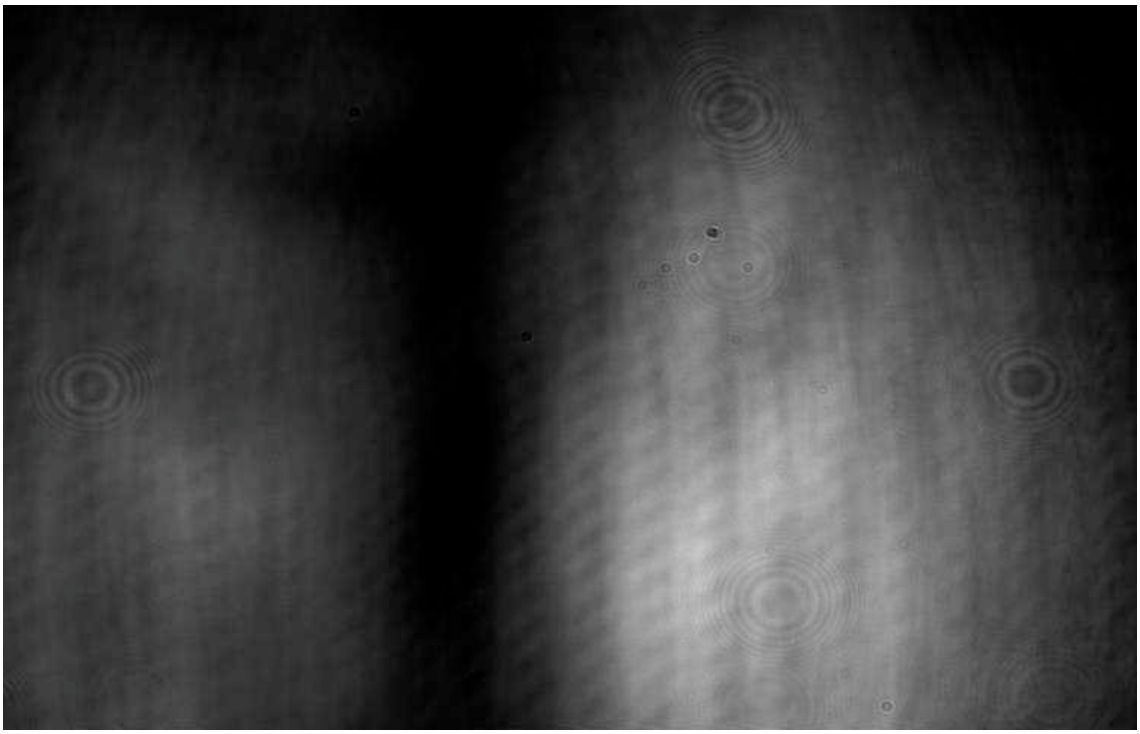

Figure 6.24: Transmitted image from the first SPR sensor of the first laboratory implementation of the SPR WSN

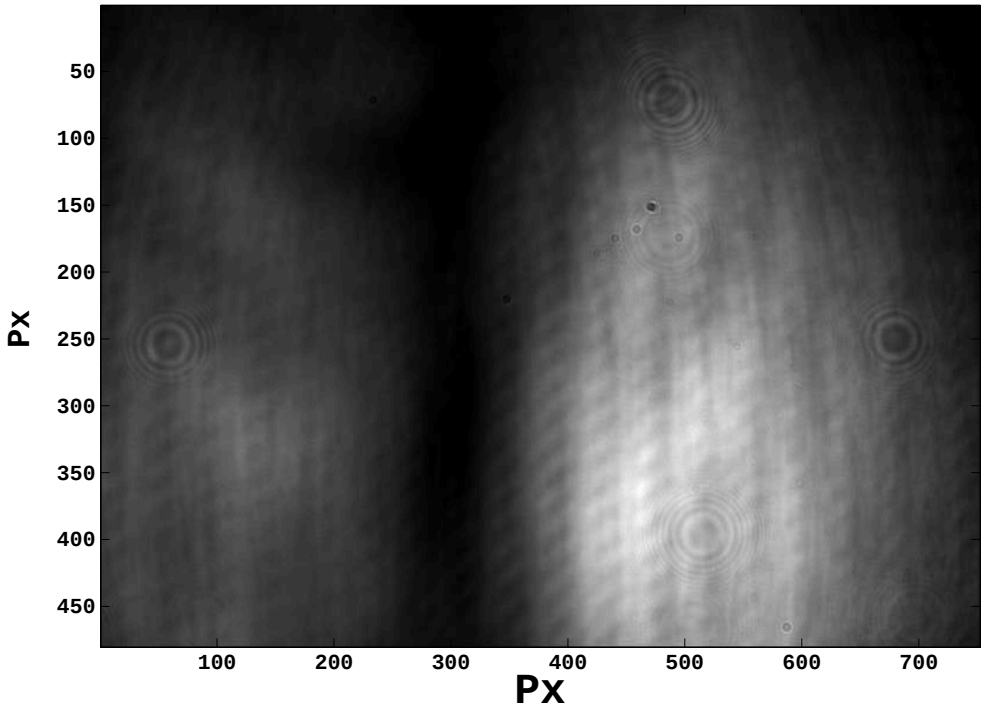

Figure 6.25: Received grayscale image from the first SPR sensor of the first laboratory implementation of the SPR WSN

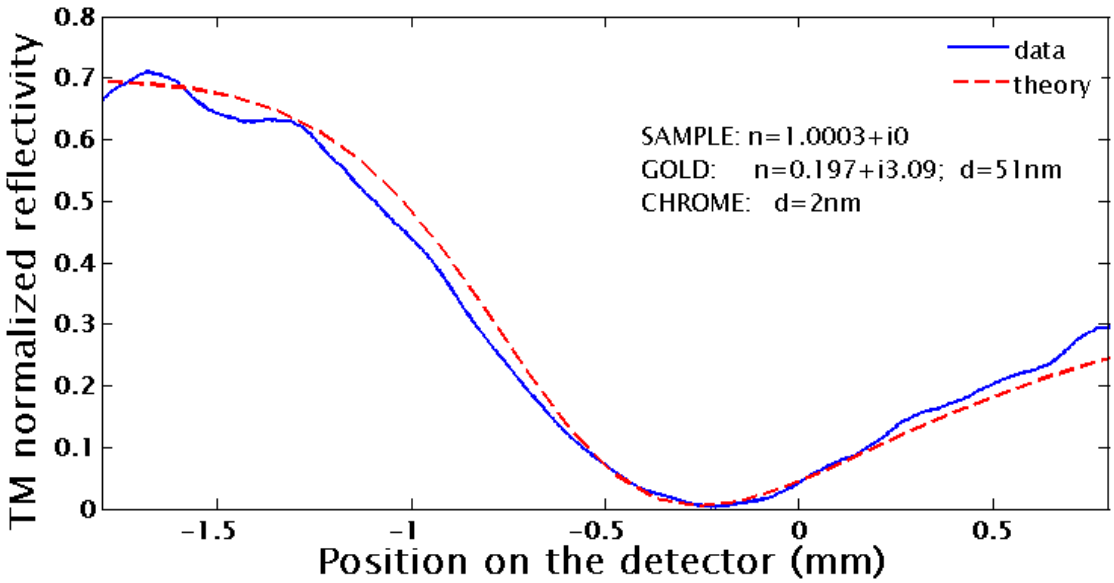

Figure 6.26: Example of the fit of the first laboratory implementation of the SPR WSN first mote data with the theoretical values

The second Surface Plasmon Resonance sensor was similar to the first and composed of

- ⋆ a red laser diode from Apinex.com,
- ⋆ a TM polarizer
- ⋆ a 200 μm pinhole
- ⋆ a BK7 diverging lens (focal length -150 mm)
- ⋆ two mirrors
- ⋆ a circular slit to select the central airy disk of the light beam
- ⋆ a BK7 collimating lens (focal length 150 mm)
- ⋆ some neuter filters for decreasing the beam intensity
- ⋆ an SF6 cylindrical prism with a coating of 2 nm of Chrome for adherence and 50 nm of Gold
- ⋆ a HP 1300 CMOS camera, described above,

and the node was composed also by

1. a SX Arm Linux 1L microcontroller
2. a XBEE-WHIP-S2 ZigBee Series 2 antenna
3. An SX20 board

Picture 6.27 is a photo of the second SPR sensor controlled by the ARM microcontroller.

An example of the images transmitted by this mote is shown in figure (6.28) and the corresponding received image in (6.29).

A fit of the image data with the expected values is given as image (6.30)

Picture (6.31) is a photo of the used Base Station receiving system,that was composed of a Desktop computer with a Windows XP operative system, an XBEE ZigBee antenna mounted on a SX20 board and a broadband Internet connection

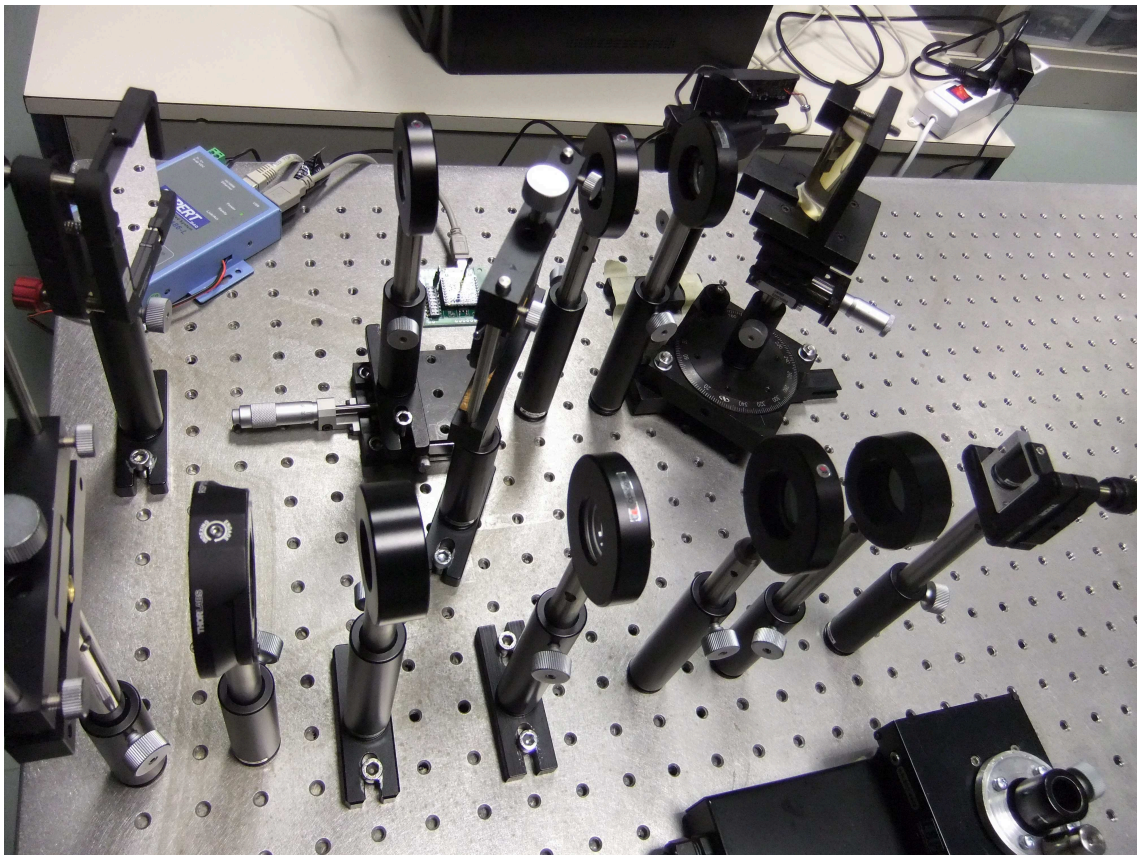

Figure 6.27: Photo of the second sensor node of the first laboratory implementation of the SPR WSN

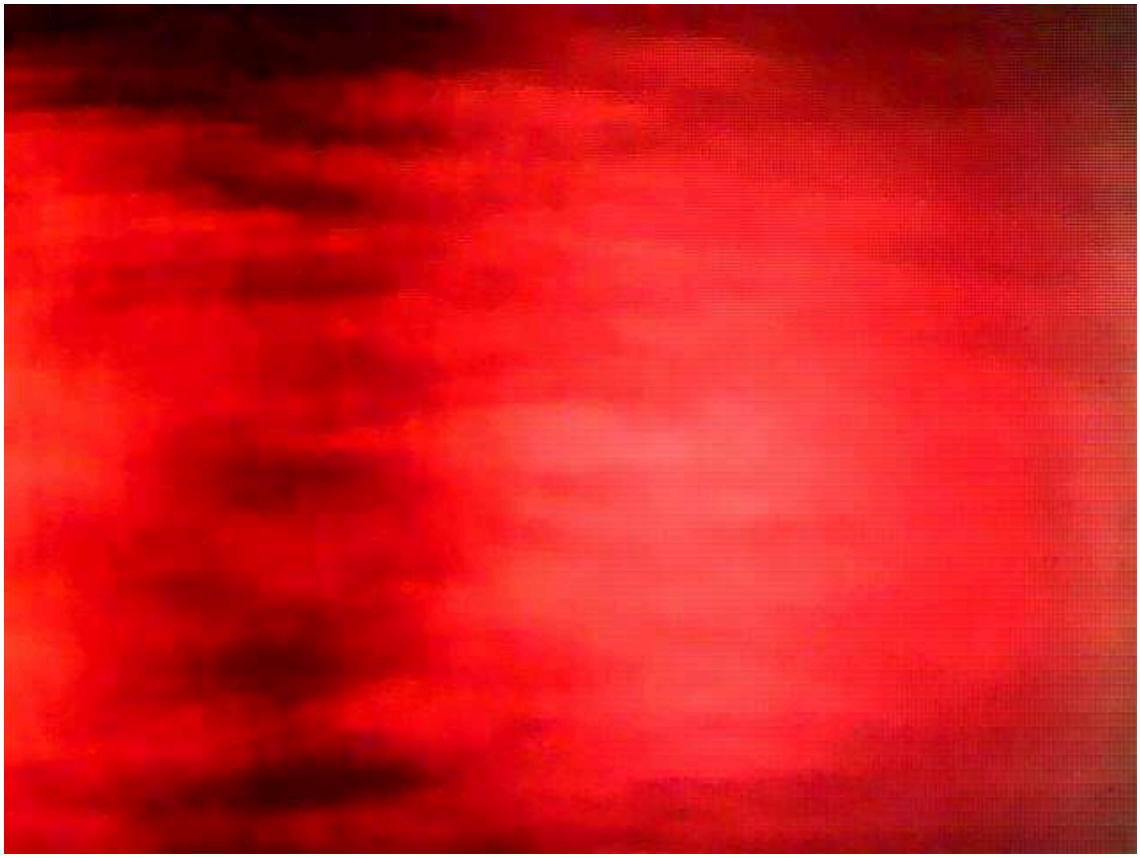

Figure 6.28: Transmitted color image from the second SPR sensor of the first laboratory implementation of the SPR WSN

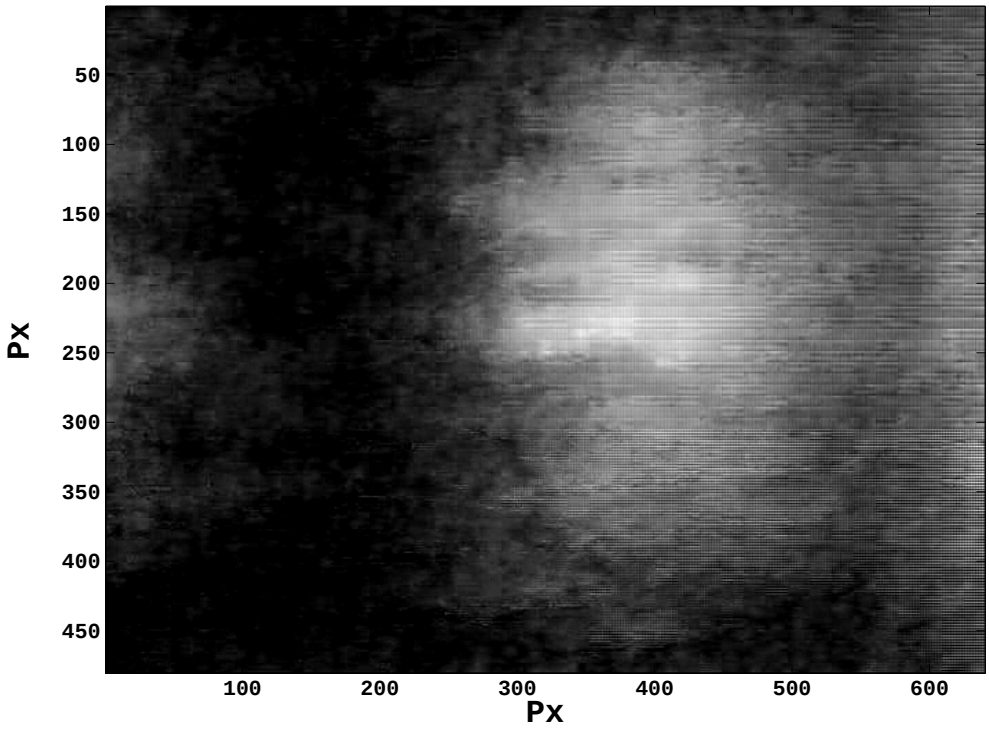

Figure 6.29: Received grayscale image from the second SPR sensor of the first laboratory implementation of the SPR WSN

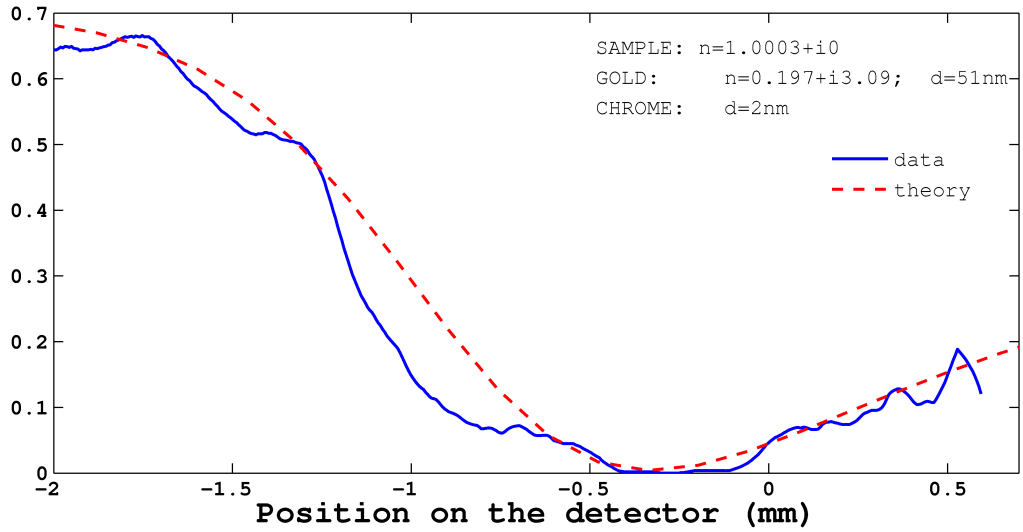

Figure 6.30: Example of fit of the first laboratory implementation of the SPR WSN second sensor node data with the theoretical values

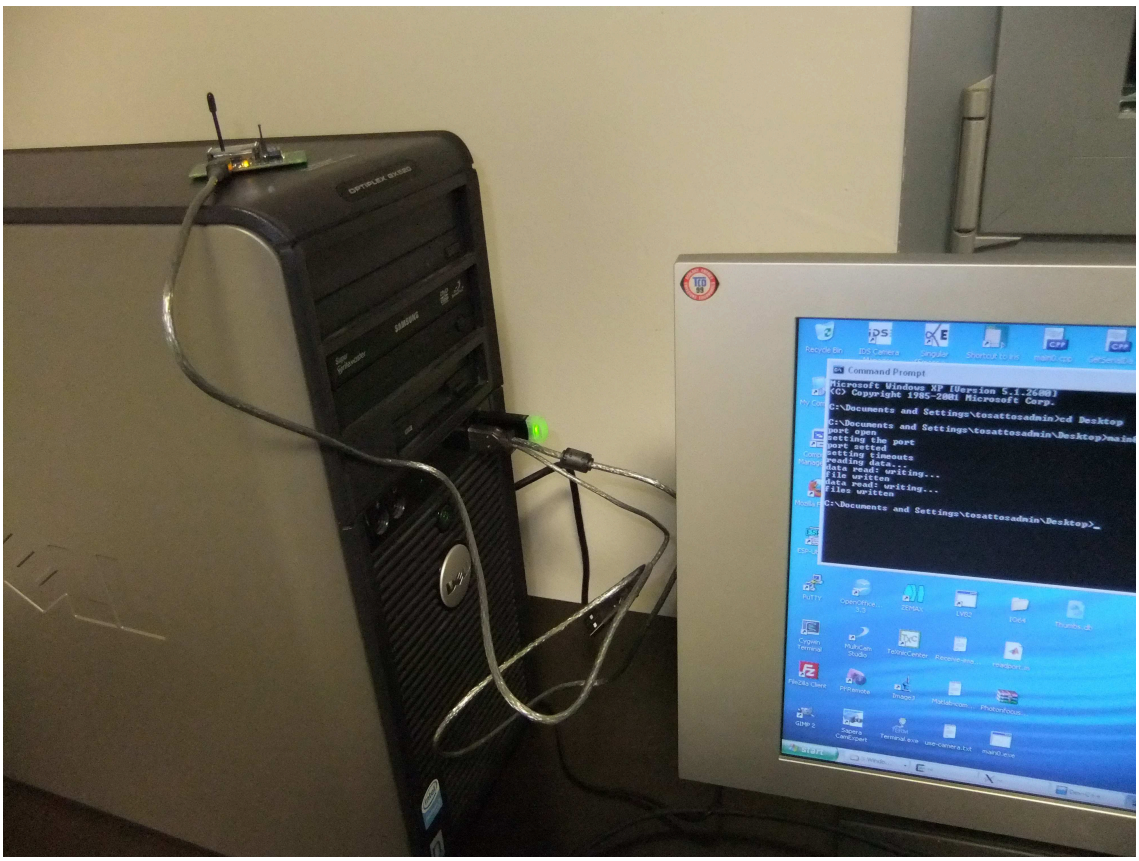

Figure 6.31: photo of the used Base Station receiving system

6.2.5 Latest implementations of a test WSN based on SPR sensors in laboratory

As a final laboratory test implementation of the test Wireless Sensor Network I created two sensor node using both the ARM microcontrollers and two different CMOS webcams.

In particular the first SPR sensor setup comprised

- ⋆ a red laser diode from Apinex.com,
- ⋆ a TM polarizer
- ⋆ a 200 μm pinhole
- ⋆ a BK7 diverging lens (focal length -150 mm)
- ⋆ two mirrors
- ⋆ a circular slit to select the central airy disk of the light beam
- ⋆ a BK7 collimating lens (focal length 125 mm)
- ⋆ an SF6 cylindrical prism with a coating of 2 nm of Chrome for adherence and 50 nm of Gold
- ⋆ a DIGITUS DA-70815 CMOS camera

and the first sensor node was formed by

1. the SPR sensor described above
2. a SX Arm Linux 1L microcontroller
3. a XBEE-WHIP-S2 ZigBee Series 2 antenna
4. An SX20 board
5. A Royaltek RGM-3600 GPS receiver (see 6.1.1)
6. a USB hub.

An image of the whole sensor mote is (6.32).

Images (6.33) and (6.34) are an example of an image transmitted from this setup and the received image respectively, while picture (6.35) is a fit of the obtained data with the theoretical values.

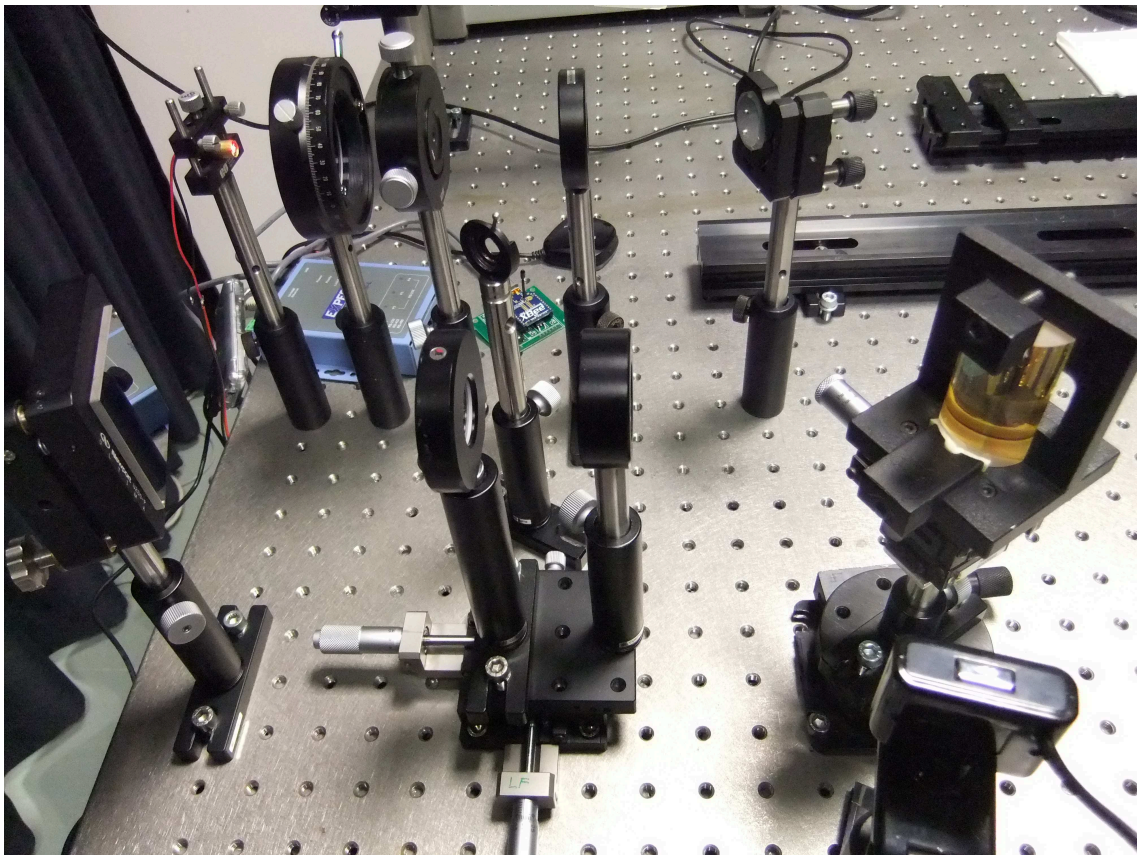

Figure 6.32: Photo of the first SPR sensor and the corresponding sensor node of the final laboratory implementation of the test SPR WSN

Figure 6.33: Transmitted image from the first SPR sensor of the last laboratory implementation of the test SPR WSN

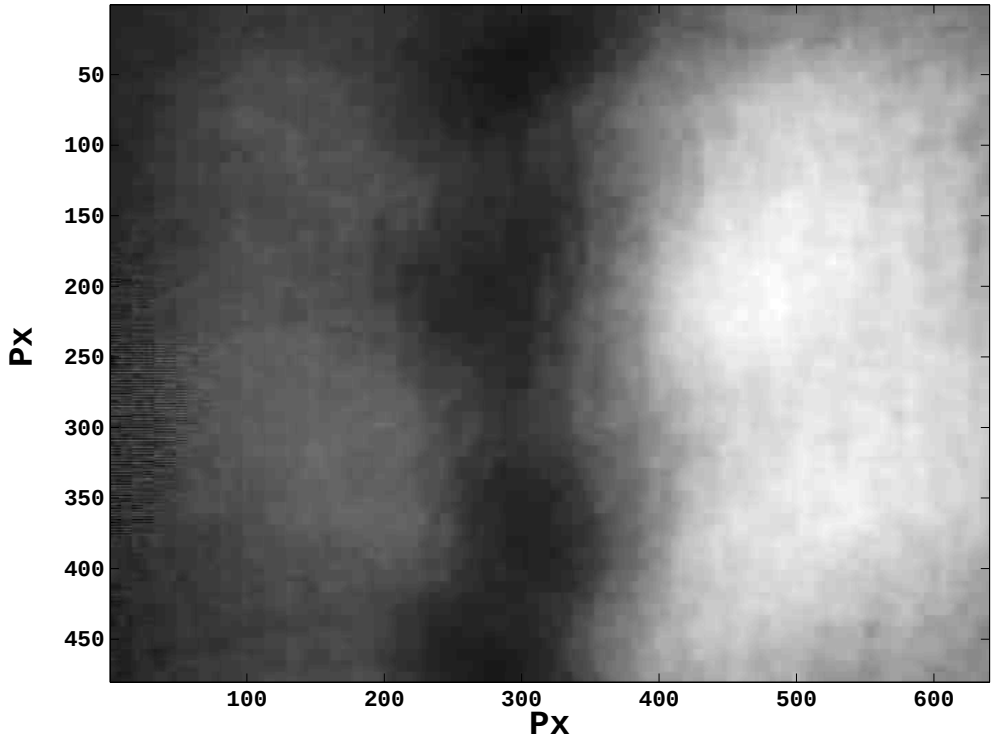

Figure 6.34: Received grayscale image from the first SPR sensor of the last laboratory implementation of the SPR WSN

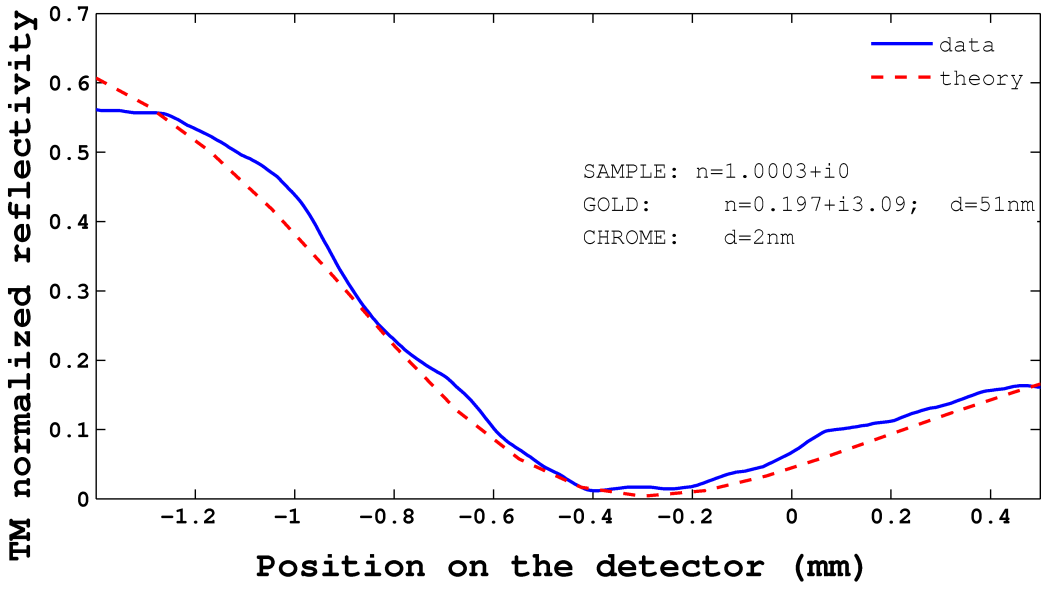

Figure 6.35: Example of the fit of the final laboratory implementation of the SPR WSN first sensor node data with the theoretical values

The second sensor node of this final setup and its SPR sensor are depicted in image (6.36).
The SPR sensor setup was formed by

- ⋆ a red laser diode from Apinex.com,
- ⋆ a TM polarizer
- ⋆ a 200 μm pinhole
- ⋆ a BK7 diverging lens (focal length -150 mm)
- ⋆ two mirrors
- ⋆ a circular slit to select the central airy disk of the light beam
- ⋆ a BK7 collimating lens (focal length 150 mm)
- ⋆ an SF6 cylindrical prism with a coating of 2 nm of Chrome for adherence and 50 nm of Gold
- ⋆ a DIGITUS DA-70815 CMOS camera

and as previously the node comprised also

1. an SX Arm Linux 1L microcontroller
2. a XBEE-WHIP-S2 ZigBee Series 2 antenna
3. An SX20 board

(6.37) is one color image transmitted by this sensor node and (6.38) is the received image, rendered in greyscale.
A fit of the sensor data with the expected values is traced in picture (6.39).

The two sensor nodes with the respective Surface Plasmon resonance sensors, along with the receiving system, are imaged together in picture (6.40).

The used Base Station receiving system is the same as in the previous configuration and it is shown in image (6.31).

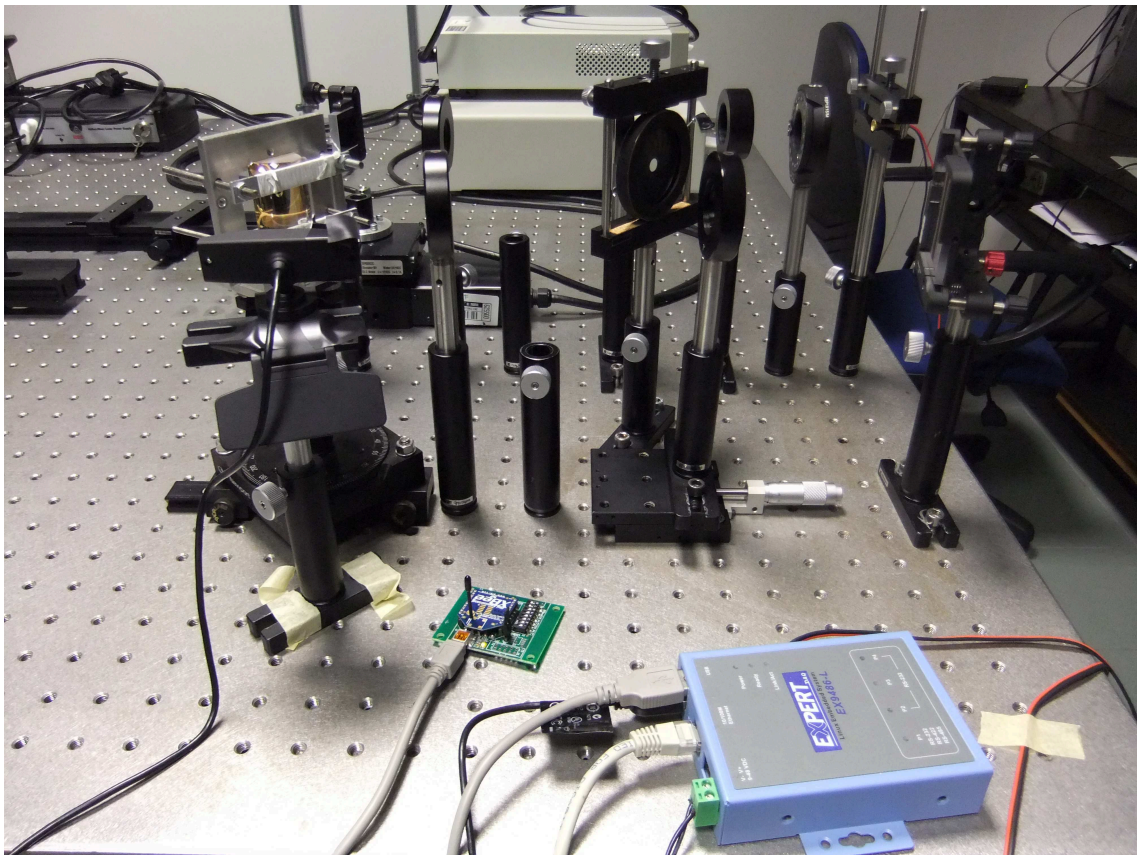

Figure 6.36: Photo of the second SPR sensor node of the final laboratory implementation of the test SPR WSN

Figure 6.37: Transmitted image from the second SPR sensor of the last laboratory implementation of the test SPR WSN

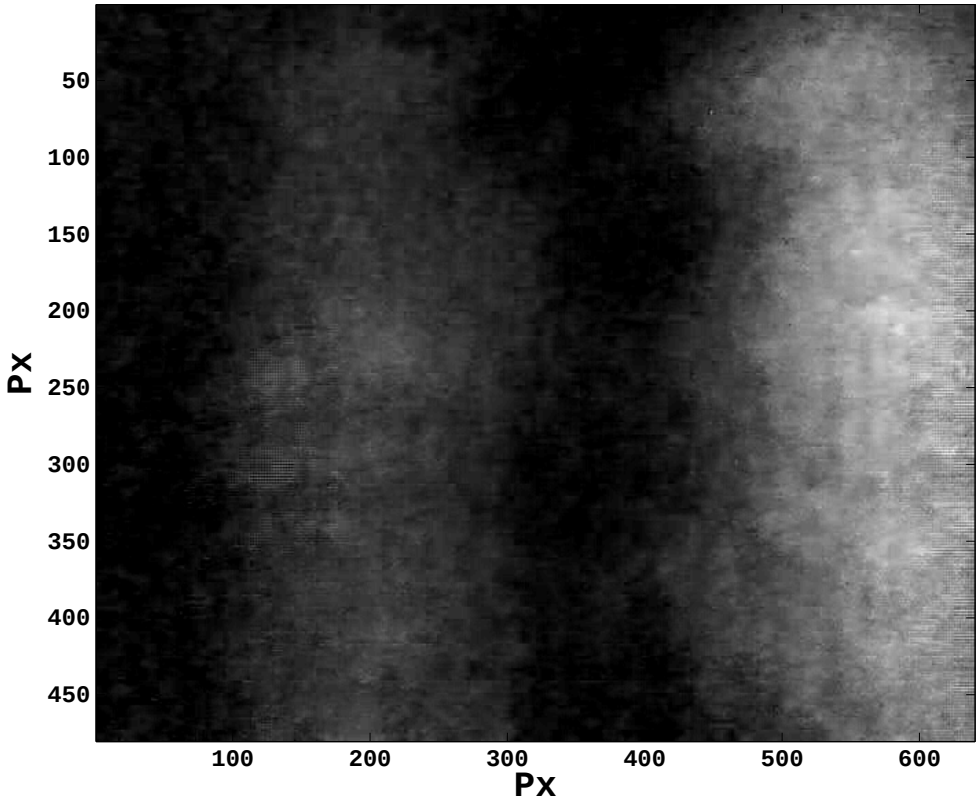

Figure 6.38: Received grayscale image from the second SPR sensor of the last laboratory implementation of the test SPR WSN

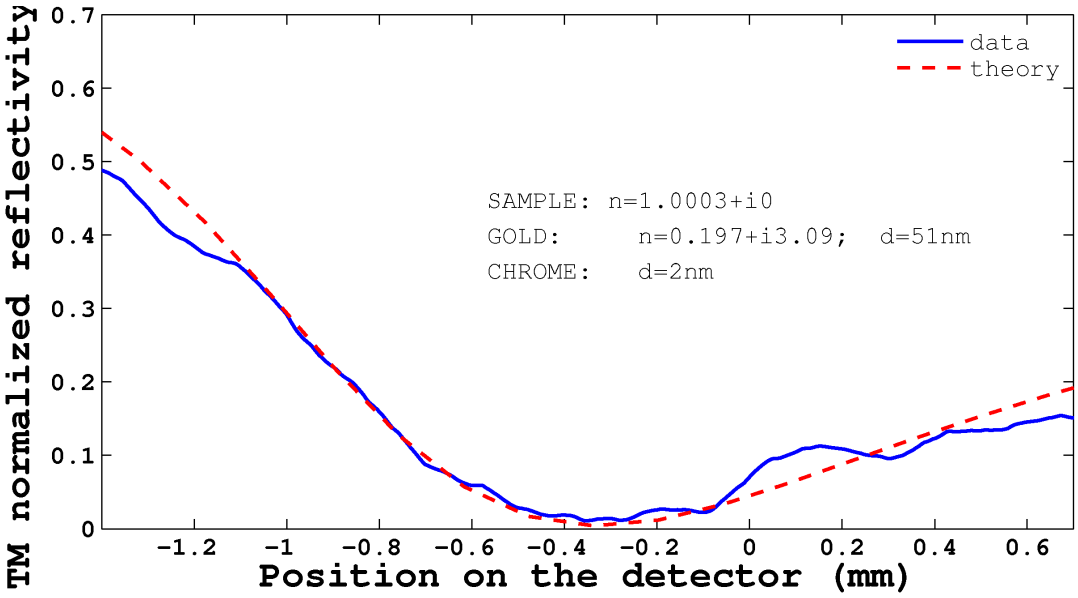

Figure 6.39: Example of fit of the last laboratory implementation of the SPR WSN second node data with the theoretical values

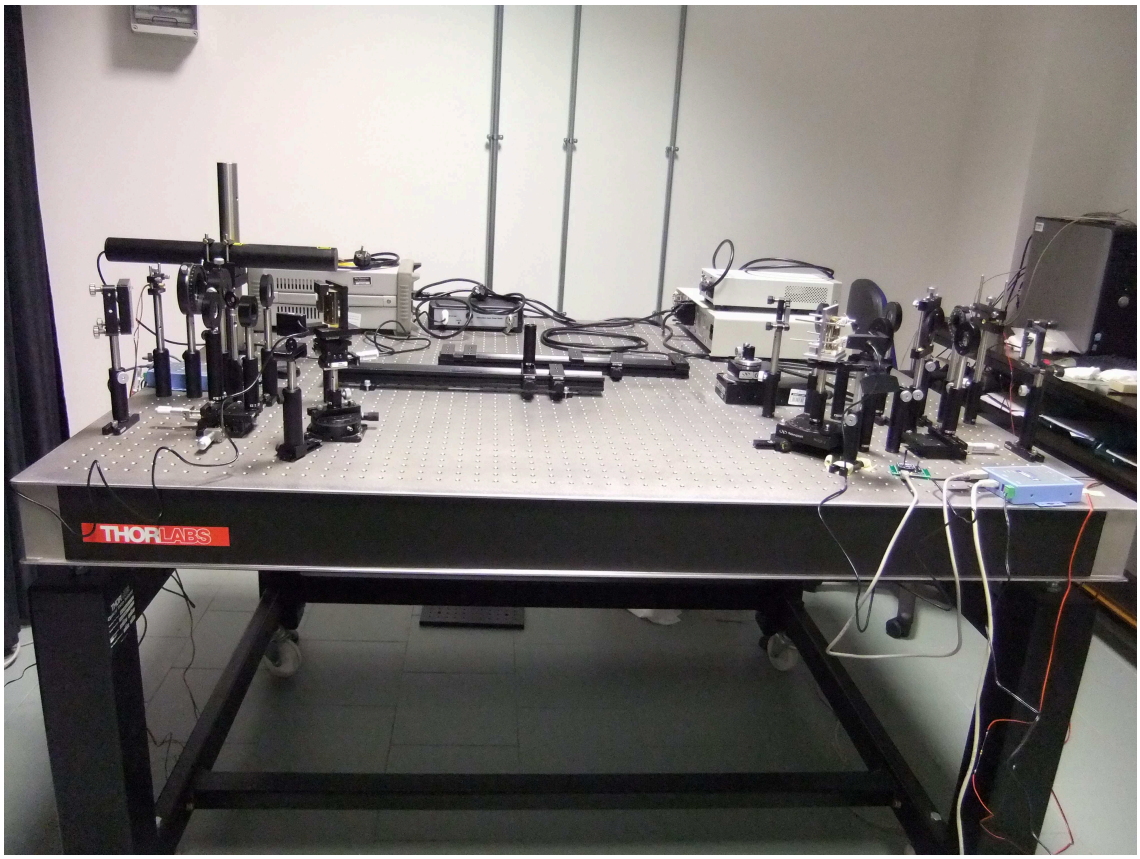

Figure 6.40: Photo of the final laboratory implementation of the test SPR WSN, showing the two sensor nodes with their Surface Plasmon based sensors, and the receiving system

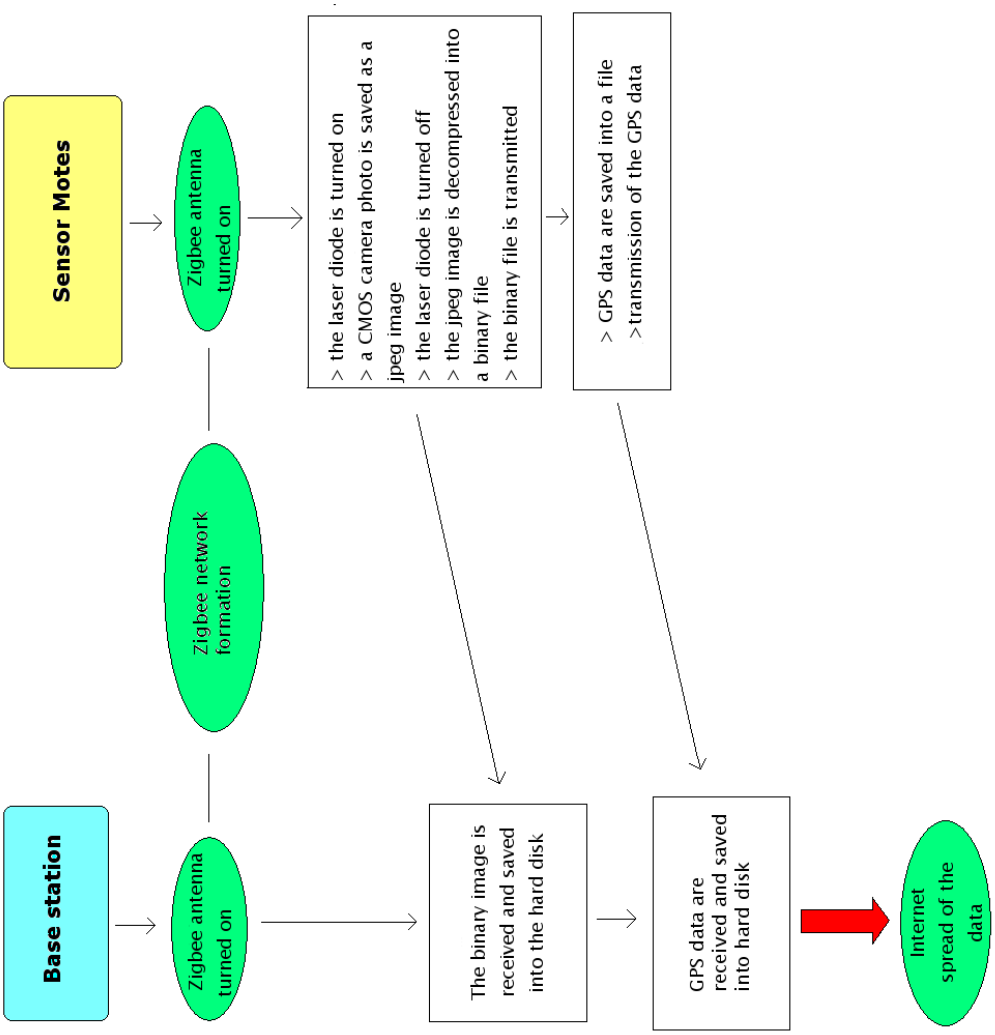

Figure 6.41: Basic idea of the main operations that must be performed in the test WSN

6.2.6 Control of the various elements of the WSN

Image (6.41) illustrates the main operations that must be performed in the test WSN for it to be operative.

I thus implemented C/C++ programs that perform the necessary operations for the SPR based WSN to operate. In particular these are:

- ⋆ control the laser diode
- ⋆ read the GPS data from the GPS receiver and save them in a file
- ⋆ take a photo from the detector and save it as a jpg image
- ⋆ decompress the jpeg image into a binary image
- ⋆ transmit the data by means of the Zigbee antennas

⋆ receive the data and save them

The books I referred to for C/C++ programming are Kernighan and Ritchie (1989), Banahan et al. (1991) and Eckel (2000). Some more specific references I used to create the reported programs are IDS-GmbH (2012), Sweet (2010),Bayer (2008),
Laska et al. (2004), Prabhakar (2009).

As a first step I configured the Zigbee antennas data settings, that is 8 bit signal, no parity and 1 bit stop, and the symbols per second transmission (baud) rate, for example 9600.
These settings chosen accordingly to MaxStream (2007) have been therefore used in every C program.

Control of the GPS receiver

The GPS receiver can be interrogated by the following C program that stores the GPS signal in a .txt file:

```
 /*  References:
 * 1)Serial Programming Guide for
 *   POSIX Operating Systems
 *   5th Edition, 6th Revision
 *   2010, Michael R. Sweet
 *   http://www.easysw.com/~mike/serial/index.html
 */
   #include <stdio.h>  /* UNIX standard input/output */
   #include <string.h>  /* String function definitions */
    #include <unistd.h>  /* UNIX standard function definitions */
    #include <fcntl.h>   /* File control definitions */
    #include <errno.h>   /* Error number definitions */
    #include <termios.h> /* POSIX terminal control definitions */
    #include <string.h>
    #include <sys/types.h>
    #include <sys/stat.h>
    #include <fcntl.h>

int readGPS(char *usbport, char *GPSfile)
{
  FILE * pFile;
   int fd; /* File descriptor for the port */
   int fd1;
   int i;

/* buffer for writing the GPS data
  char buffer[4000];

  struct termios options;
  struct termios stdio;

   close(fd); /* make sure port is closed */
   /* opens the port in readonly mode */
   fd = open(usbport,O_RDONLY);
```

```
   if (fd == -1)
      {
       /* Cannot open the port */

perror("open_port: Unable to open /dev/ttyUSB0 - ");

      }
   if (fd!= -1) {
   printf("fd is %d\n", fd);

/* sets baud rate at 4800 */
   cfsetispeed(&options, B4800);
   cfsetospeed(&options, B4800);

/* Select 8 data bits, 1 bit stop, no parity */
   options.c_cflag |= CS8;
   options.c_cflag &= ~PARENB;
   options.c_cflag &= ~CSTOPB;


   /* for raw input */

       options.c_lflag &= ~(ICANON | ECHO | ECHOE | ISIG);


      /* for  canonical input */

     /* options.c_lflag |= (ICANON | ECHO | ECHOE); */

/* set the minimum reading time */
      options.c_cc[VTIME] = 60;
      /* set the minimum data to be read */
    options.c_cc[VMIN] =480;
    /* enables the port as a receiver */
      options.c_cflag |= (CLOCAL | CREAD);


   /* writes the settings to the port */
 tcsetattr(STDOUT_FILENO,TCSANOW, &stdio);
 tcsetattr(STDOUT_FILENO, TCSAFLUSH, &stdio);


       tcsetattr(fd, TCSANOW, &options);
       fcntl(fd, F_SETFL, 0);

      printf("..reading..\n");


   ssize_t  n;
  int i=0;
```

```
/* reads the port */
   for ( i=0; i<8; i++) {
   n= read(fd, buffer, sizeof(buffer));
   /* opens the txt file for writing GPS data */
   fd1 = open(GPSfile, O_CREAT | O_WRONLY | O_APPEND, S_IRUSR | S_IWUSR);
   /* writes the GPS data into the file */
      write(fd1,buffer,n);
      /* closes the file */
     close(fd1);

   }

   /* closes the port */
   close(fd);

/* done */
    return 0;
   }
 }

/* int main ()
{
readGPS("/dev/ttyUSB0","gps.txt");
return 0;
   } */
```

The gps.txt file has a size of 1792 bytes.

The GPS receiver bit transmission rate and settings have been established accordingly to (RoyalTek (2008)) and (Betke (2001))

Control of the CMOS camera detector

The Edmund Optics USB CMOS camera can be used by a computer with Linux OS by means of this C++ program called EOcamera.cpp

```
  /*  References:
  * 1)  IDS Imaging Development Systems GmbH
  *     uEye Camera Manual, 2012,
  *     http://www.ids-imaging.de/frontend/files/uEyeManuals/
  *     Manual_eng/uEye_Manual/index.html
       */
    #include <stdio.h>
    #include <string.h>  /* String function definitions */
    #include <unistd.h>  /* UNIX standard function definitions */
    #include <fcntl.h>   /* File control definitions */
    #include <errno.h>   /* Error number definitions */
    #include <termios.h> /* POSIX terminal control definitions */
```

```
    #include <string.h>
    #include <sys/types.h>
    #include <sys/stat.h>
    #include </usr/include/uEye.h>

int takeaphoto(const IS_CHAR* savepath)
{
void * dlopen(const char * libueye_api, int flag);

/*  Opens the camera with ID 1  */

HIDS hCam = 1;
INT nRet=is_InitCamera (&hCam, NULL);
INT nNumCam;


if (nRet== IS_SUCCESS)

/* sees if there is a camera connected */
/*  At least one camera must be available */

if( is_GetNumberOfCameras ( &nNumCam ) == IS_SUCCESS)
{
 if( nNumCam >= 1 )
 {
   /* Create new camera list with suitable size */
   UEYE_CAMERA_LIST* pucl;
   pucl = (UEYE_CAMERA_LIST*) new BYTE [sizeof (DWORD)
                              + nNumCam * sizeof (UEYE_CAMERA_INFO)];
   pucl->dwCount = nNumCam;

   /* Retrieve camera info */
   if (is_GetCameraList(pucl) == IS_SUCCESS)
   {
     int iCamera;
     for (iCamera = 0; iCamera < (int)pucl->dwCount; iCamera++)
     {
       //Test output of camera info on the screen
       printf("Camera %i Id: %d", iCamera,
       pucl->uci[iCamera].dwCameraID);
      // delete [] pucl;
     }
   }
 }

}


INT Mode_c;
INT Mode;
```

```
 Mode_c=IS_CM_MONO8 ;      /* for grayscale */
/* Mode_c=IS_CM_SENSOR_RAW8; */ /* for raw data  */
/* sets the way in which images will be displayed */
is_SetColorMode(hCam, Mode_c);

/*  Bitmap mode (images are digitized and stored in system memory): */
Mode=IS_SET_DM_DIB;
is_SetDisplayMode (hCam, Mode);


/*  Enable trigger mode, set high-active flash mode
    and capture an image: */
is_SetExternalTrigger(hCam, IS_SET_TRIGGER_SOFTWARE);

/* Set the flash to a high active pulse for each image
in the trigger mode */
/* UINT nMode = IO_FLASH_MODE_TRIGGER_HI_ACTIVE;
is_IO(hCam, IS_IO_CMD_FLASH_SET_MODE, (void*)&nMode, sizeof(nMode)); */

 const int width = 752;
const int height = 480;
INT pid;
/* Variables used by IDS API for storing the process iD
 * and the address of the image in memory
 */
char* ppcImgMem;
/* Allocates image memory */
  is_AllocImageMem(hCam, width, height, 8, &ppcImgMem, &pid);
 /* Set the allocated image memory to active */
is_SetImageMem(hCam, ppcImgMem, pid);
 UINT nPar = 0;

/* reads the exposure time and print it */
INT nRet1 = is_Exposure(hCam, IS_EXPOSURE_CMD_GET_EXPOSURE,

(void*)&nPar, sizeof(nPar));
printf("Camera exposure: %d", nRet1);

/* takes a photo */
is_FreezeVideo(hCam, IS_WAIT);

/* Saves the image to disk as jpg with quality 75% */
is_SaveImageEx(hCam, savepath, IS_IMG_JPG, 75);

/* closes the camera */
 is_ExitCamera (hCam);

}
```

```
/*
int main ()
{
takeaphoto("/home/luxor/A.jpg");
return 0;
}
*/
```

Jpg image decompression into a binary file

To read a jpeg image and store the pixel values as a matrix of binary numbers the following C program jpegtobin.c can be used

```
 /*  References:
 * 1) USING THE IJG JPEG LIBRARY
 *    1994-2011, Thomas G. Lane, Guido Vollbeding.
 *    Part of the Independent JPEG Group's software.
  * 2)inspiration also from jpeg2bmp.c by Arun Prabhakar,
      http://digitalpbk.blogspot.it/  */

#include <stdio.h>
#include <jpeglib.h>
#include <stdlib.h>
#include <string.h>

/*  uninitialized pointer used to store the uncompressed image */
unsigned char *binary_image = NULL;

/* dimensions of the image we want to write */
int width;
int height;
int bytes_per_pixel;

/*
 * Reads from a jpeg file  and saves it into the
 * raw_image buffer in an uncompressed format.
 */

int read_jpeg_file( char *filename )
{
 /* standard libjpeg structures for decompression */
 struct jpeg_decompress_struct cinfo;
 struct jpeg_error_mgr jerr;
 /* libjpeg data structure for storing one row of an image */
 JSAMPROW bufferOfTheLine[1];

 FILE *infile = fopen( filename, "rb" );
```

```
 unsigned long px = 0;
 int i = 0;

if ((infile = fopen(filename, "rb")) == NULL) {
    fprintf(stderr, "can't open %s\n", filename);
    exit(1);
}

/* if ( !infile )
 {
  printf("Error opening jpeg file %s\n!", filename );
  return -1;
 } */
 /* standard libjpeg error handler */
 cinfo.err = jpeg_std_error( &jerr );
 /* setup decompression process, reads JPEG header */
 jpeg_create_decompress( &cinfo );
 /* the libjpeg library invokes the standard source module */
 jpeg_stdio_src( &cinfo, infile );
 /* reads the image header which contains the image informations */
 jpeg_read_header( &cinfo, TRUE );


 printf( "JPEG File Information: \n" );
 printf( "Image width and height: %d pixels and %d pixels.\n",
 width=cinfo.image_width, height=cinfo.image_height );
 printf( "Color components: %d.\n", bytes_per_pixel =
   cinfo.num_components );
 printf( "Color space: %d.\n", cinfo.jpeg_color_space );

 /* Starts jpeg decompression  */
 jpeg_start_decompress( &cinfo );

 /* allocates memory to hold the uncompressed image */
 binary_image = (unsigned char*)malloc(
  cinfo.output_width*cinfo.output_height*
   cinfo.num_components );
 /* reads the jpeg and writes it into the raw buffer */
/* allocates memory to hold the line buffer */
 bufferOfTheLine[0] = (unsigned char *)malloc( cinfo.output_width*
 cinfo.num_components );
 /* read one  line at a time */
 while( cinfo.output_scanline < cinfo.image_height )
 {
  jpeg_read_scanlines( &cinfo, bufferOfTheLine, 1 );
  for( i=0; i<cinfo.image_width*cinfo.num_components;i++)
   binary_image[px++] = bufferOfTheLine[0][i];
 }
 /* ends decompression, destroys objects and closes open files */
 jpeg_finish_decompress( &cinfo );
```

```
 jpeg_destroy_decompress( &cinfo );
 free( bufferOfTheLine[0] );
 fclose( infile );
  return 1;
}


int write_bin_file( char *filename )
{

 /* number of bytes per line  */
 int LineBytes;
 LineBytes = width * 1;
 /*  LineBytes = width * 1 for 8 bit gray images,
  or width * 3 for 24 bit RGB images) */

/* output binary file */
 FILE * outputfile;

 printf("Bytes per line of the output binary file : %d\n", LineBytes);

/* opens output file */
 outputfile = fopen(filename, "wb");

 /* error opening the output file */
 if (outputfile == NULL)
    {
    printf("Error opening output file\n");
        exit (1);
    }

/* buffer of the jpeg image line scanning */
  char *bufferLine;

 bufferLine = (char *) calloc(1, LineBytes);
     /* error in the memory allocation */
 if (bufferLine == NULL)
    {
     printf ("Error allocating memory\n");
    free(binary_image);
     exit (1);
    }
 int line,i;

 for (line = height-1; line >= 0; line --)
 /* for (line >= 0; line = height-1;  line ++) */
    {
/* fills the buffer bufferOfTheLine with the corresponding

line image data  */
```

```
  for( i =0 ; i < width; i++ )
  {
   /* for monochromatic grey images
   */

 *(bufferLine+i*bytes_per_pixel) =
 *(binary_image+(i+line*width)*bytes_per_pixel+0);

/* for  RGB  images */

/*  *(bufferLine+i*bytes_per_pixel) =
 *(binary_image+(i+line*width)*bytes_per_pixel+2);
*(bufferLine+i*bytes_per_pixel+1) =
 *(binary_image+(i+line*width)*bytes_per_pixel+1);
*(bufferLine+i*bytes_per_pixel+2) =
 *(binary_image+(i+line*width)*bytes_per_pixel+0);*/
  }

  fwrite(bufferLine, 1, LineBytes, outputfile);
    }
 free(bufferLine);
 fclose(outputfile);
}

/*int main(int argc,char **argv)
{ */

 /* Opens a jpeg image */
/* if( read_jpeg_file( argv[1] ) > 0 ) write_bin_file( argv[2] );

 else return -1;

 free(binary_image);
 return 0;
} */

/* int main()
{
   char *infile= "A.jpg";
   char *outfile= "A.bin";

  if (read_jpeg_file(infile) >0 ) write_bin_file(outfile);

 else return -1;

 free(binary_image);
 return 0;
} */
```

Data transmission

Then the data can be sent to the Zigbee antenna connected trough the X20 board by means of the following writetoportv2.c program

```
 /*  References:
 * 1)Serial Programming Guide for
 *   POSIX Operating Systems
 *   5th Edition, 6th Revision
 *   2010, Michael R. Sweet
 *   http://www.easysw.com/~mike/serial/index.html
 */

#include <string.h>
#include <stdlib.h>
#include <stdio.h>
#include <unistd.h>
#include <fcntl.h>
#include <termios.h>
#include <string.h>
#include <time.h>

/* int main ()
 {
sendtoport("/dev/ttyUSB0","A.jpg" );
return 0;
  } */

int sendtoport(char *portname,char *binfile )
 {

/* port descriptor */
 int fd;

/* data file descriptor */
FILE *fl;

/* file length */
unsigned long fileLen;

 struct termios optio;
 struct termios stdio;

/*
 * opens the port
 */

    fd_set rdset;

    /* opens the USB port */
```

```
    fd = open(portname, O_RDWR | O_NOCTTY | O_NDELAY);

     /* error in opening the port */
     if (fd == -1)
      {
       /* Could not open the port */
perror("open_port: Unable to open /dev/ttyUSB0 - ");
return -1;
      }
/*
 * sets the port
 */
    memset(&stdio,0,sizeof(stdio));
    stdio.c_iflag=0;
    stdio.c_oflag=0;
    stdio.c_cflag=0;
    stdio.c_lflag=0;
    stdio.c_cc[VMIN]=1;
    stdio.c_cc[VTIME]=200000;
    tcsetattr(STDOUT_FILENO,TCSANOW,&stdio);
    fcntl(STDIN_FILENO, F_SETFL, O_NONBLOCK);
    /* makes the reads non-blocking */

    memset(&optio,0,sizeof(optio));
    optio.c_iflag=0;
    optio.c_oflag=0;
       // 8n1
       /* Selects 8 data bits */
      optio.c_cflag |= CS8;
      /* no parity*/
      optio.c_cflag &= ~PARENB;
      /* 1 bit stop*/
      optio.c_cflag &= ~CSTOPB;
     /* Enables the receiver and sets local mode */
    /* optio.c_cflag |= (CLOCAL | CREAD); */
    optio.c_lflag=0;
    /*minimum bit amount to read */
    optio.c_cc[VMIN]=1;
    /* minimum read time */
    optio.c_cc[VTIME]=200000;

     /* sets 9600 baud rate */
    cfsetospeed(&optio,B9600);
    cfsetispeed(&optio,B9600);
      /* Set the new options for the port */
    tcsetattr(fd,TCSANOW,&optio);

/*
 * opens the file to read
 */
```

```
fl = fopen(binfile, "rb");
  printf("fl is %s\n", fl );

  /* error handling */
  /*    if (!fl ) {
    perror("Can't open file ");
    return -1;
     }
  */

 /*Gets the file length */
fseek(fl, 0, SEEK_END);
fileLen=ftell(fl);
fseek(fl, 0, SEEK_SET);

/* allocates the data buffer */
unsigned char buffer[(fileLen)+1];

/* error handling */
/* if (!buffer)
{
fprintf(stderr, "Memory error!");
        fclose(fl);
exit(1);
}*/

printf("FileLen %li\n", fileLen  );

 /*
  * Sends the file contents to the port
  */

/* introduces a sleeping time between data packets if needed */
struct timespec tim, tim2;
/* seconds */
tim.tv_sec  = 0;
/* nanoseconds */
tim.tv_nsec = 50000000L;

/* divides the data into packets of packbytes bytes each */
int packbytes=10;
/* number of packets to send */
int npack=fileLen/packbytes;
 char pacchetto[packbytes] ;

 int x;
 int y;
 int Step;
 x = 0;
```

```
 y=0;

int data;
data=0;

/* ideally sent data */
int writtenbytes;
writtenbytes=0;

/* number of bytes to send */
int bytestosend;
bytestosend=fileLen;

/* reads the file */

 numbytes = fread (buffer, 1, fileLen, fl) ;
 /* return the number of bytes read */
printf("numbytes is %d\n", numbytes );

/* divides data into packets */
 while ( numbytes >0 ) {
while ( y < npack) {

 Step = packbytes*y;

  for ( x = 0; x < packbytes; x++ ) {

 pacchetto[x]=((unsigned char *)buffer)[Step+x];
 data++;
   }

 y++;

/* writes the data packets into the port */
  write(fd,pacchetto,packbytes);


writtenbytes +=packbytes;
bytestosend -= packbytes;

/* invokes the sleeping time if needed */
  if(nanosleep(&tim , &tim2) < 0 )
   {
      printf("Nano sleep system call failed \n");
      return -1;
   }

 /*  printf("Nano sleep successfull \n"); */
 }
printf("sent byte  are %d\n",data  );
```

```
/* finishes the reading and writing */
return 0;
  }

/* closes the file */
  fclose(fl);
/* closes the port */
  close(fd);
/* finished */
return 1;

 }
```

Diode laser control

The diode lasers can be controlled and alimented by means of the SX Arm Linux 1L board GPIOs. In particular the ARM microcontroller pin 1 is set as an output and its upper and lower states turn the laser on and off respectively.

Therefore the diode laser module can be turned on with the following program

```
#include <stdio.h>
#include <sys/types.h>
#include <sys/stat.h>
#include <fcntl.h>
#include <ex9486.h>

int diodeon(void)
{
int gpio, dip_sw, i;
int fd = open("/dev/gpio",O_RDWR);

/*gets count of GPIO*/
/* if(ioctl(fd, GPIO_IOCTL_COUNT, &gpio) == 0)
printf("GPIO count:%d\n",gpio); */
/* gets count of DIPSW */
/* if(ioctl(fd, GPIO_IOCTL_DIPSW, &dip_sw) == 0)
printf("DIP_SW count:%d\n",dip_sw); */
 /* shows status of GPIO and DIPSW */
 /* for(i=0; i<(gpio+dip_sw); i++){
printf("GPIO%d->%d\n", i,ioctl(fd, GPIO_IOCTL_GET, &i));
} */

// set pin 1 to output
int pin;
pin=1;
ioctl(fd, GPIO_IOCTL_OUTPUT, &pin);

// sets Pin 1 to High state.
ioctl(fd, GPIO_IOCTL_SET, &pin);
```

```
printf("GPIO%d->%d\n", pin,ioctl(fd, GPIO_IOCTL_GET, &pin));
  close(fd);
return 0;
}

/* int main(void)
{
diodeon();
return 0;
} */
```

and turned off with the following

```
#include <stdio.h>
#include <sys/types.h>
#include <sys/stat.h>
#include <fcntl.h>
#include <ex9486.h>

int diodeoff(void)
{
int gpio, dip_sw, i;
int fd = open("/dev/gpio",O_RDWR);

// sets pin 1 as an output
int pin;
pin=1;
ioctl(fd, GPIO_IOCTL_OUTPUT, &pin);

// sets Pin 1 to Low state.
ioctl(fd, GPIO_IOCTL_CLEAR, &pin);
printf("GPIO%d->%d\n", pin,ioctl(fd, GPIO_IOCTL_GET, &pin));
close(fd);
return 0;
}

/* int main(void)
{
diodeoff();
return 0;
}
*/
```

Overall main sensor node programs

When the Linux PC is used as a controller and the EO camera as a detector the overall program that accomplish all the needed operations is the following SPR-WSN-test.cpp program, which has been compiled with the Linux command

```
sudo g++  -o SPR-WSN-test.exe  SPR-WSN-test.cpp -I/usr/include
 -I/usr/lib/ -lueye_api -I/usr/bin -ljpeg -I/home/luxor/SPRWSNproject.

#include <stdio.h>
#include <jpeglib.h>
#include <stdlib.h>
#include <string.h>
#include <unistd.h>
#include <fcntl.h>
#include <errno.h>
#include <termios.h>
#include <string.h>
#include <sys/types.h>
#include <sys/stat.h>
#include </usr/include/uEye.h>

/* project files */

 #include <EOcamerav2.cpp>
 #include <readGPS.c>
 #include <jpegtobinv2.c>
 #include <writetoportv2.c>

int main ()
{

/* jpg photo */
 char *infile= "A.jpg";
/* binary file of the photo */
 char *outfile= "A.bin";

/*
 * takes a photo with the EO CMOS camera
 * and saves it as a jpg image
 */
takeaphoto("/home/luxor/SPRWSNproject/A.jpg");

  /* opens the jpg image and decompress it, then
  writes its data into a binary file */

   if (read_jpeg_file(infile) >0 ){ write_bin_file(outfile);}
  else { return -1;}

/* releases the memory of the temporary buffer image */
 free(binary_image);

/* sends the binary image to the port */
int go;
go=sendtoport("/dev/ttyUSB0",outfile );
```

```
/* reads GPS data and writes them into a file */
char *GPSfile="gps.txt";
readGPS("/dev/ttyUSB1",GPSfile);

/* sends the GPS file to the port */
int go2;
go2=sendtoport("/dev/ttyUSB0",GPSfile );

/* finished */
return 0;
}
```

The ARM Linux controller must instead be set up with the following program

```
  #include <stdio.h>
     #include <jpeglib.h>
     #include <stdlib.h>
     #include <string.h>
    #include <unistd.h>
    #include <fcntl.h>
    #include <errno.h>
    #include <termios.h>
    #include <string.h>
    #include <sys/types.h>
    #include <sys/stat.h>
    #include <sys/mount.h>
int setARM()
{

/* the SD card is mounted into /mnt/mmc */

        int ret;
ret = mount("/dev/mmc0", "/mnt/mmc", "vfat", MS_SYNCHRONOUS, NULL);
if (ret == -1) {
printf("no device found\r\n");
return;
} else {
printf("found /dev/mmc0\r\n");
}

/* sets the libjpeg by linking it to the appropriate folder */

system("ln -s /mnt/disk/video/mjpg_streamer/libjpeg.so.62

/lib/libjpeg.so.8");

/* enables the UVC drivers if a webcam if used */

system("insmod /mnt/disk/video/driver/v4l1-compat.ko ");
```

```
system("insmod /mnt/disk/video/driver/videodev.ko ");
system("insmod /mnt/disk/video/driver/v4l2-common.ko ");
system("insmod /mnt/disk/video/driver/uvcvideo.ko ");

return 0;
}



int main ()
{
setARM();
return 0;
}
```

and the main program for the ARM board was compiled with the command

```
arm-linux-gcc  -o SPR-WSN-arm.exe SPR-WSN-arm.c  -I/usr/local/arm-linux
 -I/home/luxor/SPRWSNproject/ -L/usr/crosscomp/lib/ -ljpeg
```

If a Webcam is made use of as a detector, the CaptureFrame program provided by Area SX s.r.l. can be used in order to acquire the jpeg images.

The main program to use the SX Arm Linux 1L as a node controller is thus

```
#include <stdio.h>
     #include <jpeglib.h>
     #include <stdlib.h>
     #include <string.h>
    #include <unistd.h>
    #include <fcntl.h>
    #include <errno.h>
    #include <termios.h>
    #include <string.h>
    #include <sys/types.h>
    #include <sys/stat.h>


/* project files */

  #include <readGPS.c>
   #include <jpegtobinv2.c>
   #include <writetoportv2.c>
  #include <gpio-open.c>
  #include <gpio-close.c>
   #include <ex9486.h>

int main ()
{
```

```
 char *infile= "/mnt/mmc/a.jpg";
 char *outfile= "/mnt/mmc/A.bin";

/*
 * turns the diode laser on
 */

 diodeon();

/*
 *  takes a photo and saves it as a jpg image
 */

 system("./CaptureFrame -D /dev/video0 -O /mnt/mmc/a.jpg ");

/*
 *  turns  the diode laser off
 */

  diodeoff();

/*
 *  decompresses the jpg image into a binary file
 */

   if (read_jpeg_file(infile) >0 ){ write_bin_file(outfile);}

 else { return -1;}

 free(binary_image);

/*
 *  transmits the binary file to the antenna
 */
int go;
go=sendtoport("/dev/ttyUSB0",outfile );

/*
 *  reads GPS data
 */
char *GPSfile="/mnt/mmc/gps.txt";
readGPS("/dev/ttyUSB1",GPSfile);

/*
 *  transmits the GPS data to the antenna
 */

int go2;
go2=sendtoport("/dev/ttyUSB0",GPSfile );
```

```
/*
 * releases some memory space deleting sent files
 */

/* system("rm /mnt/mmc/A.jpg");
 system("rm /mnt/mmc/A.bin");
 system("rm /mnt/mmc/gps.txt"); */

return 0;
}
```

Regarding the usage of this programs, when the sensor node is assembled the Zigbee antenna should be first connected, so that it is associated with "/dev/ttyUSB0", and only after the camera and the GPS receiver should be plugged in,in order for the latter to be handled as "/dev/ttyUSB1". Otherwise the program should be accordingly modified.

Data reception

The binary image data and the GPS data can be received and saved form a computer with Windows operative system by means of the following c program.
The first time this program is used it is important to check that the correct COM port and settings are used, for example by means of the XCTU program.

```
#include <cstdlib>
#include <iostream>
#include <windows.h>
using namespace std;

int main(int argc, char *argv[])
{

 /*
  * 1) opens the COM port
  */

   HANDLE hCom;
   // create the COM port
hCom = CreateFile("COM06:",
GENERIC_READ | GENERIC_WRITE,
0, // exclusive access
NULL, // no security attributes
OPEN_EXISTING, //only existing ports
FILE_ATTRIBUTE_NORMAL,
0);
if(hCom==INVALID_HANDLE_VALUE){
if(GetLastError()==ERROR_FILE_NOT_FOUND){
printf(" error: choose another COM port\n");

}
```

```
printf(" error opening the port\n" );
}
printf("port open\n");

/* 2)
 * sets the port
 */

printf("setting the port \n");
DCB dcbSerialParams = {0};
dcbSerialParams.DCBlength=sizeof(dcbSerialParams);
if (!GetCommState(hCom, &dcbSerialParams)) {
    fprintf(stderr, "failed reading the port settings\n");
    exit(EXIT_FAILURE);
}
// sets 9600 baud
dcbSerialParams.BaudRate=CBR_9600;
// sets 8n1 signal
dcbSerialParams.ByteSize=8;
dcbSerialParams.StopBits=ONESTOPBIT;
dcbSerialParams.Parity=NOPARITY;
if(!SetCommState(hCom, &dcbSerialParams)){
  fprintf(stderr, "error in setting the port \n");
  exit(EXIT_FAILURE);
}
printf("port setted \n");
printf("setting timeouts \n");
// setting timeuts
COMMTIMEOUTS timeouts={0};
timeouts.ReadIntervalTimeout=50000;
timeouts.ReadTotalTimeoutConstant=50000;
timeouts.ReadTotalTimeoutMultiplier=10000;


/* 3)
 * receives and saves binary image data
 */

// n= data bytes=pixels*(pixel color components)

 // with EO CMOS camera, 752*480 px
 // int n=360960;

 //with a camera with 640*480 RGB pixels
int n=921600;

// 3a) allocates data buffer
unsigned char Buff[n + 1];
 // initializing the buffer to 0
 int i;
```

```
 for (i = 0; i < n+1; i++) {
Buff[i] = 0;
}

// 3b) receive image data
DWORD dwBytesRead = 0;
DWORD dwWritten = 0;
ReadFile(hCom, Buff, n, &dwBytesRead, NULL);

/* if(!ReadFile(hCom, Buff, n, &dwBytesRead, NULL)){
printf(" error in data receiving \n");
} */
printf("data read: writing... \n");

 // 3c) writes image data into "C:\\filedaimagejpg.bin"

HANDLE hfile = CreateFile("C:\\filedaimagejpg.bin",
GENERIC_WRITE | GENERIC_READ,
FILE_SHARE_READ, // share for reading
NULL, // no security
CREATE_ALWAYS, // always create the file
FILE_ATTRIBUTE_NORMAL, // normal file
NULL);
   if(hfile == NULL)
   {
     printf("Error opening the file for writing. ");
   }

  WriteFile(hfile, Buff, n, &dwWritten, NULL);

 printf("file written \n");
 CloseHandle(hfile);


 /*
 * 4) receives and saves the GPS data
 */

 // p= GPS data bytes
    int p=1792;
// 4a) allocates data buffer
   unsigned char Buff1[p + 1];
 // initialising the buffer to 0
 int j;
 for (j = 0; j < p+1; j++) {
Buff1[j] = 0;
}

/* 4b) Receives GPS data */
```

```
DWORD dwBytesReadGPS = 0;
DWORD dwWrittenGPS = 0;
ReadFile(hCom, Buff1, p, &dwBytesReadGPS, NULL);

printf("data read: writing... \n");

 /* 4c)writes GPS data into file "C:\\gps.txt" */


HANDLE hfileGPS = CreateFile("C:\\gps.txt",
GENERIC_WRITE | GENERIC_READ,
FILE_SHARE_READ, // share for reading
NULL, // no security
CREATE_ALWAYS, // always create the file
FILE_ATTRIBUTE_NORMAL, // normal file
NULL);
   if(hfileGPS == NULL)
   {
     printf("Error opening the GPS file for writing. ");
   }

  WriteFile(hfileGPS, Buff1, p, &dwWrittenGPS, NULL);


 printf("files written \n");

  CloseHandle(hfileGPS);

 /*
  * 5) closes COM port
  */

    CloseHandle(hCom);

    return EXIT_SUCCESS;

}
```

In a sensor network the procedures 4) and 5) must be repeated for every sensor node and GPS receiver in use, and in addition to that every node could also send to the base station computer its identity, for example by means of its own 64-bit Address.

After that the image or images can be handled with Matlab.

In the case of the Edmund Optics CMOS camera the commands below should be used,

```
% reads the image data
A=fopen('B.bin');
% saves the image data into the B matrix
% The dimensions of B are the image pixel number
% in width and height
[B,count]=fread(A,[752,480]);
```

```
% displays the image
image(B);
% then handle it ....
```

while if only the red pixels from a 640 X 480 RGB image should be made use of, as for the chosen CMOS webcam, they can be selected from the original sent image data by means of the following commands

```
% reads the image data
A=fopen('filedaimagejpg.bin');
% saves the image data into the B matrix
% The dimensions of B are the image pixel number
% in width and height
 [B,count]=fread(A,[1920,480]);

 % selects the red pixels
 % and write them into the C matrix

  C=zeros(640,480);
C(1:640, 1:480)=B(3:3:end, 1:1:480);

% displays the image
image(C)
% then handle it ....
```

This was the used procedure for the test implementation of the sensor network in labotatory, however it is possible to directly receive the data in Matlab by means of the GetSerialData.cpp and StdAfx.h files and the procedure from Laska et al. (2004).
In particular the corresponding Matlab commands are:

```
% compiles the GetSerialData.cpp program so to use it in Matlab
mex GetSerialData.cpp

% y is the received data vector.
% GetSerialData parameters: COM port to use, bit transmission rate
% and number of bytes of the data respectively
y = GetSerialData('com6', 9600, 360960)
% then handle it ....
```

This procedure is very useful as otherwise Matlab isn't always able to correctly handle the COM ports.

6.3 Conclusions

I demonstrated the feasibility of a Wireless Sensor Network based on SPR sensors and with broadband internet connection, and I succeeded in implementing two setups of a test Wireless Sensor Network based on Surface Plasmon Resonance Sensors.

However its physical implementation offered some challenges.

In particular the most difficult aspect was the control of the detectors by means of a microcontroller.

Adapting some camera drivers so that they could be used with the SX Arm Linux 1L microcontroller has proven to be difficult and some of the tested web cameras weren't compatible with the board drivers.

Other characteristics that should be taken into account in choosing the detectors for Surface Plasmon Resonance based sensors are the optical devices, such as lenses, placed before the CMOS sensor itself, in order to avoid the unwanted beam collimation on the detector or optical interferences.

The realized SPR sensors still reveal some noise but this could be solved with future refinements.

Appendices

Appendix A

Possible sites in the Solar System for astrobiology research with Surface Plasmon Resonance sensors

In this appendix I add a part of the research about the possible astronomical sites in the Solar System for astrobiological research with Surface Plasmon Resonance sensors I made for the Geology and Exploration of the terrestrial planets course of the Ph. D. School in Sciences Technologies and Measures for Space of the University of Padova.

A.1 Conditions for life

The most important preconditions for life on a planetary surface as we humans know it are, as stated by Jakosky and Shock (1998) :

- ⋆ the presence of liquid water
- ⋆ sufficient time for primitive life forms to develop
- ⋆ a source of energy
- ⋆ the presence of nutrients in the environment such as carbon compounds and various elements required for plant growth (e.g., potassium, nitrogen, phosphorus, iron, etc.)

A.2 Terrestrial bacteria to look at as examples

According to Pudritz et al. (2007), McKey (1993),
Painter et al. (2001), van-der Wielen et al. (2005) ,
Vishnivetskaya et al. (2001), Garcia-Pichel et al. (1998),
Cox and Battista (2005),
terrestrial bacteria that would be useful to study in order to obtain informations about possible life outside Earth are among the others

- ⋆ Antarctic cryptoendolithic microbial ecosystems: organisms that live below the surfaces of rocks or sand

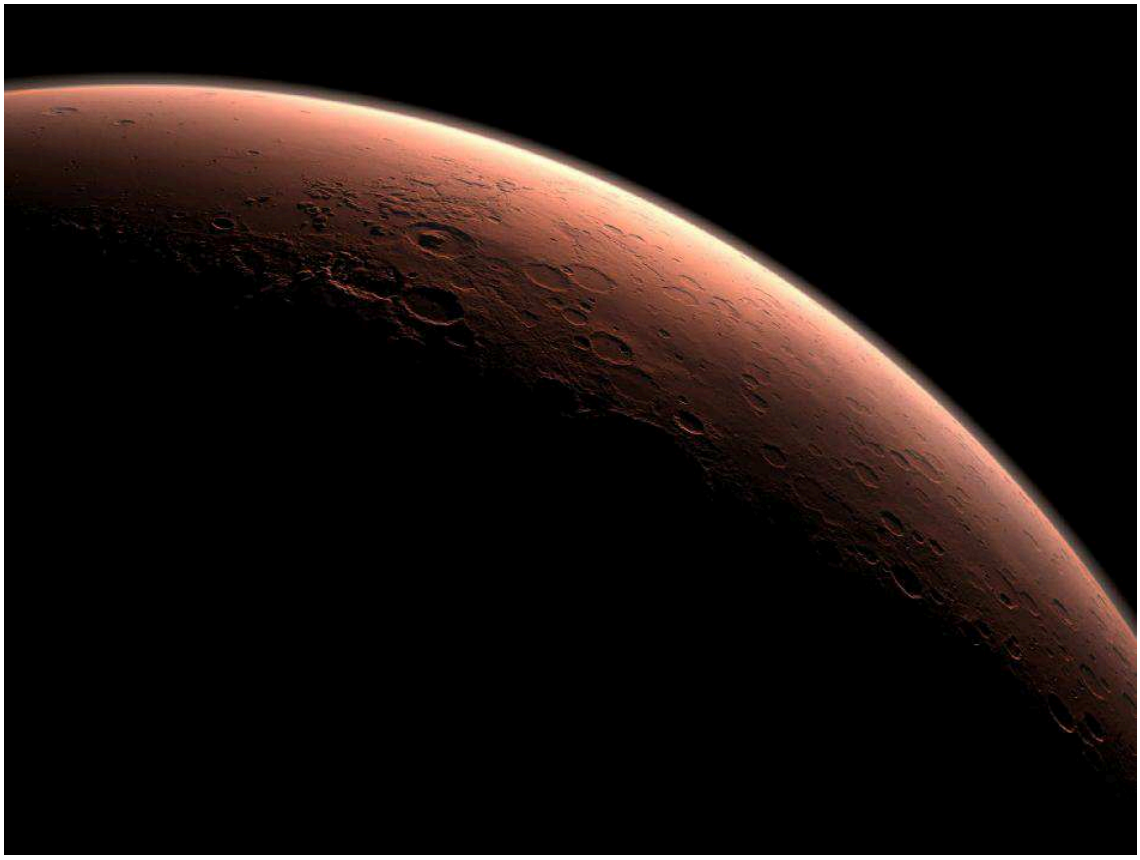

Figure A.1: Image of Mars by NASA/JPL-Caltech

- ⋆ cyanobacteria: bacteria which have pigments (as scytonemin and gloeocapsin) in their mucilaginous sheath that protect them from the ultraviolet radiation
- ⋆ halophiles: bacteria that can survive to elevated levels of salinity
- ⋆ Deinococcus radiodurans and other bacteria able to repair their DNA and thus surviving to high levels of ionizing radiation (up to 10,000 Gray)

A.3 Mars

At the present time the surface of Mars generally doesn't support life because of its dryness, oxidizing chemical composition (as Fe2O3 or haematite) and because of the unshielded ionizing radiation. On the other hand,however, the presence of liquid water on the surface of Mars during the Noachian and early Hesperian Eons (4.5 to 3.0 Ga) satisfies one of the preconditions for life on a planetary surface. At that time, the surface of Mars was much more similar to the surface of the Earth than it is at the present time (Faure et al. (2007b)). Therefore, life could be existed on Mars and some particular habitats could have preserved it.

Possible target sites for the search for life or its remnants on Mars are :

- ⋆ northern polar region (image A.2), where there could be liquid water because of pressure above triple point (610 Pa), the presence of ice near the surface and because this region has the higher insulation of the planet surface during summer, so ice could melt

  (Pudritz et al. (2007), Haberle et al. (2001))

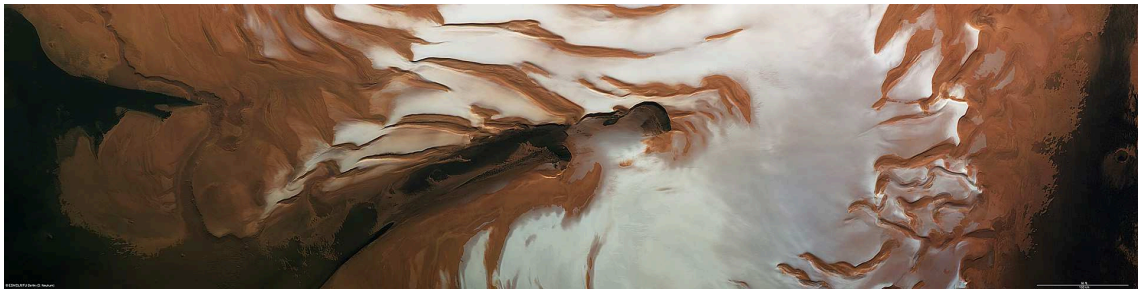

Figure A.2: Image from ESA/DLR/FU Berlin (G. Neukum): Mars' northern polar regions

⋆ on subsurface near the poles,(Pudritz et al. (2007),

Haberle et al. (2001)), where volcanic or geothermal activity could melt some permafrost or if present subsurface water sources as hydrothermal systems. Moreover volcanic gases as CH4, H2, H2S with water could allow microbial life based on chemolithoautotrophy (for example methanogens)

⋆ On Dark dunes spots (DDSs),(Pudritz et al. (2007)),

Kereszturi et al. (2011), Malin and Edgett (2000), which are spots on shadowed dunes found on the floors of craters in the polar regions of Mars, with latitudes between -60Âř and -80Âř (see image A.3) and where

- The soil of the dunes is covered by frost during the winter so there could be a little amount of liquid water even below the ice
- Sand, Ice and frost if present could protect bacteria from ultraviolet radiation and from the Martian atmosphere but the thin frost could allow photosynthesis
- The dunes are assumed to be composed of basaltic sand that could be less oxidant than the common surface of Mars, which is composed of haematite (Fe_2O_3)

⋆ dead organisms in Martian permafrost 3-4 Gy old or in salt if present

⋆ Haberle et al. (2001) present a model that propose Hellas and Argyre in the Southern Hemisphere as the best sites to search for Sun-melted water.

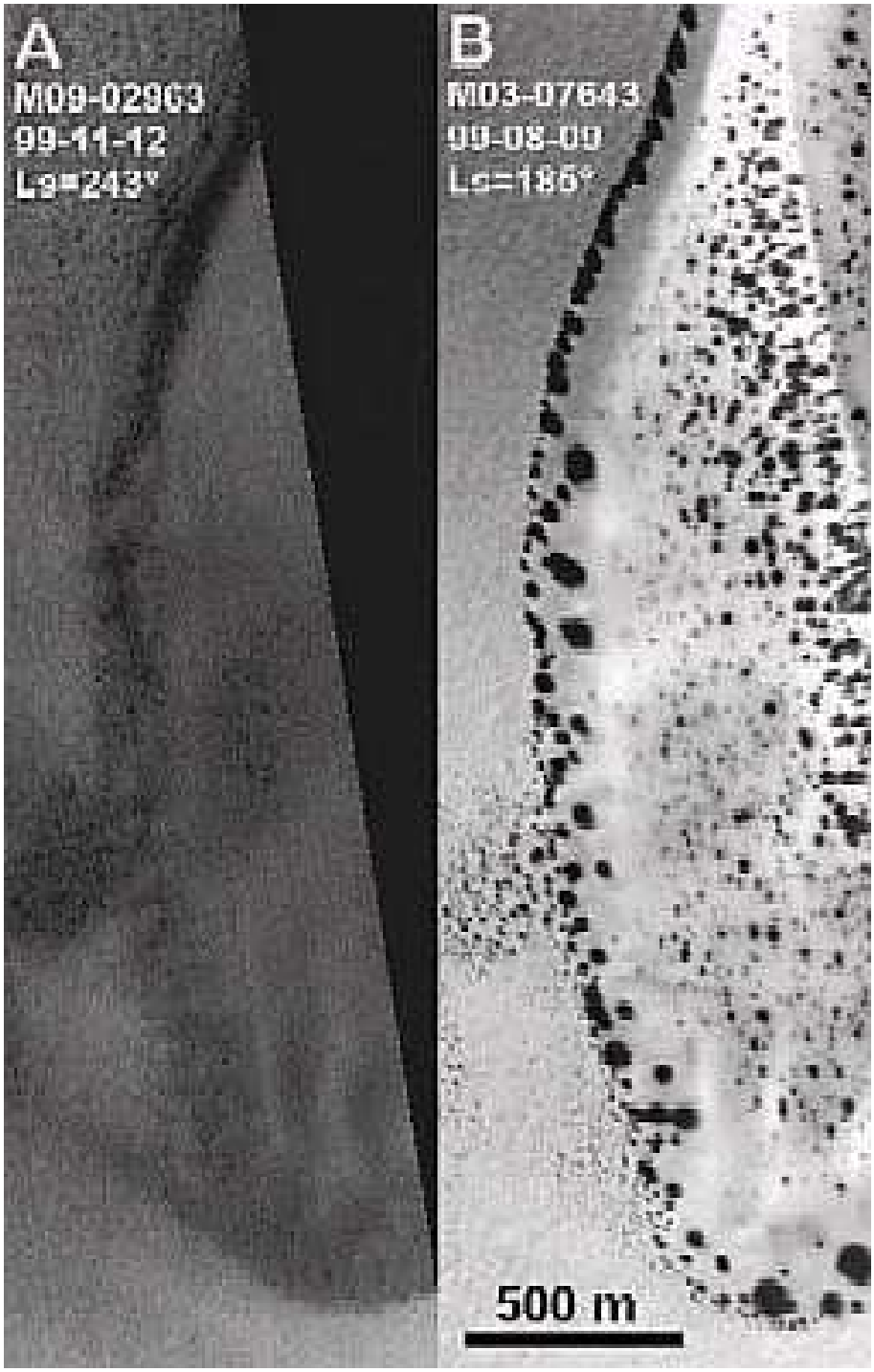

Figure A.3: Image of DDSs:Mars Orbiter Camera image processed by Malin Space Science Systems

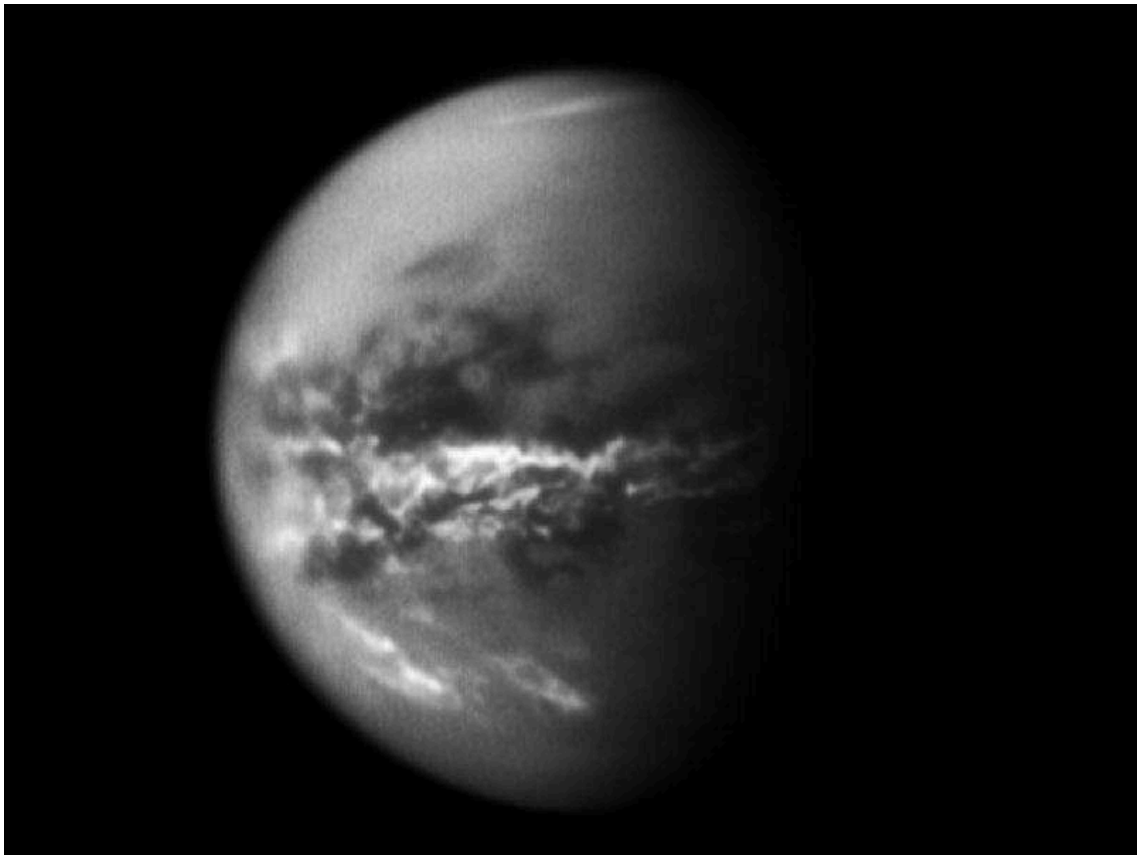

Figure A.4: Image of Titan by NASA's Cassini spacecraft

A.4 Titan

Titan is the largest moon of Saturn. It can be a candidate for astrobiology because

- ⋆ It has a dense secondary (Pudritz et al. (2007)) atmosphere, composed of N2(molecular nitrogen), CH4 (methane) and traces of H2 (molecular hydrogen), (Flasar et al. (2005)) , methane seas.
- ⋆ There is a complex N2 and CH4 based chemistry: C2H2 and HCN could form in the high atmosphere and then diffuse on the surface (Hébrard et al. (2005)).
- ⋆ Prebiotic important molecules as HCN (hydrogen cyanide) , HC3N (cyanoacetilene) and C2N2 (cyanogen) could be present

  (Pudritz et al. (2007))
- ⋆ From the Cassini and SSP instrument (Zarnecki et al. (2005)) is suggested the presence of water ice

Acetylene, ethane and organic solids, would release energy when consumed with atmospheric hydrogen. So if bacteria are consuming complex hydrocarbons at the surface of Titan, it could be observed complete consumption of C2H2 at the surface, reduction in C2H6 and a decrease of hydrogen at the surface (McKay and Smith (2005)).

It could so be possible to put floating sensors on the surfaces of the Titan's methane seas.

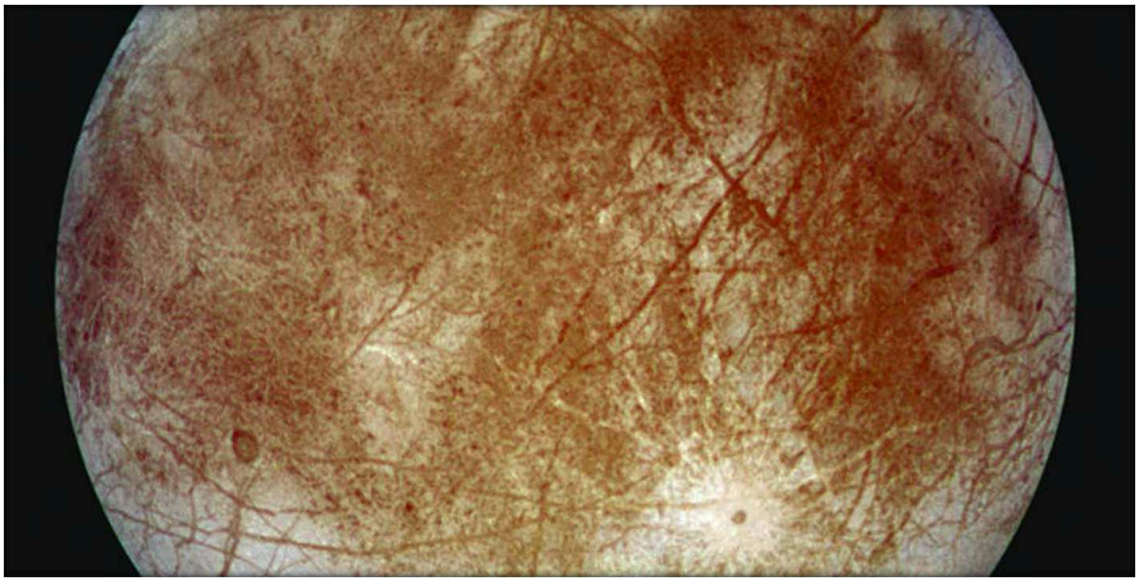

Figure A.5: Image of Europa by NASA/JPL-Caltech

A.5 Europa

Europa is the smallest of the Galilean satellites. It can be a candidate for astrobiology because Jupiter's tidal friction allows a non neglectable heating and tectonic movements on this moon (Pudritz et al. (2007)).

Observations that could support the thesis of the existence of favorable conditions for the development of life on Europa are:

- ⋆ Europa is heated by tidal friction caused by the deformation of its shape as it revolves around Jupiter(Faure et al. (2007a))
- ⋆ The geophysical measurements indicate the presence of a saline water ocean under an ice shell (Lipps and Rieboldt (2005)),

  Greenberg et al. (1998))
- ⋆ Heat could warm the ocean through the bottom, possibly by means of hotsprings
- ⋆ The most plausible explanation for the origin of chaotic terrain is by melt-through of the ice crust by plumes of warm water rising from the floor of the ocean
- ⋆ The environmental conditions described above have lasted for four billion years (Faure et al. (2007a))
- ⋆ From the study of Europa its crust is believed to be thin, around 10 km (Faure et al. (2007a)), and a spatially or temporally thin crust would allow better communication of the ocean with the surface

  (Pudritz et al. (2007))
- ⋆ Europa's water column might provide a variety of habitats having different water mass distribution, oceanic structure, tidal and current patterns (Pudritz et al. (2007))
- ⋆ Furthermore cracks and fissures that penetrate from the bottom of the ice upwards could be possible habitats for life (Greenberg (2002))

- ⋆ The bottom of the ice might also contain abundant brine channels and pores that could be occupied (Lipps and Rieboldt (2005)). Organisms in these habitats might be fueled by nutrients and organic matter leaking down from higher places in the ice or from the surface
- ⋆ Cracks, caves, overhangs, holes and other areas that protect from the surface radiation could bear potential habitats

  (Lipps and Rieboldt (2005))

In conclusion if life has ever happened on Europa it would have appeared in habitats and it would likely be preserved and transported to the icy shell.

Sampling surface sites where the subshell or within-shell habitats may be exposed provides thus a reasonable search strategy (Figueredo et al. (2003))

Appendix B

The NMEA 0183 sentences supported by the RGM-3600 GPS receiver

The Royaltek RGM-3600 supports the following NMEA-0183 Messages: GGA, GLL, GSA, GSV, RMC and VTG.

In this appendix all this messages are explained as stated by (Betke (2001)). As reported in () All data of NMEA0183 code are transmitted in the form of sentences. Only printable ASCII characters are allowed, plus `CR` (carriage return) and `LF` (line feed). Each sentence starts with a "`$`" sign and ends with `<CR><LF>`.

B.1 GGA: Global Positioning System Fix Data. Time, Position and fix related data

The message is in the form

```
          1        2        3 4         5 6 7  8   9  10 11 12 13  14   15
          |        |        | |         | | |  |   |   | |  | |   |    |
$--GGA,hhmmss.ss,llll.ll,a,yyyyy.yy,a,x,xx,x.x,x.x,M,x.x,M,x.x,xxxx*hh
```

being

1. Time (UTC)
2. Latitude
3. N or S (North or South)
4. Longitude
5. E or W (East or West)
6. GPS Quality Indicator,
   - ⋆ 0 - fix not available,
   - ⋆ 1 - GPS fix,
   - ⋆ 2 - Differential GPS fix

7. Number of satellites in view, 00 - 12
8. HDOP (Horizontal Dilution of precision) in meters
9. Antenna Altitude above/below mean-sea-level (geoid)
10. Units of antenna altitude, meters
11. Geoidal separation, the difference between the WGS-84 Earth ellipsoid and mean-sea-level (geoid), "-" means mean-sea-level below ellipsoid
12. Units of geoidal separation, meters
13. Age of differential GPS data, time in seconds since last SC104 type 1 or 9 update, null field when DGPS is not used
14. Differential reference station ID, 0000-1023
15. Checksum

and a message example is

```
$GPGGA, 161229.487, 3723.2475, N, 12158.3416,
W, 1, 07, 1.0, 9.0, M, , , ,0000*18
```

B.2 GLL: Geographic Position (Latitude/Longitude)

Message is

```
       1       2 3        4 5         6 7
       |       | |        | |         | |
$--GLL,llll.ll,a,yyyyy.yy,a,hhmmss.ss,A*hh
```

with

1. Latitude
2. N or S (North or South)
3. Longitude
4. E or W (East or West)
5. Time (UTC)
6. Status A - Data Valid, V - Data Invalid
7. Checksum

B.3 GSA: GPS DOP and active satellites

The GSA signal is setted as

```
       1 2 3    ...                  14 15  16  17  18
       | | | | | | | | | | | | | | | |   |   |   |
$--GSA,a,a,x,x,x,x,x,x,x,x,x,x,x,x,x,x,x.x,x.x,x.x*hh
```

referring to

1. Mode 1
2. Mode 2
3. ID of 1st satellite used for fix
4. ID of 2nd satellite used for fix
5. ID of 3rd satellite used for fix
6. ID of 4th satellite used for fix
7. ID of 5th satellite used for fix
8. ID of 6th satellite used for fix
9. ID of 7th satellite used for fix
10. ID of 8th satellite used for fix
11. ID of 9th satellite used for fix
12. ID of 10th satellite used for fix
13. ID of 11th satellite used for fix
14. ID of 12th satellite used for fix
15. PDOP (Position Dilution of Precision) in meters
16. HDOP (Horizontal Dilution of Precision) in meters
17. VDOP (Vertical Dilution of Precision) in meters
18. Checksum

The values for Mode 1 are shown in table (B.1) while the ones for Mode 2 in table (B.2)

B.4 GSV: Satellites in view

The GSV message is instead

```
       1 2 3 4 5 6 7     n
       | | | | | | |     |
$--GSV,x,x,x,x,x,x,x,...*hh
```

being

Table B.1: GSA Mode 1 Values

Value	Description
M	Manual-forced to operate in 2D or 3D mode
A	Automatic-allowed to automatically switch 2D/3D

Table B.2: GSA Mode 2 Values

Value	Description
1	Fix not available
2	2D
3	3D

1. total number of messages
2. message number
3. satellites in view
4. satellite number
5. elevation in degrees
6. azimuth in degrees to true
7. SNR in dB

... more satellite infos like 4-7
n. Checksum

B.5 RMC: Recommended Minimum Navigation Information

RMC Signal is in the form

```
        1         2 3        4 5         6 7   8   9    10 11 12
        |         | |        | |         | |   |   |    |   | |
$--RMC,hhmmss.ss,A,llll.ll,a,yyyyy.yy,a,x.x,x.x,xxxx,x.x,a*hh
```

with

1. Time (UTC)
2. Status, V = Navigation receiver warning
3. Latitude

4. N or S
5. Longitude
6. E or W
7. Speed over ground, knots
8. Track made good, degrees true
9. Date, ddmmyy
10. Magnetic Variation, degrees
11. E or W
12. Checksum

B.6 VTG: Track Made Good and Ground Speed

VTG message is expressed as

```
        1   2 3   4 5   6 7   8 9
        |   | |   | |   | |   | |
$--VTG,x.x,T,x.x,M,x.x,N,x.x,K*hh
```

referring to

1. Track Degrees
2. T = True
3. Track Degrees
4. M = Magnetic
5. Speed Knots
6. N = Knots
7. Speed Kilometers Per Hour
8. K = Kilometres Per Hour
9. Checksum

Bibliography

Aguirre, N. M., Perez, L. M., Colin, J. A., and Buenrostro-Gonzalez, E. (2007). Development of a surface plasmon resonance n-dodecane vapor sensor. *Sensors*, 7(9):1954–1961.

Azofeifa, D., Clark, N., and Vargas, W. (2005). Optical and electrical properties of terbium films as a function of hydrogen concentration. *physica status solidi (b)*, 242(10):2005–2009.

Banahan, M., Brady, D., and Doran, M. (1991). *The C Book*. Addison Wesley, second edition.

Bayer, R. (2008). Windows serial port programming. www.robbayer.com/files/serial-win.pdf.

Benson, O. (2011). Assembly of hybrid photonic architectures from nanophotonic constituents. *Nature*, 480:193 – 199.

Betke, K. (2001). The nmea 0183 protocol. www.nmea.org.

Bevenot, X., Trouillet, A., Veillas, C., Gagnaire, H., and Clément, M. (2002). Surface plasmon resonance hydrogen sensor using an optical fibre. *Measurement Science and Technology*, 13(1):118–124.

Bonora, S. (2011). Distributed actuators deformable mirror for adaptive optics. *Optics Communications*, 284:3467–3473.

Bonora, S., Capraro, I., Poletto, L., Romanin, M., Trestino, C., and Villoresi, P. (2006). Wave front active control by a digital-signal-processor-driven deformable membrane mirror. *Review of Scientific Instruments*, 77(9):093102.

Born, M. and Wolf, E. (1986). *Principles of Optics: Electromagnetic Theory of Propagation, Interference and diffraction of Light*. Pergamon Press, London.

Boulart, C., Mowlem, M. C., Connelly, D. P., Dutasta, J.-P., and German, C. R. (2008). A novel, low-cost, high performance dissolved methane sensor for aqueous environments. *OPTICS EXPRESS*, 16(17):12607–12617.

Bruna, M. and Borini, S. (2009). Optical constants of graphene layers in the visible range. *Applied Physics Letters*, 94(3):031901.

Bunch, J. S., Verbridge, S. S., Alden, J. S., van der Zande, A. M., Parpia, J. M., Craighead, H. G., and McEuen, P. L. (2008). Impermeable atomic membranes from graphene sheets. *Nano Letters*, 8(8):2458–2462.

Burton, W. (1908). The refractive index and dispersion of light in argon and helium. *Proceedings of the Royal Society of London. Series A, Containing Papers of a Mathematical and Physical Character*, 80(540):390–405.

Cardell-oliver, R., Smettem, K., Kranz, M., and Mayer, K. (2004). Field testing a wireless sensor network for reactive environmental monitoring. In *In International Conference on Intelligent Sensors, Sensor Networks and Information Processing*, pages 14–17.

Chantharat, W. and Pirak, C. (2011). Image transmission over zigbee network with transmit diversity. In *2011 International Conference on Circuits, System and Simulation, IPCSIT vol.7*, pages 139–143. IACSIT Press, Singapore.

Chinowsky, T. M., Soelberg, S. D., Baker, P., Swanson, N. R., Kauffman, P., Mactutis, A., Grow, M. S., Atmar, R., Yee, S. S., and Furlong, C. E. (2007). Portable 24-analyte surface plasmon resonance instruments for rapid, versatile biodetection. *Biosensors Bioelectronics 22 issue 9-10*, pages 2268–2275.

Choi, S. H., Kim, Y. L., and Byun, K. M. (2011). Graphene-on-silver substrates for sensitive surface plasmon resonance imaging biosensors. *Optics Express*, 19(2):458–466.

Chuo, Y. and Kaminska, B. (2009). Design for modular testing of a multilayer flexible wireless multisensor platform. In *Proceedings of the 2009 IEEE 15th International Mixed-Signals, Sensors, and Systems Test Workshop*, IMS3TW '09, pages 1–6, Washington, DC, USA. IEEE Computer Society.

Ciddor, P. E. (1996). Refractive index of air: new equations for the visible and near infrared. *Applied Optics*, 35(9):1566–1573.

Connor, S. (2009). The lost world beneath the antarctic ice. http://www.independent.co.uk/news/science/the-lost-world-beneath-the-antarctic-ice-1639247.html.

Connor, S. (2011). To coldly go... british team to drill into lost antarctic world. http://www.independent.co.uk/news/science//to-coldly-go-british-team-to-drill-into-lost-antarctic-world -2368639.html#.

Coraux, J., N'Diaye, A. T., Busse, C., and Michely, T. (2008). Structural coherency of graphene on ir(111). *Nano Letters*, 8(2):565–570.

Cox, M. M. and Battista, J. R. (2005). Deinococcus radiodurans - the consummate survivor. *Nature Reviews Microbiology*, 3:882–892.

Delin, K. A. (2004). Sensor webs in the wild. *AGU Fall Meeting Abstracts*, page A1.

Delin, K. A., Harvey, R., Chabot, N. A., Jackson, S. P., Adams, M., Johnson, D. W., and Britton, J. T. (2003). Sensor web in antarctica: Developing an intelligent, autonomous platform for locating biological flourishes in cryogenic environments. In Mackwell, S. and Stansbery, E., editors, *Lunar and Planetary Institute Science Conference Abstracts*, volume 34 of *Lunar and Planetary Institute Science Conference Abstracts*, page 1929, Houston, Texas, U.S.A.

Dudak, F. C. and Boyaci, I. H. (2007). Development of an immunosensor based on surface plasmon resonance for enumeration of escherichia coli in water samples. *Food Research International*, 40:803–807.

Eckel, B. (2000). *Thinking In C++*. Prentice Hall Inc., Upper Saddle River, New Jersey, second edition.

El-Basaty, A., El-Brolossy, T., Abdalla, S., Negm, S., Abdalla, R., and Talaat, H. (2006). Surface plasmon cobalt phthalocyanine sensor for no2 gas. *Egypt. J. Solids Vol.29, No.1*, pages 121–129.

Elhadj, S., Singh, G., and Saraf, R. F. (2004). Optical properties of an immobilized dna monolayer from 255 to 700 nm. *Langmuir*, 20(13):5539–5543.

Farinha, J., Relogio, P., Charreyre, M. T., Prazeres, T., and Martinho, J. (2007). Understanding fluorescence quenching in polymers obtained by raft. *Macromolecules*, 40(13):4680–4690.

Farrington, S. P., Haas, J. W., and Van-Wyck, N. (2003). Final topical report long-term monitoring sensor network. Technical Report Contract number DE-AC26-01NT41303, U.S. Department of Energy, National Energy Technology Laboratory, 626 Cochrans Mill Road, P.O. Box 10940, Pittsburgh, PA 15236-0940.

Faure, G., Mensing, T. M., Faure, G., and Mensing, T. (2007a). Galilean satellites: Jewels of the solar system. In *Introduction to Planetary Science: The Geological Perspective*, pages 297–333. Springer Netherlands.

Faure, G., Mensing, T. M., Faure, G., and Mensing, T. M. (2007b). Mars: The little planet that could. In *Introduction to Planetary Science: The Geological Perspective*, pages 211–259. Springer Netherlands.

Feltis, B., Sexton, B., Glenn, F., Best, M., Wilkins, M., and Davis, T. (2008). A hand-held surface plasmon resonance biosensor for the detection of ricin and other biological agents. *Biosensors and Bioelectronics*, 23(7):1131 – 1136.

Figueredo, P. H., Greeley, R., Neuer, S., Irwin, L., and Schulze-Makuch, D. (2003). Locating potential biosignatures on europa from surface geology observations. *Astrobiology*, 3(4):851–861.

Flasar, F. M., Achterberg, R. K., Conrath, B. J., Gierasch, P. J., Kunde, V. G., Nixon, C. A., Bjoraker, G. L., Jennings, D. E., Romani, P. N., Simon-Miller, A. A., BÃl'zard, B., Coustenis, A., Irwin, P. G. J., Teanby, N. A., Brasunas, J., Pearl, J. C., Segura, M. E., Carlson, R. C., Mamoutkine, A., Schinder, P. J., Barucci, A., Courtin, R., Fouchet, T., Gautier, D., Lellouch, E., Marten, A., Prangè, R., Vinatier, S., Strobel, D. F., Calcutt, S. B., Read, P. L., Taylor, F. W., Bowles, N., Samuelson, R. E., Orton, G. S., Spilker, L. J., Owen, T. C., Spencer, J. R., Showalter, M. R., Ferrari, C., Abbas, M. M., Raulin, F., Edgington, S., Ade, P., and Wishnow, E. H. (2005). Titan's atmospheric temperatures, winds, and composition. *Science*, 308(5724):975–978.

Forzani, E., Foley, K., Westerhoff, P., and Tao, N. (2007). Detection of arsenic in groundwater using a surface plasmon resonance sensor. *Sensors and Actuators B No. 123*, pages 82–88.

Garcia-Pichel, F., Nubel, U., and Muyzer, G. (1998). The phylogeny of unicellular, extremely halotolerant cyanobacteria. *Archives of Microbiology*, 169:469–482.

Garcia-Sanchez, A.-J., Garcia-Sanchez, F., Losilla, F., Kulakowski, P., Garcia-Haro, J., Rodriguez, A., Lopez-Bao, J.-V., and Palomares, F. (2010). Wireless sensor network deployment for monitoring wildlife passages. *Sensors*, 10(8):7236–7262.

Gobi, K., Matsumoto, K., Toko, K., Ikezaki, H., and Miura, N. (2007). Enhanced sensitivity of self-assembled-monolayer-based spr immunosensor for detection of benzaldehyde using a single-step multi-sandwich immunoassay. *Analytical and Bioanalytical Chemistry*, 387:2727–2735.

Gray, D., CaseGreen, S., Fell, T., Dobson, P., and Southern, E. (1997). Ellipsometric and interferometric characterization of DNA probes immobilized on a combinatorial array. *LANGMUIR*, 13(10):2833–2842.

Greenberg, R. (2002). Tides and the biosphere of europa. *American Scientist*, 90(1):48–55.

Greenberg, R., Geissler, P., Hoppa, G., Tufts, B., Durda, D. D., Pappalardo, R., Head, J. W., Greeley, R., Sullivan, R., and Carr, M. H. (1998). Tectonic processes on europa: Tidal stresses, mechanical response, and visible features. *Icarus*, 135(1):64 – 78.

Haberle, R. M., McKay, C. P., Schaeffer, J., Cabrol, N. A., Grin, E. A., Zent, A. P., and Quinn, R. (2001). On the possibility of liquid water on present-day mars. *Journal of Geophysical Research*, 106(E10):23317–23326.

Hale, G. M. and Querry, M. R. (1973). Optical constants of water in the 200-nm to 200-μm wavelength region. *Applied Optics*, 12(3):555–563.

Hart, J. K. and Martinez, K. (2006). Environmental sensor networks:a revolution in the earth system science? *Earth-Science Reviews*, 78:177–191.

Hart, J. K., Martinez, K., Ong, R., Riddoch, A., Rose, K. C., and Padhy, P. (2006). An autonomous multi-sensor subglacial probe: design and preliminary results from briksdalsbreen, norway. *Journal of Glaciology*, 52(178):89 – 397.

Hartung, C., Han, R., Seielstad, C., and Holbrook, S. (2006). Firewxnet: a multi-tiered portable wireless system for monitoring weather conditions in wildland fire environments. In *Proceedings of the 4th international conference on Mobile systems, applications and services*, MobiSys '06, pages 28–41, New York, NY, USA. ACM.

Hébrard, E., Bénilan, Y., and Raulin, F. (2005). Sensitivity effects of photochemical parameters uncertainties on hydrocarbon production in the atmosphere of titan. *Advances in Space Research*, 36(2):268 – 273. Space Life Sciences: Astrobiology: Steps toward Origin of Life and Titan before Cassini.

Hock, B., Seifert, M., and Kramer, K. (2002). Engineering receptors and antibodies for biosensors. *Biosensors and Bioelectronics*, 17(3):239 – 249.

Homola, J. (1997). On the sensitivity of surface plasmon resonance sensors with spectral interrogation. *Sensors and Actuators B: Chemical*, 41(1 - 3):207 – 211.

Homola, J. (2003). Present and future of surface plasmon resonance biosensors. *Analytical and Bioanalytical Chemistry*, 377:528–539.

Homola, J. (2008). Surface plasmon resonance sensors for detection of chemical and biological species. *Chemical Reviews No.108*, pages 462–493.

Homola, J., Dostalek, J., Jiang, S., Ladd, J., Lofas, S., McWhirter, A., Myszka, D. G., Navratilova, I., Piliarik, M., J.Stepanek, Taylor, A., and Vaisocherova, H. (2006). *Surface Plasmon Resonance Based Sensors*. Springer-Verlag, Berlin Heidelberg.

Homola, J., Koudela, I., and Yee, S. S. (1999). Surface plasmon resonance sensors based on diffraction gratings and prism couplers: sensitivity comparison. *Sensors and Actuators B: Chemical*, 54(1 - 2):16 – 24.

Horne, K., Printz, M., Barnes, W., and Sambles, J. (1994). Surface plasmon resonances showing reflectivity maxima. *Optics Communications*, 110(1 - 2):80 – 86.

Hu, C. and Liu, D. (2010). High-performance grating coupled surface plasmon resonance sensor based on al-au bimetallic layer. *Modern Applied Science*, 4(6):8 – 13.

Hu, J., Wang, L., Cai, W., Li, Y., Zeng, H., Zhao, L., and Liu, P. (2009). Smart and reversible surface plasmon resonance responses to various atmospheres for silver nanoparticles loaded in mesoporous sio2. *The Journal of Physical Chemistry C*, 113(44):19039–19045.

Husale, B. S., Sahoo, S., Radenovic, A., Traversi, F., Annibale, P., and Kis, A. (2010). ssdna binding reveals the atomic structure of graphene. *Langmuir*, 26(23):18078–18082.

IDS-GmbH (2012). ueye camera manual. http://www.ids-imaging.de/frontend/files/uEyeManuals/Manual_eng/uEye_Manual/index.html.

Islam, M. S. and Kouzani, A. Z. (2011). Variable incidence angle localized surface plasmon resonance graphene biosensor. In *CME 2011 : Proceedings of the 2011 IEEE/ICME International Conference on Complex Medical Engineering*, pages 58–63, Harbin Heilongjiang, China.

Izenberg, N. R., Murrray, G. M., Pilato, R. S., Baird, L. M., Levin, S. M., and Van-Houten, K. A. (2009). Astrobiological molecularly imprinted polymer sensors. *Planetary and Space Science*, 57:846–853.

Izenberg, N. R., Murrray, G. M., Van-Houten, K. A., Strauch, L., Hofstra, A., and Uy, O. (2006). Development of astrobiological molecularly imprinted polymer sensors. In *37th Lunar and Planetary Science Conference Abstracts, LPI Contribution no. 1372*. Lunar and Planetary Institute, Houston.

Jakosky, B. M. and Shock, E. L. (1998). The biological potential of mars, the early earth, and europa. *Journal of geophysical research*, 103(E8):19359–19364.

Jiang, D.-e., Cooper, V. R., and Dai, S. (2009). Porous graphene as the ultimate membrane for gas separation. *Nano Letters*, 9(12):4019–4024.

Jung, L. S., Campbell, C. T., Chinowsky, T. M., Mar, M. N., and Yee, S. S. (1998). Quantitative interpretation of the response of surface plasmon resonance sensors to adsorbed films. *Langmuir*, 14(19):5636 – 5648.

Kang, T., Hong, S., Moon, J., Oh, S., and Yi, J. (2005). Fabrication of reusable sensor for detection of cu2+ in an aqueous solution using a self-assembled monolayer with surface plasmon resonance spectroscopy. *Chemical Communications*, pages 3721–3723.

Kereszturi, A., Vincendon, M., and Schmidt, F. (2011). Water ice in the dark dune spots of richardson crater on mars. *Planetary and Space Science*, 59(1):26 – 42.

Kernighan, B. W. and Ritchie, D. M. (1989). *Linguaggio C, seconda edizione*. Gruppo Editoriale Jackson, Milano.

Kim, S. J., Gobi, K. V., Iwasaka, H., Tanaka, H., and Miura, N. (2007). Novel miniature spr immunosensor equipped with all-in-one multi-microchannel sensor chip for detecting low-molecular-weight analytes. *Biosensors and Bioelectronics*, 23(5):701 – 707.

Kitade, Y., Takei, Y., Misawa, T., Kubota, N., Oyabu, Y., and Nanto, H. (2004). Odour sensor utilizing surface plasmon resonance phenomenon. In *Proceedings of the Fifth Asia Pacific Industrial Engineering and Management Systems Conference*, pages 10.7.1–10.7.8.

Kitenge, D., Joshi, R. K., Hirai, M., and Kumar, A. (2009). Nanostructured Silver Films for Surface Plasmon Resonance-Based Gas Sensors. *IEEE Sensors Journal*, 9:1797–1801.

Koblizek, M., Maly, J., Masojidek, J., Komenda, J., Kuera, T., Giardi, M. T., Mattoo, A. K., and Pilloton., R. (2002). A biosensor for the detection of triazine and phenylurea herbicides designed using photosystem ii coupled to a screen-printed electrode. *Biotechnol. Bioeng. No.78*, pages 110–116.

Kohns, P., Logacheva, E., Makin, V., and Pestov, Y. (2005). Inverted sp resonance in palladium in kretchmann configuration. In *Advanced Optoelectronics and Lasers, 2005. Proceedings of CAOL 2005. Second International Conference on*, volume 2, pages 340 – 344.

Konopsky, V. N. (2010). Plasmon-polariton waves in nanofilms on one-dimensional photonic crystal surfaces. *New Journal of Physics N0. 12,093006*, pages 1–18.

Kota, S., Giambene, G., and Kim, S. (2011). Satellite component of ngn: Integrated and hybrid networks. *International Journal of Satellite Communications and Networking*, 29(3):191–208.

Koubova, V., Brynda, E., Karasova, L., Skvor, J., Homola, J., Dostalek, J., Tobiska, P., and Rosicky, J. (2001). Detection of foodborne pathogens using surface plasmon resonance biosensors. *Sensors and Actuators B: Chemical*, 74(1-3).

Kowalczyk, S. W., Tuijtel, M. W., Donkers, S. P., and Dekker, C. (2010). Unraveling single-stranded dna in a solid-state nanopore. *Nano Letters*, 10(4):1414–1420.

Kurita, R., Yokota, Y., Sato, Y., Mizutani, F., and Niwa, O. (2006). On-chip enzyme immunoassay of a cardiac marker using a microfluidic device combined with a portable surface plasmon resonance system. *Anal Chem*, 78(15):5525–31.

Kwon, S.-Y., Ciobanu, C. V., Petrova, V., Shenoy, V. B., Bareño, J., Gambin, V., Petrov, I., and Kodambaka, S. (2009). Growth of semiconducting graphene on palladium. *Nano Letters*, 9(12):3985–3990.

Laan, E., HenkLeeuwis, ten Kate, I. L., and Boom, E. (2006). The life marker chip (lmc) onboard the exomars rover. In *4th Interplanetary Probe Workshop, June 2006, Pasadena, California, USA*.

Laska, J., Berry, M., and Sachs, D. (2004). Using the serial port with a matlab gui. http://cnx.org/content/m12062/latest/.

Lee, K.-L., Lee, C.-W., Wang, W.-S., and Wei, P.-K. (2007). Sensitive biosensor array using surface plasmon resonance on metallic nanoslits. *Journal of Biomedical Optics*, 12(4):044023.

Leinse, A., Leeuwis, H., Prak, A., Heideman, R., and Borst, A. (2011). The life marker chip for the exomars mission. In *Information Photonics (IP), 2011 ICO International Conference on*, pages 1–2.

Libelium, C. D. S. L. (2010). *Waspmote Technical Guide*. Libelium Comunicaciones Distribuidas S. L., 0.9 edition.

Liedberg, B., Lundström, I., and Stenberg, E. (1993). Principles of biosensing with an extended coupling matrix and surface plasmon resonance. *Sensors and Actuators B: Chemical*, 11(1 - 3):63 – 72.

Lipps, J. H. and Rieboldt, S. (2005). Habitats and taphonomy of europa. *Icarus*, 177(2):515 – 527.

Logacheva, E. I., Makin, V. S., Pestov, Y. I., and Kohns, P. (2006). Sensors and inverted resonance on surface plasmons in palladium. *J. Opt. Technol.*, 73(6):409–412.

Lopes, M., Candini, A., Urdampilleta, M., Reserbat-Plantey, A., Bellini, V., Klyatskaya, S., Marty, L., Ruben, M., Affronte, M., Wernsdorfer, W., and Bendiab, N. (2010). Surface-enhanced raman signal for terbium single-molecule magnets grafted on graphene. *ACS Nano*, 4(12):7531–7537.

Lowery, H. and Hartley, T. S. (1931). The refraction and dispersion of gaseous pentane and chloroform. *Proceedings of the Physical Society*, 43(5):559.

Maciak, E., Opilski, Z., and Pustelny, T. (2001). Effect of humidity on nh3 gas sensitivity of nafion/wo3 sensing structure of spr sensor. *Molecular and Quantum Acoustics*, 26:205–215.

Mainwaring, A., Culler, D., Polastre, J., Szewczyk, R., and Anderson, J. (2002). Wireless sensor networks for habitat monitoring. In *Proceedings of the 1st ACM international workshop on Wireless sensor networks and applications*, WSNA '02, pages 88–97, New York, NY, USA. ACM.

Malin, M. C. and Edgett, K. S. (2000). Frosting and defrosting of martian polar dunes. In *Lunar and Planetary Science XXXI*, Houston, Texas. Lunar and Planetary Institute.

Marchesini, G., Koopal, K., Meulenberg, E., Haasnoot, W., and Irth, H. (2007). Spreeta-based biosensor assays for endocrine disruptors. *Biosensors and Bioelectronics*, 22(9-10):1908 – 1915. Selected Papers from the Ninth World Congress On Biosensors. Toronto, Canada 10 - 12 May 2006.

Mauriz, E., Calle, A., Abad, A., Montoya, A., Hildebrandt, A., Barcelo, D., and Lechuga, L. (2006a). Determination of carbaryl in natural water samples by a surface plasmon resonance flow-through immunosensor. *Biosensors and Bioelectronics*, 21(11):2129 – 2136.

Mauriz, E., Calle, A., Lechuga, L., Quintana, J., Montoya, A., and Manclus, J. (2006b). Real-time detection of chlorpyrifos at part per trillion levels in ground, surface and drinking water samples by a portable surface plasmon resonance immunosensor. *Analytica Chimica Acta*, 561:40 – 47.

Mauriz, E., Calle, A., Montoya, A., and Lechuga, L. (2006c). Determination of environmental organic pollutants with a portable optical immunosensor. *Talanta*, 69(2):359 – 364. 1st Swift-WFD Workshop on Validation of Robustness of Sensors and Bioassays for Screening Pollutants.

MaxStream, I. (2007). *XBee ^{TM} Series 2 OEM RF Modules Product Manual v 1.x.1x - ZigBee Protocol*. MaxStream, Inc.

McKay, C. and Smith, H. D. (2005). Possibilities for methanogenic life in liquid methane on the surface of titan. *Icarus*, 178:274–276.

McKey, C. P. (1993). Relevance of antarctic microbial ecosystems to exobiology. In *Antarctic microbiology*, pages 593–601. In E. I. Friedmann (ed.), Wiley-Liss, New York.

Mouvet, C., Harris, R. D., Maciag, C., Luff, B. J., Wilkinson, J. S., Piehler, J., Brecht, A., Gauglitz, G., Abuknesha, R., and Ismail., G. (1997). Determination of simazine in water samples by waveguide surface plasmon resonance. *Anal. Chim. Acta No.338*, pages 109–117.

Naimushin, A. N., Soelberg, S. D., Nguyen, D. K., Dunlap, L., Bartholomew, D., Elkind, J., Melendez, J., and Furlong, C. E. (2002). Detection of staphylococcus aureus enterotoxin b at femtomolar levels with a miniature integrated two-channel surface plasmon resonance (spr) sensor. *Biosensors and Bioelectronics*, 17(6-7):573 – 584.

Nakamoto, K., Kurita, R., Sekioka, N., and Niwa, O. (2008). Simultaneous on-chip surface plasmon resonance measurement of disease marker protein and small metabolite combined with immuno- and enzymatic reactions. *Chemistry Letters*, 37(7):698–699.

Oh, B.-K., Lee, W., Kim, Y.-K., Lee, W. H., and Choi, J.-W. (2004). Surface plasmon resonance immunosensor using self-assembled protein g for the detection of salmonella paratyphi. *Journal of Biotechnology*, 111(1):1 – 8.

Otto, A. (1968). Excitation of nonradiative surface plasma waves in silver by method of frustrated total reflection. *Z. Phys.*, pages 216–398.

Padhy, P., Dash, R. K., Martinez, K., and Jennings, N. R. (2010). A utility-based adaptive sensing and multihop communication protocol for wireless sensor networks. *ACM Trans. Sen. Netw.*, 6(3):27:1–27:39.

Page, L. (2009). Expedition to probe cavern lake 3km beneath antarctic ice. http://www.theregister.co.uk/2009/03/03/ lake_ellsworth_expedition_approved/.

Painter, T. H., Duval, B., Thomas, W. H., Mendez, M., Heintzelman, S., and Dozier, J. (2001). Detection and quantification of snow algae with an airborne imaging spectrometer. *Applied and Environmental Microbiology*, 67(11):5267–5272.

Palik, E. D. (1991). *Handbook of Optical Constants of Solids*. Academic Press, Boston.

Palumbo, M., Pearson, C., Nagel, J., and Petty, M. (2003). Surface plasmon resonance sensing of liquids using polyelectrolyte thin films. *Sensors and Actuators B: Chemical*, 91(1-3):291 – 297.

Pekhteryev, G., Sahinoglu, Z., Orlik, P. V., and Bhatti, G. (2005). Image transmission over ieee 802.15.4 and zigbee networks. In *International Symposium on Circuits and Systems (ISCAS 2005), 23-26 May 2005, Kobe, Japan*, pages 3539–3542. IEEE.

Pluchery, O., Vayron, R., and Van, K.-M. (2011). Laboratory experiments for exploring the surface plasmon resonance. *Eur. J. Phys.*, pages 585–599.

Popov, E., Bozkov, B., and Neviere, M. (1996). The inverted surface plasmon resonance: Phenomenological explanation. *Journal of Modern Optics*, 43(6):1001 – 1110.

Prabhakar, A. (2009). C code to convert jpeg to bmp in linux using libjpeg. http://digitalpbk.blogspot.it/.

Prak, A., Leeuwis, H., Heideman, R. G., Leinse, A., and Borst, G. (2011). Integration of optical waveguides and microfluidics in a miniaturized antibody micro-array system for life detection in the nasa/esa exomars mission. In *Proc. SPIE 7928, 79280L (2011)*.

Pudritz, R., Higgs, P., and Stone, J. (2007). *Planetary Systems and the Origins of Life*. Cambridge University Press, Cambridge.

Raether, H. (1988). *Surface plasmons on smooth and rough surfaces and on gratings*. Springer tracts in modern physics 111. Springer-Verlag, Berlin.

Roche, P. J. R., Filion-Côté, S., Cheung, M. C.-K., Chodavarapu, V. P., and Kirk, A. G. (2011). A camera phone localised surface plasmon biosensing platform towards low-cost label-free diagnostic testing. *Journal of Sensors*, 2011:1 – 7. Article ID 406425.

RoyalTek, L. T. D. (2008). Rgm-3600 operational manual. http://www.royaltek.com.

Schlecht, U., Nomura, Y., Bachmann, T., and Karube, I. (2002). Reversible surface thiol immobilization of carboxyl group containing haptens to a biacore biosensor chip enabling repeated usage of a single sensor surface. *Bioconjugate Chemistry*, 13(2):188–193.

SCHOTT (2011). Schott glasses database. http://www.schott.com/advanced_optics /english/tools_downloads/.

Schulte, W., Hofer, S., Hofmann, P., Thiele, H., von Heise-Rotenburg, R., Toporsk, J., and Rettberg, P. (2007). Automated payload and instruments for astrobiology research developed and studied by german medium-sized space industry in cooperation with european academia. *Acta Astronautica*, 60(12):966 – 973.

Seifert, M., Haindl, S., and Hock, B. (1999). Development of an enzyme linked receptor assay (elra) for estrogens and xenoestrogens. *Analytica Chimica Acta*, 386(3):191 – 199.

Sharma, A. K. and Mohr, G. J. (2008). Theoretical understanding of an alternating dielectric multilayer-based fiber optic spr sensor and its application to gas sensing. *New Journal of Physics*, 10(2):023039.

Sherry, L. J., Chang, S.-H., Schatz, G. C., Van Duyne, R. P., Wiley, B. J., and Xia, Y. (2005). Localized surface plasmon resonance spectroscopy of single silver nanocubes. *Nano Letters*, 5(10):2034–2038.

Shulz, L. G. (1954). The optical constants of silver, gold, copper and aluminum. 1) the absorption coefficient k and 2) the index of refraction n. *Journal of Optical Society of America*, 44(5):357–368.

Siegert, M., Behar, A., Bentley, M., Blake, D., Bowden, S., Christoffersen, P., Cockell, C., Corr, H., Cullen, D., Edwards, H., Ellery, A., Ellis-Evans, C., Griffiths, G., Hindmarsh, R., Hodgson, D., King, E., Lamb, H., Lane, L., Makinson, K., Mowlem, M., Parnell, J., Pearce, D., Priscu, J., Rivera, A., Sephton, M., Sims, M., Smith, A., Tranter, M., Wadham, J., Wilson, G., and Woodward, J. (2007). Exploration of ellsworth subglacial lake: a concept paper on the development, organisation and execution of an experiment to explore, measure and sample the environment of a west antarctic subglacial lake. *Rev Environ Sci Biotechnol, No. 6*, pages 161–179.

Sims, M., Cullen, D., Bannister, N., Grant, W., Henry, O., Jones, R., McKnight, D., Thompson, D., and Wilson, P. (2005). The specific molecular identification of life experiment (smile). *Planetary and Space Science*, 53(8):781 – 791.

SOPRALAB (2012). Basic n and k database. http://www.sopra.sa.com/.

Stewart, M. E., Anderton, C. R., Thompson, L. B., Maria, J., Gray, S. K., Rogers, J. A., and Nuzzo, R. G. (2008). Nanostructured plasmonic sensors. *Chemical Reviews*, 108(2):494–521.

Sweet, M. R. (2010). Serial programming guide for posix operating systems, 5th edition, 6th revision. http://www.easysw.com/~mike/serial/index.html.

Szewczyk, R., Mainwaring, A., Polastre, J., Anderson, J., and Culler, D. (2004). An analysis of a large scale habitat monitoring application. In *Proceedings of the 2nd international conference on Embedded networked sensor systems*, SenSys '04, pages 214–226, New York, NY, USA. ACM.

Szunerits, S., Castel, X., and Boukherroub, R. (2008). Surface Plasmon Resonance Investigation of Silver and Gold Films Coated with Thin Indium Tin Oxide Layers: Influence on Stability and Sensitivity. *Journal of Physical Chemistry C*, 112(40):15813 – 15817.

Tobiska, P., Hugon, O., Trouillet, A., and Gagnaire, H. (2001). An integrated optic hydrogen sensor based on spr on palladium. *Sensors and Actuators B: Chemical*, 74(1 - 3):168 – 172. Proceedings of the 5th European Conference on Optical Chemical Sensors and Biosensors.

Tolle, G., Polastre, J., Szewczyk, R., Culler, D., Turner, N., Tu, K., Burgess, S., Dawson, T., Buonadonna, P., Gay, D., and Hong, W. (2005). A macroscope in the redwoods. In *Proceedings of the 3rd international conference on Embedded networked sensor systems*, SenSys '05, pages 51–63, New York, NY, USA. ACM.

Tran, H., Leong, C., Loke, W. K., Dogovski, C., and Liu, C.-Q. (2008). Surface plasmon resonance detection of ricin and horticultural ricin variants in environmental samples. *Toxicon*, 52(4):582 – 588.

van-der Wielen, P. W. J. J., Bolhuis, H., Borin, S., Daffonchio, D., Corselli, C., Giuliano, L., D'Auria, G., de Lange, G. J., Huebner, A., Varnavas, S. P., Thomson, J., Tamburini, C., Marty, D., McGenity, T. J., Timmis, K. N., and Party, B. S. (2005). The enigma of prokaryotic life in deep hypersaline anoxic basins. *Science*, 307(5706):121–123.

Vanderwerf, D. F. (2010). *Applied Prismatic and Reflective Optics*, pages 61–70. SPIE Press.

Vedrine, C., Leclerc, J.-C., Durrieu, C., and Tran-Minh, C. (2003). Optical whole-cell biosensor using chlorella vulgaris designed for monitoring herbicides. *Biosens. Bioelectron. No.18*, pages 457–453.

Vishnivetskaya, T. A., Rokhina, L. G., Spinna, E. V., Shatilovich, A. V., Vorobyova, E. A., and Gilichinsky, D. A. (2001). Ancient viable phototrops within the permafrost. *Nova Hedwigia*, 123:427–441.

von Blanckenhagen, B. (2006). Practical layer designs for polarizing beam-splitter cubes. *APPLIED OPTICS Vol. 45, No. 7*, pages 1539–1543.

Watanabe, K., Matsumoto, K., Ohgaki, T., Sakaguchi, I., Ohashi, N., Hishita, S., and Haneda, H. (2010). Development of zno-based surface plasmon resonance gas sensor and analysis of uv irradiation effect on no2 desorption from zno thin films. *Journal of the Ceramic Society of Japan*, 118(1375):193–196.

Werner-allen, G., Johnson, J., Ruiz, M., Lees, J., and Welsh, M. (2005). Monitoring volcanic eruptions with a wireless sensor network. In *in Proceedings of the Second European Workshop on Wireless Sensor Networks (EWSN' 05*.

Werner-allen, G., Lorincz, K., Johnson, J., Lees, J., and Welsh, M. (2006). Fidelity and yield in a volcano monitoring sensor network. In *In Proceedings of the 7th USENIX Symposium on Operating Systems Design and Implementation (OSDI 2006*, pages 381–396.

Werner-Allen, G., Lorincz, K., Ruiz, M., Marcillo, O., Johnson, J., Lees, J., and Welsh, M. (2006). Deploying a wireless sensor network on an active volcano. *Internet Computing, IEEE*, 10(2):18 – 25.

Wu, L., Chu, H. S., Koh, W. S., and Li, E. P. (2010). Highly sensitive graphene biosensors based on surface plasmon resonance. *Optics Express*, 18(14):14395–14400.

Zacher, T. and Wischerhoff, E. (2002). Real-Time Two-Wavelength Surface Plasmon Resonance as a Tool for the Vertical Resolution of Binding Processes in Biosensing Hydrogels. *Langmuir*, 18(5):1748–1759.

Zarnecki, J. C., Leese, M. R., Hathi, B., Ball, A. J., Hagermann, A., Towner, M. C., Lorenz, R. D., McDonnell, J. A. M., Green, S. F., Patel, M. R., Ringrose, T. J., Rosenberg, P. D., Atkinson, K. R., Paton, M. D., Banaszkiewicz, M., Clark, B. C., Ferri, F., Fulchignoni, M., Ghafoor, N.

A. L., Kargl, G., Svedhem, H., Delderfield, J., Grande, M., Parker, D. J., Challenor, P. G., and Geake, J. E. (2005). A soft solid surface on titan as revealed by the huygens surface science package. *Nature*, 438:792 – 795.

Zhang, J., Zhang, L., and Xu, W. (2012). Surface plasmon polaritons: physics and applications. *Journal of Physics D: Applied Physics*, 45(11):113001.

Zhao, J., Zhang, X., Yonzon, C. R., Haes, A. J., and Van Duyne, R. P. (2006). Localized surface plasmon resonance biosensors. *Nanomedicine*, 1(2):219–228.

Appendix C

Acknowledgements

Ringrazio il mio supervisore, la Dott. Pelizzo, per i consigli e le opportunitàă datemi durante il periodo del mio dottorato,
la mia corelatrice Dott. Zuppella, l' Ing. Corso, la Dott. Polito, l' Ing. Miozzi, il Dott. Rossi, il Dott. Natali, l' Ing. Coccola, il Dott. Bonora, l' Ing. Favero per l' aiuto fornitomi nella mia attività di ricerca.

Ad Andrea, mia madre, mio padre ed a Roberto: grazie con tutto il cuore, per tutto.